Ultrafast manipulation of single photons using dispersion and sum-frequency generation

by

John Matthew Donohue

A thesis
presented to the University of Waterloo
in fulfillment of the
thesis requirement for the degree of
Doctor of Philosophy
in
Physics (Quantum Information)

Waterloo, Ontario, Canada, 2016

© John Matthew Donohue 2016

I hereby declare that I am the sole author of this thesis, except where noted. This is a true copy of the thesis, including any required final revisions, as accepted by my examiners.

I understand that my thesis may be made electronically available to the public.

Abstract

Single photons provide a natural platform for quantum communication and quantum networking, as they can be entangled in many degrees of freedom and maintain coherence over long-distance links. However, while their minimal interactions with the environment isolate them from detrimental noise, it can make them difficult to measure and manipulate. In particular, manipulation on the ultrafast timescale is necessary to fully exploit the energy-time (or spectral) photonic degree of freedom. Full control over the spectral properties of single photons is key to many quantum technologies and opens the door to natural high-dimensional quantum encodings.

In this thesis, we theoretically and experimentally examine the use of nonlinear optical processes mediated by strong laser pulses as a method to control the spectral properties of ultrafast single photons. By mixing single-photon pulses with strong escort pulses that have been shaped through dispersion in a nonlinear crystal, the shape of the escort is imprinted on the photon, resulting in a custom-tailored upconverted pulse. We theoretically examine this process for quadratic spectral phases and show that it has the potential to be simultaneously effective and efficient for the customization of single-photon spectral waveforms, and can be performed in an entanglement-conserving manner.

We then experimentally demonstrate the range of this technique through three applications. First, we show that sum-frequency generation with shaped pulses can be used to coherently measure time-bin encoded photons with bin separations on the order of picoseconds, well below the timing resolution of our detectors. Secondly, we show that this technique can be adapted to convert a train of pulses to a frequency comb, which can be read out in a straightforward manner using diffraction-based spectrometry. We also show here that this process can be performed in a polarization-maintaining fashion, and demonstrate that entanglement with a partner photon is conserved with high fidelity. Finally, we show that this process can be viewed as a time lens, which modulates a temporal waveform in an analogous fashion to a lens focusing a beam of light. We apply the time lens to a photon from an energy-time entangled pair, and show negative magnification of the joint spectrum through a reversal of the spectral correlations. Such processes could find application in quantum state engineering and high-speed single-photon measurement.

Acknowledgements

Where to start? The graduate student experience is often called out as five-plus years of being over-stressed and under-appreciated, but thanks to so many fantastic people around the University of Waterloo and the Institute for Quantum Computing, I've never really felt that way (give or take scholarship application season). While there are some individuals who deserve special thanks for their help, support, friendship, and guidance over the past five years, I can best sum up my feelings with a simple and sincere thank you to everyone whose path I've crossed here.

I'd like to start by thanking my supervisor, Kevin Resch. Thank you for your seemingly infinite knowledge, your incredibly constructive comments on every piece of paper sent your way, your willingness to examine a troubled experiment, your enthusiasm at any hint of promising data, and getting that trivia question about Lobot. I'd also like to thank my examining committee of Norbert Lütkenhaus, Thomas Jennewein, and Chris Wilson for showing up to numerous tedious meetings (and agreeing to show up to one more), and Franco Wong for agreeing to hop on as my external examiner.

My time at IQC wouldn't have been nearly as enjoyable and productive were it not for the entire Quantum Optics and Quantum Information group. Jonathan Lavoie deserves a special thanks for teaching me everything I know about experimental quantum optics, from lab book etiquette to beam height vigilance. From office sports to synchronized balloon tossing to actually figuring out some science, my office mates Mike Mazurek and Kent Fisher have made the past five years enjoyable, fruitful, and memorable, and have set absolutely unreasonable standards for future office environments. Mike's scientific reasoning is only matched by his foosball prowess, and Kent's endless patience and diligence in his experimental work is only rivalled by his commitment to local headline investigation. The praise extends to the rest of the QOQI group throughout the years. Thanks to Deny Hamel for showing us around a snow-covered Moncton and for setting one heck of an example to follow; to Jean-Philippe MacLean for eventually accepting that Peezy was a thing and ensuring that the upconversion setup will keep working after I leave; to Maggie Agnew for teaching me the basics of scientific grammar and making Bill like us more through mere association; to Jeff Salvail for being the first to answer the hip-hop question

iv

A ray of sunlight is made of many atoms.

\- Eros, *Plan 9 from Outer Space*

Table of Contents

List of Tables

List of Figures

xiv

Chapter 1

Quantum optics and entanglement

Chapter overview

The control of coherent light has been undeniably one of the most important advancements of the 20th century, stemming from the advent of the laser and its applications in medicine and technology. In addition to its use in spectroscopy, atom trapping, and microscopy, lasers have enabled the study of the quantum properties of light itself. The study of photons has proven incredibly fruitful, both in terms of demonstrating fundamental concepts in quantum theory such as entanglement but also as a potent platform for quantum computing [1, 2, 3], quantum communication [4, 5], and quantum metrology [6, 7].

In order to fully realize the potential of photons for quantum information technologies, precise, noiseless, efficient, and complete control over their many degrees of freedom is essential. In this thesis, we will discuss in detail how to control the temporal and spectral properties of single photons in just this manner. In this chapter, we will discuss how to describe a photon mathematically, and some of the properties that differentiate and unite it with the classical picture of a laser beam.

1.1 Photons and photonic quantum information

1.1.1 Quantum description of the electromagnetic field (or What is a photon?)

We first define the photon as a unit excitation of the electromagnetic field in a specified mode. We will (very) briefly outline the meaning of this statement, but it is covered in more detail in any quantum optics text [8, 9, 10]. We consider standing-wave modes in a one-dimensional cavity, with oscillations along the $\hat{z}$ direction. A family of solutions to Maxwell's equations in a cavity of length L_z with electric field polarization along the $\hat{x}$ axis are given by

$$\vec{E}_k = E_0 \left(\sin kz \sin \omega_k t \right) \hat{x}, \ \vec{B}_k = \frac{E_0}{c} \left(\cos kz \cos \omega_k t \right) \hat{y}, \tag{1.1}$$

where the wave number k is some multiple of $2\pi/L_z$ and the angular frequency is $\omega = ck$. The classical energy, and thus the Hamiltonian, of this electromagnetic field mode integrated over the length L_z and a cross-sectional area $\mathcal{A}$ is

$$\begin{aligned} H_k &= \frac{1}{2} \int_0^{L_z} \mathrm{d}z \int \mathrm{d}\mathcal{A} \left(\epsilon_0 E_{x,k}^2 + \frac{1}{\mu_0} B_{y,k}^2 \right) \\ &= \frac{1}{2} \left[\omega_k^2 \left(\sqrt{\frac{\epsilon_0 V}{2\omega_k^2}} E_0 \sin \omega_k t \right) + \left(\sqrt{\frac{\epsilon_0 V}{2}} E_0 \cos \omega_k t \right) \right] \\ &= \frac{1}{2} \left[\omega_k^2 q(t) + p(t) \right], \end{aligned} \tag{1.2}$$

where $V = L_z \mathcal{A}$ is the volume of integration. This Hamiltonian has the form of the classical simple harmonic oscillator, with canonical position $q(t)$ and momentum $p(t) = \frac{\mathrm{d}}{\mathrm{d}t} q(t)$.

To find the energy eigenvalues of this Hamiltonian, we can follow the Dirac approach by introducing the operators $\hat{a} = (i\hat{p} + \omega \hat{q})/\sqrt{2\hbar\omega}$ and $\hat{a}^\dagger = (-i\hat{p} + \omega \hat{q})/\sqrt{2\hbar\omega}$. Given that the commutator of the canonical position and momentum is $[\hat{q}, \hat{p}] = i\hbar$, the commutator of

2

the $\hat{a}$ operators is $[\hat{a}, \hat{a}^\dagger] = 1$. The Hamiltonian of Eq. (1.2) can be rewritten as

$$\hat{H}_k = \hbar\omega_k \left(\hat{a}_k^\dagger \hat{a}_k + \frac{1}{2} \right). \tag{1.3}$$

This expression is very familiar for anyone who has taken an introductory quantum mechanics class, and by noting the commutation relation, it can be easily seen that for eigenstates of the Hamiltonian $|\psi_{n,k}\rangle$ with energy $\mathcal{E}_n$,

$$\hat{H}_k|\psi_{n,k}\rangle = \mathcal{E}_n|\psi_{n,k}\rangle, \ \ \hat{H}_k\hat{a}_k|\psi_{n,k}\rangle = (\mathcal{E}_n - \hbar\omega_k)\hat{a}_k|\psi_{n,k}\rangle, \ \ \hat{H}_k\hat{a}_k^\dagger|\psi_{n,k}\rangle = (\mathcal{E}_n + \hbar\omega_k)\hat{a}_k^\dagger|\psi_{n,k}\rangle, \tag{1.4}$$

implying that $\hat{a}_k$ and $\hat{a}_k^\dagger$ lower and raise the energy in mode k by a unit $\hbar\omega$. Because of this, they are often referred to as the *annihilation* and *creation* operators, and the units of energy they annihilate and create are *photons*. We can write our electric field operators in terms of these operators by defining the electric field operator in a mode defined by k as [10]

$$\begin{aligned}
\hat{\vec{E}}_k &= i\sqrt{\frac{\hbar\omega_k}{2\epsilon_0 V}} \left(\hat{a}_k e^{-i\omega_k t + i\vec{k}\cdot\vec{r}} - \hat{a}_k^\dagger e^{i\omega_k t - i\vec{k}\cdot\vec{r}} \right) \hat{\varepsilon}_k \\
&= \hat{\vec{E}}_k^{(+)} + \hat{\vec{E}}_k^{(-)},
\end{aligned} \tag{1.5}$$

where $\hat{\varepsilon}_k$ denotes the direction of polarization and the second line breaks the operator into positive and negative frequency components. Note that $\hat{\vec{E}}_k^{(+)\dagger} = \hat{\vec{E}}_k^{(-)}$, and thus the electric field is self-adjoint, $\hat{\vec{E}}_k^\dagger = \hat{\vec{E}}_k$.

Electric field operators in the continuum

One issue with the electric field operators as currently defined is the pesky volume term $V = L_z\mathcal{A}$ that survives in Eq. (1.5). In this thesis, our discussion will be limited to photons in a single spatial mode, and the length of the z-axis may be realistically assumed to be much longer than any optical wavelengths under consideration. In this situation, it is advantageous to remove the fictional volume and instead work in the continuum [11]. To do so, we first consider the total electric field operator. We will consider the electric field in a linear and lossless dielectric, and thus straightforwardly replace ϵ_0 with $n^2\epsilon_0$, where n

is the index of refraction and is implicitly a function of the frequency ω and direction $\vec{k}$. We will also neglect the polarization vector for simplicity. With these modifications, we write the positive-frequency electric field operator as

$$\hat{E}^{(+)}(\vec{r},t) = \sum_{k_x,k_y,k_z} \hat{E}_k^{(+)}(\vec{r},t) = i \sum_{k_x,k_y,k_z} \sqrt{\frac{\hbar\omega_k}{2\epsilon_0 n^2 L_z \mathcal{A}}} \hat{a}_{k_x,k_y,k_z} e^{-i\omega_k t + ik_x x + ik_y y + ik_z z}. \quad (1.6)$$

The allowable k_z values in a medium of length of L_z are separated by $\Delta k_z = \frac{2\pi}{L_z}$. We then take the limit $L_z \gg \frac{2\pi}{k_z}$ for any relevant spatial frequencies, which takes us from a discrete spectrum to an effective continuum. To facilitate this, the sum over possible k_z values must be converted to an integral by the substitutions $\sum_{k_z} \mapsto \frac{1}{\Delta k_z} \int dk_z$. Additionally, the commutation relations must be re-addressed; in the discrete case, $[\hat{a}_{k_{z,i}}, \hat{a}_{k_{z,j}}] = \delta_{i,j}$, where $\delta_{i,j}$ is the (discrete) Kronecker delta function. For the continuum case, $\delta_{i,j} \mapsto \Delta k_z \delta(k_{z,i} - k_{z,j})$ [11], where $\delta(x - x')$ is the Dirac delta function. To ensure that the continuum ladder operators still maintain the proper commutation relations, $[\hat{a}_{k_z}, \hat{a}_{k_z'}] = \delta(k_z - k_z')$, we make the substitution $\hat{a}_{k_z} \mapsto \sqrt{\Delta k_z} \hat{a}_{k_z}$. With these substitutions, and writing L_z as $\frac{2\pi}{\Delta k_z}$, we can rewrite Eq. (1.6) as

$$\hat{E}^{(+)}(\vec{r},t) = i \sum_{k_x,k_y} \frac{1}{\Delta k_z} \int dk_z \sqrt{\frac{\hbar\omega \Delta k_z}{4\pi\epsilon_0 n^2 \mathcal{A}}} \sqrt{\Delta k_z} \hat{a}_{k_x,k_y,k_z} e^{-i\omega_k t + ik_x x + ik_y y + ik_z z} \quad (1.7)$$

$$= i \sum_{k_x,k_y} \int dk_z \sqrt{\frac{\hbar\omega}{4\pi\epsilon_0 n^2 \mathcal{A}}} \hat{a}_{k_x,k_y,k_z} e^{-i\omega_k t + ik_x x + ik_y y + ik_z z}. \quad (1.8)$$

We next make similar transformations to the transverse operators, which are quantized by $\Delta k_T = \frac{2\pi}{\sqrt{\mathcal{A}}}$. We assume that this discrete spectrum is well-approximated by a continuum, and apply identical transformations to obtain the continuum electric field operator,

$$\hat{E}^{(+)}(\vec{r},t) = i \iiint dk_x dk_y dk_z \sqrt{\frac{\hbar\omega}{16\pi^3 \epsilon_0 n^2}} \hat{a}_{k_x,k_y,k_z} e^{-i\omega_k t + ik_x x + ik_y y + ik_z z}.$$

$$= i \iiint d^3\mathbf{k} \sqrt{\frac{\hbar\omega}{16\pi^3 \epsilon_0 n^2}} \hat{a}_{\mathbf{k}} e^{-i\omega_k t + i\mathbf{k}\cdot\mathbf{r}}. \quad (1.9)$$

1.1.2 Quantum states of light

Fock states and the beamsplitter

The ground state of the Hamiltonian of Eq. (1.3) is the state such that the expectation value of the Hamiltonian is its lowest, defined as the state $|0\rangle$ with $\hat{a}|0\rangle = 0$. $|0\rangle$ is also called the vacuum state, and is the state with zero photons present. The state $\hat{a}^\dagger|0\rangle = |1\rangle$ is the state of a *single* photon. The *Fock basis* is the basis of representation for a state of light with a well defined photon number, $|n\rangle$. These basis states can be linked through the operator relations $\hat{a}^\dagger|n\rangle = \sqrt{n+1}|n+1\rangle$ and $\hat{a}|n\rangle = \sqrt{n}|n-1\rangle$. The photon number operator $\hat{n}_m = \hat{a}_m^\dagger \hat{a}_m$ is a useful observable whose interpretation is the number of photons occupying mode m.

The behaviour of Fock states is particularly interesting when considering how they interact with each other in various optical devices. The simplest of these is the two-mode beamsplitter, which mediates an interaction of modes defined by the annihilation operators $\hat{a}$ and $\hat{b}$ through the unitary [8]

$$\hat{U}_{BS}(\theta) = \exp\left[-i\theta\left(\hat{a}\hat{b}^\dagger + \hat{a}^\dagger\hat{b}\right)\right]. \tag{1.10}$$

This unitary conserves total photon number and swaps photons between modes a and b with a coupling constant θ. The reflectance and transmittance of the beamsplitter are then given by

$$R = \sin^2(\theta), \quad T = \cos^2(\theta). \tag{1.11}$$

In particular, if $\theta = \frac{\pi}{4}$, the beamsplitter has a 50/50 splitting ratio, and transforms the annihilation operators as

$$\hat{U}_{BS}^\dagger\left(\frac{\pi}{4}\right)\hat{a}\hat{U}_{BS}\left(\frac{\pi}{4}\right) = \frac{1}{\sqrt{2}}\left(\hat{a} + i\hat{b}\right) \tag{1.12}$$

$$\hat{U}_{BS}^\dagger\left(\frac{\pi}{4}\right)\hat{b}\hat{U}_{BS}\left(\frac{\pi}{4}\right) = \frac{1}{\sqrt{2}}\left(i\hat{a} + \hat{b}\right). \tag{1.13}$$

The relative phase between the transformed $\hat{a}$ and $\hat{b}$ operators is necessary to preserve the orthogonality of the two input modes and overall photon number.

One particularly striking quantum effect is photon bunching, often called the Hong-Ou-Mandel (or HOM) effect [12]. If a state with one photon in each mode is incident on a beamsplitter, applying the beamsplitter transformations results in an output state of

$$|11\rangle = \hat{a}^\dagger \hat{b}^\dagger |00\rangle \stackrel{BS}{\mapsto} \frac{1}{2} \left[-i(\hat{a}^\dagger)^2 + \hat{a}^\dagger \hat{b}^\dagger - \hat{b}^\dagger \hat{a}^\dagger - i(\hat{b}^\dagger)^2 \right] |00\rangle = -i \frac{|20\rangle + |02\rangle}{\sqrt{2}}. \qquad (1.14)$$

Thus, when two photonic modes containing one photon each are split, both photons always exit the same port. Note that applying a phase to either input photon does not affect this result. If the two photons do not perfectly overlap or the beamsplitter is imperfect, the cancellation of the different-port terms will be imperfect, resulting in a signature HOM dip as the input photons are scanned in a certain degree of freedom, such as time [12]. See Sec. 2.3.5 for more details on the HOM dip and its applications in ultrafast measurement.

Bucket detectors

Independent of the degrees of freedom present, one extremely important practical tool is the *single-photon detector*. While there is continuous and very promising research in photon-number resolving detectors [13, 14, 15], the work in this thesis is based entirely on *bucket detectors*, which output either a "click" or no click depending on whether or not they saw a photon. Examples of this type of detector used in experiments in this thesis are avalanche photodiodes (APDs) and some photomultiplier tubes (PMTs). Bucket detectors may seem weak at a glance, but have many advantages. They are generally much cheaper than superconducting number-resolving detectors, have detection efficiencies around 50%, and do not require cryogenic cooling [16]. Multiplexing a signal into many bucket detectors can also approximate a photon-number resolving detector [17, 18].

In the ideal case, the no-click scenario corresponds to a projective measurement $\hat{M}_{no-click} = |0\rangle\langle 0|$, where the click corresponds to the measurement $\hat{M}_{click} = \mathbb{1} - |0\rangle\langle 0|$. In reality, these detectors do not have perfect detection efficiency, and occasionally detect either ambient light or electronic fluctuations in what is known as a *dark count*. We model the detector

with some efficiency η and a dark count probability ϵ as

$$\hat{M}_{click} = \sum_n \left\{ 1 - (1-\eta)^n + \epsilon - \epsilon \left[1 - (1-\eta)^n \right] \right\} |n\rangle\langle n|, \qquad (1.15)$$

where the $1-(1-\eta)^n$ term corresponds to the probability of detecting one of n photons and the ϵ corresponds to a dark count. The no-click measurement operator can be expressed simply as $\hat{M}_{no-click} = \mathbb{1} - \hat{M}_{click}$ since the detector either does or does not click. In general, one also has to take into account factors such as frequency-dependence; in the cases we consider, the bandwidths of light we send in will be narrow enough such that η is constant.

Coherent states

Fock states are intrinsically quantum, as they arise from the discretization of the electromagnetic field. A classical laser pulse is not simply a state of large photon number, as unlike classical coherent light, the electric field arising from high-number Fock states is zero ($\langle n|\hat{E}|n\rangle = 0$) and the interference of two independent sources at a beamsplitter is independent of phase. Rather, a state that has Poissonian distribution in photon number—known as a *coherent state*—is generally viewed as the state with corresponds to classical coherent light in the limit of large photon number, as it has the same energy fluctuations and carries phase as expected [9]. Given a phase reference [19], the coherent state is defined as

$$|\alpha\rangle = e^{-\frac{1}{2}|\alpha|^2} \sum_{n=0}^{\infty} \frac{\alpha^n}{\sqrt{n!}} |n\rangle. \qquad (1.16)$$

It is easy to show that this state is an eigenstate of the annihilation operator, i.e. $\hat{a}|\alpha\rangle = \alpha|\alpha\rangle$. The mean number of photons and variance in that mean are

$$\langle\alpha|\hat{n}|\alpha\rangle = |\alpha|^2, \ \ \Delta n = \sqrt{\langle\hat{n}^2\rangle - \langle\hat{n}\rangle^2} = |\alpha|. \qquad (1.17)$$

The coherent state as defined is the eigenstate of the annihilation operator, but not of the creation operator $\hat{a}^\dagger$; indeed, $\hat{a}^\dagger|\alpha\rangle$ is known as a photon-added coherent state and has interesting quantum properties in its own right [20]. However, in the limit where $|\alpha|$

is very large, we may approximate the coherent state to be an eigenstate of the creation operator as well by noting that the relative uncertainty in the photon number is small for bright pulses, $\Delta n / \langle n \rangle = 1/|\alpha|$. In the representation of the coherent state as in Eq. (1.16), we can approximate $n\alpha^{n-1} \approx \alpha^* \alpha^n$ and find that

$$
\begin{aligned}
\hat{a}^\dagger |\alpha\rangle &= e^{-\frac{1}{2}|\alpha|^2} \sum_{n=0}^{\infty} \frac{\alpha^n}{\sqrt{n!}} \sqrt{n+1}|n+1\rangle \\
&= e^{-\frac{1}{2}|\alpha|^2} \sum_{n=1}^{\infty} \frac{\alpha^{n-1}}{\sqrt{(n-1)!}} \sqrt{n} \frac{\sqrt{n}}{\sqrt{n}}|n\rangle \\
&= e^{-\frac{1}{2}|\alpha|^2} \sum_{n=1}^{\infty} \frac{n\alpha^{n-1}}{\sqrt{n!}}|n\rangle \\
&\stackrel{|\alpha|^2 \gg 1}{\approx} e^{-\frac{1}{2}|\alpha|^2} \sum_{n=0}^{\infty} \frac{\alpha^* \alpha^n}{\sqrt{n!}}|n\rangle = \alpha^* |\alpha\rangle.
\end{aligned}
\tag{1.18}
$$

This large-amplitude limit gives the expected classical electric field intensities and will prove immensely useful in describing nonlinear processes involving a quantum-level signal and a strong laser beam.

1.1.3 Single-photon character from second-order coherences

The Hong-Ou-Mandel interference of Eq. (1.14) is one example of an effect unique to quantum states of light, but measuring it requires two photons and a carefully aligned interferometer. To confirm the single-photon character of a state, it is often more convenient to look at correlation functions, specifically the degree of second-order coherence, or $g^{(2)}$ [8, 9, 10][1]. This function defines correlations in intensity fluctuations, and is defined classically as

$$
g^{(2)} = \frac{\langle I(t)^2 \rangle}{\langle I(t) \rangle^2}.
\tag{1.19}
$$

---

[1]The $g^{(2)}$ function is often defined as the degree of second-order temporal coherence $g^{(2)}(\tau)$, or an analogous form in space. For our purposes, we are only interested in $g^{(2)}(0)$, and neglect the temporal term completely. The temporal second-order degree of coherence can be interpreted as defining the timescale on which intensity fluctuations are correlated, and classically obeys the relation $g^{(2)}(0) \geq g^{(2)}(\tau)$.

This quantity is bounded from below by one, which can be seen by writing the intensity in terms of its time average and its fluctuations from that average, $I(t) = I + \Delta I(t)$ [9]. While intensity is always positive, the fluctuations are allowed to be negative but have an expectation value of zero. The $g^{(2)}$ value can be expanded as

$$g^{(2)} = \frac{I^2 + \langle \Delta I(t)^2 \rangle}{I^2} = 1 + \frac{\langle \Delta I(t)^2 \rangle}{I^2}. \tag{1.20}$$

For a laser source with constant intensity, the $g^{(2)}$ is one, but for a chaotic source, the $g^{(2)}$ may be higher. For example, a single-mode thermal source has a $g^{(2)}$ value of two. However, the $g^{(2)}$ is lower bounded by one.

For single photons, the same limit need not apply. As the intensity of a beam of light is proportional to the number of photons, we can write the quantum degree of second-order coherence as

$$g^{(2)} = \frac{\langle : \hat{n}^2 : \rangle}{\langle \hat{n} \rangle^2} = \frac{\langle \hat{a}^\dagger \hat{a}^\dagger \hat{a} \hat{a} \rangle}{\langle \hat{a}^\dagger \hat{a} \rangle^2}, \tag{1.21}$$

where :: is the normal ordering operator, which removes vacuum contributions. Using this expression and the definition of the coherent state as $\hat{a}|\alpha\rangle = \alpha|\alpha\rangle$, it can be quickly shown that $g^{(2)} = 1$ for a coherent state, consistent with the classical picture. An incoherent state with a thermal photon number distribution can be shown to have a second-order coherence of $g^{(2)} = 2$, once again consistent with the classical results [8]. However, using the ladder operator relationship $\hat{a}|n\rangle = \sqrt{n}|n-1\rangle$, a photon number state $|n\rangle$ for $n > 0$ can be shown to have a second-order coherence of

$$g^{(2)}_{|n\rangle} = 1 - \frac{1}{n}, \tag{1.22}$$

which is less than one. In particular, the second-order coherence of the single photon Fock state, $|1\rangle$, is zero.

To measure a $g^{(2)}$ in experiment, one can use a simple Hanbury-Brown Twiss (HBT) interferometer [21], as shown in Fig. 1.1a. Light in a mode defined by the operator $\hat{a}$ is split at a 50/50 beamsplitter into modes defined by $\hat{c}$ and $\hat{d}$, with vacuum in the other port. The modes $\hat{c}$ and $\hat{d}$ are then measured in coincidence, such that the product of their simultaneous intensity is recorded. Given the beamsplitter transformations of Eq. (1.13)
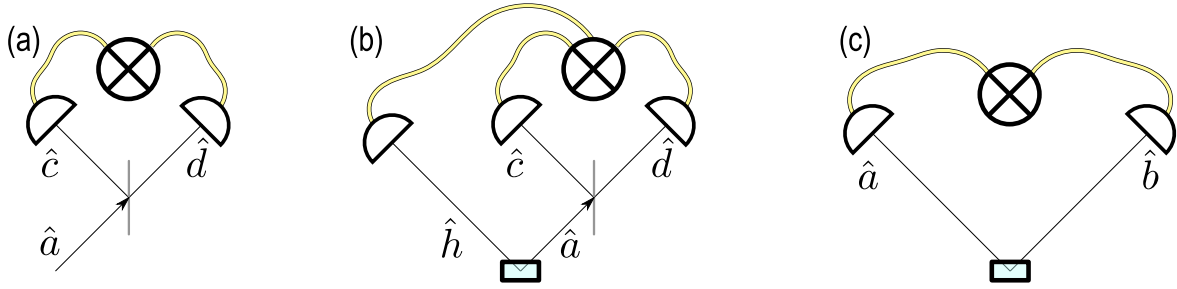
Figure 1.1: **Measuring second-order coherence functions.** (a) A Hanbury-Brown Twiss interferometer, which splits an incoming beam into two detectors which record simultaneous events, can be used to measure second-order coherence functions, or $g^{(2)}$s. (b) In a heralded single-photon source, a detection of a herald photon in mode $\hat{h}$ gates the normal operator of the HBT interferometer. (c) The cross-correlation of two modes, $g_{a,b}^{(1,1)}$, can be calculated by measuring both and recording simultaneous results.

with vacuum in the $\hat{b}$ port, the measurement implemented is

$$\langle \hat{n}_c \hat{n}_d \rangle = \langle \hat{c}^\dagger \hat{d}^\dagger \hat{c} \hat{d} \rangle = \frac{1}{4} \langle \hat{a}^\dagger \hat{a}^\dagger \hat{a} \hat{a} \rangle, \tag{1.23}$$

which is exactly proportional to the numerator of Eq. (1.21). The single-detection events, where we look at only of the detectors, are both found to effectively implement the measurement

$$\langle \hat{n}_c \rangle = \frac{1}{2} \langle \hat{a}^\dagger \hat{a} \rangle. \tag{1.24}$$

Putting these together, we find that the HBT measurement is precisely

$$\frac{\langle \hat{n}_c \hat{n}_d \rangle}{\langle \hat{n}_c \rangle \langle \hat{n}_d \rangle} = \frac{\langle \hat{a}^\dagger \hat{a}^\dagger \hat{a} \hat{a} \rangle}{\langle \hat{a}^\dagger \hat{a} \rangle^2} = g^{(2)}. \tag{1.25}$$

The interpretation of the single-photon $g^{(2)}$ from the Hanbury-Brown Twiss experiment is clear. Eq. (1.25) can be read as the number of coincidences between $\hat{c}$ and $\hat{d}$ divided by the number of photons measured in each mode individually $N_{cd}/N_c/N_d$, or equivalently, the probability of measuring a coincidence normalized by the probability of measuring anything at all, $\frac{P(c\&d)}{P(c)P(d)}$. If the input state is a coherent state, the beamsplitter will split the state into

10

two identical coherent states with expected photon number $|\alpha|^2/2$ [8, 10]. The probability of measuring a coincidence between the two detectors is the same as the product of the probabilities of measuring single-detection events, and the $g^{(2)}$ is one. However, if the state is a single photon, it cannot be split in such a way that both detectors will register a simultaneous event, and the numerator of Eq. (1.25) goes to zero. Observation of this phenomenon through HBT interferometry is a key indicator of single-photon character [22].

Many single-photon sources, including those used in this thesis, act in a heralded fashion, as seen in Fig. 1.1b. Such sources will be discussed in more detail later in the thesis, but their operational principle is straightforward. The photon state in the arm defined by the operator $\hat{a}$ is only of interest given that a detection was measured in the mode defined by the operator $\hat{h}$. This conditional state may have different properties than the unheralded state if the two are correlated in some way. For example, the state $|\psi\rangle = |0\rangle_a|0\rangle_h + \epsilon|1\rangle_a|1\rangle_h$ is mostly vacuum in the $\hat{a}$ arm, but is exactly a single photon Fock state if conditioned upon a herald detection. The coincidence and single-detection events in a $g^{(2)}$ measurement are then also taken to be dependent on a herald detection, with the number of herald detections defining the number of trials run. The $g^{(2)}$ of a herald source can be written as

$$g^{(2)} = \frac{\langle \hat{n}_c \hat{n}_d \hat{n}_h \rangle / \langle \hat{n}_h \rangle}{\langle \hat{n}_c \hat{n}_h \rangle \langle \hat{n}_d \hat{n}_h \rangle / \langle \hat{n}_h \rangle^2} = \frac{P(c\&d\&h)P(h)}{P(c\&h)P(d\&h)} = \frac{N_{cdh}N_h}{N_{ch}N_{dh}}. \tag{1.26}$$

The Hanbury-Brown Twiss measurement of a heralded single photon source as in Fig. 1.1b can also be used to determine other notable properties of the source; notably, if measured without regarding the herald, the $g^{(2)}$ measured will be related to the number of effective modes in the source [23].

The previous discussion has been related to the second-order coherence of a single source, and are often called the *autocorrelation* $g^{(2)}$ functions. We can also consider cross-coherences between two spatially or temporally distinct beams as the *cross-correlation* $g^{(2)}$, sometimes labelled $g^{(1,1)}$ to indicate that it is first-order in each beam. Classically, this cross-correlation is written as [24]

$$g_{a,b}^{(1,1)} = \frac{\langle I_a(t)I_b(t)\rangle}{\langle I_a(t)\rangle\langle I_b(t)\rangle}. \tag{1.27}$$

By the Cauchy-Schwarz inequality [25], this value is bounded by

$$g_{a,b}^{(1,1)} = \frac{\langle I_a(t)I_b(t)\rangle}{\langle I_a(t)\rangle\langle I_b(t)\rangle} \leq \frac{\sqrt{\langle I_a(t)^2\rangle\langle I_b(t)^2\rangle}}{\langle I_a(t)\rangle\langle I_b(t)\rangle} = \sqrt{g_a^{(2)}g_b^{(2)}} \qquad (1.28)$$

This cross-correlation coherence function can be written in a quantum form similar to Eq. (1.21) for single-mode detection as [23]

$$g_{a,b}^{(1,1)} = \frac{\langle \hat{n}_a\hat{n}_b\rangle}{\langle \hat{n}_a\rangle\langle \hat{n}_b\rangle} = \frac{P(a\&b)}{P(a)P(b)}. \qquad (1.29)$$

The scheme for this measurement is simply a detector in each arm, as seen in Fig. 1.1c.

If the $g^{(2)}$s of the individual modes are assumed to be no greater than two (thermal), the classical cross-correlation of Eq. (1.28) is bounded by $g_{a,b}^{(1,1)} \leq 2$ [26, 27]. However, the quantum form of Eq. (1.29) is subject to no such bounds. Consider once again the state $|\psi\rangle = |0\rangle_a|0\rangle_b + \epsilon|1\rangle_a|1\rangle_b$. The $g^{(2)}$ of this state in each mode is, according to Eq. (1.21), zero, but $g_{a,b}^{(1,1)} = 1/\epsilon$, where $\epsilon \ll 1$. The classical bound is thus violated for an idealized heralded single-photon source.

1.1.4 The three-wave mixing Hamiltonian (briefly)

At this point, we introduce one of the primary tools used throughout this thesis: three-wave mixing (3WM). 3WM is an optical process in which three optical fields interact in a medium with an optical nonlinearity, exchanging photons between the different modes they occupy. We will discuss the details of this process for broadband fields in the next chapter along with the classical description of three-wave mixing, but it is worth mentioning here both to connect with our quantum description of the electric field and to describe a key process used to generate single photons.

The strength of the three-wave mixing process is given by the second-order nonlinear susceptibility, $\chi^{(2)}$. The second-order nonlinear material polarization[2] is dependent on the

---

[2]Not to be confused with the polarization vector.

electric field as [28]

$$P_i^{(2)}(t) = \epsilon_0 \chi_{ijk}^{(2)} E_j(t) E_k(t), \tag{1.30}$$

where the total electric field is a sum over all subscripts. Note that, while $\chi_{ijk}^{(2)}$ is a tensor relating different polarization components of the polarization field, we will only ever be concerned with one set of polarizations at a time, and will treat it as simply a number. Additionally, we will assume that we are well removed from any material resonances, such that $\chi^{(2)}$ can be taken to be constant in frequency (i.e. $\mathrm{d}\chi^{(2)}/\mathrm{d}\omega \approx 0$)[3]. The energy in a medium can be found as $\langle \vec{D} \cdot \vec{E} \rangle / 2 = \langle (\epsilon_0 \vec{E} + \vec{P}) \cdot \vec{E} \rangle / 2$, which results in a second-order nonlinear energy correction as in Eq. (1.5.15) of Ref. [28] of

$$\mathcal{E}^{(2)} = \frac{\epsilon_0}{3} \chi^{(2)} E_i^*(t) E_j(t) E_k(t). \tag{1.31}$$

Working in the interaction picture, this energy term becomes our interaction Hamiltonian, with the form

$$\hat{H}_{NL}(t) = -\int \mathrm{d}^3 \vec{r} \frac{\epsilon_0}{3} \chi^{(2)} E_i^*(\vec{r}, t) E_j(\vec{r}, t) E_k(\vec{r}, t). \tag{1.32}$$

If the electromagnetic field can be broken down into three distinct modes, each expressed as $\hat{E} = \hat{E}^{(+)} + \hat{E}^{(-)}$, eight possible combinations of raising and lowering operators are present in this Hamiltonian. Two of them ($\hat{E}_1^{(+)}\hat{E}_2^{(+)}\hat{E}_3^{(+)}$ and $\hat{E}_1^{(-)}\hat{E}_2^{(-)}\hat{E}_3^{(-)}$) create or destroy a photon in all three modes, while the other six exchange photons from one mode to another. If none of the modes are degenerate, only one pair of these combinations should be capable of conserving energy. We arbitrarily choose mode 3 to be the most energetic (i.e. the highest frequency), such that we can write the Hamiltonian in terms of only the potentially energy-conserving terms as

$$\hat{H}_{3WM}(t) = -\int \mathrm{d}^3 \vec{r} \frac{\epsilon_0}{3} \chi^{(2)} \left(\hat{E}_1^{(+)}\hat{E}_2^{(+)}\hat{E}_3^{(-)} + \hat{E}_1^{(-)}\hat{E}_2^{(-)}\hat{E}_3^{(+)} \right). \tag{1.33}$$

While enforcing energy conservation is arbitrary at this point (no matter how well motivated heuristically), these terms will naturally drop out in a later step; the mathematics

---

[3]$\chi^{(2)}$ viewed in this fashion, as a frequency-independent constant rather than a tensor, is usually denoted by an effective nonlinearity d_{eff} instead. We stubbornly call our effective nonlinearity $\chi^{(2)}$ anyways, where the conversion is $\chi^{(2)} = 2d_{eff}$ [28].

13
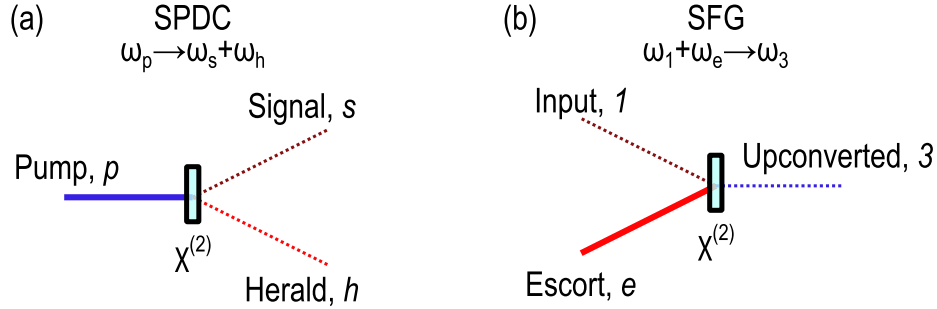
Figure 1.2: **Three-wave mixing.** The two three-wave mixing processes that will form the focus of this thesis are (a) spontaneous parametric downconversion (SPDC) and (b) sum-frequency generation (SFG). In spontaneous parametric downconversion (SPDC), a strong pump field in mode p is split into a signal in mode s and idler/herald in mode h. In sum-frequency generation (SFG), an input in mode 1 is guided to an upconverted mode 3 via a strong escort field in mode e. Note that second-harmonic generation (SHG) is a special case of SFG with two degenerate strong inputs.

are cleaner by simply removing them now.

We will return to this Hamiltonian in Sec. 3.1 to derive its more precise behaviour (to follow the previous train of thought to its natural conclusion, skip to there immediately). For the moment, we will concern ourselves with simply the form of it. Ignoring the time and space dependence and treating the Hamiltonian as broken into a series of orthogonal (i.e. $[\hat{a}_{i,m}, \hat{a}_{i,n}^{\dagger}] = \delta_{mn}$) modes, the Hamiltonian is directly linked to the evolution of the state as

$$|\psi\rangle \mapsto e^{-\frac{it}{\hbar}\hat{H}_I}|\psi\rangle = \exp\left[-i\sum_{m}\gamma_m(\hat{a}_{1,m}\hat{a}_{2,m}\hat{a}_{3,m}^{\dagger} + \hat{a}_{1,m}^{\dagger}\hat{a}_{2,m}^{\dagger}\hat{a}_{3,m})\right]|\psi\rangle, \qquad (1.34)$$

where γ_m is some coupling constant determining the strength of the interaction for the mth mode set. By expanding the exponential in a Taylor series, it is seen that the creation and annihilation operators in the Hamiltonian will be applied to directly the state. The two terms of the Hamiltonian are Hermitian conjugates of one another, where the first term corresponds to two photons being annihilated in modes 1 and 2 to create a photon in

mode 3, and the second term to a photon in mode 3 being annihilated to create a photon pair in modes 1 and 2. These two processes are referred to, respectively, as *sum-frequency generation* (SFG) and *spontaneous parametric downconversion* (SPDC), and are sketched in Fig. 1.2. In each of these cases, we will usually assume one of the three modes is a strong coherent state and look at the large-amplitude limit, also known as the classical approximation; we briefly discuss the implications of this below.

Spontaneous parametric downconversion

As seen in Fig. 1.2a, spontaneous parametric downconversion (SPDC) is the case where a strong laser pulse, known as the *pump*, is incident on a $\chi^{(2)}$ nonlinear medium. With some (typically small) probability, the pump will downconvert into a pair of photons, known as the *signal* and *herald*[4]. By assuming that the pump is a strong coherent state such that $\hat{a}_{p,m} \approx \xi_{p,m}$, we can write the SPDC evolution operator from Eq. (1.34) as

$$\hat{U}_{SPDC} = \exp\left[-i\sum_m \left(\xi_m^* \hat{a}_{s,m}\hat{a}_{h,m} + \xi_m \hat{a}_{s,m}^\dagger \hat{a}_{h,m}^\dagger\right)\right], \tag{1.35}$$

where $\xi_m = \alpha_{p,m}\gamma_m$. This operator is equivalent to a multimode version of the two-mode squeezing operator [8].

Assuming for the moment that only one mode is populated, applying this operator to an initial state with vacuum in the signal and herald mode and expanding to second order, we find that the state is

$$\hat{U}_{SPDC}|00\rangle = \left[\mathbb{1} - i\left(\xi^* \hat{a}_s\hat{a}_h + \xi \hat{a}_s^\dagger \hat{a}_h^\dagger\right) - \frac{1}{2}\left(\xi^* \hat{a}_s\hat{a}_h + \xi \hat{a}_s^\dagger \hat{a}_h^\dagger\right)^2 + \mathcal{O}(|\xi|^3)\right]|00\rangle \tag{1.36}$$

$$= (1 - |\xi|^2)|00\rangle - i\xi|11\rangle - \xi^2|22\rangle + \mathcal{O}(|\xi|^3), \tag{1.37}$$

which contains an equal number of signal and herald photons. If $|\xi|$ is small enough that $|\xi| \gg |\xi|^2$, then detecting one photon in the herald mode signifies the presence of a photon

---

[4]Traditionally, the pair is known as the signal and idler. In the experiments outlined in this thesis, one photon will be operated on while the other will be mostly unmodified and often act to simply herald the presence of the other. For consistency, we will solely refer to this second photon as the herald.

in the signal mode; this is the operating principle of the *heralded single-photon source*, as previously mentioned in Sec. 1.1.3. See Sec. 3.2 for a more detailed description of SPDC.

Sum-frequency generation

In sum-frequency generation, as seen in Fig. 1.2b, a strong laser pulse known as the *escort* mediates the transition of an input mode to an output upconverted mode (labelled 1 and 3). Taking the escort to be a strong coherent state that loses effectively no photons throughout the interaction (the undepleted pump approximation) and merging the strength of the escort into the constant γ_m, we find that the SFG evolution operator is

$$\hat{U}_{SFG} = \exp\left[-i\sum_m \left(\gamma_m \hat{a}_{1,m}\hat{a}_{3,m}^\dagger + \gamma_m^* \hat{a}_{1,m}^\dagger \hat{a}_{3,m}\right)\right]. \tag{1.38}$$

This operator describes a beamsplitter operation between the mth input mode and the mth output mode with a coupling defined by the constant γ_m, as seen by comparison to Eq. (1.10). See Sec. 2.1.2 and Sec. 3.3 for a more detailed description of the classical and quantum pictures of SFG, respectively.

1.2 Photonic qubits and qudits

Photons have numerous degrees of freedom. It is possible to encode binary information in their polarization, discrete information in their photon number, and continuous-value information in their spectrum, transverse spatial profile, and field quadratures. If not used for storing information, the extra degrees of freedom can be utilized as flexible register modes to facilitate delicate operations, as in Ref. [29] for example. Photon number states are notoriously susceptible to loss, and photon-number resolving detectors are only just beginning to show promising results [13, 14, 15]. There has been much recent interest in the transverse spatial modes of a photon, in particular the Laguerre-Gauss or orbital angular momentum (OAM) modes [30, 31, 32]. The work in this thesis makes use of the polarization and spectral degrees of freedom, which are described in detail in the remainder

of this section. The description of polarization also encompasses a broader description of two-level qubits[5].

1.2.1 Qubits and polarization

In order to craft a qubit, it is important to have two orthogonal modes which can be measured, manipulated, and superimposed. These criteria are all easily met by using polarization modes of photons. For any beam of light travelling in the $\hat{z}$ direction, the light may be polarized along the $\hat{x}$ or $\hat{y}$ axis. We define these directions relative to the surface of an optical table as horizontal and vertical, and label the ladder operators of these polarization modes accordingly as $\hat{a}_H$ and $\hat{a}_V$. We define a shorthand for a single photon in each polarization mode as

$$\hat{a}_H^\dagger |0\rangle = |H\rangle, \ \ \hat{a}_V^\dagger |0\rangle = |V\rangle, \tag{1.39}$$

and define the Bloch/Jones matrix representation of these states as [35, 36, 33]

$$|H\rangle = \begin{pmatrix} 1 \\ 0 \end{pmatrix}, \ \ |V\rangle = \begin{pmatrix} 0 \\ 1 \end{pmatrix}, \tag{1.40}$$

where use of the matrix representation implies a single photon. The H/V basis consists of the eigenstates of the Pauli σ_z operator, and forms a mutually unbiased set with the eigenstates of the σ_x and σ_y operators, where

$$\sigma_z = \begin{pmatrix} 1 & 0 \\ 0 & -1 \end{pmatrix}, \ \ \sigma_x = \begin{pmatrix} 0 & 1 \\ 1 & 0 \end{pmatrix}, \ \ \sigma_y = \begin{pmatrix} 0 & -i \\ i & 0 \end{pmatrix}. \tag{1.41}$$

---

[5]We restrict our attention to two-level qubits in this discussion, but qubits can be defined more generally as objects which behave as expected under Pauli operations and measurements. In particular, constructing qubits out of multiple two-level systems can be useful for constructing fault-tolerant logical qubits, and is the foundation of the field of quantum error correction [33, 34].

The eigenstates of the σ_x operator are the linearly polarized diagonal and anti-diagonal states $|D\rangle$ and $|A\rangle$, defined as superpositions of the H/V basis states as

$$|D\rangle = \frac{1}{\sqrt{2}}\left(|H\rangle + |V\rangle\right) = \frac{1}{\sqrt{2}}\begin{pmatrix} 1 \\ 1 \end{pmatrix}, \quad |A\rangle = \frac{1}{\sqrt{2}}\left(|H\rangle - |V\rangle\right) = \frac{1}{\sqrt{2}}\begin{pmatrix} 1 \\ -1 \end{pmatrix}, \qquad (1.42)$$

and the eigenstates of the σ_y operator are the left- and right-circularly polarized states $|R\rangle$ and $|L\rangle$, defined as

$$|L\rangle = \frac{1}{\sqrt{2}}\left(|H\rangle + i|V\rangle\right) = \frac{1}{\sqrt{2}}\begin{pmatrix} 1 \\ i \end{pmatrix}, \quad |R\rangle = \frac{1}{\sqrt{2}}\left(|H\rangle - i|V\rangle\right) = \frac{1}{\sqrt{2}}\begin{pmatrix} 1 \\ -i \end{pmatrix}. \qquad (1.43)$$

Qubits, the Bloch sphere, and measurements

In general, a pure coherent superposition of the z-basis states can be represented in terms of the angles θ and ϕ as [33]

$$|\psi\rangle = \cos\frac{\theta}{2}|H\rangle + e^{i\phi}\sin\frac{\theta}{2}|V\rangle, \qquad (1.44)$$

where the angles θ and ϕ can be visualized as polar co-ordinates on the surface of a sphere. This *Bloch sphere* can be used to represent any qubit state, with the points in the middle corresponding to incoherent mixtures rather than coherent superpositions. Incoherent mixtures can be thought of as the states that can be made using classical probability distributions rather than interferometric superposition principles; as an example, contrast the state $|D\rangle\langle D|$ with the mixed density operator $\varrho = (|H\rangle\langle H| + |V\rangle\langle V|)/2$, which corresponds to flipping a coin and preparing either a horizontally or a vertically polarized photon. A general qubit density operator can be written as [33]

$$\varrho(r, \theta, \phi) = \frac{\mathbb{1} + \vec{r}\cdot\vec{\sigma}}{2}; \quad \vec{r} = \begin{pmatrix} r\sin\theta\cos\phi \\ r\sin\theta\sin\phi \\ r\cos\theta \end{pmatrix}, \quad \vec{\sigma} = \begin{pmatrix} \sigma_x \\ \sigma_y \\ \sigma_x \end{pmatrix} \qquad (1.45)$$

18

If $|r| = 1$, the state is said to be *pure*, and if $|r| = 0$, the density operator is the identity matrix and is said to be maximally mixed. The degree of purity can be expressed as $\text{Tr}\varrho^2$. For a d-dimensional state, the purity of a maximally mixed state is $1/d$, while a pure state has a purity of 1. The *fidelity* of two quantum states, a measure of their degree of closeness, can be found for density matrices ϱ and σ as [37]

$$\mathcal{F}(\varrho, \sigma) = \text{Tr}\left[\sqrt{\sqrt{\sigma}\varrho\sqrt{\sigma}}\right]^2 \overset{\text{pure}}{=} |\langle\psi_\varrho|\psi_\sigma\rangle|^2. \tag{1.46}$$

We will generally consider the post-selected fidelity, ignoring vacuum contributions arising due to loss and focusing solely on the states that result in detection events.

When measuring a qubit, we are interested in finding some property of the system that depends on the state, but the measurement may not depend solely on the state due to errors such as noise. In general, we can represent the measurement of an observable $\hat{A}$ as a *positive operator-valued measure* (POVM) with POVM elements $\{\hat{A}_n\}$ corresponding to outcome values $\{a_n\}$, where the operator is defined by

$$\hat{A} = \sum_n^N a_n \hat{A}_n, \tag{1.47}$$

its expectation value is defined by

$$\langle\hat{A}\rangle = \text{Tr}[\hat{A}\varrho] \overset{\text{pure}}{=} \langle\psi|\hat{A}|\psi\rangle, \tag{1.48}$$

and the POVM elements must satisfy $\sum_n^N \hat{A}_n = \mathbb{1}$.

A special case that corresponds to the ideal case for most of this thesis is the *projective measurement* or *projector-valued measurement* (PVM), which for a qubit is necessarily a set of two POVM elements where $\hat{A}_1 = |\phi\rangle\langle\phi|$ and $\hat{A}_2 = \mathbb{1} - \hat{A}_1 = |\phi^\perp\rangle\langle\phi^\perp|$. In this case, the measurement gives outcome a_1 if the state is $|\phi\rangle$ and outcome a_2 if the state is the orthogonal state $|\phi^\perp\rangle$, and thus perfectly distinguishes these two cases. Usually, we will set $a_1 = +1$ and $a_2 = -1$ and treat our measurements as ± 1 observables; for example, in this form, σ_z is the observable corresponding to the states $|\phi\rangle = |H\rangle$ and $|\phi^\perp\rangle = |V\rangle$. The

outcome (i.e. success probability) of a projective measurement of the pure qubit state $|\psi\rangle$ of Eq. (1.44) onto the state $|\chi\rangle = \cos\frac{\alpha}{2}|0\rangle + e^{i\beta}\sin\frac{\alpha}{2}|1\rangle$ can be found to be

$$
\begin{aligned}
|\langle\chi|\psi\rangle|^2 &= \left|\cos\frac{\theta}{2}\cos\frac{\alpha}{2} + e^{i(\phi-\beta)}\sin\frac{\theta}{2}\sin\frac{\alpha}{2}\right|^2 \\
&= \frac{1}{2}\left(1 + \cos\alpha\cos\theta + \cos(\beta-\phi)\sin\alpha\sin\theta\right).
\end{aligned}
\tag{1.49}
$$

Even for a two-outcome measurement on a qubit, PVMs are far from general. As an extreme counter-example, one could imagine an apparatus which ignores the state, flips a coin, and outputs a ± 1 result based on the flip. This measurement would be described by the POVM elements $\hat{A}_+ = \hat{A}_- = \mathbb{1}/2$. As another extreme case, a device may simply output $+1$ regardless of the input, which would be described by the POVM elements $A_+ = \mathbb{1}$ and $A_- = 0$. We can represent a general POVM element for a two-outcome observable $a = \pm 1$ acting on a qubit as [38, 39]

$$
\hat{A}_a(\kappa, \vec{r}) = \frac{(1 + a\kappa) \times \mathbb{1} + a\vec{r}\cdot\vec{\sigma}}{2},
\tag{1.50}
$$

where $\vec{r}$ and $\vec{\sigma}$ are defined as in Eq. 1.45. As the POVM element must be positive, the parameters within are bounded by $|\vec{r}| \leq 1$ and $|\vec{r}| - 1 \leq \kappa \leq 1 - |\vec{r}|$ [38]. If the bounds are saturated, e.g. $|\kappa| = 1 - |\vec{r}|$, the POVM element is free of innate randomness; while the measurement outcome may depend both on the state being measured and some process in the device itself, there is no "coin-flipping" in the measurement device. However, any POVM element which does not saturate the bounds has inherent state-independent randomness. The completely random POVM corresponds to $\kappa = 0$ and $|\vec{r}| = 0$; the PVM limit corresponds to $\kappa = 0$ and $|\vec{r}| = 1$. POVMs can also be extended to a boundless number of outcomes for a finite-dimensional Hilbert space, so long as they satisfy the completeness relationship, $\sum_i \hat{A}_i = \mathbb{1}$ [33].

Tomography

Measurements as described above provide very specific information about a quantum system. Given enough repetitions of the experiment (enough "clicks" in photon-detector

parlance), one could construct a two-outcome measurement which outputs, say, the expectation value $\langle\sigma_z\rangle$. Much of the time, particularly in fundamental and proof-of-principle experiments, the goal is not to use the system to accomplish some task but rather to identify or characterize the system. *Quantum state tomography* is the process of measuring a state with specific and well-characterized measurements in order to determine the density matrix corresponding to the measured system. The forms of tomography used in this thesis have been described elsewhere, including previous theses from our group [40, 41, 42], but are summarized in brief here.

In order to fully specify a density operator, it is necessary to have at least as much information as there are degrees of freedom in the operator. For a single-qubit density matrix, for example, the fact that the density operator is Hermitian ($\varrho = \varrho^\dagger$), positive semi-definite ($\langle\psi|\varrho|\psi\rangle \geq 0$ for all $|\psi\rangle$), and has a trace of one ($\mathrm{Tr}\varrho = 1$) reduces it to having three free parameters, expressible in terms of the Pauli operators used in Eq. (1.45) as

$$\varrho_{gen} = \frac{1}{2}\begin{pmatrix} 1+z & x-iy \\ x+iy & 1-z) \end{pmatrix},$$ (1.51)

where x, y, and z are all real numbers where $z \in \{0,1\}$ and $x^2 + y^2 + z^2 \leq 1$. To calculate this density matrix directly from projective measurements, it is necessary to make at least three measurements plus one extra for normalization; directly calculating the parameters from this method is known as *linear inversion*. For composite systems of many (n) qubits, it is necessary to make a total of at least 4^n projective measurements (or 3^n two-outcome measurements) [43].

Linear inversion is relatively simple, but is prone to error. Given that all measurements are noisy, there is no guarantee that the matrix calculated will correspond to a physical density matrix, i.e. be positive semi-definite. One technique often used is *maximum likelihood reconstruction*, which endeavours to find the legitimate density matrix which comes closest to describing the measurement results. One possible method constructs the density matrix as

$$\varrho = \frac{T^\dagger T}{\mathrm{Tr}(T^\dagger T)}$$ (1.52)

and optimizes for the lower-triangular matrix T rather than ϱ [43, 44, 45]. This con-

struction, known as the Cholesky decomposition [46], ensures that the density matrix ϱ is Hermitian, as $(T^\dagger T)^\dagger = T^\dagger T$, and also guarantees that it will be positive semi-definite as

$$\langle \psi | T^\dagger T | \psi \rangle = \langle \psi | \psi \rangle \geq 0. \tag{1.53}$$

A penalty function is then assigned to how much the choice of T deviates from the actual measurement, which is minimized to obtain a best estimate of the state measured [43, 44, 45]. This also allows for more measurements to be involved without introducing necessary contradictions as they would for linear inversion; more information will simply add in to the penalty function. The iterative code used to reconstruct density matrices in the work done in this thesis is adapted from Eq. (4-7) of Ref. [44].

Practical polarization tools

The Jones matrix formalism can be used to represent transformations to polarization states in a much simpler fashion than exponentiated Hamiltonians. The equivalent of the beam-splitter in Eq. 1.10 between the horizontal and vertical modes can be written as a rotation about the σ_x axis as

$$U_{BS} = \begin{pmatrix} \cos\frac{\theta}{2} & -i\sin\frac{\theta}{2} \\ -i\sin\frac{\theta}{2} & \cos\frac{\theta}{2} \end{pmatrix}. \tag{1.54}$$

The beamsplitter for polarization modes is usually referred to a polarization rotator, and is realized by a *wave plate*. Wave plates have a fast axis and a slow axis, and work by delaying one polarization element relative to another. By rotating the waveplate, the choice of which elements are given a relative delay is adjusted.

The Jones matrix for the effect of a *half-wave plate*, which has a phase difference of π between the fast and slow axis, is given by

$$U_{HWP}(\theta) = \begin{pmatrix} \cos 2\theta & \sin 2\theta \\ \sin 2\theta & -\cos 2\theta \end{pmatrix}. \tag{1.55}$$

If the half-wave plate is aligned to $\theta = 0$, the polarization $|H\rangle$ and $|V\rangle$ are eigenstates of operation, while the state $|D\rangle$ will be flipped to $|A\rangle$ due to the π phase difference between

22
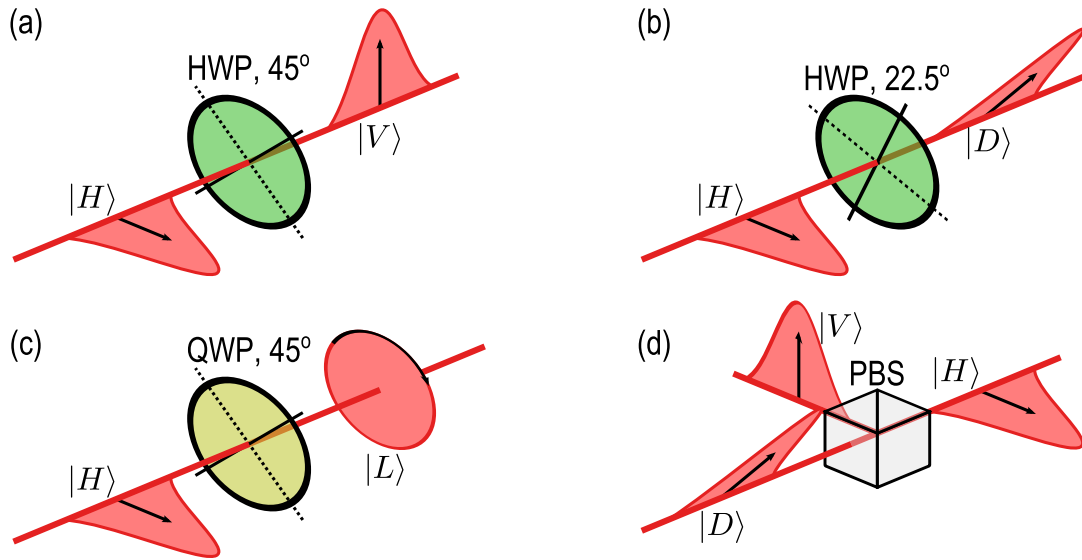
Figure 1.3: **Tools for polarization manipulation.** Four common uses of polarization-controlling optics are shown above. (a) A half-wave plate (HWP) with its optic axis at 45 degrees rotates horizontal polarization to vertical and vice-versa. (b) A HWP with its optic axis at 22.5 degrees acts as a Hadamard gate, rotating horizontal to diagonal polarization and vice-versa. (c) A quarter-wave plate (QWP) set at 45 degrees brings a horizontally polarized photon to the left-circularly polarized state. (d) A polarizing beamsplitter (PBS) separates horizontal and vertical components into separate spatial modes.

the horizontal and vertical polarizations. If the half-wave plate is aligned to 22.5 degrees ($\pi/8$), it will instead act as a Hadamard operation, coupling $|H\rangle$ to $|D\rangle$ and $|V\rangle$ to $|A\rangle$. In this fashion, the half-wave plate can switch between the σ_z and σ_x bases. Note that, no matter what the angle is, the half-wave plate flips $|R\rangle$ to $|L\rangle$ and vice-versa. This part of its operation differentiates it from a rotation about the σ_y axis. Example operations of the half-wave plate are shown in Fig. 1.3a-b.

To leave the X-Z plane of the Bloch sphere, a wave plate with a relative delay of $\pi/2$

known as a *quarter-wave plate* can be used, which implements the operation

$$U_{QWP} = \begin{pmatrix} \frac{1+i\cos 2\theta}{\sqrt{2}} & i\sqrt{2}\sin\theta\cos\theta \\ i\sqrt{2}\sin\theta\cos\theta & \frac{1-i\cos 2\theta}{\sqrt{2}} \end{pmatrix}. \tag{1.56}$$

At an angle of 45 degrees, the quarter-wave plate converts $|H\rangle$ to $|L\rangle$ and $|V\rangle$ to $|R\rangle$, switching the σ_z and σ_y bases, as shown in Fig. 1.3c.

With half- and quarter-wave plates, we can implement any polarization rotation [47]. To complete our basic polarization state manipulation toolbox, we simply need to introduce a measurement. This can be accomplished using a polarizing beamsplitter (PBS), as shown in Fig. 1.3d. The PBS links the polarization and spatial mode degrees of freedom, implementing the operator transform

$$\begin{aligned} \hat{a}_H &\mapsto \hat{a}_H, \quad \hat{a}_V \mapsto \hat{b}_V, \\ \hat{b}_H &\mapsto \hat{b}_H, \quad \hat{b}_V \mapsto \hat{a}_V. \end{aligned} \tag{1.57}$$

If the photon in question is in the "a" mode, detectors in each spatial mode assigned ± 1 values per detection (or "click") can be used to implement binary-outcome projective measurements.

1.2.2 Photonic spectral and temporal modes

Polarization states are a natural choice for constructing single-photon qubits, but they are not extendible to higher dimensions. Additionally, while polarization has been shown to maintain coherence well in free space [48, 49], they are subject to unwanted random rotations in media such as optical fiber. Spatial modes, whether individual rails or transverse profile modes, are extendible to high dimension but have similar drawbacks for long-distance photonic links.

The spectral degree of freedom, on the other hand, maintains coherence over incredible distances in fiber [50, 51, 52], is widely utilized in existing infrastructure [53, 54], and may be used to construct high-dimensional quantum states [55, 56, 57]. There are two main

categories that we will outline briefly in this section: temporal modes [58, 59, 60, 61, 62, 63] and time-bin qudits [64, 65, 51].

We can view a quantum state of light with some spectral uncertainty as

$$|\psi\rangle = \frac{1}{\sqrt{2\pi}} \int d\omega F_\psi(\omega) e^{-i\omega t} \hat{a}_\omega |0\rangle, \tag{1.58}$$

where $F_\psi(\omega)$ is normalized such that $|\langle\psi|\psi\rangle|^2 = 1$. If we can find another quantum state $|\phi\rangle$ with a spectral wavefunction $F_\phi(\omega)$ such that $|\langle\phi|\psi\rangle|^2 = 0$, the states are orthogonal and can thus be perfectly distinguished. This orthogonality can be written directly in terms of the spectral wavefunctions as $\langle\phi|\psi\rangle = \int d\omega\, F_\phi^*(\omega) F_\psi(\omega)$. The two categories take different approaches to ensuring that this overlap is zero for the basis functions. Temporal modes are designed analogously to Hermite-Gauss spatial modes where they each occupy the same temporal extent but are field orthogonal as seen in Fig. 1.4a, which allows them to be extended to high dimension within the same extent by simply using higher order Hermite modes. To measure and manipulate these modes, one can use quantum pulse gates based on dispersion-engineered waveguides [58, 63].

On the other hand, time bins can be (somewhat) simpler to prepare and measure at a cost of having a wide temporal extent when operating with large dimensionality. Instead of being field orthogonal, time bin modes are simply separated in time by an amount larger than their temporal extent, forming a train of pulses as seen in Fig. 1.4b, each of which can be defined as identical spectral fields with different time delays τ as

$$|\psi_i\rangle = \frac{1}{\sqrt{2\pi}} \int d\omega F(\omega) e^{i\omega\tau_i} e^{-i\omega t} \hat{a}_\omega |0\rangle. \tag{1.59}$$

The overlap between two time bin states with Gaussian spectral functions of temporal standard deviation[6] Δt is given by

$$\langle\psi_2|\psi_1\rangle = \int d\omega\, F^*(\omega) F(\omega) e^{i(\tau_1 - \tau_2)\omega} = e^{-\frac{1}{8}\frac{\tau^2}{\Delta t^2}}, \tag{1.60}$$

---

[6]The standard deviation width, often denoted σ, will be used commonly throughout this thesis, and is equal to the square root of the variance or $1/\sqrt{e}$ width of the corresponding Gaussian function.

which sets the fundamental limit on how close in time two bins can be while being approximately orthogonal. Note that the overlap of time bin and field-orthogonal temporal modes is unaffected by dispersion, as it can always be corrected with an equal amount of the opposite dispersion.

Creating these states and measuring them can be done with an unbalanced interferometer [64] as seen in Fig. 1.4c, which split the photon into an early bin $|e\rangle$ and a late bin $|\ell\rangle$. By adjusting the reflectivity of the beamsplitters and the preparation phase, a general state of the form of Eq. 1.44 can be prepared with $|e\rangle$ and $|\ell\rangle$ taking the role of the computation σ_z basis. Extending to more complicated interferometers can lead to higher dimensional states, although the distance between bins times the number of bins must be less than the distance between overall pulses to avoid cross-talk. With long separations between bins, fast electronics or nonlinear optical transformations can be used to isolate time bins [66, 67, 68], with space or polarization acting as a register mode to facilitate operations [29].

1.3 Entanglement and nonlocality

Having defined the qubit, we next explore perhaps the most unfairly mythified aspect of quantum mechanics: entanglement. While it is not quite as magical as pop science sometimes makes it out to be, entanglement is nonetheless the workhorse of many quantum ideas and technologies, and a recurring feature in this thesis. In this section, we will define entanglement between two qubits and how to verify its presence through Bell inequalities, as well as how to generate two-qubit polarization entanglement through SPDC. We will abstract the concept to the device-independent formalism, viewing the experimental results as probability distributions rather than quantum systems.

1.3.1 Entanglement

A number of parties separated by some reasonable definition (such as a large spatial distance) can be thought of as having access to quantum systems in distinct local Hilbert
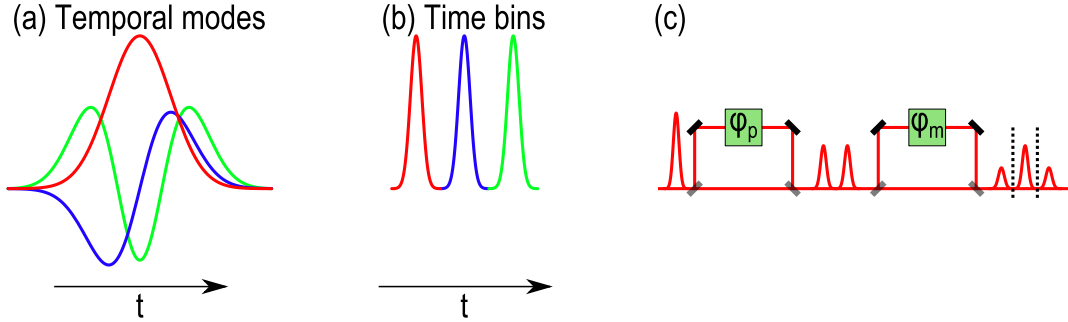
Figure 1.4: **Encoding quantum information in temporal modes.** Two methods of encoding information in the photonic temporal degree of freedom are demonstrated by showing their first three modes, for (a) field-orthogonal temporal modes and (b) time bins. The temporal modes occupy the same space, no matter the dimension, but require quantum pulse gates to separate. The time bins encounter practical limitations in terms of space at high dimension, but can be relatively simple to prepare and isolate. Note that the shapes above could be either the temporal field or the spectra and still be effective. (c) Time bin states can be created by sending a pulse through an unbalanced interferometer with a preparation phase φ_p in the long arm, and measured by a matched unbalanced interferometer with measurement phase φ_m. As shown, any state on the X-Y plane of the Bloch sphere may be created; by adjusting the reflectivities of the beamsplitters, states on the entire sphere may be accessed.

spaces[7], which divide a global Hilbert space as

$$\mathcal{H}_{global} = \mathcal{H}_A \otimes \mathcal{H}_B \otimes \mathcal{H}_C \otimes \ldots \tag{1.61}$$

The key notion to this divide is that any measurements the parties may make necessarily commute [69]; for example, if party "A" (traditionally named Alice) makes a measurement, it can be represented as a measurement operator

$$\hat{M}_A := \hat{M}_A \otimes \mathbb{1}_B \otimes \mathbb{1}_C \otimes \ldots \tag{1.62}$$

---

[7]For the purposes of this discussion, a Hilbert space may be thought of as a space of arbitrary-but-defined dimension where the inner product behaves as expected.

which by construction commutes with a measurement operator in the subspace of party "B" (traditionally named Bob). For the remainder of this section, we will restrict our discussion to the smaller Hilbert space accessible by just Alice and Bob. If the quantum state existing in these Hilbert spaces also respects such a division, i.e.

$$\varrho_{prod} = \varrho_A \otimes \varrho_B, \tag{1.63}$$

it is called a *product state*. In this case, measurements that Alice makes give no information about Bob's system and vice-versa.

This is clearly a subset of the possible states out there. Classically, if Alice and Bob are randomly given a shoe from the same pair, and Alice has the left shoe, she knows that Bob has the right shoe. For qubits, this kind of correlation can be written as the mixed state $\frac{1}{2}[|LR\rangle\langle LR| + |RL\rangle\langle RL|]$. In general, a state with correlations realizable in classical physics can be written as

$$\varrho_{sep} = \sum_m c_m \varrho_{A,m} \otimes \varrho_{B,m}, \tag{1.64}$$

where $\sum_m c_m = 1$. States of this form are known as *separable*. Note that the set of separable states is clearly convex; the convex combination of two separable density matrices is simply a different separable state. This set of states can also be generated as the convex hull of (i.e. all states that can be represented as a convex combination of) the set of density matrices corresponding to product states.

Strictly speaking, the definition of a state that is *entangled* is one that is *not* separable [70, 71]. Entangled states cannot be written as existing in two separate subsystems, and require a description in terms of the global Hilbert space to explain their features. As an illustrative example, contrast the states $|\Psi^-\rangle = \frac{1}{\sqrt{2}}[|HV\rangle - |VH\rangle]$ with the mixed state $\varrho_{50/50} = \frac{1}{2}[|HV\rangle\langle HV| + |VH\rangle\langle VH|]$. While the first is a coherent superposition of the two basis states, the second simply produces one or the other with 50% probability. In the mixed case, while measurements in the horizontal/vertical basis yield anti-correlations, measurements in the diagonal/anti-diagonal basis are completely random. However, measurements in the diagonal/anti-diagonal basis of $|\Psi^-\rangle$ remain anticorrelated. $|\Psi^-\rangle$ forms a

complete two-qubit basis when combined with the other *Bell states*, which are written as

$$
\begin{aligned}
|\Psi^-\rangle &= \tfrac{1}{\sqrt{2}}\left(|HV\rangle - |VH\rangle\right) = \tfrac{1}{\sqrt{2}}\left(|DA\rangle - |AD\rangle\right) = \tfrac{i}{\sqrt{2}}\left(|LR\rangle - |RL\rangle\right) \\
|\Psi^+\rangle &= \tfrac{1}{\sqrt{2}}\left(|HV\rangle + |VH\rangle\right) = \tfrac{1}{\sqrt{2}}\left(|DD\rangle - |AA\rangle\right) = \tfrac{i}{\sqrt{2}}\left(|LL\rangle - |RR\rangle\right) \\
|\Phi^+\rangle &= \tfrac{1}{\sqrt{2}}\left(|HH\rangle + |VV\rangle\right) = \tfrac{1}{\sqrt{2}}\left(|DD\rangle + |AA\rangle\right) = \tfrac{i}{\sqrt{2}}\left(|LR\rangle + |RL\rangle\right) \\
|\Phi^-\rangle &= \tfrac{1}{\sqrt{2}}\left(|HH\rangle - |VV\rangle\right) = \tfrac{1}{\sqrt{2}}\left(|DA\rangle + |AD\rangle\right) = \tfrac{i}{\sqrt{2}}\left(|LL\rangle + |RR\rangle\right)
\end{aligned}
\tag{1.65}
$$

Note that the set of entangled states is not convex, as can be seen immediately by noting that $\frac{1}{2}\left[|\Psi^-\rangle\langle\Psi^-| + |\Psi^+\rangle\langle\Psi^+|\right] = \varrho_{50/50}$, which is separable.

Entanglement is notoriously complex beyond the two-qubit case [71], but the concept extends quite easily to high-dimensional and continuous-variable systems. Assuming bipartite pure states for the time being, a continuous variable system shared between two parties with amplitude $f(x_1, x_2)$ is entangled if $f(x_1, x_2) \neq f_1(x_1)f_2(x_2)$, or else it is a product state. We can always break a pure amplitude $f(x_1, x_2)$ into a superposition of (potentially many) orthonormal modes, whether it is continuous-variable or discrete, using the *Schmidt decomposition* [72, 33]. We denote these modes as $|i_A\rangle$ and $|i_B\rangle$, and write the Schmidt-decomposed form as

$$
|\psi\rangle = \sum_i^N c_i |i_A\rangle |i_B\rangle,
\tag{1.66}
$$

where $\sum_i^N c_i = 1$ and N is the minimum number of modes required to describe the system, known as the Schmidt number or Schmidt rank. The Schmidt decomposition breaks down for mixed states and states with more than two parties [73], but is an essential tool for describing two-party entanglement. We discuss the Schmidt rank for continuous-variable systems in Sec. 3.2.2.

If the Schmidt coefficients are all non-zero and equal, as in the Bell states of Eq. (1.65) or more generally a two-party state of dimension d^2 with a Schmidt decomposition

$$
|\psi\rangle_{max.} = \sum_i^d \frac{1}{\sqrt{d}}|ii\rangle,
\tag{1.67}
$$

the state is said to be *maximally entangled* as it is a pure state with the maximal amount of uncertainty in the individual subsystems. For pure states, this can be quantified by the purity of the partial trace, $\text{Tr}\left[\varrho_A^2\right]$, where $\varrho_A = \text{Tr}_B\left[|\psi\rangle\langle\psi|\right]$ is the density operator correspond to Alice's subsystem with disregard to Bob's. For a maximally entangled state, the purity of the partial trace is minimal $(1/d)$, whereas for a pure product state the subsystems are individually pure, i.e. $\text{Tr}\left[\varrho_A^2\right] = 1$.

1.3.2 Device-independent formalism

As we have just seen, entangled states are best defined as not-separable. Tasks which require entangled states are similarly best defined as those which cannot be accomplished with separable states. To determine what those tasks are, we first ask what *can* be done with separable states. To do this, we remove ourselves from the physical nature of the situation and take a *device-independent* approach [74, 75, 76, 77, 78, 39]. If n parties are involved, we abstract their measurements to boxes that have m input settings $\{x, y, z, \ldots\}$ and v potential outputs $\{a, b, c, \ldots\}$, as shown in Fig. 1.5a. A symmetric scenario, where each party has the same box dimension, is denoted as a $(n\text{-}m\text{-}v)$ scenario. Regardless of the actual physical setup, the behaviour of the devices will obey the laws of probability, and the conditional probability of observing the outputs $\{a, b, c, \ldots\}$ given the inputs $\{x, y, z, \ldots\}$ will be $p(abc\ldots|xyz\ldots)$. Such a conditional probability distribution is often called a "box", as it describes an effective black box.

According to quantum mechanics, this probability can be found from the global density operator ϱ and the measurement operators $\hat{A}_{a|x}$ corresponding to the POVM element for outcome a given input x as [39]

$$p(abc\ldots|xyz\ldots) = \text{Tr}\left[\varrho\left(\hat{A}_{a|x}\otimes\hat{B}_{b|y}\otimes\hat{C}_{c|z}\otimes\ldots\right)\right]. \tag{1.68}$$

On the other hand, boxes corresponding to classical probability theory with some shared hidden variable λ instead of a quantum state can be thought of in analogy with the de-
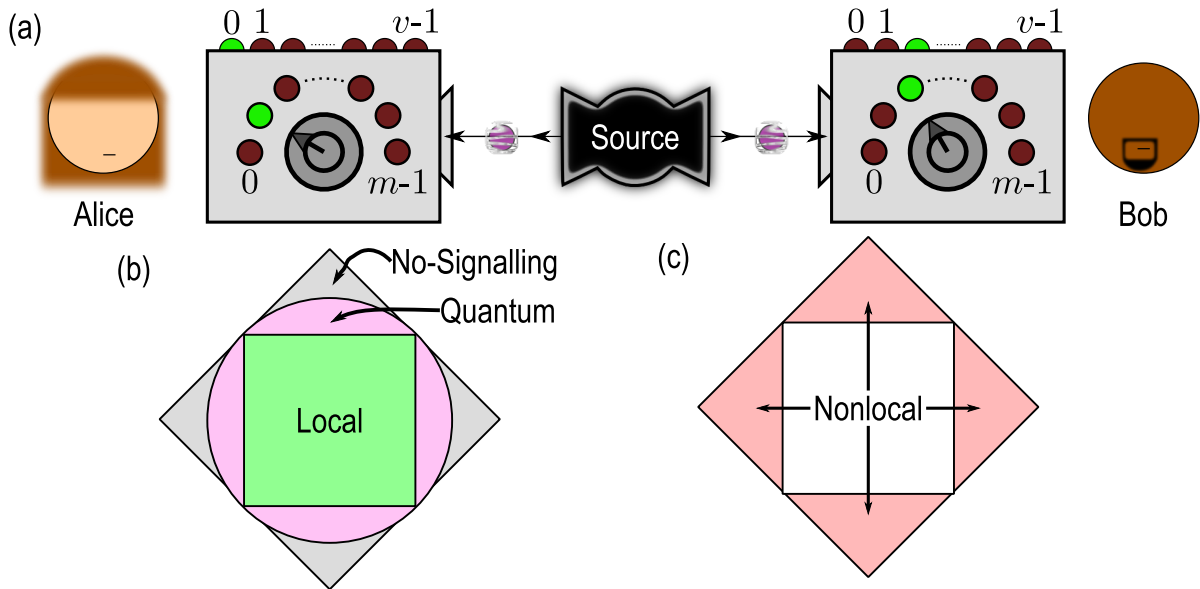
Figure 1.5: **Local, quantum, and nonlocal correlations.** (a) A two-party scenario can be abstracted to one where Alice and Bob each have a device with m settings and v possible outputs. Their measurement results may be related by how their devices respond to a (potentially quantum) source. (b) The sets of correlations given unlimited shared randomness form a hierarchy of convex sets. Any local correlation can be described with quantum mechanics, and the set of all possible correlations which obey no-signalling is more general than even quantum mechanics. The corners of the square representing local distributions are the deterministic local distributions. (c) The term "non-local" should be taken to mean correlations that are not describable as a mixture of local correlations.

scription of separable states of Eq. (1.64) as

$$p(abc\dots|xyz\dots) = \sum_{\lambda=0}^{|\lambda|-1} p(\lambda)p(a|x\lambda)p(b|y\lambda)p(c|z\lambda)\dots, \tag{1.69}$$

where $|\lambda|$ is the dimension of the shared randomness (e.g. 2 for a shared bit), which may not be directly observable to the parties involved. The shared random value λ is often called a *local hidden variable*. Any box fitting this form is dubbed *local*, and the set of these

31

boxes is clearly convex if $|\lambda|$ is unbounded [39]. Each can be written in terms of a sum over the locally deterministic boxes, i.e. where $p(a|x) = 1$ or 0 for any a, by incorporating any non-determinism into the hidden variable λ, and thus the set of local boxes is the convex hull of the local deterministic boxes [79, 78]. By expressing the conditional probability distributions in terms of measurements on separable quantum states as in Eq. (1.68), it can easily be shown that the set of distributions achievable using quantum mechanics is at least as large as those obtainable classically [78].

The probability distributions that correspond to illustrations like Fig. 1.5a must obey some very basic properties in order to be sensible. We will restrict our attention from here on out to two-party scenarios for simplicity. As probabilities, each element must be positive, $p(ab|xy) > 0$, and the sum over all outputs must be normalized, $\sum_{a,b} p(ab|xy) = 1$. Importantly, the individually observed distribution, known as a marginal, must be independent of the input of the other parties, for example

$$\sum_{b=0}^{\nu-1} p(a, b|x, y) = \sum_{b=0}^{\nu-1} p(a, b|x, y') = p(a|x). \tag{1.70}$$

This condition is known as *no-signalling* as it ensures that Bob cannot instantaneously communicate with Alice by changing his input; in the case where Alice and Bob are space-like separated, this would imply information travels faster than the speed of light [80, 78]. The set describing correlations that obey no-signalling is conveniently known as the *no-signalling set*. As seen in Fig. 1.5b, both the quantum and local set respect no-signalling. However, the *non-local* set, seen in Fig. 1.5c, is larger than the quantum set, meaning that there are some boxes that respect relativity but still cannot be expressed quantumly; the most famous example is the Popescu-Rohrlich (PR) box [80].

For the most part, we will be interested in $(2 - 2 - 2)$ scenarios, where we assign values of $a \in \pm 1$ to the outputs and two possible measurements are available. In this case, with eight degrees of freedom removed from normalization and no-signalling, each probability distribution is uniquely specified in terms of eight parameters [39]. It is often convenient to parameterize in terms of expectation values with four joint expectation values measuring

parity

$$\langle A_x B_y \rangle = \sum_{a,b} (a \times b) p(ab|xy) \tag{1.71}$$

and four marginal biases of the form

$$\langle A_x \rangle = \sum_{a,b} a \, p(ab|xy). \tag{1.72}$$

These expectation values are very natural for quantum systems, by defining $\hat{A}_x = \hat{A}_{+1|x} - \hat{A}_{-1|x}$, and can be related back to the probability distribution as

$$p(ab|xy) = \frac{1 + a\langle A_x \rangle + b\langle B_y \rangle + ab\langle A_x B_y \rangle}{4}. \tag{1.73}$$

Most importantly, they provide a natural way to understand Bell inequalities, which provide an experimentally accessible way to confirm entanglement.

1.3.3 Bell inequalities

We've established what a local distribution is now, but have yet to show that quantum mechanics can produce non-local distributions. A necessary and sufficient condition for a distribution to be local is that it satisfies a *Bell inequality*, which can be shown to be explicitly disobeyed for quantum scenarios [81, 79, 78]. Note that the topic of Bell inequalities as boundaries of the set of local boxes is deep and beyond the scope of this thesis; see, for example, Ref. [78].

Given ± 1 outcomes and two measurement choices indexed as 0 and 1, a particularly famous Bell inequality known as the *CHSH inequality* [82] can be written as

$$|S| = |\langle A_0 B_0 \rangle + \langle A_1 B_0 \rangle + \langle A_0 B_1 \rangle - \langle A_1 B_1 \rangle| \leq 2. \tag{1.74}$$

An intuitive proof of this inequality for classical systems can be shown by attempting to assign values to each observable assuming that they are independent of each other, i.e. $\langle A_0 \otimes B_0 \rangle \mapsto A_0 \times B_0$ where the observables are bounded to be between ± 1. Regrouping

the terms as $S = A_0(B_0 + B_1) + A_1(B_0 - B_1)$, it is immediately clear that the algebraic maximum is two [33]. Adding shared randomness such that $S = \sum_m c_m S_m$ will not allow violation, as $\sum_m c_m S_m \leq S_m^{(max)}$ since $\sum_m c_m = 1$.

Let's examine what can be done if we allow for $\langle A_x B_y \rangle$ to be determined quantumly. We restrict ourselves to observables with projective POVM elements which lie on the XZ plane of the Bloch sphere, written as

$$\hat{A}_x = \vec{r} \cdot \vec{\sigma} = \cos \frac{\theta_{A,x}}{2} \sigma_z + \sin \frac{\theta_{A,x}}{2} \sigma_x. \tag{1.75}$$

If the state available is $|\Psi^-\rangle$ from Eq. (1.65), the joint expectation value will be

$$\langle \hat{A}_x \hat{B}_y \rangle = -\cos \left(\frac{\theta_{A,x} - \theta_{B,y}}{2} \right). \tag{1.76}$$

If $\theta_{A,0} = 0$, $\theta_{A,1} = \pi$, $\theta_{B,0} = \pi/2$, and $\theta_{B,1} = -\pi/2$, the Bell parameter $|S| = 2\sqrt{2}$, which violates the classical bound of Eq. (1.74). This inequality could also have been violated with any entangled state and a different combination of Pauli operators. The value $2\sqrt{2}$ is also provably the highest value possible even with quantum mechanics [83]; higher violations (up to the algebraic maximum of 4 achieved by the PR box [80]) are within the purview of no-signalling, but lack a physical implementation.

Perhaps most notably, a Bell inequality violation is directly measurable in experiment, unlike the density matrix and probability distributions which require post-processing[8]. Because of this, the violation of a Bell-type inequality has become the standard experimental threshold in provably demonstrating two-qubit entanglement [86]. The earliest violations from the 1970s and 1980s involving two-photon emission from atomic cascades [87, 88, 89] have evolved into very recent violations with electron spins [90] and photons from SPDC [91, 92] which prove entanglement operates regardless of physical distance without assumptions such as fair-sampling. When dealing with more parties or higher dimensionality, Bell-type inequalities become more complicated [78] and their experimental violation more involved [93, 94, 95, 86, 96].

---

[8]There are schemes, mostly involving weak measurement, to directly measure the density matrix [84, 85], but no demonstration so far for a two-party system.

Other entanglement measures

The Bell inequalities provide a well-known and device-independent platform for falsifying local hidden variable theories, but assuming that we believe in the structure of quantum mechanics, there are other ways to verify entanglement which prove useful in different contexts. To use fewer measurements, observables known as entanglement witnesses may be constructed which only take a negative value for entangled states [70, 71, 97, 98]. The negativity of the partial transposition is often used for bipartite systems [99], but does not confirm entanglement for special states known as bound entangled states which may exist when more parties are involved [71, 100].

The *concurrence* of a state $\mathcal{C}(\varrho)$ is a popular measure of entanglement for bipartite systems as it has a semi-analytic expression for mixed states and, unlike entanglement witnesses, does not have an optimal setting depending on which state is measured. It is defined for two-qubit systems as [101, 71]

$$\mathcal{C}(\varrho) = \max\{0, \lambda_1 - \lambda_2 - \lambda_3 - \lambda_4\}, \tag{1.77}$$

where λ_i are the decreasingly ordered eigenvalues of the matrix

$$\sqrt{\sqrt{\varrho}(\sigma_y \otimes \sigma_y)\varrho^*(\sigma_y \otimes \sigma_y)\sqrt{\varrho}}.$$

A concurrence of zero implies no entanglement, while higher concurrences correspond to higher degrees of entanglement. For pure states, the concurrence simplifies nicely to [71]

$$\mathcal{C}(\varrho) \stackrel{\text{pure}}{=} \sqrt{2[1 - \text{Tr}(\varrho_A^2)]}, \tag{1.78}$$

where ϱ_A is Alice's subsystem after a partial trace. The concurrence-squared is known as the *tangle* [101, 102].

For pure states, the purity of the subsystems is used as a definition of entanglement. A pure state has no innate randomness by definition, but by ignoring half of the state, the result for the individual subsystem will have some randomness. Quantifying this randomness from the purity also quantifies the amount of entanglement that existed before. The fact

that this relies on the purity of the state makes it a problematic measure in experiment, but useful in theoretical modelling of idealized systems. This definition also corresponds to the exponentiated Rényi-2 entropy $\Upsilon(\varrho)$, defined as [103]

$$\Upsilon(\varrho) = -\ln \mathrm{Tr}\left[\varrho_A^2\right]. \tag{1.79}$$

1.3.4 Generation of polarization-entangled photons

Now that we've established some tools for analyzing entanglement, we next focus on how to create it in the lab. Two-photon energy-time and position entanglement is fairly natural to create with SPDC [104], and will be discussed in more detail in Sec. 3.2. Polarization is in many ways the ideal degree of freedom for qubits, and creating polarization-entangled states will be the focus of this section.

SPDC was discussed briefly in Sec. 1.1.4 as a process which downconverts a pump photon into a signal and a herald. In the low-efficiency limit with a single populated mode, the final state may be written as in Eq. (1.37). On the other hand, if two polarization modes H and V (for example) were populated, two first-order terms would appear as

$$\hat{U}_{SPDC}|0_H 0_V\rangle \otimes |0_H 0_V\rangle \approx |0_H 0_V\rangle \otimes |0_H 0_V\rangle - i\xi_H |1_H 0_V\rangle \otimes |1_H 0_V\rangle - i\xi_V |0_H 1_V\rangle \otimes |0_H 1_V\rangle. \tag{1.80}$$

Post-selecting out the vacuum terms and using the polarized photon shorthand, the state of SPDC with two pump modes is

$$|\psi\rangle_{SPDC} = \frac{1}{\sqrt{\xi_H + \xi_V}} \left(\xi_H |HH\rangle + \xi_V |VV\rangle\right). \tag{1.81}$$

If we set $\xi_H = \xi_V$, this is the maximally entangled state $|\Phi^+\rangle$.

Depending on the geometry of the nonlinear crystal and its birefringent properties, the relation of the polarization of the output photons to the input pump may vary. This setup-specific categorization, related to phasematching, will be discussed in the Sec. 2.1.3; for now, all that is important is that there are three main scenarios, known as Type-0, Type-I, and Type-II [28, 108]. In Type-I phasematching, the signal and herald have

36

(a)

$$V \mapsto |HH\rangle \qquad + \qquad H \mapsto |VV\rangle \qquad = \qquad D \mapsto \tfrac{1}{\sqrt{2}}\left(|HH\rangle + |VV\rangle\right)$$

(b)

$$V \mapsto |HV\rangle \qquad + \qquad H \mapsto |VH\rangle \qquad = \qquad D \mapsto \tfrac{1}{\sqrt{2}}\left(|HV\rangle + |VH\rangle\right)$$
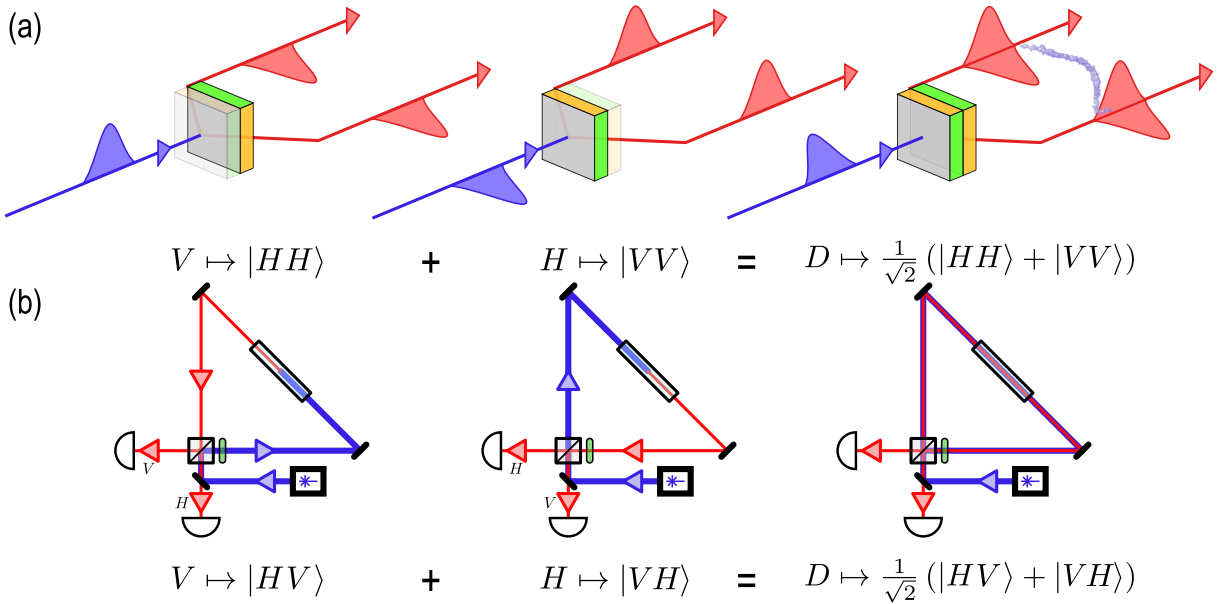
Figure 1.6: **Generation of polarization entanglement.** Two methods of superimposing two SPDC processes are shown, both of which can be used to generate high-quality two-photon polarization entanglement. (a) The sandwich source [105] consists of two type-I crystals rotated 90 degrees relative to each other, such that one downconverts a vertically polarized pump to two horizontal photons and the second a horizontal pump to two vertical photons. By pumping with a diagonal polarization, both processes are stimulated, and a $|\Phi^+\rangle$ state can be created. (b) The Sagnac source [106, 107] operates with a type-II crystal, such that a horizontal pump downconverts into a horizontal and a vertical photon. The blue pump is divided with a polarizing beamsplitter, such that the horizontal (vertical) pump creates a clockwise (counter-clockwise) propagating $|HV\rangle$ pair. That pair then hits the PBS again, such that the left (bottom) port sees a vertical (horizontal) photon from a vertical pump, and vice-versa for a horizontal pump. The state are measured at each port is thus $|\Psi^+\rangle$ with some phase.

the same polarization as each other, but oppose the pump; for example, if the pump is vertically polarized[9], the two photons will be horizontally polarized $|HH\rangle$. Type-0 processes are similar in that both photons have the same polarization, but in this case

---

[9]What is more important than the pump polarization is the crystal orientation; the Type-I process is better described as an extraordinarily polarized pump splitting into two ordinary polarized photons.

37

they have the same polarization as the pump. Type-II processes are those such that the two photons have opposite polarizations; for example, a horizontally polarized pump may downconvert into a vertically polarized signal and a horizontally polarized herald. Additionally, downconversion sources are not naturally degenerate nor collinear, which allows an extra degree of freedom to separate the signal and herald into distinct modes. For example, type-I downconversion from a 400 nm pump may produce two indistinguishable 800 nm photons, but may instead produce a 755 nm signal and an 850 nm herald photon.

Two methods of producing (ideally) maximally entangled polarization states using $\chi^{(2)}$ materials are shown in Fig. 1.6. The first, the sandwich source of Fig. 1.6a [105], is best used with Type-I or Type-0 materials. It can be constructed by placing two orthogonal crystals together, such that one functions to convert a horizontal pump to vertical photons, and the other a vertical pump to horizontal photons. For this source to function, it is important that the photonic modes that the horizontal and vertical photons inhabit are identical. Ensuring that each couples into the same single-mode fiber can be used to align the spatial modes, and small beam displacers can facilitate this [95]. To ensure temporal overlap, thin birefringent materials may be used to remove any temporal walkoff [109], as discussed further in Sec. 3.2.3. Once the modes are overlapped, the source naturally produces the entangled state $|\Phi^+\rangle$ up to a phase shift.

Walkoff and focus limitations prevent the sandwich source from being effective for long crystal lengths, which limits the brightness. One natural alternative method one might think to superimpose two SPDC events is to place one in each arm of a Mach-Zehnder interferometer and then recombine them [110]. The problem with this method is that any small phase shifts, for example from a mirror vibration, will decohere the collective state, requiring active stabilization. One way around this is to instead combine the two processes in a Sagnac interferometer [106, 107, 102, 41], as seen in Fig. 1.6b. The Sagnac source is particularly well-suited for type-II crystals, but can be effective with type-I crystals provided an alternative degree of freedom (such as frequency) can be used to separate the signal and herald. In the Sagnac, both of the opposing processes hit the same mirrors in the opposite order, thus obtaining the same phase if local variations exist. The Sagnac is thus intrinsically phase stable, with high-fidelity performance stable over long periods of time.

Chapter 2

Ultrafast nonlinear optics

Chapter overview

In this chapter, we discuss ultrafast optics and how to model nonlinear effects with broadband pulses. This builds off of the discussion in the previous chapter on three-wave mixing and temporal modes in Sec. 1.1.4. We will first discuss the nonlinear wave equation, sum-frequency generation, and phasematching in Sec. 2.1. We will then look at the analogy between space and time and how to construct "time lenses" with nonlinear optics in Sec. 2.2. Finally, we will examine some classical tools to create, measure, and manipulate ultrafast pulses in Sec. 2.3.

2.1 Classical nonlinear optics

Before discussing quantum nonlinear optics, it is first important to understand the process classically. While applying the techniques used in this thesis to quantum systems opens up new applications and has its own unique challenges, the actual process of sum-frequency generation and the concept of temporal imaging is entirely native to classical nonlinear optics. Understanding nonlinear optical effects on electromagnetic waves with broad spectra

will be central to the remainder of this thesis, although we will not be overly concerned with the materials-science aspects of nonlinear optics.

2.1.1 Pulse propagation in nonlinear media

Our aim in this section is to derive a differential equation governing the propagation of an electromagnetic field through a medium with a nonlinear response. This derivation is based heavily on Chapter 13 of [28]. To do so, we start from Maxwell's equations in non-magnetic matter with no free charges or currents, ignoring the vector nature of the fields for simplicity. In this case, the magnetic field B is linearly related to auxiliary field H as $B = \mu_0 H$, but the electric displacement field D is related to the electric field E and polarization field P as [111]

$$D(\vec{r}, t) = \epsilon_0 E(\vec{r}, t) + P(\vec{r}, t), \tag{2.1}$$

where the polarization vector defines the dipole moment per unit volume induced by the electric field and may contain terms with nonlinear dependence on the electric field. The fields can be expressed as time-dependent or in terms of angular frequency ω, where the two domains are linked through the Fourier transform, defined as

$$F(\omega) = \mathcal{F}\left[f(t)\right] = \frac{1}{\sqrt{2\pi}} \int_{-\infty}^{\infty} \mathrm{d}t\, f(t) e^{-i\omega t}, \tag{2.2}$$

where the $\sqrt{2\pi}$ convention has been chosen to maintain normalization when transforming field amplitudes. The inverse Fourier transform is then

$$f(t) = \mathcal{F}^{-1}\left[F(\omega)\right] = \frac{1}{\sqrt{2\pi}} \int_{-\infty}^{\infty} \mathrm{d}t\, F(\omega) e^{i\omega t}. \tag{2.3}$$

We can simplify Maxwell's equations in this case to relate the evolution of E and D as

$$\frac{1}{\epsilon_0 c^2} \frac{\partial^2}{\partial t^2} D = -\nabla \times \nabla \times E \approx \nabla^2 E, \tag{2.4}$$

where the approximation assumes $\nabla(\nabla \cdot E) = 0$, which is identically true in linear optical media and a good approximation in nonlinear media [28]. In the case of free-space propagation, $D = \epsilon_0 E$ and the familiar wave equation is obtained. To generalize to nonlinear media, we expand the electric displacement field as

$$D = \epsilon_0 E + P^{(1)} + P^{NL}, \tag{2.5}$$

where P^{NL} collects all nonlinear terms of the polarization field and the linear term is written in terms of the linear electric susceptibility $\chi^{(1)}$ as $P^{(1)} = \epsilon_0 \chi^{(1)} E$. We can then use the Fourier relation

$$\mathcal{F}\left[\frac{\partial^n}{\partial t^n}(i)^n f(t)\right] = \omega^n F(\omega) \tag{2.6}$$

to rewrite Eq. 2.4 in the frequency domain as

$$\int d\omega \left[\nabla^2 E(\vec{r}, \omega) - \frac{(-i\omega)^2}{\epsilon_0 c^2} D^{(1)}(\vec{r}, \omega)\right] e^{-i\omega t} = \int d\omega \left[\frac{(-i\omega)^2}{\epsilon_0 c^2} P^{NL}(\vec{r}, \omega)\right] e^{-i\omega t}. \tag{2.7}$$

If the medium is lossless and homogenous, we can define a real-valued index of refraction [111] , $n(\omega) = \sqrt{1 + \chi^{(1)}}$, and rewrite the linear part of the electric displacement field in the frequency domain as

$$D^{(1)}(\vec{r}, \omega) = \epsilon_0 n^2(\omega) E(\vec{r}, \omega), \tag{2.8}$$

allowing us to write the frequency-domain nonlinear wave equation in terms of just the electric field and the nonlinear polarization as

$$\nabla^2 E(\vec{r}, \omega) + \frac{n^2(\omega)\omega^2}{c^2} E(\vec{r}, \omega) = -\frac{\omega^2}{\epsilon_0 c^2} P^{NL}(\vec{r}, \omega). \tag{2.9}$$

We then aim to find an equation for the slowly varying field amplitude $A(\vec{r}, t)$, where

$$E(\vec{r}, t) = A(\vec{r}, t) e^{-i(k_0 z - \omega_0 t)} + c.c. \tag{2.10}$$

with $k_0 = n_0\omega_0/c$. We use the Fourier relation

$$\mathcal{F}\left[f(t)e^{i\omega_0 t}\right] = F(\omega - \omega_0) \tag{2.11}$$

to find that

$$
\begin{aligned}
E(\vec{r}, \omega) &= \frac{1}{\sqrt{2\pi}} \int dt\, E(\vec{r}, t)e^{-i\omega t} \\
&= \frac{1}{\sqrt{2\pi}} \int dt\, \left[A(\vec{r}, t)e^{-ik_0 z}e^{-i(\omega-\omega_0)t} + A^*(\vec{r}, t)e^{ik_0 z}e^{-i(\omega+\omega_0)t}\right] \\
&= A(\vec{r}, \omega - \omega_0)e^{-ik_0 z} + A^*(\vec{r}, \omega + \omega_0)e^{ik_0 z} \approx A(\vec{r}, \omega - \omega_0)e^{-ik_0 z},
\end{aligned}
\tag{2.12}
$$

where the approximation eliminates the conjugate by assuming $A(\vec{r}, t)$ is much longer than single-cycle, i.e. varies on a much slower timescale than $1/\omega_0$ and does not have a significant component at $2\omega_0$. We make a similar substitution for the nonlinear polarization, defining $P^{NL}(\vec{r}, t) = p(\vec{r}, t)e^{-i(k_p z - \omega_0 t)} + \text{c.c.}$ to allow us to write

$$P^{NL}(\vec{r}, \omega) \approx p(\vec{r}, \omega - \omega_0)e^{-ik_p z}. \tag{2.13}$$

where k_p represents the wavenumber of the fields affecting the polarization; for example, this could be $k_{01} + k_{02}$ for sum-frequency generation.

We define $\tilde{\omega} = \omega - \omega_0$ for brevity. We substitute Eq. (2.12) and Eq.(2.13) into Eq. (2.9) as

$$\nabla^2\left[A(\vec{r}, \tilde{\omega})e^{-ik_0 z}\right] + k^2(\omega)A(\vec{r}, \tilde{\omega})e^{-ik_0 z} = -\frac{\omega^2}{\epsilon_0 c^2}p(\vec{r}, \tilde{\omega})e^{-ik_p z} \tag{2.14}$$

where $k(\omega) = n(\omega)\omega/c$. We next assume that the beams in question are paraxial and propagating in the $\hat{z}$ direction. We split the Laplacian term into $\nabla^2 = \nabla_\perp^2 + \frac{\partial^2}{\partial z^2}$ and find

$$\nabla_\perp^2 A(\vec{r}, \tilde{\omega}) - i2k_0\frac{\partial}{\partial z}A(\vec{r}, \tilde{\omega}) + (k^2(\omega) - k_0^2)A(\vec{r}, \tilde{\omega}) = -\frac{\omega^2}{\epsilon_0 c^2}p(\vec{r}, \tilde{\omega})e^{i(k_0 - k_p)z} \tag{2.15}$$

where we neglect $\frac{\partial^2}{\partial z^2}A(\vec{r}, \omega)$ terms through the paraxial approximation. If the medium does not have a rapidly varying index, we can take a first-order expansion to substitute $k^2(\omega) - k_0^2$ with $2k_0(k(\omega) - k_0)$. We also assume that the pulses in question are narrowband

relative to their central frequency ($\Delta\omega \ll \omega_0$), such that the terms polynomial in ω can be replaced with ω_0. We take a second-order expansion of the wavevector about ω_0, such that $k(\omega) \approx k_0 + k_1\tilde{\omega} + k_2\tilde{\omega}^2/2$ where k_1 is the inverse of the group velocity and k_2 describes linear chromatic dispersion. While higher-order chromatic dispersion is not always negligible, in this treatment we will use the term "dispersion" to describe linear chromatic dispersion unambiguously.

We can then express our frequency domain nonlinear wave equation as

$$\left(\frac{\partial}{\partial z} + ik_1\tilde{\omega}\right) A(\vec{r}, \tilde{\omega}) = \frac{\omega_0^2}{2ik_0\epsilon_0 c^2} p(\vec{r}, \tilde{\omega}) e^{i(k_0 - k_p)z} + \frac{1}{2ik_0}\nabla_\perp^2 A(\vec{r}, \tilde{\omega}) + \frac{k_2}{2i}\tilde{\omega}^2 A(\vec{r}, \tilde{\omega}) \quad (2.16)$$

We may also Fourier transform back to the time domain to obtain

$$\left(\frac{\partial}{\partial z} - k_1\frac{\partial}{\partial t}\right) A(\vec{r}, t) = \frac{\omega_0^2}{2ik_0\epsilon_0 c^2} p(\vec{r}, t) e^{i(k_0 - k_p)z} + \frac{1}{2ik_0}\nabla_\perp^2 A(\vec{r}, t) + \frac{ik_2}{2}\frac{\partial^2}{\partial t^2} A(\vec{r}, t). \quad (2.17)$$

In the absence of the terms on the right-hand side, the left-hand side describes a field which travels at the group velocity $1/k_1$ in the $\hat{z}$ direction. The three correction terms on the right-hand side represent the nonlinear contribution, spatial diffraction, and linear chromatic dispersion, respectively, as shown in Fig. 2.1a. Careful treatment requires consideration of all three (in addition to terms dropped already throughout this process), but we will concern ourselves mostly with the nonlinear term.

2.1.2   Sum-frequency generation

The differential equation governing wave propagation in nonlinear media in Eq. (2.16) and Eq. (2.17), despite the numerous simplifications made, can still be used to describe processes such as self-focusing and solitons [28]. We limit our interest to three-wave mixing effects, and define the polarization terms as those arising from three fields interacting. We assume that only the terms corresponding to sum-frequency generation occur (i.e. no competing second-harmonic generation processes). The nonlinear polarization in a $\chi^{(2)}$ material is given simply as

$$P^{(2)}(t) = \epsilon_0 \chi^{(2)} E^2(t), \quad (2.18)$$

43
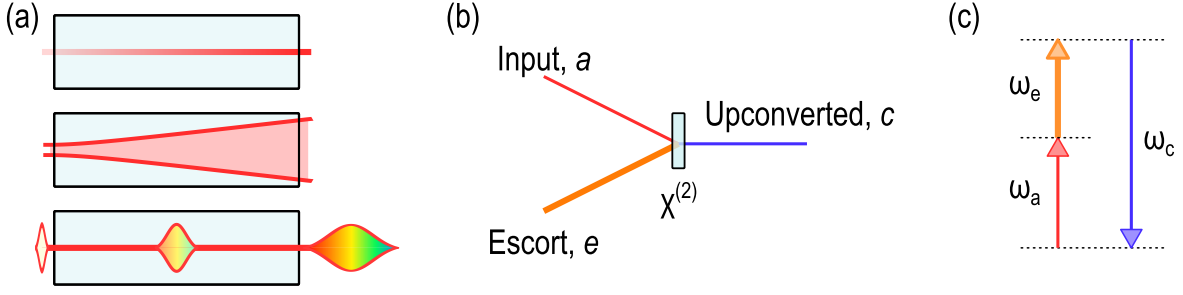
Figure 2.1: **Semi-classical picture of sum-frequency generation.** (a) The three competing processes described by the nonlinear wave equation of Eq. (2.16) and Eq. (2.17) are, from top to bottom, a nonlinear source term, beam expansion through spatial diffraction, and beam spreading through chromatic dispersion. (b) Sum-frequency generation is a three-wave mixing process in a $\chi^{(2)}$ material where an input signal in mode a is mixed with a strong escort pulse in mode e to create an upconverted beam in mode c. (c) The semi-classical energy level picture for this process is that a photon each from the escort and input modes are absorbed to a short-lived virtual energy level and re-emitted as a single photon at energy $\hbar\omega_c = \hbar(\omega_a + \omega_e)$.

where $E(t)$ itself is a superposition of three fields in general for three-wave mixing, labelled the input, escort, and output as in Fig. 2.1b, with subscripts a, e, and c, respectively. Substituting in our slowly-varying fields of Eq. (2.12) and assuming that ω_{0c} is larger than ω_{0e} and ω_{0a}, we find our slowly-varying polarizations as

$$
\begin{aligned}
p_a(\vec{r},t)e^{-ik_{pa}z} &= 2\epsilon_0\chi^{(2)}_{eff}A_c(\vec{r},t)A_e^*(\vec{r},t)e^{-i(k_{0c}-k_{0e})z} \\
p_e(\vec{r},t)e^{-ik_{pe}z} &= 2\epsilon_0\chi^{(2)}_{eff}A_c(\vec{r},t)A_a^*(\vec{r},t)e^{-i(k_{0c}-k_{0a})z} \\
p_c(\vec{r},t)e^{-ik_{pc}z} &= 2\epsilon_0\chi^{(2)}_{eff}A_a(\vec{r},t)A_e(\vec{r},t)e^{-i(k_{0a}+k_{0e})z}.
\end{aligned}
\tag{2.19}
$$

To write these in the frequency domain, we make use of the convolution theorem [112], which relates the multiplication of two functions to their convolution in the Fourier domain as

$$
\mathcal{F}[F(\omega)] \times \mathcal{F}[G(\omega)] = \mathcal{F}[F(\omega) \circ G(\omega)],
\tag{2.20}
$$

44

where convolution is defined as

$$F(\omega) \circ G(\omega) = \int d\omega' \, F(\omega')G(\omega - \omega').$$

(2.21)

For an intuitive view of sum-frequency generation, we neglect the dispersive terms k_2 and assume plane-wave input such that $\nabla_\perp^2 A(\vec{r},t) = 0$. We also assume that the escort pulse is much stronger than the other two pulses, such that the effect on $p_e(\vec{r},t)$ is negligible, and thus the escort field evolves simply as $A_e(z,\tilde{\omega}) = A_e(\tilde{\omega})e^{-ik_{1e}\tilde{\omega}z}$. The nonlinear wave equation of Eq. 2.16 then reduces to a set of two coupled differential equations, expressible in the frequency domain as

$$
\begin{aligned}
\left(\frac{\partial}{\partial z} + ik_{1a}\tilde{\omega}\right) A_a(z,\tilde{\omega}) &= \frac{\omega_{0a}^2}{ik_{0a}c^2}\chi_{eff}^{(2)} \left[A_c(z,\tilde{\omega}) \circ A_e^*(\tilde{\omega})e^{ik_{1e}\tilde{\omega}z}\right] e^{i(k_{0a}+k_{0e}-k_{0c})z} \\
\left(\frac{\partial}{\partial z} + ik_{1c}\tilde{\omega}\right) A_c(z,\tilde{\omega}) &= \frac{\omega_{0c}^2}{ik_{0c}c^2}\chi_{eff}^{(2)} \left[A_a(z,\tilde{\omega}) \circ A_e(\tilde{\omega})e^{-ik_{1e}\tilde{\omega}z}\right] e^{i(k_{0c}-k_{0a}-k_{0e})z}
\end{aligned}
$$

(2.22)

In order to make concrete statements, we next look at two highly simplified cases. First, we will apply the strong-pulse approximation to the input mode a as well, corresponding to the low-efficiency regime. Secondly, we will treat the case where the group velocities are all equal, which corresponds to the broad-phasematching limit. This will be followed immediately by a discussion of phasematching considerations.

Low-efficiency sum-frequency generation

In the low-efficiency regime, we can assume that the input field $A_a(z,\tilde{\omega})$ is relatively unaffected by the nonlinear polarization source term in Eq. (2.16), and write its evolution as simply $A_a(\tilde{\omega})e^{-ik_{1a}\tilde{\omega}z}$. This simplifies Eq. (2.22) to a single differential equation,

$$\left(\frac{\partial}{\partial z} + ik_{1c}\tilde{\omega}\right) A_c(z,\tilde{\omega}) = \frac{\omega_{0c}^2}{ik_{0c}c^2}\chi_{eff}^{(2)} \left[A_a(\tilde{\omega})e^{-ik_{1a}\tilde{\omega}z} \circ A_e(\tilde{\omega})e^{-ik_{1e}\tilde{\omega}z}\right] e^{i(k_{0c}-k_{0a}-k_{0e})z}.$$

(2.23)

We note that

$$\left(\frac{\partial}{\partial z} + ik_{1c}\tilde{\omega}\right) A_c(z,\tilde{\omega}) = e^{-ik_{1c}\tilde{\omega}z}\frac{\partial}{\partial z}\left[A_c(z,\tilde{\omega})e^{ik_{1c}\tilde{\omega}z}\right],$$

(2.24)

45

and simplify Eq. (2.23) to

$$\frac{\partial}{\partial z}\left[A_c(z,\tilde{\omega})e^{ik_{1c}\tilde{\omega}z}\right] = \frac{\omega_{0c}^2}{ik_{0c}c^2}\chi_{eff}^{(2)}\left[A_a(\tilde{\omega})e^{-ik_{1a}\tilde{\omega}z} \circ A_e(\tilde{\omega})e^{-ik_{1e}\tilde{\omega}z}\right]e^{i(k_{0c}-k_{0a}-k_{0e})z}e^{ik_{1c}\tilde{\omega}z}.$$

(2.25)

We can then use the definition of the convolution to write the above in full as

$$\frac{\partial}{\partial z}\left[A_c(z,\tilde{\omega})e^{ik_{1c}\tilde{\omega}z}\right] = \frac{\omega_{0c}^2\chi_{eff}^{(2)}}{ik_{0c}c^2}\int d\tilde{\omega}'\, A_a(\tilde{\omega}')e^{-ik_{1a}\tilde{\omega}'z}A_e(\tilde{\omega}-\tilde{\omega}')e^{-ik_{1e}(\tilde{\omega}-\tilde{\omega}')z}e^{ik_{1c}\tilde{\omega}z}e^{i(k_{0c}-k_{0a}-k_{0e})z}.$$

(2.26)

The interaction medium is assumed to have a length L, so to find the output spectral waveform we integrate over z from $\pm L/2$. The right-hand side of Eq. (2.26) integrated over z is defined as the *phasematching function*, defined to first order as

$$\begin{aligned}\Phi^{(1)}(\tilde{\omega}_a,\tilde{\omega}_e,\tilde{\omega}_c) &= \frac{1}{L}\int_{-L/2}^{L/2}dz\, e^{i(k_{0c}+k_{1c}\tilde{\omega}_c-k_{0a}-k_{1e}\tilde{\omega}_e-k_{0e}-k_{1e}\tilde{\omega}_e)z}\\ &= \operatorname{sinc}\left[\frac{L}{2}\left(k_{0c}+k_{1c}\tilde{\omega}_c-k_{0a}-k_{1e}\tilde{\omega}_e-k_{0e}-k_{1e}\tilde{\omega}_e\right)\right]\\ &= \operatorname{sinc}\left[\frac{L\Delta k^{(1)}}{2}\right]\end{aligned}$$

(2.27)

where $\Delta k^{(1)}$ is the first-order *phase mismatch* and is intrinsically a function of all three frequencies. We will discuss how to obtain the phasematching function and how it varies for different materials in the next section. For now, we note that while we have expressed it as a first order expansion, it readily generalizes to higher orders.

Assuming that mode c was initially empty, the low-efficiency sum-frequency waveform is

$$A_c(z,\tilde{\omega})e^{ik_{1c}\tilde{\omega}z} = \frac{\omega_{0c}\chi_{eff}^{(2)}L}{in_{0c}c}\int d\tilde{\omega}'\, A_a(\tilde{\omega}')A_e(\tilde{\omega}-\tilde{\omega}')\Phi(\tilde{\omega}',\tilde{\omega}-\tilde{\omega}',\tilde{\omega}),$$

(2.28)

which is the convolution of the two input spectra modulated by the phasematching function of the material. Note that, if the phasematching function is flat $(\Phi(\tilde{\omega}',\tilde{\omega}-\tilde{\omega}',\tilde{\omega}) \propto 1)$, we can make use of the convolution theorem from Eq. (2.20) to write Eq. (2.28) in the time

domain as

$$A_c(z,t) \propto \chi_{eff}^{(2)} L \, A_a(t) \times A_e(t). \tag{2.29}$$

We will rederive a similar expression from a first-order perturbative expansion of the 3WM Hamiltonian for the quantum case in Sec. 3.3.

Group-velocity matched solution

We can analytically solve the coupled differential equations of Eq. (2.22) in the time domain if we make the additional assumption that the fields are group-velocity matched, i.e. $k_{1a} = k_{1c} = k_{1e} = k_1$. In this case, we Fourier transform the coupled equations to find

$$
\begin{aligned}
\left(\frac{\partial}{\partial z} - k_1 \frac{\partial}{\partial t}\right) A_a(z,t) &= \frac{\omega_{0a}}{in_{0a}c} \chi_{eff}^{(2)} A_c(z,t) A_e^*(z,t) e^{-i\Delta k^{(0)}z} \\
\left(\frac{\partial}{\partial z} - k_1 \frac{\partial}{\partial t}\right) A_c(z,t) &= \frac{\omega_{0c}}{in_{0c}c} \chi_{eff}^{(2)} A_a(z,t) A_e(z,t) e^{-i\Delta k^{(0)}z}.
\end{aligned}
\tag{2.30}
$$

We make a change of variables such that $z' = z$ and $\tau = t + k_1 z$, and thus $\frac{\partial}{\partial z'} = \frac{\partial}{\partial z} - k_1 \frac{\partial}{\partial \tau}$ and $\frac{\partial}{\partial t} = \frac{\partial}{\partial \tau}$. This allows us to simplify our coupled equations to

$$
\begin{aligned}
\frac{\partial}{\partial z'} A_a(z', \tau - k_1 z') &= \frac{\omega_{0a}}{in_{0a}c} \chi_{eff}^{(2)} A_c(z', \tau - k_1 z') A_e^*(z', \tau - k_1 z') e^{-i\Delta k^{(0)}z'} \\
\frac{\partial}{\partial z'} A_c(z', \tau - k_1 z') &= \frac{\omega_{0c}}{in_{0c}c} \chi_{eff}^{(2)} A_a(z', \tau - k_1 z') A_e(z', \tau - k_1 z') e^{-i\Delta k^{(0)}z'}.
\end{aligned}
\tag{2.31}
$$

These coupled equations are solved in the same way as the monochromatic case [28].

If we assume that the upconverted mode c is initially empty ($A_c(0,t) = 0$) and that the phasematching condition is satisfied ($\Delta k^{(0)} = 0$), we obtain the output from a medium of length L as

$$
\begin{aligned}
A_a(L,t) &= A_a(0,t) \cos\left[\sqrt{\frac{\omega_{0a}\omega_{0c}}{n_{0a}n_{0c}}} \frac{\chi_{eff}^{(2)} L}{c^2} |A_e(0,t)|\right] \\
A_c(L,t) &= A_a(0,t) \frac{A_e(0,t)}{|A_e(0,t)|} \sqrt{\frac{n_{0a}\omega_{0c}}{n_{0c}\omega_{0a}}} \sin\left[\sqrt{\frac{\omega_{0a}\omega_{0c}}{n_{0a}n_{0c}}} \frac{\chi_{eff}^{(2)} L}{c^2} |A_e(0,t)|\right].
\end{aligned}
\tag{2.32}
$$

These solutions are inaccurate for any phase mismatch, which is never completely avoidable, but give an idea of the behaviour at high efficiency, where a field in mode a is converted to a field in mode c and back again as the escort strength is increased. This is consistent with the description in Sec. 1.1.4 of SFG as a beamsplitter. If $A_e(0, t)$ is not flat in time, different temporal components will convert at different rates, and complete upconversion will be impossible. We will discuss this further in Sec. 3.4.

2.1.3 Phasematching

In wave-mixing processes, both energy and momentum must generally be conserved. The interactions are assumed to not be modulated quickly in time, which would allow violation of energy conservation in the subsystem (in the same way that the escort pulse may be viewed as providing energy to upconvert a signal). We are also assuming a lossless medium, which avoids loss of energy in the sense of photon number. However, the medium is not assumed to be infinite in length, and thus momentum conservation is not strict. The function that describes the tightness of momentum conservation is the *phasematching function*, which we expressed to first order in Eq. (2.27) and express in full for generic modes a, b, and c with $\omega_{0c} \sim \omega_{0a} + \omega_{0b}$ as

$$
\begin{aligned}
\Phi(\omega_a, \omega_b, \omega_c) &= \frac{1}{L} \int_{-L/2}^{L/2} \mathrm{d}z \, e^{i(k_c(\omega_c) - k_b(\omega_b) - k_a(\omega_a))z} \\
&= \mathrm{sinc}\left[\frac{L}{2} \left(k_c(\omega_c) - k_b(\omega_b) - k_a(\omega_a) \right) \right] \\
&= \mathrm{sinc}\left[\frac{L \Delta k}{2} \right],
\end{aligned}
\tag{2.33}
$$

where

$$
\Delta k = k_c(\omega_c) - k_b(\omega_b) - k_a(\omega_a) = \frac{1}{c} \left[n_c(\omega_c)\omega_c - n_b(\omega_b)\omega_b - n_a(\omega_a)\omega_a \right]
\tag{2.34}
$$

with the indices of refraction defined according to the polarization and crystal axis in addition to the frequency of the light. As L is increased, phasematching is tightened but efficiency within the phasematched portion increases quadratically. For ease of calculation,

48

we will often use a Gaussian approximation to the sinc function, as

$$\mathrm{sinc}(x) \approx e^{-0.193x^2}, \tag{2.35}$$

where the value 0.193 is chosen such that the full-width at half-maximum is maintained [113].

If $n(\omega)$ was constant, the phasematching condition would be equivalent to energy conservation. This is far from the case though, and most of the glass and crystal materials we use have a higher refractive index on the blue end than the red end of the visible spectrum. The indices of refraction can be found from the Sellmeier equations of the material, which are empirical formulae describing the wavelength dependence of the index of refraction; many relevant Sellmeier equations can be found at Ref. [114]. To allow for different wavelengths to satisfy the phasematching condition, the blue and red fields involved will usually have different polarizations. As seen in Fig. 2.2a, while the ordinary and extraordinary axes of a crystal follow the same patterns, situations can arise where phasematching is met if the fields are polarized on different axes. For example, in bismuth triborate (BiBO), light at 400 nm polarized along the ordinary crystal axis can have the same index of refraction at light at 800 nm travelling between the ordinary and the extraordinary axis, such that

$$\frac{1}{400 \text{ nm}}n_o(400 \text{ nm}) = \frac{2}{800 \text{ nm}}n_e(800 \text{ nm}). \tag{2.36}$$

Processes where the highest energy field is orthogonal to the lower-energy fields are known as type-I, with the SFG process described as $o + o \to e$ or $e + e \to o$, and processes where the lower energy fields are orthogonal to each other are known as type-II, $o + e \to e$ or $o + e \to o$.

There are three main techniques used to adjust the effective indices of refraction to tune phasematching. Quasi-phasematching, or periodic poling, introduces a periodic phase component to the nonlinear coefficient, which introduces high-order Fourier components that may correct the phase mismatch [119, 40]. Quasi-phasematching can be used to phasematch even when all three waves are polarized along the same direction (known as type-0), which enables nonlinear interactions that would be otherwise impossible. Changing the temperature of the crystal can also affect the phasematching conditions.
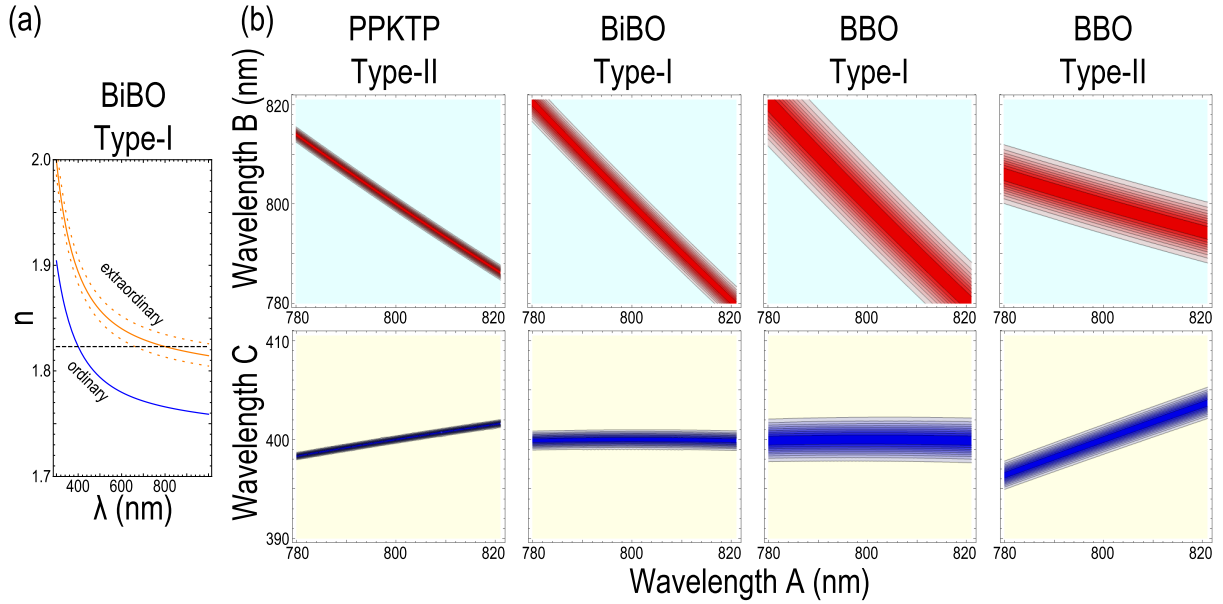
Figure 2.2: **Phasematching curves of NIR-to-UV crystals.** (a) While the index of refraction at 400 nm is larger than the same index at 800 nm, the ordinary index (blue) at 400 nm can be made equal to the effective extraordinary index (orange) at 800 nm, allowing type-I phasematching $e + e \rightarrow o$. The dotted orange lines show the effective extraordinary index when the crystal has been tilted by 10 degrees in either direction. (b) Phasematching functions for four crystal geometries effective at mixing NIR (800 nm) light with near-UV (400 nm) light are shown. The top row shows $\Phi(\omega_a, \omega_b, \omega_a + \omega_b)$, relevant for SPDC, while the bottom row shows the same functions written as $\Phi(\omega_a, \omega_c - \omega_a, \omega_c)$ as is relevant for SFG. Note that the type-I crystals tend to have phasematching curves that align with energy conservation, while the type-II materials do not. Each curve was calculated for a 1 mm crystal from its Sellmeier equations [114], and the crystals are listed from left-to-right in descending nonlinearity strength, $\chi^{(2)}_{eff}$ [115]. The crystals are periodically poled potassium titanyl phosphate ($KTiOPO_4$, or PPKTP) [116], bismuth triborate (BiB_3O_6, or BiBO) [117], and beta-barium borate (BaB_2O_4, or BBO) [118].

The sources and upconversion materials used in this thesis are all phasematched through *angle tuning*, where the effective index of the extraordinary axis is tuned by having the field polarized somewhere between the ordinary and extraordinary axis. Depending on the relative angle of the crystal to the propagation of light, the effective extraordinary index

50

$n_e(\theta)$ can be defined in terms of the ordinary index n_o and the principle extraordinary index $\bar{n}_e$[1] as [28]

$$\frac{1}{n_e(\theta)^2} = \frac{\sin^2\theta}{\bar{n}_e^2} + \frac{\cos^2\theta}{n_o^2}. \tag{2.37}$$

One major disadvantage of angle-tuned phasematching is that it requires that the fields do not propagate along a principle axis, which causes them to walk off from one another; see Sec. 3.2.3 for more details. Because of this, angle-tuned crystals are strongly limited in how long they can be. Additionally, some crystals with large nonlinear coefficients cannot be phasematched using these techniques, requiring periodic poling.

The structure of the phase mismatch function determines the shape of the phasematching function, as seen in Fig. 2.2b. We can see from these curves that type-I phasematching lends itself to phasematching functions that favour interactions that also satisfy energy conservation. This can be seen more directly by expanding the phase mismatch of Eq. (2.34) to first order about the central frequency of each field,

$$\Delta k^{(1)} = k_{0c} - k_{0b} - k_{0a} + k_{1c}(\omega_c - \omega_{0c}) - k_{1b}(\omega_b - \omega_{0b}) - k_{1a}(\omega_a - \omega_{0a}). \tag{2.38}$$

Conservation of energy dictates that $\omega_c = \omega_a + \omega_b$, and we assume that the fields chosen such that $\omega_{0c} = \omega_{0a} + \omega_{0b}$. If we also assume that the zeroth-order phasematching condition is met, $k_{0c} = k_{0a} + k_{0b}$, we can write the first order phase mismatch (also known as the *group velocity mismatch*) as

$$\Delta k^{(1)} = k_{1c}(\tilde{\omega}_a + \tilde{\omega}_b) - (k_{1b}\tilde{\omega}_b + k_{1a}\tilde{\omega}_a), \tag{2.39}$$

re-introducing the notation $\tilde{\omega} = \omega - \omega_0$. If the fields in modes a and b are identically polarized and nearly identical in central frequency and incoming angle, their wavevectors will be nearly degenerate, $k_{1a} \approx k_{1b}$. In this case,

$$\Delta k^{(1)} \stackrel{\text{degenerate}}{=} (k_{1c} - k_{1a})(\tilde{\omega}_a + \tilde{\omega}_b). \tag{2.40}$$

---

[1]We assume here that the indices of refraction can be classified as simply ordinary or extraordinary. This holds for a uniaxial crystal, such as BBO, but not generally for a biaxial crystal, such as BiBO. However, Eq. (2.37) holds for a biaxial crystal if the beams are propagating in a plane of the index ellipsoid, which renders one axis effectively meaningless.

This phase mismatch is insensitive to equal-and-opposite frequency shifts, e.g. $\tilde{\omega}_a \mapsto \tilde{\omega}_a + \delta$ and $\tilde{\omega}_b \mapsto \tilde{\omega}_b - \delta$. Because of this, the phasematching function in type-I near-degenerate processes always supports energy conserving processes to first order. This leads to very broad spectra in type-I spontaneous parametric downconversion, and allows much greater flexibility in the upconversion of equal-and-oppositely chirped pulses. This flexibility will be used to great advantage throughout the work done in thesis.

2.2 Temporal imaging via dispersion and upconversion

Now that we have established the guiding principles of ultrafast nonlinear optics in a simplified framework, we next discuss ultrafast pulses in more detail. We will first draw an analogy between ultrafast pulse propagation and the more familiar spatial diffraction. Using this analogy, we will build up temporal imaging systems based on diffraction and objects called time lenses [120, 121, 122, 123].

2.2.1 Spatial imaging as quadratic phases

We can get an intuitive view of spatial propagation by considering the wave equation of Eq. (2.16) in the absence of a polarization term and with the assumption that the beam in question is monochromatic. In this case, the frequency dependence of k becomes irrelevant, and the wave equation of Eq. (2.17) simplifies to the paraxial Helmholtz equation [36, 121],

$$\left(\frac{\partial^2}{\partial x^2} + \frac{\partial^2}{\partial y^2} \right) A(\vec{r}) = i2k_0 \frac{\partial}{\partial z} A(\vec{r}).$$

(2.41)

We neglect the y-coordinate and focus on the two-dimensional case, as it will prove more relevant in future discussion. One solution to this equation is the Gaussian beam [36],

$$A(x, z) = \frac{A_0}{\sqrt{z + iz_0}} \exp\left[-i\frac{k_0 x^2}{2(z + iz_0)}\right]$$

$$= \frac{A_0}{\sqrt{z + i\frac{k_0 w_0^2}{2}}} \exp\left[-\frac{x^2}{w_0^2 + \frac{4z^2}{k_0^2 w_0^2}}\right] \exp\left[-\frac{2ik_0 z}{k_0^2 w_0^4 + 4z^2} x^2\right]. \tag{2.42}$$

w_0 is the $\frac{1}{e^2}$ beam waist radius, $z_0 = \frac{\pi w_0^2}{\lambda} = \frac{k_0 w_0^2}{2}$ is the Rayleigh range, and it is assumed that the focus is at $z = 0$. We will use the second formulation from here on out.

We define a normalized spatial beam profile $f(x, z)$ such that $\int \mathrm{d}x |f(x, z)|^2 = 1$ as

$$f(x, z) = \frac{\left(\frac{2}{\pi}\right)^{\frac{1}{4}}}{\sqrt{iw_0 + \frac{2z}{k_0 w_0}}} \exp\left[-\frac{x^2}{w_0^2 + \frac{4z^2}{k_0^2 w_0^2}}\right] \exp\left[-i\frac{2k_0 z}{k_0^2 w_0^4 + 4z^2} x^2\right]. \tag{2.43}$$

The Fourier transform of this profile gives the distribution of transverse momentum $k_x = k_0 \sin\theta_x$, and is found as

$$F(k_x, z) = \mathcal{F}_x [f(x, z)] = \frac{\sqrt{w_0}}{(2\pi)^{\frac{1}{4}}} \exp\left[-\frac{k_x^2 w_0^2}{4}\right] \exp\left[i\frac{z}{2k_0} k_x^2\right]. \tag{2.44}$$

Eq. (2.43) and Eq. (2.44) both represent amplitudes with Gaussian intensity distributions and a quadratic phase. They differ in that the intensity of the transverse momentum distribution, $|F(k_x, z)|^2$, is z-independent, while $|f(x, z)|^2$ expands in the x direction for growing values of $|z|$. We can also look at the central transverse momentum of each point of the spatial distribution as the derivative of the quadratic phase[2], given by

$$k_x(x) = \frac{\mathrm{d}}{\mathrm{d}x}\left(\frac{-2k_0 z}{k_0^2 w_0^4 + 4z^2} x^2\right) = -\frac{4k_0 z}{k_0^2 w_0^4 + 4z^2} x \stackrel{z \gg k_0 w_0^2}{=} -k_0 \frac{x}{z} = -k_0 \tan\theta_x \approx -k_0 \sin\theta_x, \tag{2.45}$$

---

[2]The relationship between space-dependent momenta and the derivative of the spatial phase is the same as the relationship between instantaneous frequency and the derivative of the spectral phase, which will be discussed in Sec. 2.2.2.

where the large-diffraction and paraxial limits allows us to simplify back to the definition of the transverse momentum. Thus, the propagation of a Gaussian beam spreads out the transverse momentum components in space with quadratic phase fronts, and in the large-diffraction limit maps each transverse momentum to a unique point in space.

In contrast, we can think of a perfectly parabolic thin glass spatial lens as implementing a quadratic phase in space, which gives each point in space a unique shift in transverse momentum. In the thin-lens limit where the lens is placed at $x = 0$, it will implement the phase [121]

$$f(x, z) \mapsto f(x, z) \exp\left[i\frac{k_0}{2f}x^2\right], \tag{2.46}$$

where f is the focal length of the lens. If we apply this phase to the profile of Eq. (2.44) after propagating a distance z_1, the transverse momentum profile after the lens will be

$$F(k_x, z_1) \mapsto \frac{\left(\frac{2}{\pi}\right)^{\frac{1}{4}}\sqrt{fw_0}}{\sqrt{k_0w_0^2 + 2i(f - z_1)}} \exp\left[-\frac{f^2w_0^2}{k_0^2w_0^4 + 4(f - z_1)^2}k_x^2\right] \exp\left[-i\frac{f}{2k_0}\frac{4(f - z_1)z_1 - k_0^2w_0^4}{4(f - z_1)^2 + k_0^2w_0^4}k_x^2\right]$$

$$\stackrel{|f-z_1|\gg k_0w_0^2}{=} \frac{\left(\frac{2}{\pi}\right)^{\frac{1}{4}}\sqrt{fw_0}}{\sqrt{k_0w_0^2 + 2i(f - z_1)}} \exp\left[-\frac{f^2w_0^2}{4(f - z_1)^2}k_x^2\right] \exp\left[-i\frac{1}{2k_0}\frac{fz_1}{(f - z_1)}k_x^2\right], \tag{2.47}$$

where we focus on the case where $|f - z_1| \gg k_0w_0^2$, implying that the beam has expanded to many times its waist radius and that $z \neq f$, as an intuitive example. The remaining quadratic phase on the transverse momentum profile can be undone in this limit with propagation over a distance z_2 of

$$z_2 = \frac{fz_1}{f - z_1} = \left(\frac{1}{f} - \frac{1}{z_1}\right)^{-1}, \tag{2.48}$$

which corresponds to the familiar thin lens equation, usually shown as in Fig. 2.3. The waist of the beam w_0 is modified from its original form in Eq. (2.44) by a magnification factor M,

$$M = \frac{f}{(f - z_1)} = -\frac{z_2}{z_1}. \tag{2.49}$$

Note that the momentum distribution is magnified by a factor of $1/M$, consistent with the

Propagation z_1=2f   Spatial lens f   Propagation z_2=2f
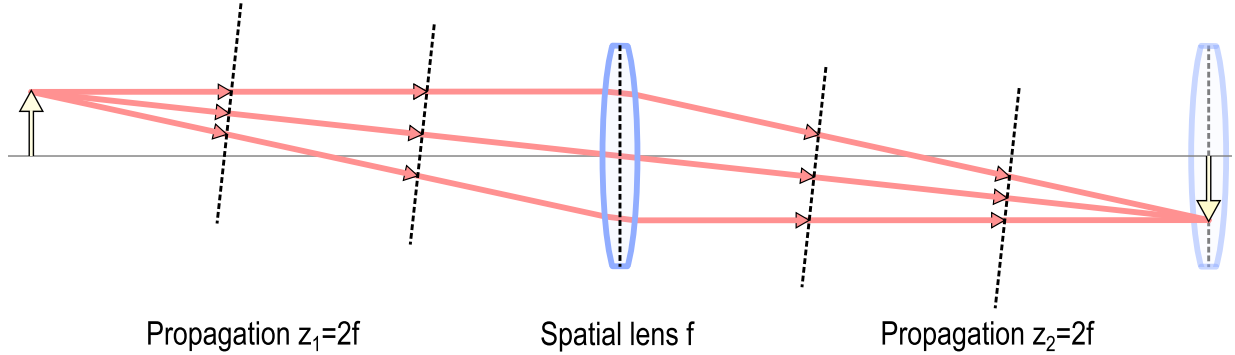
Figure 2.3: **Imaging with a spatial lens.** A spatial imaging system consists of propagation and glass lenses, each of which can be thought of as quadratic phases. As the beam propagates, its phase fronts take a quadratic form as the momentum components spread out in space. The lens, approximated as parabolic, directly implements a quadratic phase in space, which redirects each momentum component while not affecting the spatial profile. Further propagation may refocus the beam. In the case shown, $z_1 = z_2 = 2f$, corresponding to an imaging system with a magnification of $M = -1$. Generally, a second lens is required to complete the telescope for waveform reshaping.

Fourier scaling property.

Note that the above example only corresponds to the large-diffraction limit with a restricted relation between z_1 and f. Nonetheless, the essential points are contained within that example; viewing free-space propagation and glass lenses as quadratic momentum and spatial phases, respectively, allows us to derive the familiar imaging equations. In a general telescopic imaging system, a second lens is required to recollimate the output beam. One particularly interesting case that does not fit into the above description is collimation, where $z_1 = f$. This process is also called the lens Fourier transform in certain limits. In this case, the output transverse momentum profile after the lens is

$$F(k_x, f) \mapsto \frac{\left(\frac{2}{\pi}\right)^{\frac{1}{4}} \sqrt{f w_0}}{\sqrt{k_0 w_0^2}} \exp\left[-\frac{f^2}{k_0^2 w_0^2} k_x^2\right] \exp\left[i\frac{f}{2k_0} k_x^2\right]. \tag{2.50}$$

Note that the w_0 term in the intensity profile is now in the denominator, and will be in the

numerator of the Fourier transform. Therefore, a beam that started large will now have a larger momentum distribution, and vice versa. In this way, the spatial profile is mapped to the momentum profile and vice-versa.

2.2.2   Chirped pulses and dispersion

Having shown that quadratic phases play an important role in spatial imaging, we next find that they play a similar role when considering temporal pulse shapes. From inspecting Eq. (2.16) in the absence of a polarization term, it is clear that a pulse of light with a spectral field $F(\omega)$ travelling as a plane wave (such that $\nabla_\perp A(\vec{r}, \omega) = 0$) through a medium will evolve as

$$F(\omega) \mapsto F(\omega)e^{ik(\omega)z} \approx F(\omega)e^{ik_0 z + ik_1(\omega-\omega_0)z + i\frac{k_2}{2}(\omega-\omega_0)^2 z}. \tag{2.51}$$

The zeroth-order term k_0 is simply an overall phase, and the first order term k_1 represents a group delay to the temporal distribution of $\tau = k_1 z$. Higher-order terms will shape the temporal distribution $|f(t)|^2$, representing a frequency-dependent delay or group velocity dispersion (GVD) . The group delay is dependent on the first derivative of the wavenumber,

$$k_1 = \frac{\mathrm{d}k}{\mathrm{d}\omega} = \frac{n}{c} + \frac{\omega}{c}\left(\frac{\mathrm{d}n}{\mathrm{d}\omega}\right) = \frac{n}{c} - \left(\frac{\lambda}{c}\right)\left(\frac{\mathrm{d}n}{\mathrm{d}\lambda}\right) = \frac{\tau}{z}. \tag{2.52}$$

The amount of linear dispersion is dependent on the second derivative of the wavenumber [124],

$$k_2 = \frac{\mathrm{d}^2 k}{\mathrm{d}\omega^2} = \frac{2}{c}\frac{\mathrm{d}n}{\mathrm{d}\omega} + \frac{\omega}{c}\frac{\mathrm{d}^2 n}{\mathrm{d}\omega^2} = \frac{\lambda^3}{2\pi c^2}\frac{\mathrm{d}^2 n}{\mathrm{d}\lambda^2} = \frac{2A}{z}, \tag{2.53}$$

where A is the *chirp parameter* quantifying the total amount of dispersion applied to the pulse. Note that dispersion is often given in terms of a dispersion parameter D_λ, with units of ps/(nm·km). The two can be interchanged as [125]

$$k_2 = -\frac{\lambda^2}{2\pi c}D_\lambda. \tag{2.54}$$

56

If we assume that the spectral field is well described in Gaussian form as

$$F(\omega) = \frac{1}{(2\pi\sigma^2)^{\frac{1}{4}}} \exp\left[-\frac{(\omega-\omega_0)^2}{4\sigma^2}\right] \exp\left[i\tau(\omega-\omega_0) + iA(\omega-\omega_0)^2\right], \quad (2.55)$$

then its temporal distribution will be given by the Fourier transform $\mathcal{F}[F(\omega)]$,

$$f(t) = \frac{\left(\frac{2}{\pi}\right)^{\frac{1}{4}}}{\sqrt{\frac{1}{\sigma} - 4iA\sigma}} \exp\left[-\frac{\sigma^2(t+\tau)^2}{1 + 16A^2\sigma^4}\right] \exp\left[-\frac{4iA\sigma^4(t+\tau)^2}{1+16A^2\sigma^4} + i\omega_0 t\right]. \quad (2.56)$$

We can find the instantaneous frequency $\omega(t)$ of the a pulse, defined as the central carrier frequency at a given time, by taking the first derivative of the spectral phase to find the frequency at which the phase variations are smallest at each time [126]. For the stretched pulse of Eq. (2.56), we find that

$$\omega(t) = \frac{\mathrm{d}}{\mathrm{d}t}\left(\frac{-4A\sigma^4(t+\tau)^2}{1+16A^2\sigma^4} + \omega_0 t\right) = \omega_0 - \frac{8A\sigma^4(t+\tau)}{1+16A^2\sigma^4} \overset{LCL}{=} \omega_0 - \frac{(t+\tau)}{2A}, \quad (2.57)$$

where the simplification is in the large-chirp limit (LCL) where the pulse is stretched to many times its original temporal width, $A \gg 1/\sigma^2$. If the chirp parameter A is positive, the leading edge of the pulse will be red-shifted while the trailing edge will be blue-shifted relative to the centre. This corresponds to dispersion through a normally dispersive material ($k_2 > 0$), while the opposite would occur in a material with anomalous dispersion ($k_2 < 0$). See Fig. 2.4a for a depiction of GVD in optical fibre.

The formal similarities between the spectral profile after propagating through a dispersive material in Eq. (2.55) and the transverse momentum profile after propagating in free space in Eq. (2.44) are deeper than surface level. With the plane-wave and monochromatic assumptions in each respective case, the two degrees of freedom evolve in analogous fashions, and techniques used in one can be adapted to the other given proper implementations [120, 121, 127]. In the same way that a lens enacts a quadratic phase in space per Eq. (2.46), an element that implements a quadratic phase in time can be used along with dispersion to image the temporal properties of light. This device would ideally enact the

transformation

$$f(t) \mapsto f(t) \exp\left[iBt^2\right].$$ (2.58)

The effect of the *time lens* is sketched in Fig. 2.4b. Before diving into an examination of the time lens, we will look at an alternate representation of Fourier-related fields which can be used to provide an intuitive picture at how dispersion and time lenses link the time and frequency domains.

2.2.3 Wigner representation of pulsed fields

Field descriptions like Eq. (2.55) and Eq. (2.56) contain all the necessary information to describe a pure and coherent pulse in the time or frequency domain. It is possible to view both the temporal and spectral distributions simultaneously by considering the chronocyclic Wigner function [128, 122], which can be calculated from either the temporal or spectral field as

$$\begin{aligned}
W(t,\omega) &= \frac{1}{\sqrt{2\pi}} \int \mathrm{d}t' f(t + \frac{t'}{2}) f^*(t - \frac{t'}{2}) e^{-it'\omega} \\
&= \frac{1}{\sqrt{2\pi}} \int \mathrm{d}\omega' F(\omega + \frac{\omega'}{2}) F^*(\omega - \frac{\omega'}{2}) e^{i\omega' t}.
\end{aligned}$$ (2.59)

The chronocyclic Wigner function is always real-valued, and its marginals correspond to the spectral and temporal intensities as

$$|f(t)|^2 = \frac{1}{\sqrt{2\pi}} \int \mathrm{d}\omega \, W(t,\omega) \quad \text{and} \quad |F(\omega)|^2 = \frac{1}{\sqrt{2\pi}} \int \mathrm{d}t \, W(t,\omega)$$ (2.60)

For quantum systems, four-dimensional extensions of the chronocyclic Wigner function can be used to describe energy-time entangled states [129].

The chronocyclic Wigner function is particularly useful when dealing with chirped pulses. If the pulse is Fourier limited, the Gaussian spectral field of Eq. (2.55) with zero

chirp has a Wigner function of

$$W_{FL}(t, \omega) = \sqrt{\frac{2}{\pi}} \exp\left[-2\sigma^2(t+\tau)^2 - \frac{(\omega - \omega_0)^2}{2\sigma^2}\right]. \tag{2.61}$$

When a dispersive chirp A is introduced as shown in Eq. (2.55), the Wigner functions transforms to

$$W_{GVD}(t, \omega) = \sqrt{\frac{2}{\pi}} \exp\left[-2\sigma^2(t+\tau+2A(\omega-\omega_0))^2 - \frac{(\omega - \omega_0)^2}{2\sigma^2}\right]. \tag{2.62}$$

If a time lens of the form of Eq. (2.58) is applied instead, the Wigner function transforms to

$$W_{TL}(t, \omega) = \sqrt{\frac{2}{\pi}} \exp\left[-2\sigma^2(t+\tau)^2 - \frac{(\omega - \omega_0 - 2Bt)^2}{2\sigma^2}\right]. \tag{2.63}$$

The action of the dispersive chirp and time lens is thus to take the initial Wigner function $W_0(t, \omega)$ to

$$W_{GVD}(t, \omega) = W_0(t + 2A(\omega - \omega_0), \omega) \quad \text{and} \quad W_{TL}(t, \omega) = W_0(t, \omega - 2Bt). \tag{2.64}$$

These elements correspond to shears in chronocyclic space, as seen in Fig. 2.4c.

2.2.4   Using and constructing a time lens

By direct comparison with the spatial analogues of Eq. (2.44) and Eq. (2.46), we can define the equivalents of propagation distance and focal length for a temporal imaging system from Eq. (2.55) and Eq. (2.58) as

$$z_t = 2\omega_0 A, \quad \text{and} \quad f_t = \frac{\omega_0}{2B}. \tag{2.65}$$

As the mathematical representation is exactly analogous, the equivalent of the thin lens equation of Eq. (2.48) for a temporal imaging system will be [121, 130]

$$\frac{1}{A_1} + \frac{1}{A_2} = 4B, \tag{2.66}$$

59

which will implement a *temporal* magnification of

$$M_{\text{temporal}} = \frac{1}{M_{\text{spectral}}} = -\frac{A_2}{A_1}. \tag{2.67}$$
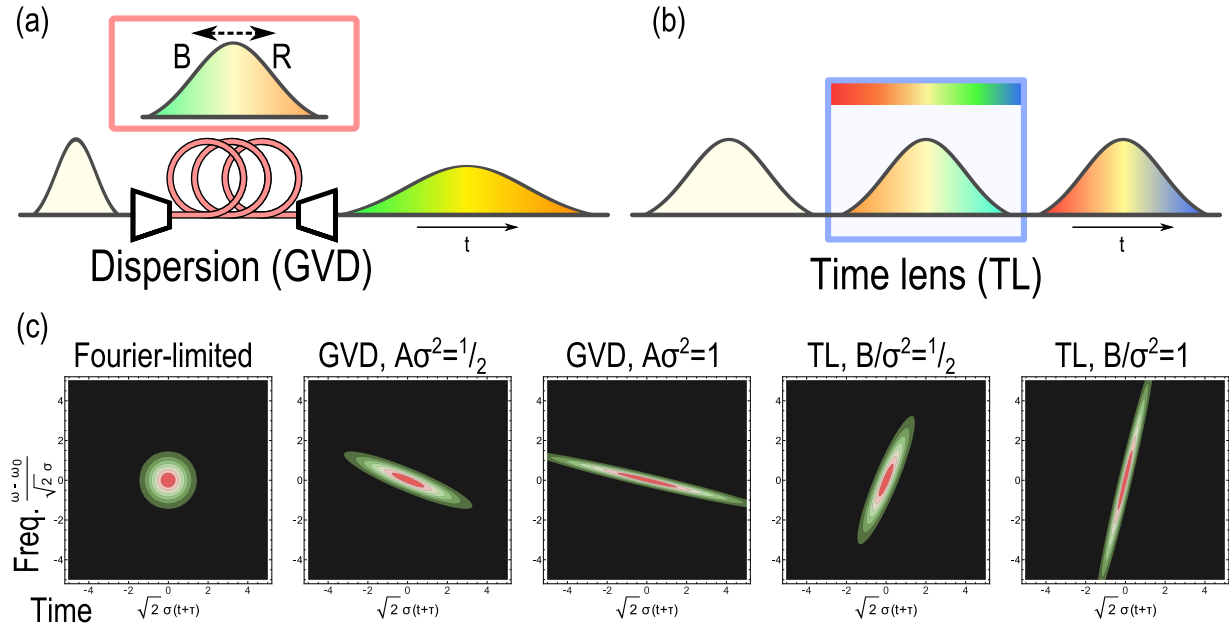
Figure 2.4: **Group velocity dispersion compared with a time lens.** (a) Group velocity dispersion (GVD) stretches a pulse in time, such that the leading edge is red-shifted relative to the trailing edge (for normal dispersion). It can be viewed as a frequency-dependent temporal shift, and occurs naturally for light propagating through optical fiber. (b) A time lens implements a time-dependent phase on a waveform, which does not affect the temporal amplitude but adds new frequencies. It can be viewed as a time-dependent frequency shift, and can be engineered using nonlinear optics or fast electronics. (c) Chronocyclic Wigner functions are shown for a Fourier limited pulse and its response under GVD and time lenses (TL). It is seen that GVD shears the Wigner functions in such a way that the temporal distribution is expanded, while the time lenses extends the spectrum. Note that the slope actually decreases as more chirp is applied, and the distribution narrows, implying that a large chirp can be used to map each frequency to an arrival time in the large-chirp limit.

60

The limits in which the "thin time lens" limit may be taken vary from implementation from implementation. In this section, we provide a brief overview of the method studied in this thesis, the upconversion time lens [131, 132], as well as other methods used elsewhere.

The upconversion time lens

To show how upconversion can implement the phase required for a time lens shown in Eq. (2.58), we refer back to the group-velocity-matched (i.e. broadly phasematched) equations for sum-frequency generation in Eq. (2.32). If we write our input temporal field as $f_i(t)$, our output upconverted field as $f_o(t)$, and our escort as $|g(t)|e^{i\phi_e(t)}$, as shown in Fig. 2.5, we can rewrite the solution as

$$f_o(t) = f_i(t)e^{i\phi_e(t)} \sin\left[\chi_{eff}^{(2)} L |g(t)|\right], \tag{2.68}$$

where we have absorbed some constant terms into the fields for simplicity. In the limit where the escort pulse is much broader in time than the waveform it is escorting, we can assume that the amplitude of the escort does not change very much over the course of the
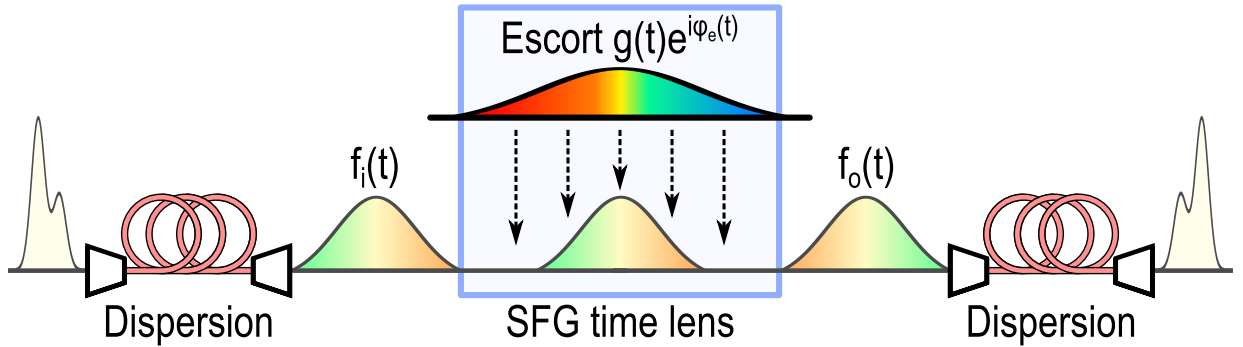
Figure 2.5: **Temporal imaging with an upconversion time lens.** The upconversion time lens imparts a time-dependent phase onto an input waveform, $f_i(t)$, through a sum-frequency generation (SFG) process with an escort pulse. If the escort pulse's amplitude $|g(t)|$ is much broader than the input signal and phasematching is non-dominant, it will not modulate the amplitude and simply impart its phase $\phi_e(t)$ to the final field $f_o(t)$.

interaction. In this case, we can assume that $|g(t)| \approx |g(0)|$ for all relevant t, and find that

$$f_o(t) \propto f_i(t)e^{i\phi_e(t)}. \tag{2.69}$$

In this complete-coverage limit, the escort does not affect the temporal shape of the input waveform, but does impart a temporal phase. If the escort has a quadratic phase as in Eq. (2.56), this phase will be

$$\phi_e(t) = \omega_{0e}t - \frac{4A_e\sigma_e^4(t + \tau_e)^2}{1 + 16A_e^2\sigma_e^4} \stackrel{LCL}{=} \omega_{0e}t - \frac{1}{4A_e}(t + \tau_e)^2. \tag{2.70}$$

The action of the simplified upconversion in Eq. (2.69) is therefore equivalent to the idealized time lens of Eq. (2.58), with a frequency shift of ω_{0e} and $B = -\frac{1}{4A_e}$ in the large-chirp limit. A central frequency shift of ω_{0e} is unavoidable with this method, although it could be corrected with another frequency shifting process. Note that the large chirp limit corresponds to a time lens with a small temporal chirp and thus a low temporal focusing power; the maximum temporal chirp B achievable with this method is $B_{max} = \frac{1}{2}\sigma_e^2$ with $A_e = 1/4\sigma_e^2$. The temporal thin lens equation simplifies nicely in this large-chirp limit to

$$\frac{1}{A_i} + \frac{1}{A_o} = -\frac{1}{A_e} \quad \text{and} \quad M_{\text{temporal}} = \left(1 + \frac{A_i}{A_e}\right)^{-1}. \tag{2.71}$$

Alternate implementations of a time lens

Sum-frequency generation will be the time lens implementation focused on in our experimental work, but it is not the only implementation. Four-wave mixing can be used instead of three-wave mixing in the exact same way, and can be operated with a minimal frequency shift between the input and output. Four-wave mixing techniques can be made incredibly efficient at low power using photonic crystal fibre or microring resonators [133, 134, 135], but suffer from difficult-to-suppress noise sources such as Raman scattering [28]. Four-wave mixing time lenses have, however, been highly successful for temporal imaging of classical signals [136, 137, 138, 139, 140, 141].

Other nonlinear processes can also be used to implement the necessary temporal phase.

Self-phase modulation, a third-order process in which an intensity-dependent refractive index causes a field to reshape itself as it propagates [28], will introduce a quadratic phase so long as the shape of the pulse is roughly quadratic. However, this effect must be balanced with material dispersion, and requires a third-order self-interaction, which cannot occur with single-photon input. Cross-phase modulation is also a third-order nonlinear process, but instead of depending on the field itself, an escort field is used to dynamically change the refractive index of the material to induce a phase [28, 122]. While effort is required to ensure that the cross pulse and the signal maintain overlap throughout the process, cross-phase modulation can be used characterize classical pulses [142, 143, 144, 122], and has been used to reshape [145] and switch [146] quantum signals.

Perhaps most commonly, a temporal phase can be introduced to an optical signal using electro-optic modulators (EOMs). It is possible to find second-order nonlinear media which allow interactions between an optical field and a static (DC) or low-frequency (AC) electric field [28]. This effect can be used to construct fast polarization switches, referred to as Pockels' cells, as well as phase modulators. If an alternating current of the form $V(t) = V_0 \cos(\omega_M t)$ is applied to a pulse centred at $t = 0$ which is shorter than the modulation period $2\pi/\omega_M$, the phase of the optical pulse will pick up a phase of $\phi(t) \approx c_\chi V_0 \left(1 - \omega_M^2 t^2/2\right)$, where c_χ is a constant depending on the properties of the material [120, 28]. Large temporal chirps can be implemented with highly nonlinear materials, high voltages, and fast modulators, but the modulation frequency must be slow enough that the optical pulses remain in the quadratic region of the modulation (where the second-order expansion is accurate). Current EOMs can operate at tens of GHz, and thus have quadratic regions with widths on the order of tens of picoseconds. Phase-modulating EOMs were the original proposed implementation of a time lens [120], have found application in reconstructing the temporal properties of pulses [147, 122], and have even been used to apply linear and quadratic phases to single photon waveforms [148, 149].

Time lens resolution and the temporal f-number

In spatial imaging systems, one is often concerned with the maximum achievable resolution. The waist radius of a focused beam with an initial waist w_0 incident on a lens of focal

length f is approximately given by $w_0' \approx \frac{\lambda f}{\pi w_0}$. To achieve a small waist (and thus a high resolution), a large object and tightly focusing lens is required. This is often characterized by the *f-number*, or $f^\#$, of the lens, written as the focal length divided by the aperture D, $f^\# = f/D$ [35], where high resolution is associated with small f-numbers. Note that this related to the numerical aperture as $f^\# = 1/(2\text{NA})$. This resolution comes at the expense of depth of field, as objects will defocus more rapidly as they deviate from the image plane.

We can define an analogous expression for temporal imaging systems, dubbed the temporal f-number $f_t^\#$ [121] as

$$f_t^\# = \frac{f_t}{\sigma_t}, \tag{2.72}$$

where σ_t is the temporal aperture and f_t is the temporal focal length. This value will determine how narrowly one can focus a feature in time, with the minimum temporal resolution defined by $\delta t = \frac{2\pi}{\omega_0} f_t^\#$ [121]. Smaller f-numbers will correspond to time lenses with more focusing power and tighter resolutions, while those with high f-numbers will be less sensitive to small shifts in time (the equivalent of a wide depth of field for spatial imaging).

In an ideal upconversion time lens, the temporal focal length and aperture can be found from the escort phase in Eq. (2.56) as

$$f_t = \frac{\omega_0}{2B} = -\left(\frac{\omega_0}{2}\right)\frac{1 + 16A_e^2\sigma_e^4}{4A_e\sigma_e^4} \tag{2.73}$$

and

$$\sigma_t = \frac{\sqrt{1 + 16A_e^2\sigma_e^4}}{\sqrt{2}\sigma_e}. \tag{2.74}$$

The temporal aperture has been defined in terms of the RMS width somewhat arbitrarily. The f-number then simplifies to

$$f_t^\# = \frac{\omega_0}{\sqrt{2}\sigma_e}\sqrt{\frac{1 + 16A_e^2\sigma_e^4}{16A_e^2\sigma_e^4}} \overset{\text{LCL}}{=} \frac{\omega_0}{\sqrt{2}\sigma_e}. \tag{2.75}$$

Therefore, to construct a high-resolution upconversion time lens, the escort bandwidth must be on the same scale as the central frequency. This result is sensible, as in the large-

chirp limit, the focal length is independent of the bandwidth, and broadband pulses stretch to a much greater extent than narrowband. However, it is fundamentally impossible to obtain f-numbers close to zero with an upconversion time lens, as the bandwidth cannot be greater than the central frequency even in the case of supercontinuum sources.

2.3 Measuring and manipulating ultrafast pulses

Now that we have established the guiding principles of ultrafast nonlinear optics in a simplified framework, we next explain some classical tools that will prove immensely useful in manipulating pulses. We first discuss sources of ultrafast pulsed light, followed by chirped pulses and pulse stretching. We then discuss how to measure the spectral profile of light with spectrometers. We close out the chapter by talking about measuring the temporal profile of pulses through autocorrelation, cross-correlation, and Hong-Ou-Mandel interference.

2.3.1 Ultrafast laser sources

For experiments in ultrafast optics, sources of ultrafast pulsed light are an obvious necessity. While an in-depth discussion of pulsed laser sources is outside of the scope of this thesis, we take a moment here to go over the laser source used in the experiments in this thesis: the titanium sapphire, or Ti:Sapph, laser. Two different Ti:Sapphs were used in this thesis, one being a Spectra-Physics Tsunami 3960 and the other a Coherent Chameleon Ultra II. While both operate differently for an end user, the underlying principles behind their operation are similar.

Pulsed laser sources have the same basic building blocks as continuous-wave laser sources, but with additional elements to facilitate mode-locking. Still, the laser must contain an external pump (usually a very strong cw laser, itself electronically pumped) and a gain medium. The pumping excites the gain medium to the point where its constituent atoms have a higher electronic population in excited states rather than ground states; this population inversion allows for stimulated emission to dominate over atomic absorption,

and light at the transition frequency will gain in intensity as it transmits through the medium [150, 36, 127]. The gain medium is placed in a cavity to allow for multiple round trips. The coherence length will depend on the atomic lifetime of the gain medium, but a pulse train is not automatically formed.

To create a pulse train, a broadband gain medium is necessary to allow for many different frequencies to be simultaneously amplified. It is then necessary to force the different allowed frequencies of the laser cavity to travel together in phase as a coherent pulse. This can be done actively with an externally driven modulator acting as a periodic shutter, or passively using nonlinear processes that react to the intensity of light. In Q-switched cavities for example, a saturable absorber is placed in the laser cavity which blocks weak pulses and transmits intense light. Only when the different frequency modes of the cavity are locked in phase does an intense enough pulse exist to transmit, and further gain will be locked in phase to that absorber.

An alternative approach, *Kerr lens mode-locking*, takes advantage of the nonlinear refractive index of third-order nonlinear materials and how it affects the spatial distribution of the beam. This is known as the Kerr lens effect [28, 127] and is the operating principle of the Ti:Sapph lasers used in this thesis. Interestingly, lasers based on Kerr lens mode-locking were initially called self mode-locked before the specifics of their operation was understood as they require a specific alignment to begin mode-locking but are self-sustaining once mode-locked even under external perturbation [151]. For this reason, the classic method of hitting the laser with a screwdriver to find mode-locking is oddly effective for these systems. In the photon picture of this effect, two photons are absorbed and two are re-emitted, with no change in the frequency of the beam. The effect occurs with a probability proportional to the intensity $|E(t)|^2$, and results in an effective nonlinear term added to the refractive index, $n = n_0 + n_2 I(t)$ [28]. If the beam has spatial structure, the effective index of the material will take on some of that structure, which can lead to so-called self-lensing. When the frequency modes overlap, the beam is focused tightly by the Kerr lens it creates, which can be used as an effective saturable absorber by placing a slit in the beam path or by using this tight focus to obtain high overlap with a focused pump laser. The Kerr effect can be effective for broadband light and relaxes very quickly (on the femtosecond scale [28]), and is therefore highly effective as an ultrafast shutter. As the mode-locking

causes the frequency components to travel together as a single pulse, the distance between subsequent pulses will be determined by the length of the laser cavity. The number of pulses per second is called the *repetition rate* of the laser, and the time between pulses is simply the inverse of the repetition rate.

A simplified schematic of a typical Ti:Sapph cavity is shown in Fig. 2.6. Note that the cavity is usually folded to minimize space. While the Ti:Sapph crystal is capable of acting as a gain medium for a broad range of frequencies, from 700 nm to 1050 nm [36, 127], it is
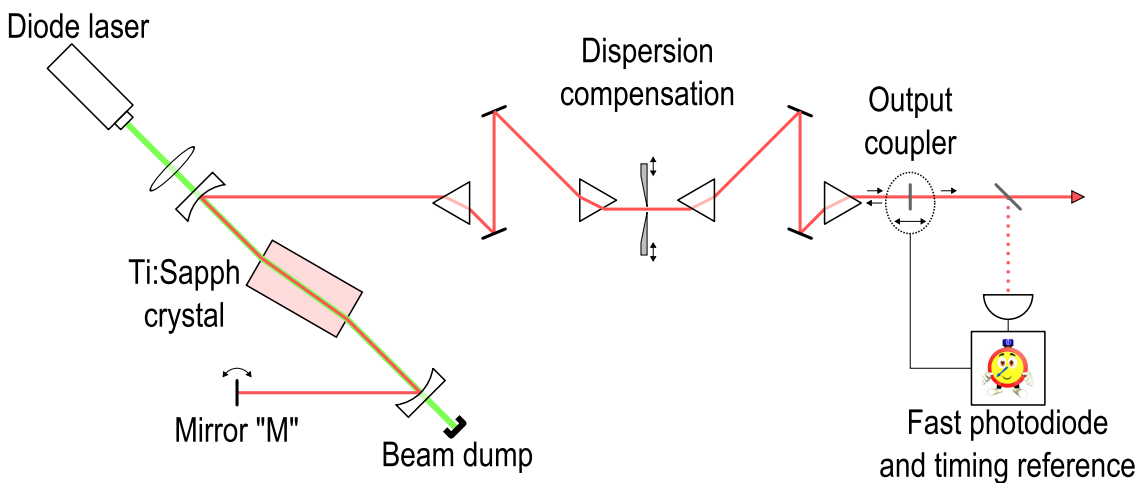
Figure 2.6: **Simplified Ti:Sapph cavity.** A titanium sapphire (Ti:Sapph) laser cavity operates by inserting a Ti:Sapph crystal in a cavity pumped by a diode laser (green). The stimulated emission from the crystal (red) can be steered by mirror M, which controls how well different emitted frequencies will overlap with the pump and mode-lock together. A series of prisms are used to compensate for dispersion throughout the cavity, and a moveable and tunable slit is used to select bandwidth and central frequency. A partially transmissive output coupler caps the cavity, and a beamsplitter is inserted just before the output to beat against a time reference. The length of the cavity is adjusted to match the reference frequency, ensuring a stable repetition rate. Figure based on schematics for the Spectra-Physics Tsunami Ti:sapphire laser [152].

nontrivial to mode-lock many of these frequencies such that an ultrashort pulse is obtained. Spatial walkoff in the Ti:Sapph crystal is frequency dependent, and thus different tilts into the crystal (as controlled by mirror M in Fig. 2.6) will change which frequencies overlap with the pump beam. Additionally, dispersion throughout the medium will spread the pulse, and result in a lower intensity and lower Kerr nonlinearity. The dispersion can be compensated in-cavity using a sequence of prisms; an equivalent system using gratings will be detailed in Sec. 2.3.2. An output coupler at the end of the cavity partially transmits the beam, completing the cavity. A piece of the beam can be picked off and measured against a timing reference to determine the repetition rate. This can be used to actively stabilize the repetition rate by shrinking or enlarging the cavity. The Lok-to-Clock of the Tsunami system operates in this fashion, stabilizing the repetition rate at 80 MHz with picosecond-scale timing jitter.

Due to the number of pieces involved, Ti:Sapph lasers are subject to drift and generally require daily reoptimization. In particular, stabilizing the wavelength is important for the experiments performed in this thesis, as wavelength drift will be measured as broadening when integrated over long periods of time. For the setup shown in Fig. 2.6, the central wavelength can be adjusted by tuning the slit in the dispersion compensation system or the horizontal tilt of mirror M. In the experiments using the Tsunami Ti:Sapph system, the wavelength was stabilized by attaching a rotation mount to the knob controlling the tilt of mirror M. A small amount of the output beam was picked off and sent to a spectrometer, which fit the spectrum in real time. LabView code was built to feedback any changes in the spectra to the motor for automatic correction. This allowed for experiments to be run overnight with no need for constant monitoring.

The exact wavelength ranges, bandwidths, and powers available vary from one Ti:Sapph to another. Oftentimes in ultrafast optics, we are less interested in the average power (as measured on a thermal power meter) than the peak power, or how much energy is contained in the shortest amount of time [153]. Given the average power P_{avg}, the repetition rate R, and the full-width at half-maximum (FWHM) temporal duration Δt_p, the peak power of a Gaussian beam is found as

$$P_p \approx 0.94 \frac{P_{avg}}{R \Delta t_p} = 0.41 \frac{c P_{avg} \Delta \lambda}{R \lambda_0^2}, \tag{2.76}$$

68

where the form in terms in central wavelength λ_0 and wavelength FWHM $\Delta\lambda$ assumes a Fourier-limited pulse. The Tsunami system outputs pulses with bandwidths of approximately 12 nm at 790 nm central wavelength with an 80 MHz repetition rate and an average power of approximately 2.3 W, corresponding to a temporal duration of approximately 75 fs and a peak power of 350 kW. Meanwhile, the Chameleon system is capable of producing bandwidths of approximately 5.5 nm at central wavelengths of 775 nm with an 80 MHz repetition rate and an average power of approximately 4 W, corresponding to a temporal duration of 160 fs and a peak power near 300 kW. Sources that are even broader exist, with bandwidths above 200 nm commercially available (at a cost of average power). In other cases, picosecond Ti:Sapphs with broader temporal features are advantageous. The differences between sources are non-trivial, and need to be taken into account when designing any experiment.

2.3.2 Pulse stretching and compression

While dispersive materials are easy to find, implementing controlled dispersion can be difficult. Any amount of dispersion can be applied (in principle) solely with linear optics, but not necessarily with material dispersion. In the visible regime, fused silica optical fibre is normally dispersive, and can be used to apply positive chirp; in the telecom regime, it is anomalously dispersive and applies negative chirp [36]. As seen in Eq. (2.53), travelling a distance z in single-mode fibre imparts a chirp of $A = k_2 z/2$. To apply dispersion of the opposite sign, geometric techniques based on gratings and prisms can be used. As the traditional application of negative dispersion is to compress pulses which have broadened in material or fibre, these tools are often called *pulse compressors*. Despite their name, when used on an unchirped pulse, compressors will instead stretch a pulse.

Prism-based compressors have low loss and can be made compact, and are key components in cavities for ultrafast lasers, as seen in Fig. 2.6; however, the amount of anti-chirp they can apply within a small space is strongly limited by the materials available as it depends on the size of the prisms and the wavelength dependence of their refractive indices [36, 154]. Grating-based systems are somewhat lossier, although they can be constructed to be more than 70% efficient with the use of blazed gratings. Importantly,

grating-based systems are capable of imparting a larger amount of negative dispersion than prism compressors before geometrical limitations set in [155, 36, 124, 156]. Chirped fibre Bragg gratings, which have an aperiodic lengthwise modulation in their refractive index, can also be used to implement a set amount of dispersion of either sign [157, 148]. A 4f pulse shaper with a spatial light modulator can also be used to impart the necessary phase, limited by higher-order contributions to the phase due to limited modulator resolution [158, 159, 127, 160, 156]. The work done in this thesis made extensive use of grating based compressors, in the configuration shown in Fig. 2.7, as detailed below.

A reflective diffraction grating is a mirror with a holographic phase mask whose period is given by Λ, usually expressed in lines per millimeter (ℓ/mm). The different Fourier components of the reflective surface result in many orders of diffraction, labelled m, which each reflect at an angle $\theta(\lambda)$ relative to the normal of the grating given by [35, 36]

$$\sin \theta(\lambda) = m\lambda\Lambda - \sin \theta_i, \tag{2.77}$$

where θ_i is the angle of incidence. The grating can be made such that the majority of the beam energy is diffracted into a desired mode through a process known as blazing, which adds sawtooth features to the phase gradient [35]. Many commercial gratings are designed to be most efficient when the portion of the diffracted beam at the central wavelength λ_c travels back along the incident beam, with $\theta(\lambda_c) = \theta_i = \arcsin\left(\frac{m\lambda\Lambda}{2}\right)$; this configuration is known as the *Littrow configuration*.

The grating compressor of Fig. 2.7a imparts an anti-chirp such that blue-shifted wavelengths lead the red-shifted ones at the output, equivalent to a large amount of anomalous dispersion. This can be calculated directly by finding the optical path length L traversed by each frequency component, which corresponds to the phase accumulated as $\phi = \frac{2\pi}{\lambda}L = \frac{\omega}{c}L$. If two parallel gratings blazed for first-order diffraction are separated by a distance D, the path length each frequency component takes is given by $L_{GG} = \frac{D}{\cos \theta(\lambda)}$. At the second grating, the frequency components are each incident at an angle of $\theta(\lambda)$, and are thus reflected at an angle of θ_i regardless of their wavelength; in this way, the frequency components are recollimated. If a mirror is placed normal to θ_i in the plane shown in Fig. 2.7a, the optical path length between the second grating and the mirror is given by

$L_{GM} = \frac{D}{\cos\theta(\lambda)}\cos[\theta_i - \theta(\lambda)]$. Note that shifting the mirror plane is irrelevant so long as it is not rotated, as the derivative of the phase is the important value. Upon reflection, the beam will retrace its previous steps and re-emerge travelling against the incident beam with no space-frequency coupling; a slight vertical deflection in the mirror can be used to tilt the output beam out of the plane of incidence so that it can be separated.
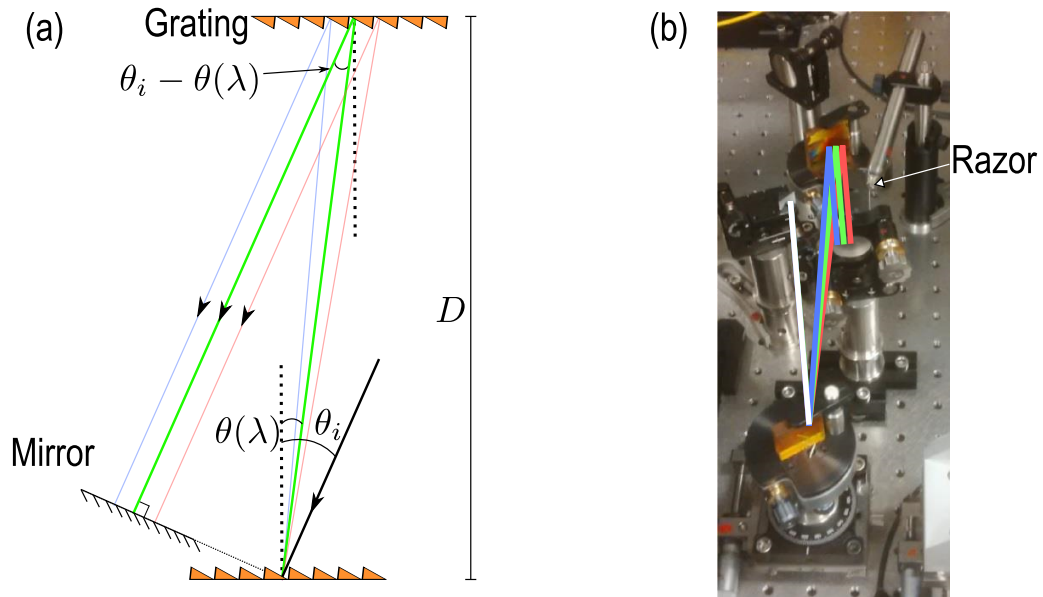
Figure 2.7: **Anti-chirp with a grating compressor.** (a) A schematic for a grating-based compressor is shown, with a broadband beam incident on the grating at an angle θ_i. Depending on their wavelength, the different components of the beam will reflect at an angle $\theta(\lambda)$. A second grating recollimates the beams, and the beam is then reflected such that it traverses the system again in reverse. This double-pass removes the space-frequency coupling of the beam, and tilting the mirror vertically allows the forward and backward propagating beams to be separated. In this configuration, red-shifted portions of the beam travel a longer optical path length than blue-shifted ones [155]. (b) A photograph of the grating-based compressor used in Chapter 6 and Ref. [130], with a cartoon mockup to show the different optical paths. Note that $\theta_i < \theta(\lambda)$ in this setup as opposed to the schematic. A razor blade can be inserted near the second grating to act as a controllable edge filter.

The wavelength-dependent total path length of the double-pass compressor is given by

$$L = 2 \times (L_{GG} + L_{GM}) = \frac{2D}{\cos\theta(\lambda)} \left\{ 1 + \cos\left[\theta_i - \theta(\lambda)\right] \right\}. \tag{2.78}$$

To find the phase imparted, it is necessary to add a corrective term which accounts for the variation of the phase seen by the broadened beam on the second grating due to different wavelengths seeing different parts of the hologram [155], which can be done as

$$\phi(\lambda) = \frac{2\pi}{\lambda} \frac{2D}{\cos\theta(\lambda)} \left\{ 1 + \cos\left[\theta_i - \theta(\lambda)\right] \right\} - 4\pi D\Lambda \tan\theta(\lambda). \tag{2.79}$$

The effective linear chirp applied to the double-pass system can be found from the quadratic term of the Taylor expansion of the phase, given by

$$A = \frac{1}{2} \frac{\mathrm{d}^2\phi}{\mathrm{d}\omega^2}\bigg|_{\omega_c} = \frac{-4\pi^2 c D\Lambda^2}{\omega_c^3 \cos^3\left[\theta(\omega_c)\right]} = \frac{-D\lambda_c^3\Lambda^2}{2\pi c^2 \cos^3\left[\theta(\lambda_c)\right]} \overset{\theta_i \approx \theta(\lambda_c)}{\approx} \frac{-D\lambda_c^3\Lambda^2}{2\pi c^2 \left(1 - \frac{1}{4}\lambda_c^2\Lambda^2\right)^{\frac{3}{2}}}. \tag{2.80}$$

The approximation of the final term is that the system is in a near-Littrow configuration ($\theta(\lambda_c) \approx \theta_i \approx \lambda\Lambda/2$). The chirp parameter is negative, and depends linearly on the distance between the two gratings. The amount of dispersion that can be imparted using this compressor is limited by the size of the gratings, as the beam spread at the second grating is effectively responsible for the frequency-dependent optical delay. When we use these systems with 100-fs Ti:Sapph pulses, 1200 lines/mm gratings, and a grating separation D of roughly one half-metre, chirp parameters on the order of $A \sim 1 \times 10^6\,\mathrm{fs}^2$ are easily achievable [161]. More direct experimental tips for the alignment of grating-based compressors can be found in Sec. A.2.

2.3.3 Grating-based spectrometers

The mapping of frequency to space via diffraction is a natural way to measure the spectrum of light, and has been around since at least the days of Newton. Other methods exist, and have found application in quantum optics; notably, frequency-to-time mapping through highly dispersive material can be used to craft a fibre spectrometer which can measure like

a camera with a single spatial pixel so long as it has sufficient temporal resolution [162, 163]. By far, however, the most widely used method for measuring a spectrum of a pulse of light is to measure its spatial profile after a diffraction grating. While the concept is intuitive, we nonetheless take a moment to discuss basic limitations on spectrometer resolution.

A grating-based spectrometer can be constructed as seen in Fig. 2.8. We consider a grating in Littrow configuration for simplicity, such that $\sin\theta(\lambda_c) = \sin\theta_i = \frac{\Lambda\lambda_c}{2}$, where Λ is once again the line density of the grating. In this situation, the angular difference between beams is given by $\sin\theta(\lambda) - \sin\theta_i = \Lambda(\lambda - \lambda_c)$, which we approximate to be small such that $\theta - \theta_i \approx \Lambda(\lambda - \lambda_c)$. If a lens with focal length f is placed in the system distance z_1 away from the grating, the beam z_2 away from the lens can be found from ray optics ABCD matrices to have an expected transverse position x_f and angle of propagation $\theta_f - \theta_i$ of

$$\langle x_f \rangle = \Lambda(\lambda - \lambda_c)\left[z_2 + z_1\left(1 - \frac{z_2}{f}\right)\right], \quad \langle\theta_f - \theta_i\rangle = \left(1 - \frac{z_1}{f}\right)\Lambda(\lambda - \lambda_c), \qquad (2.81)$$

defining $\langle x_f \rangle = 0$ for the central wavelength λ_c. If a lens is placed one focal length away
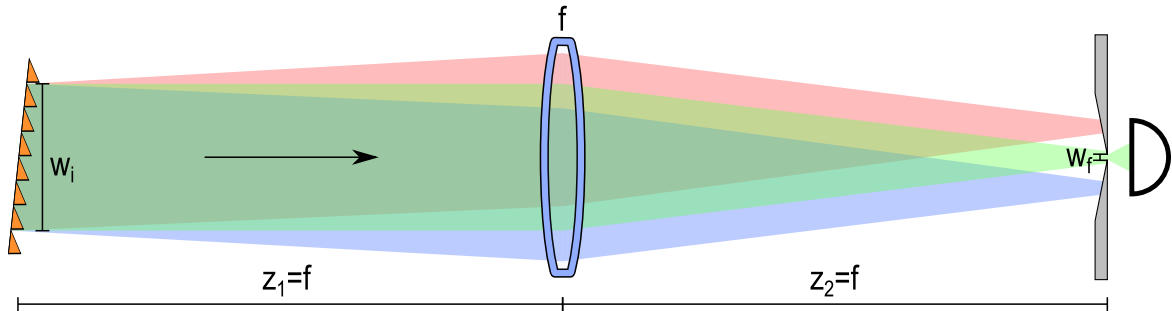
Figure 2.8: **A grating-based spectrometer.** A diffraction grating separated frequency components by imparting a frequency-dependent shift in the wavevector, giving each an independent angle of propagation. Using a lens Fourier transform, the angles are converted to spatial locations, which can be read out on a camera or using a scanning slit to measure the spectrum of the pulse. A larger input beam or greater diffraction power will result in higher resolution, while the focal length of the lens can be adjusted to balance the size of the spectrometer and the resolution requirements of the camera or slit. Doubling this setup to recollimate the beam effectively creates a tunable filter or monochromator.

$(z_1 = f)$, it will have the effect of collimating the different frequency components such that they propagate with parallel wavevectors and come to a focus in the same plane (ignoring lens aberrations). The expected transverse position in the plane of incidence of the grating after the lens is given by

$$\langle x_f \rangle = f\Lambda(\lambda - \lambda_c). \tag{2.82}$$

If $z_2 = f$ as well and the beams started collimated, they will come to a focus at this distance. If a camera or scanning slit is placed at z_2, each individual frequency can be isolated and a full spectrum can be measured.

The resolution of the system is determined by how well two different frequencies can be resolved. This may be limited by the pixel size of a camera or the minimum width of a slit, but is fundamentally limited by how tightly focused each frequency component is at the focal plane z_2. The output $1/e^2$ waist radius w_f of a Gaussian beam is given as

$$w_f = \frac{w_i}{\sqrt{1 + \left(\frac{z_0}{f}\right)^2}} \approx \frac{\lambda_c}{\pi w_i} f, \tag{2.83}$$

where w_i is the initial waist radius and z_0 is the Rayleigh range. With an idealized camera or fully tunable slit, the minimum resolvable spectral features would be those which take up a space of $\Delta x_f \sim 2w_f$, and therefore

$$\Delta\lambda_{min} = \frac{\Delta x_f}{f\Lambda} \sim \frac{2\lambda_c}{\pi w_i \Lambda}. \tag{2.84}$$

The resolution is independent of the focal length of the lens, but can be improved by using a grating with more lines-per-millimetre (higher density Λ) or with a large initial radius w_i. However, from a practical standpoint, a lower focal length lens allows the spectrometer to be made smaller, and a longer focal length spaces out the different frequency components more, reducing the demand on the slit or spatial measurement device.

2.3.4 Autocorrelation and cross-correlation

The temporal resolution of the single-photon detectors used in most quantum optics laboratories is on the order of hundreds of picoseconds [16], which is sufficient for discriminating signals from neighbouring pulses of high-repetition rate lasers but insufficient for directly measuring the temporal profile. It is possible to infer and characterize the temporal profile of ultrashort pulses using interferometric and nonlinear effects. Since the temporal resolution of these methods is dependent not on an external source but rather the timescales of the pulses used, they are often called *all-optical* processes. Here, we detail nonlinear cross- and auto-correlation, and in the next section we discuss a quantum interferometric method using the Hong-Ou-Mandel effect. This list is far from complete, and does not include more informative spectrographic techniques such as frequency-resolved optical gating [127, 122]. However, the techniques outlined are relatively simple and can be used to quickly characterize the temporal widths of ultrafast pulses.

Nonlinear cross-correlation is a slight generalization of ultrafast gating, and perhaps the most straightforward method to measure the temporal profile of an optical pulse, as shown in Fig. 2.9a. In cross-correlation, a pulse of interest is mapped by mixing it and a known measurement pulse in a nonlinear medium with a controllable time delay τ. The sum-frequency signal can then be measured with a slow detector or power meter. If the pulse of interest and the measurement pulse have temporal fields $f(t)$ and $g(t)$, respectively, the intensity measured in the ideal case can be found from Eq. (2.29) as

$$I_{cc} \propto \int \mathrm{d}t \, |f(t)g(t - \tau)|^2 \,, \tag{2.85}$$

which is the cross-correlation of the two temporal profiles. If the measurement pulse is not known, but is an exact copy of the pulse of interest, the process is known as *autocorrelation* instead, as seen in Fig. 2.9b.

If the pulses are well-described by Gaussian functions with temporal widths Δ such that $f(t) = \exp\left[-t^2/(4\Delta^2)\right]$ and $g(t) = \exp\left[-t^2/(4\Delta_m^2)\right]$, the cross-correlation signal will be

$$I_{cc} \propto \exp\left[-\frac{\tau^2}{2\left(\Delta^2 + \Delta_m^2\right)}\right], \tag{2.86}$$

75

which is a broadened version of the original pulse shape $|f(t)|^2$. If $\Delta_m \ll \Delta$, the cross-correlation scan will act as an ultrafast gate and temporally resolve slices of the original waveform. The cross-correlation is sensitive only to intensity and provides no information on phase, but can provide a faithful intensity trace of the measured pulse, as seen in the
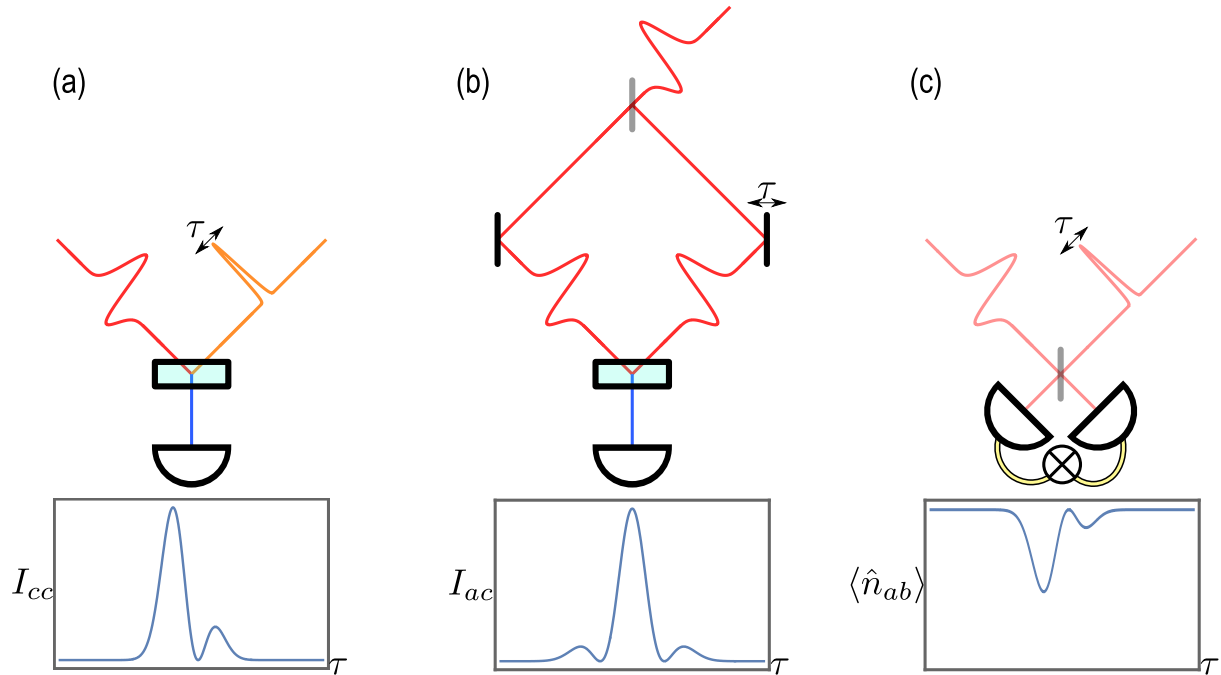
Figure 2.9: **Methods of measuring the temporal shape of pulses.** Three methods of measuring the temporal profiles of pulses are shown above, with a sample of the measurement result shown below each. (a) Cross-correlation of a pulse of interest (red) with a narrow measurement pulse (orange) in a nonlinear medium can be used to measure the temporal profile of a pulse slice-by-slice. The intensity profile measured faithfully recreates the intensity profile of the pulse so long as the measurement pulse is narrow enough. (b) If the pulse of interest is mixed with itself instead, an autocorrelation trace is obtained instead. The intensity trace is no longer necessarily a faithful recreation of the intensity profile, and must be corrected in post. (c) Mixing two signals on a 50/50 beamsplitter will result in Hong-Ou-Mandel interference, with a dip visibility proportional to the overlap of the two wavefunctions. Scanning a time delay allows for measurement of a pulse's temporal profile.

sample trace of Fig. 2.9a. On the other hand, in an autocorrelation scan, $\Delta_m = \Delta$, and the autocorrelation trace has a width broadened by a factor of $\sqrt{2}$ relative to the original pulse. Additionally, the autocorrelation scan is necessarily symmetric, and does not immediately produce an intensity trace of the measured pulse, as seen in Fig. 2.9b.

One common use of cross- and autocorrelation in this thesis is to determine the chirp of a pulse, as in Eq. (2.56). When using these techniques for such a purpose, it is often important to account for the phasematching of the nonlinear crystal used in the correlator, as phasematching will prevent certain frequencies from combining with each other in the process. This can act effectively as a frequency filter, which broadens the measured profile. Conversely, if the pulse is chirped strongly, applying a frequency filter would narrow the temporal duration of the pulse, and tight phasematching may result in a narrowing of the measured temporal profile. Characterizing the crystal used is therefore crucial when attempting to use nonlinear methods to characterize a pulse.

2.3.5 Measuring quantum signals with the HOM effect

Finally, we dip back briefly into quantum techniques to show how the Hong-Ou-Mandel (HOM) effect, first encountered in Sec. 1.1.1, can be used to characterize a single photon's temporal profile [164]. In the previous chapter, we saw that if two indistinguishable photons meet at a beamsplitter as seen in Fig. 2.9c, they bunch together such that they always exit the same port. The degree to which they bunch depends on the degree of indistinguishability of the two photons. The calculations that follow assume two single-photon states, but the effect persists for one single photon and one sufficiently weak coherent state [165, 166]; however, the dip visibility is limited to 50% if two weak coherent states are used[3].

We start with a two-photon state with some normalized joint spectral function $F(\omega_1, \omega_2)$

_____

[3]The weak coherent state ($|\alpha|^2 \ll 1$) may be used to simulate a single photon, and if it is weak enough, the case where one photon comes from the coherent state and one from the single-photon Fock state will dominate and 100% visibility can be achieved. However, with two weak coherent states, the probability of one photon coming from each coherent state is the same as the probability of both photons coming from the same coherent state, and the HOM visibility is limited to 50% even with vanishingly small photon number.

in two distinct spatial modes a and b, with a wavefunction

$$|\psi\rangle = \iint \mathrm{d}\omega_1 \mathrm{d}\omega_2 \, F(\omega_1, \omega_2) \hat{a}^\dagger_{\omega_1} \hat{b}^\dagger_{\omega_2} |00\rangle. \tag{2.87}$$

If the two spatial modes are mixed with a 50/50 beamsplitter as in Eq. (1.10), the joint state transforms to

$$
\begin{aligned}
|\psi\rangle &\mapsto \frac{1}{2} \iint \mathrm{d}\omega_1 \mathrm{d}\omega_2 \, F(\omega_1, \omega_2) \left(-i\hat{a}^\dagger_{\omega_1} \hat{a}^\dagger_{\omega_2} + \hat{a}^\dagger_{\omega_1} \hat{b}^\dagger_{\omega_2} - \hat{b}^\dagger_{\omega_1} \hat{a}^\dagger_{\omega_2} - i\hat{b}^\dagger_{\omega_1} \hat{b}^\dagger_{\omega_2} \right) |00\rangle \\
&= \iint \frac{1}{2} \mathrm{d}\omega_1 \mathrm{d}\omega_2 \left[F(\omega_1, \omega_2) \hat{a}^\dagger_{\omega_1} \hat{b}^\dagger_{\omega_2} - F(\omega_2, \omega_1) \hat{a}^\dagger_{\omega_1} \hat{b}^\dagger_{\omega_2} \right] |00\rangle + \text{noncoincident terms},
\end{aligned}
\tag{2.88}
$$

where a relabelling of the indices has been used to show that the indistinguishability between the ω_1 and ω_2 contributions is key in obtaining the HOM dip. The total coincidences can be found as

$$\langle \hat{n}_{ab} \rangle = \frac{1}{2} - \frac{1}{2} \iint \mathrm{d}\omega_1 \mathrm{d}\omega_2 \, F^*(\omega_1, \omega_2) F(\omega_2, \omega_1). \tag{2.89}$$

If the joint wavefunction is separable, with $F(\omega_1, \omega_2) = F(\omega_1) G(\omega_2)$, the HOM visibility will be given by

$$\langle \hat{n}_{ab} \rangle = \frac{1}{2} - \frac{1}{2} \left| \int \mathrm{d}\omega \, F^*(\omega) G(\omega) \right|^2. \tag{2.90}$$

The visibility of the dip is therefore dependent on how distinguishable the two photons are, as expected.

While many schemes require high visibility Hong-Ou-Mandel dips, the dependence on the distinguishability of the two fields may be used to great effect to probe a single-photon signal of interest with a known measurement pulse [164], similar to the cross-correlation measurement of Sec. 2.3.4. For example, if the two fields are both Gaussians with temporal widths Δ and Δ_m which are scanned relative to each other with a delay τ, the HOM trace will be given by

$$\langle \hat{n}_{ab} \rangle = \frac{1}{2} - \frac{\Delta \Delta_m}{(\Delta^2 + \Delta_m^2)} e^{-\frac{\tau^2}{2(\Delta^2 + \Delta_m^2)}}, \tag{2.91}$$

which has the same properties as the cross-correlation trace of Eq. (2.86) and can only reach 100% visibility if $\Delta = \Delta_m$. A sample trace seen in Fig. 2.9c shows that the dip features are

indeed similar to those in cross-correlation when one pulse is a narrow Gaussian. However, by shaping the measurement pulse in different ways, it is possible to probe the state more generally with a custom-shaped measurement pulse, akin to mode matching in homodyne detection [167] or temporal mode measurement in a quantum pulse gate [58].

Chapter 3

Quantum optical waveform conversion

Notes and acknowledgements

Parts of this chapter (Sec. 3.1, Sec 3.3, and Sec. 3.4) are adapted from material published on 2015 March 09 as [168]:

Author Contributions

Kevin Resch conceived of the study.

John Donohue and **Michael Mazurek** performed the analytic calculations and simplifications.

John Donohue, **Michael Mazurek**, and **Kevin Resch** beat their heads against a wall for a solid month figuring out what time ordering is.

John Donohue performed numeric simulations and wrote the first draft of the manuscript.

All authors contributed to the final version.

Additionally, Sec. 3.5 of this chapter was based on material previously published on 2013 March 31 as [161]:

J. Lavoie, J. M. Donohue, L. G. Wright, A. Fedrizzi, and K. J. Resch. Spectral compression of single photons. *Nature Photonics* **7** 363 (2013).

This material has previously appeared in the PhD thesis of Jonathan Lavoie [161].

Chapter Overview

In this chapter, we turn our attention strictly to single-photon applications of nonlinear optics. Having discussed the equivalent classical relations in Sec. 2.1, we first examine the three-wave mixing process quantumly by finding the Hamiltonian for the process in Sec. 3.1, including a brief discussion on the effects of time ordering. We then apply these results to examine spontaneous parametric downconversion in more detail in Sec. 3.2, and look at walkoff processes that disturb the idealized picture. We then turn our attention to sum-frequency generation with ultrafast single-photon pulses in Sec. 3.3. We provide efficiency limitations for quantum sum-frequency processes in Sec. 3.4, and examine how these processes affect energy-time entangled states. Finally, we introduce chirped-pulse bandwidth compression in Sec. 3.5.1, a process which we will put to use in Ch. 4 and Ch. 5.

3.1 The three-wave mixing Hamiltonian

We now return to our derivation of the full three-wave mixing Hamiltonian, picking up from Sec. 1.1.4. We can expand our three-wave mixing Hamiltonian of Eq. (1.33) with our

full continuum electric field operators of Eq. (1.9) as

$$\hat{H}_{3WM}(t) = \frac{\epsilon_0}{3}\chi^{(2)} \int_V d^3\mathbf{r} \int d^3\mathbf{k}_1 d^3\mathbf{k}_2 d^3\mathbf{k}_3 \frac{\sqrt{\omega_{k1}\omega_{k2}\omega_{k3}}}{n_1 n_2 n_3} \left(\frac{\hbar}{16\pi^3\epsilon_0}\right)^{3/2}$$
$$\times \left[i\hat{a}_{\mathbf{k}_1}^\dagger \hat{a}_{\mathbf{k}_2}^\dagger \hat{a}_{\mathbf{k}_3} e^{-i(\omega_{k3}-\omega_{k1}-\omega_{k2})t} e^{i(\mathbf{k}_3-\mathbf{k}_1-\mathbf{k}_2)\cdot\mathbf{r}} + \text{H.c.}\right],$$

(3.1)

where V is the volume of the interaction medium.

We next introduce the paraxial approximation into our Hamiltonian. We assume that the fields in question propagate primarily along the $\hat{z}$ direction, such that k_x and k_y contributions are small. We define $\mathbf{k}_T = k_x\hat{x} + k_y\hat{y}$ as the transverse wavevector and $\mathbf{r}_T = x\hat{x} + y\hat{y}$ as transverse position, and make the approximation that [169]

$$k_z = \sqrt{|\mathbf{k}|^2 - |\mathbf{k_T}|^2} \approx |\mathbf{k}| - \frac{1}{2|\mathbf{k}|}|\mathbf{k}_T|^2 = \frac{n\omega}{c} - \frac{c}{2n\omega}|\mathbf{k}_T|^2.$$

(3.2)

By the same token, the difference between the wavevectors can be written as

$$(\mathbf{k}_3 - \mathbf{k}_1 - \mathbf{k}_2)\cdot\hat{z} = \frac{1}{c}(n_3\omega_3 - n_1\omega_1 - n_2\omega_2) - \frac{c}{2n_3\omega_3}|\mathbf{k}_{T3}|^2 + \frac{c}{2n_1\omega_1}|\mathbf{k}_{T1}|^2 + \frac{c}{2n_2\omega_2}|\mathbf{k}_{T2}|^2. \quad (3.3)$$

We can then rewrite Eq. (3.1) in terms of ω instead of k_z by changing $dk_z \mapsto \frac{n}{c}d\omega$ and $\hat{a}_{k_z} \mapsto \sqrt{\frac{c}{n}}\hat{a}_\omega$ as

$$\hat{H}_{3WM}(t) = \frac{\epsilon_0}{3}\chi^{(2)} \int_V d^3\mathbf{r} \int d\omega_1 d\omega_2 d\omega_3 \int d^3\mathbf{k}_{T1} d^2\mathbf{k}_{T2} d^2\mathbf{k}_{T3} \sqrt{\frac{\omega_1\omega_2\omega_3}{n_1 n_2 n_3}} \left(\frac{\hbar}{16\pi^3\epsilon_0 c}\right)^{3/2}$$
$$\times \left[i\hat{a}_{\mathbf{k}_{T1},\omega_1}^\dagger \hat{a}_{\mathbf{k}_{T2},\omega_2}^\dagger \hat{a}_{\mathbf{k}_{T3},\omega_3} e^{-i(\omega_3-\omega_1-\omega_2)t + i(n_3\omega_3-n_1\omega_1-n_2\omega_2)\frac{z}{c}} \right.$$
$$\left. \times e^{-i\left(\frac{|\mathbf{k}_{T3}|^2}{n_3\omega_3} - \frac{|\mathbf{k}_{T1}|^2}{n_1\omega_1} - \frac{|\mathbf{k}_{T2}|^2}{n_2\omega_2}\right)\frac{cz}{2}} e^{i(\mathbf{k}_{T3}-\mathbf{k}_{T1}-\mathbf{k}_{T2})\cdot\mathbf{r}_T} + \text{H.c.}\right],$$

(3.4)

To further simplify, we will assume that the transverse spatial extent is much larger than the beams, allowing us to extend the x and y integrals of Eq. (3.1) to infinity. We

can then convert the transverse momentum integrals to delta functions as

$$\int \mathrm{d}^2\mathbf{r}_T \, e^{i(\mathbf{k}_{T3} - \mathbf{k}_{T1} - \mathbf{k}_{T2}) \cdot \mathbf{r}_T} = 4\pi^2 \delta^2(\mathbf{k}_{T3} - \mathbf{k}_{T1} - \mathbf{k}_{T2}) = 4\pi^2 \delta(k_{x3} - k_{x1} - k_{x2})\delta(k_{y3} - k_{y1} - k_{y2}),$$
(3.5)

implying conservation of transverse momentum. We also assume that the light we send in does not occupy nearly the full continuum, such that $\omega/\omega_0 \approx 1$ for all relevant frequencies ω, where ω_0 is the central frequency. We then replace the $\sqrt{\omega_i}$ terms with $\sqrt{\omega_{0i}}$. By also assuming that the index of refraction does not change drastically as a function of the transverse spatial momenta nor the frequency, we can also replace $1/\sqrt{n_i(\omega_i, k_x, k_y)}$ with the constant $1/\sqrt{n_i(\omega_{0i}, 0, 0)} = 1/\sqrt{n_{0i}}$.

We will also assume that the interaction occurs in a medium of length L, and evaluate the z integral as

$$\int_{-L/2}^{L/2} \mathrm{d}z \, e^{i(n_3\omega_3 - n_1\omega_1 - n_2\omega_2)\frac{z}{c}} e^{-i\left(\frac{|\mathbf{k}_{T3}|^2}{n_3\omega_3} - \frac{|\mathbf{k}_{T1}|^2}{n_1\omega_1} - \frac{|\mathbf{k}_{T2}|^2}{n_2\omega_2}\right)\frac{cz}{2}}$$

$$= L \times \mathrm{sinc}\left[\frac{L}{2c}(n_3\omega_3 - n_1\omega_1 - n_2\omega_2) - \frac{cL}{4}\left(\frac{|\mathbf{k}_{T3}|^2}{n_3\omega_3} - \frac{|\mathbf{k}_{T1}|^2}{n_1\omega_1} - \frac{|\mathbf{k}_{T2}|^2}{n_2\omega_2}\right)\right]$$
(3.6)

$$= L \times \Phi^{(c)}(\omega_1, \omega_2, \omega_3, \mathbf{k}_{T1}, \mathbf{k}_{T2}, \mathbf{k}_{T3}),$$

where $\Phi^{(c)}$ is a coupled form of the phasematching function. Usually, we will only consider cases where either the frequency or momentum dependence vanishes, such as the plane wave case considered classically in Sec. 2.1.3. We can rewrite our Hamiltonian with these simplifications and definitions as

$$\hat{H}_{3WM}(t) = \frac{\chi^{(2)}L}{48}\sqrt{\frac{\omega_{01}\omega_{02}\omega_{03}\hbar^3}{n_{01}n_{02}n_{03}\pi^5\epsilon_0 c^3}} \int \mathrm{d}\omega_1 \mathrm{d}\omega_2 \mathrm{d}\omega_3 \int \mathrm{d}^2\mathbf{k}_{T1}\mathrm{d}^2\mathbf{k}_{T2}\mathrm{d}^2\mathbf{k}_{T3}$$

$$\times \left[i\hat{a}^\dagger_{\mathbf{k}_{T1},\omega_1}\hat{a}^\dagger_{\mathbf{k}_{T2},\omega_2}\hat{a}_{\mathbf{k}_{T3},\omega_3}e^{-i(\omega_3 - \omega_1 - \omega_2)t}\delta^2(\mathbf{k}_{T3} - \mathbf{k}_{T1} - \mathbf{k}_{T2})\right.$$
(3.7)

$$\left.\times \Phi^{(c)}(\omega_1, \omega_2, \omega_3, \mathbf{k}_{T1}, \mathbf{k}_{T2}, \mathbf{k}_{T3}) + \mathrm{H.c.}\right].$$

The Hamiltonian itself is only useful to us in the context of how it controls state

83

evolution, which is described by the unitary transformation

$$\hat{U}_{3WM} \equiv \mathcal{T} \exp\left[-\frac{i}{\hbar} \int_{t_0}^{t_f} \mathrm{d}t \hat{H}_{3WM}(t)\right], \tag{3.8}$$

where $\mathcal{T}$ is the *time-ordering operator* [170, 171, 172, 173]. The time-ordering operator, as its name implies, ensures the correct ordering of sequential events, and effectively means that a Dyson series must be employed in expanding the evolution transformation rather than a Taylor expansion [174]. We can generally assume that our Hamiltonian is "always on", in the sense that the nonlinearity does not change dynamically as the pulse propagates along z. However, the time-ordering operator prevents us from simply extending all intermediary temporal integrals to $\pm\infty$. Thankfully, there are limits where time ordering can be neglected, particularly when temporal mode selectivity is not necessary or when low-efficiency solutions suffice. In the next subsection, we will go over time ordering in more detail, and then neglect it for the remainder of this thesis.

3.1.1 Time-ordering effects and the Dyson series

Perturbative solutions are usually solved by taking the Taylor expansion of expressions like Eq. (3.8). However, this is only valid for time-independent Hamiltonians, or Hamiltonians that commute with themselves at different times [170, 174]. As seen in Appendix B of Ref. [170], the three-wave mixing Hamiltonian does not generally have this feature, necessitating a more complicated treatment through the Dyson or Magnus expansion. The Dyson expansion has the advantage of being very similar to the Taylor expansion; the Magnus expansion has the advantage of being unitary to any order. While the Magnus expansion has received attention in the context of three-wave mixing [173, 113, 175], we will focus on the Dyson series here.

The Dyson expansion is the time-ordered version of the Taylor expansion, defined for the expression of Eq. (3.8) as an infinite sum of terms $|\psi\rangle_D = \sum_i |\psi^{(i)}\rangle_D$ where

$$|\psi^{(i)}\rangle_D = \left(\frac{1}{i\hbar}\right)^n \int_{t_0}^{t_f} \mathrm{d}t_n \int_{t_0}^{t_n} \mathrm{d}t_{n-1} \dots \int_{t_0}^{t_2} \mathrm{d}t_1 \hat{H}(t_n)\hat{H}(t_{n-1})\dots\hat{H}(t_1)|\psi_0\rangle. \tag{3.9}$$

If the Hamiltonian commutes with itself, then the operators may go in any order to obtain the same result; in this case, the specified integrals simply take up $1/n!$ of the total geometric space and collapse back to the Taylor series,

$$|\psi^{(i)}\rangle_T = \frac{1}{n!}\left(\frac{1}{i\hbar}\right)^n \int_{t_0}^{t_f} \mathrm{d}t_n \int_{t_0}^{t_f} \mathrm{d}t_{n-1}\ldots \int_{t_0}^{t_f} \mathrm{d}t_1 \hat{H}(t_n)\hat{H}(t_{n-1})\ldots \hat{H}(t_1)|\psi_0\rangle. \qquad (3.10)$$

The reason this is important is that the states that enter the crystal may change themselves through dispersive interactions with the material; as the pulses walk off from each other, it will matter whether a photon was annihilated at the beginning of the process or at the end. These walkoffs and aberrations are contained within the phasematching function. This complicates temporal mode selection [58, 60], which requires that the pulses walk through each other in order to see the whole mode, and pure state generation in SPDC [172]. One way around these issues is to introduce an intermediary linear pulse shaping step which reverses the aberrations [61, 63]. However, in certain relevant cases, they can be completely ignored. The Taylor and Dyson series agree to first order, so any process well described by a first-order expansion may ignore time-ordering effects (usually the low-efficiency limit).

As mentioned, the parameters which describe the aberration and walkoff are contained within the phasematching function Φ of Eq. (3.6). It is sensible that, if the phasematching function is a constant, $\Phi = 1$, the Taylor and Dyson series would be equivalent. This can also be intuited as a flat phasematching function corresponds to an instantaneous effect (a medium of length zero), for which only one "time" exists and thus "time ordering" is rendered irrelevant. To show this, we define temporal operators as

$$\hat{a}(t) = \frac{1}{\sqrt{2\pi}} \int \mathrm{d}\omega \hat{a}_\omega e^{-i\omega t}. \qquad (3.11)$$

Note that this operator obeys the commutation relationship $[\hat{a}(t_1), \hat{a}^\dagger(t_2)] = \delta(t_2 - t_1)$, as

can be seen from

$$[\hat{a}(t_1), \hat{a}^\dagger(t_2)] = \frac{1}{2\pi}\left\{\iint \mathrm{d}\omega_1\mathrm{d}\omega_2\left(\hat{a}_{\omega_1}\hat{a}^\dagger_{\omega_2} - \hat{a}^\dagger_{\omega_2}\hat{a}_{\omega_1}\right)e^{-i\omega_1 t_1 + i\omega_2 t_2}\right\}$$

$$= \frac{1}{2\pi}\left\{\iint \mathrm{d}\omega_1\mathrm{d}\omega_2\left[\hat{a}_{\omega_1}, \hat{a}^\dagger_{\omega_2}\right]e^{-i\omega_1 t_1 + i\omega_2 t_2}\right\} \tag{3.12}$$

$$= \frac{1}{2\pi}\int \mathrm{d}\omega e^{i\omega(t_2 - t_1)} = \delta(t_2 - t_1).$$

Allowing the spatial arguments to be implicit for simplicity, we can rewrite Eq. (3.7) with the flat-phasematching assumption in a simplified form as

$$\hat{H}_{3WM}(t) = C\left[i\hat{a}^\dagger(t)\hat{b}^\dagger(t)\hat{c}(t) - i\hat{a}(t)\hat{b}(t)\hat{c}^\dagger(t)\right]. \tag{3.13}$$

We next wish to show that, with the flat-phasematching assumption, the Hamiltonian commutes with itself at different times, i.e.

$$\left[\hat{H}(t_1), \hat{H}(t_2)\right] = 0. \tag{3.14}$$

We use a further simplified version of the Hamiltonian to show this with less clutter; with the definition $[a_i, a_j] = \delta(t_i - t_j)$, we use

$$\hat{H}_i = ia_i^\dagger b_i^\dagger c_i - ia_i b_i c_i^\dagger. \tag{3.15}$$

We show this by first using Eq. (3.12) to normal-order

$$\begin{aligned}\hat{H}_1\hat{H}_2 &= \left[ia_1^\dagger b_1^\dagger c_1 - ia_1 b_1 c_1^\dagger\right]\left[ia_2^\dagger b_2^\dagger c_2 - ia_2 b_2 c_2^\dagger\right]\\ &= -a_1^\dagger a_2^\dagger b_1^\dagger b_2^\dagger c_1 c_2 + a_1^\dagger a_2 b_1^\dagger b_2 c_1 c_2^\dagger + a_1 a_2^\dagger b_1 b_2^\dagger c_1^\dagger c_2 - a_1 a_2 b_1 b_2 c_1^\dagger c_2^\dagger\\ &= -a_1^\dagger a_2^\dagger b_1^\dagger b_2^\dagger c_1 c_2 + a_1^\dagger a_2 b_1^\dagger b_2\left(c_2^\dagger c_1 + \delta(t_2 - t_1)\right)\\ &\quad + \left(a_2^\dagger a_1 + \delta(t_2 - t_1)\right)\left(b_2^\dagger b_1 + \delta(t_2 - t_1)\right)c_1^\dagger c_2 - a_1 a_2 b_1 b_2 c_1^\dagger c_2^\dagger.\end{aligned} \tag{3.16}$$

Using the identity $f(x, y)\delta(x - y) = f(y, x)\delta(x - y)$, it can be seen that $\hat{H}_1\hat{H}_2 = \hat{H}_2\hat{H}_1$, and therefore the Hamiltonian indeed commutes with itself in this limit.

This statement holds independently of the input state $|\psi_i(t)\rangle$ and escort spectrum $G(\omega_2)$. Recently, Quesada and Sipe proved from the Magnus expansion that the second- and third-order corrections to the Taylor expansion vanished for broadly phasematched processes in both SPDC and SFG [173]; based on our result, we conclude that the corrections to the Taylor series vanish for all orders for both the Magnus and Dyson expansion. Note that flat phasematching is essential, and even separable phasematching would result in time-ordering corrections; introducing an envelope function $\Phi(\omega_3)$ would not lead to the proper commutation relations for the temporal operators of Eq. (3.11).

3.1.2 The three-wave mixing unitary

Without the time-ordering operator to worry about, we can simplify our three-wave mixing unitary to its final form. We keep the phasematching function Φ in our expression, assuming it is broad enough that time-ordering can be neglected; as the first-order expansion is the same with or without time ordering, it will be important to keep to describe low-yield SPDC sources in particular. We now assume that our interaction is "always on" in the sense that it does not depend on outside forces (e.g. external electronics) and extend the temporal integral of Eq. (3.8) to $\pm\infty$, yielding

$$
\begin{aligned}
-\frac{i}{\hbar}\int_{-\infty}^{\infty}\mathrm{d}t\hat{H}_{3\mathrm{WM}}(t) = -&\frac{i\chi^{(2)}L}{24}\sqrt{\frac{\omega_{01}\omega_{02}\omega_{03}\hbar}{n_{01}n_{02}n_{03}\pi^3\epsilon_0 c^3}}\int\mathrm{d}\omega_1\mathrm{d}\omega_2\mathrm{d}\omega_3\int\mathrm{d}^2\mathbf{k}_{T1}\mathrm{d}^2\mathbf{k}_{T2}\mathrm{d}^2\mathbf{k}_{T3} \\
&\times\left[i\hat{a}^{\dagger}_{\mathbf{k}_{T1},\omega_1}\hat{a}^{\dagger}_{\mathbf{k}_{T2},\omega_2}\hat{a}_{\mathbf{k}_{T3},\omega_3}\delta(\omega_3-\omega_1-\omega_2)\delta^2(\mathbf{k}_{T3}-\mathbf{k}_{T1}-\mathbf{k}_{T2})\right. \\
&\left.\times\Phi(\omega_1,\omega_2,\omega_3,\mathbf{k}_{T1},\mathbf{k}_{T2},\mathbf{k}_{T3})+\mathrm{H.c.}\right].
\end{aligned}
$$

(3.17)

The delta function corresponds to conservation of energy, justifying our previous neglect of non-energy conserving terms of the Hamiltonian[1]. The three-wave mixing unitary is simply Eq. (3.17) exponentiated.

In this thesis, we are concerned with the effect of nonlinear processes on the spectral waveform, and will purify the spatial profile of any generated states with single-mode fi-

---

[1]If time-ordering was taken into consideration, the process still would conserve energy in total, but not necessarily in each individual step of a perturbative expansion. Neglect of the non-energy conserving terms would still apply.

bres. While coupling between space and frequency will have a great effect on the heralding efficiency of single-photon sources [104, 176], modelling these processes as well overcomplicates the frequency-time picture. To simplify our wave-mixing unitary, we assume that the phasematching function is independent of the transverse momenta and can be written simply as

$$\Phi(\omega_1, \omega_2, \omega_3) = \text{sinc}\left[\frac{L}{2c}(n_3\omega_3 - n_1\omega_1 - n_2\omega_2)\right].$$ (3.18)

We can then simplify the interaction by looking at the x and y dependence rather than the transverse momenta by defining the spatial creation operators

$$\hat{a}_{x,y} = \frac{1}{2\pi}\int d^2\mathbf{k}_T\, \hat{a}_{\mathbf{k}_T} e^{ik_x x + ik_y y}.$$ (3.19)

Eq. (3.17) can be written in this form when phasematching is independent of momenta by unravelling the delta functions as

$$\int d^2\mathbf{k}_{T1}d^2\mathbf{k}_{T2}d^2\mathbf{k}_{T3}\, \hat{a}^\dagger_{\mathbf{k}_{T1},\omega_1}\hat{a}^\dagger_{\mathbf{k}_{T2},\omega_2}\hat{a}_{\mathbf{k}_{T3},\omega_3}\delta^2(\mathbf{k}_{T3} - \mathbf{k}_{T1} - \mathbf{k}_{T2})$$

$$= \frac{1}{4\pi^2}\int dxdy \int d^2\mathbf{k}_{T1}d^2\mathbf{k}_{T2}d^2\mathbf{k}_{T3}\, \hat{a}^\dagger_{\mathbf{k}_{T1},\omega_1}e^{-i\mathbf{k}_{T1}\cdot\mathbf{r}_T}\hat{a}^\dagger_{\mathbf{k}_{T2},\omega_2}e^{-i\mathbf{k}_{T2}\cdot\mathbf{r}_T}\hat{a}_{\mathbf{k}_{T3},\omega_3}e^{i\mathbf{k}_{T3}\cdot\mathbf{r}_T}$$ (3.20)

$$= 2\pi \int dxdy\, \hat{a}^\dagger_{x,y,\omega_1}\hat{a}^\dagger_{x,y,\omega_2}\hat{a}_{x,y,\omega_3}.$$

We then can write our simplified unitary in the form

$$-\frac{i}{\hbar}\int_{-\infty}^{\infty} dt\hat{H}_{3\text{WM}}(t) = -\frac{i\chi^{(2)}L}{12}\sqrt{\frac{\omega_{01}\omega_{02}\omega_{03}\hbar}{n_{01}n_{02}n_{03}\pi\epsilon_0 c^3}}\int d\omega_1 d\omega_2 d\omega_3 \int dxdy$$

$$\times \left[i\hat{a}^\dagger_{x,y,\omega_1}\hat{a}^\dagger_{x,y,\omega_2}\hat{a}_{x,y,\omega_3}\delta(\omega_3 - \omega_1 - \omega_2)\Phi(\omega_1, \omega_2, \omega_3) + \text{H.c.}\right].$$ (3.21)

Alternatively, we could use the definitions of our temporal operators as in Eq. (3.11) to define a time-domain Hamiltonian in the absence of phasematching ($\Phi \approx 1$) with the modes relabelled as a, b, and c,

$$\frac{1}{i\hbar}\int_{-\infty}^{\infty} dt\hat{H}^{(\Phi\approx1)}_{3\text{WM}}(t) = \frac{\chi^{(2)}L}{3i}\sqrt{\frac{\hbar}{2c^3\epsilon_0}\frac{\omega_{01}\omega_{02}\omega_{03}}{n_{01}n_{02}n_{03}}}\int dtdxdy\left[i\hat{a}^\dagger_{x,y,t}\hat{b}^\dagger_{x,y,t}\hat{c}_{x,y,t} + \text{H.c.}\right].$$ (3.22)

We stress that this version is only useful in the unphysical case of infinitely flat phase-matching, but is *very* useful for intuition in many cases where phasematching is not the dominant effect.

With this transformation in hand, we next will look at two cases, each of which assumes that one of the three fields involved is a strong coherent state expanding upon Sec. 1.1.4. First, we discuss a broadband first-order perturbative treatment of SPDC. Secondly, we dive into a quantum treatment of sum-frequency generation. Refer to Fig. 1.2 for a schematic representation of each of these processes.

3.2 Spontaneous parametric downconversion

3.2.1 The SPDC state

In SPDC, the high-energy pump pulse may be taken as an undepleted strong coherent state described by

$$|\psi_p\rangle = \int \mathrm{d}\omega_p \mathrm{d}x \mathrm{d}y \, |\alpha(\omega_p, x, y)\rangle, \tag{3.23}$$

where the spectrum is normalized to the average pump photon number N_p as

$$\langle \psi_p | \hat{n} | \psi_p \rangle = \int \mathrm{d}\omega_p \mathrm{d}x \mathrm{d}y \, |\alpha(\omega_p, x, y)|^2 = N_p. \tag{3.24}$$

Using the approximation of Eq. (1.18), we can simply replace the creation operator $\hat{a}_{\omega_p, x, y}$ with the function $\alpha(\omega_p, x, y)$. We will also assume that the pump is not spatially chirped, and write the pump function as separable in space and energy,

$$\alpha_p(\omega_p, x, y) = \sqrt{N_p} \xi_p(\omega_p) u_p(x, y), \tag{3.25}$$

where the frequency and spatial functions are normalized to 1 under square integration. The three-wave mixing unitary simplifies in this case to

$$
\begin{aligned}
\hat{U}_{SPDC} = \exp\Big\{ &-\frac{i\chi^{(2)}L}{12}\sqrt{\frac{\hbar N_p}{\pi c^3 \epsilon_0}\frac{\omega_{0s}\omega_{0h}\omega_{0p}}{n_{0s}n_{0h}n_{0p}}}\int \mathrm{d}\omega_s \mathrm{d}\omega_h \mathrm{d}x\mathrm{d}y \\
&\times \big[i\hat{s}^\dagger_{x,y,\omega_s}\hat{h}^\dagger_{x,y,\omega_h}\xi_p(\omega_s + \omega_h)u_p(x,y)\Phi(\omega_s, \omega_h, \omega_s + \omega_h) + \text{H.c.}\big]\Big\},
\end{aligned}
\tag{3.26}
$$

where the signal and herald modes are labelled with the operators $\hat{s}$ and $\hat{h}$, respectively.

The intuitive picture is clear; the pump will convert into a signal and a herald photon which must add to an energy within the pump bandwidth and exist at the same point in space as the pump. Note that ignoring the angular dependence of the index of refraction means that the spectral and spatial degrees of freedom are completely separable. This is generally not the case, and great case must be taken in avoiding coupling these degrees of freedom for high heralding efficiency [176, 177]. By only collecting a small angle of emission (a cone with an opening angle less than one degree), these effects can usually be avoided. This form also assumes that the pump beam does not expand significantly in the medium, implying that the length of the medium is much less than the Rayleigh range of the beam.

For single-photon sources based on SPDC, we are only concerned with the first-order expansion applied to vacuum input $|00\rangle$; indeed, emission of higher photon numbers degrades the quality of the source. We express the unnormalized first-order SPDC state, after post-selecting out the vacuum components, as

$$
|\psi^{(1)}_{SPDC}\rangle \propto \chi^{(2)}L\sqrt{N_p}u_p(x,y)\iint \mathrm{d}\omega_s \mathrm{d}\omega_h\,\xi_p(\omega_s + \omega_h)\Phi(\omega_s, \omega_h, \omega_s + \omega_h)\hat{s}^\dagger_{x,y,\omega_s}\hat{h}^\dagger_{x,y,\omega_h}|00\rangle.
\tag{3.27}
$$

We usually couple into single-mode fibre after downconversion, which effectively implements a projection onto a Gaussian spatial mode. As the two photons share a spatial mode, projecting one into a spatial mode will simultaneously project the other into the same spatial mode. In theory, this coupling efficiency can be one-hundred percent, but will be deteriorated by distortions to $u_p(x,y)$ due to spatial walkoff, as well as mixing of the spatial modes due to frequency-momentum coupling in the phasematching terms ignored in Sec. 3.1.2 [104, 176]. We parameterize this coupling through the spatial overlap $\mathcal{O}_{SPDC}$,

defined with normalized collection modes $f_{c,i}(x,y)$ as

$$\mathcal{O}_{SPDC} = \left| \iint \mathrm{d}x\mathrm{d}y f_{c,s}(x,y) f_{c,h}(x,y) u_p(x,y) \right|^2, \tag{3.28}$$

where the collection mode functions include free-space propagation and imaging terms. Note that $\mathcal{O}_{SPDC}$ is inversely proportional to the pump beam area, and thus a tighter focus produces more photons unambiguously in this approximation. However, a tighter focus will also lead to greater coupling between frequency and momentum, which will lead to mixed spatial states and poor heralding efficiencies [104, 176]. In experiment, the heralding efficiency can be calculated from the *Klyshko efficiency* η_i [178], defined in terms of the number of single-detection events S and coincidences C as

$$\eta_s = \frac{C_{sh}}{S_h}, \quad \eta_h = \frac{C_{sh}}{S_s}. \tag{3.29}$$

Intuitively, if both modes are perfectly coupled, every single-detection event should result in a coincidence. In practice, mode mismatch and detector inefficiencies preclude this; knowing the detector efficiencies, one can back out the heralding efficiency from the Klyshko efficiency.

After coupling into single-mode fiber, the remaining terms of interest in the SPDC biphoton state of Eq. (3.27) are those relating to the joint spectrum. If bandpass filters $B_i(\omega_i)$ are used to reshape the spectrum after downconversion and single-mode fibres purify the spectral-spatial state, the final joint spectrum will be

$$F_{SPDC}(\omega_s, \omega_h) \overset{renorm.}{=} B_s(\omega_s) B_h(\omega_h) \xi(\omega_s + \omega_h) \Phi(\omega_s, \omega_h, \omega_s + \omega_h). \tag{3.30}$$

If the phasematching is nonrestrictive, this will usually lead to anti-correlated joint spectrum due to energy conservation, as seen in Fig. 3.1a. However, by changing the phasematching function, it is possible to directly generate frequency uncorrelated or even frequency correlated states [179, 180, 181, 182, 183, 184, 185], as seen in Fig. 3.1b-c. Uncorrelated states may also be generated by filtering an entangled spectrum [186, 187, 188]; this process is necessarily lossy, but nonetheless the most common method due to its relative
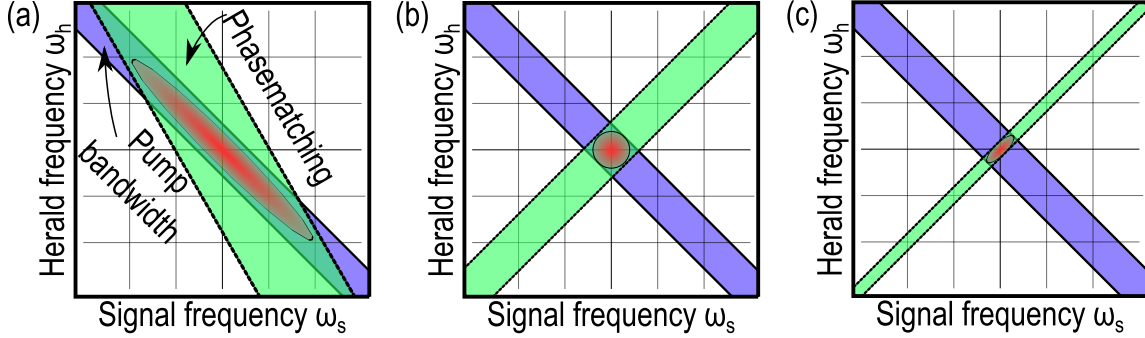
Figure 3.1: **Joint spectral wavefunctions in SPDC.** The joint spectrum from SPDC, shown in red, can be found by multiplying the pump spectrum and the phasematching function, with contours shown in blue and green, respectively. In (a), energy conservation and phasematching roughly line up, and a frequency anti-correlated state is generated. In (b), the two oppose and have roughly equal widths, resulting in an separable state. In (c), phasematching is tight and opposes energy conservation, leading to positive frequency correlations.

ease.

If we assume that all the functions in Eq. (3.27) are well-approximated by Gaussian functions, we can form a toy joint spectrum which both describes the essential features of most SPDC sources and is easy to work with mathematically. Firstly, we reintroduce the notation of Sec. 2.1.1 where $\tilde{\omega} = \omega - \omega_0$. We assume that the pump spectrum is given by a generic Gaussian spectrum with width σ_p, such that

$$\sqrt{N_p}\xi(\omega_s + \omega_h) = \frac{\sqrt{N_p}}{(2\pi\sigma_p^2)^{\frac{1}{4}}} \exp\left[-\frac{(\tilde{\omega}_s + \tilde{\omega}_h)^2}{4\sigma_p^2}\right]. \tag{3.31}$$

Each bandpass filter is similarly defined as a Gaussian filter,

$$B_i(\omega_i) = \exp\left[-\frac{\tilde{\omega}_i^2}{4\Pi_i^2}\right]. \tag{3.32}$$

The phasematching function is expanded to first order about the central frequencies, and

92

assumed to be tuned such that the zeroth order terms vanish. Using the approximation of Eq. (2.35) to convert the sinc function to a Gaussian, we can write the first-order phasematching function as

$$\Phi(\omega_s, \omega_h, \omega_s + \omega_h) \approx e^{-0.193\left(\frac{L\Delta k}{2}\right)^2} \approx e^{-\frac{0.193 L^2}{4}[k_{1p}(\tilde{\omega}_s + \tilde{\omega}_h) - k_{1s}\tilde{\omega}_s - k_{1h}\tilde{\omega}_h]^2}, \qquad (3.33)$$

where k_{1i} is the first-order expansion of the wavenumber $k = \frac{n(\omega)\omega}{c}$ about the respective central frequency. Note that this approximation does not account for dispersion within the downconversion medium.

This toy model can be used to derive the scaling rules for the relative probability of producing a photon pair given a particular crystal length, pump bandwidth, and pump power by examining the terms of $\langle \psi_{SPDC}^{(1)} | \psi_{SPDC}^{(1)} \rangle$ from Eq. (3.27). The strength of the first order term is simply linearly proportional to the number of photons in the pump beam, N_p, and quadratically proportional to the nonlinearity $\chi^{(2)}$. The dependencies on pump bandwidth and crystal length are linked through phasematching, as can be clearly seen by examining the relevant case of near-degenerate type-I SPDC, similar to Sec. 2.1.3. In this situation, $k_{1s} \approx k_{1h}$, and the first-order Gaussian approximation of the phasematching function can be expressed as

$$\Phi_{T1}(\omega_s, \omega_h, \omega_s + \omega_h) \approx e^{-\frac{0.193 L^2}{4}(k_{1p} - k_{1s})^2(\tilde{\omega}_s + \tilde{\omega}_h)^2}, \qquad (3.34)$$

from which we can define an effective phasematching bandwidth which coincides with energy conservation of

$$\sigma_{PM} = \frac{1}{\sqrt{0.193}(k_{1p} - k_{1s})L}. \qquad (3.35)$$

In this case, the photon number dependence on L, σ_p, and filter bandwidths Π_s and Π_h can be found as

$$\langle \psi_{SPDC}^{(1)} | \psi_{SPDC}^{(1)} \rangle \propto \frac{L^2 N_p}{\sqrt{1 + 0.193(k_{1p} - k_{1s})^2 L^2 \sigma_p^2}} \frac{\Pi_s \Pi_h}{\sqrt{\Pi_s^2 + \Pi_h^2}} = \frac{L^2 N_p}{\sqrt{1 + \frac{\sigma_p^2}{\sigma_{PM}^2}}} \frac{\Pi_s \Pi_h}{\sqrt{\Pi_s^2 + \Pi_h^2}}. \qquad (3.36)$$

If the phasematching bandwidth is much broader than the pump bandwidth, $\sigma_{PM} \gg \sigma_p$,

the single-photon probability increases as L^2, but in the opposite limit, $\sigma_{PM} \ll \sigma_p$, the single-photon probability is directly proportional to L. This is because, while the peak of the joint spectral intensity increases as L^2, the joint spectral intensity is also narrowed as length is increased.

While combining the above expressions gives a manageable number of parameters, it is overcomplete for mathematical manipulation. As the product of any number of Gaussian functions remains a Gaussian function, we can fit the SPDC parameters to a generic normalized Gaussian function, given by

$$F_{SPDC}(\omega_s, \omega_h) = \frac{1}{\sqrt{2\pi}\sigma_s\sigma_h(1-\rho^2)^{\frac{1}{4}}} \exp\left[-\frac{1}{4(1-\rho^2)}\left(\frac{\tilde{\omega}_s^2}{\sigma_s^2} + \frac{\tilde{\omega}_h^2}{\sigma_h^2} - \frac{2\rho\tilde{\omega}_s\tilde{\omega}_h}{\sigma_s\sigma_h}\right)\right], \quad (3.37)$$

where σ_i are the marginal bandwidths of the photons and ρ is the statistical correlation [189, 180], defined for general variables x and y with means μ_i as

$$\rho_{xy} = \frac{\langle(x-\mu_x)(y-\mu_y)\rangle}{\sqrt{\langle(x-\mu_x)^2\rangle\langle(y-\mu_y)^2\rangle}}. \quad (3.38)$$

Fitting these parameters to our SPDC state description of Eq. (3.27), we find that

$$\sigma_s = \Pi_s\sqrt{\frac{\sigma_p^2 + \Pi_h^2\left[1 + a(k_{1p}-k_{1h})^2L^2\sigma_p^2\right]}{\sigma_p^2 + \Pi_s^2 + \Pi_h^2 + 0.193L^2\left[(k_{1s}-k_{1h})^2\Pi_s^2\Pi_h^2 + (k_{1p}-k_{1s})^2\sigma_p^2\Pi_s^2 + (k_{1p}-k_{1h})^2\sigma_p^2\Pi_h^2\right]}}$$

$$\sigma_h = \Pi_h\sqrt{\frac{\sigma_p^2 + \Pi_s^2\left[1 + a(k_{1p}-k_{1s})^2L^2\sigma_p^2\right]}{\sigma_p^2 + \Pi_s^2 + \Pi_h^2 + 0.193L^2\left[(k_{1s}-k_{1h})^2\Pi_s^2\Pi_h^2 + (k_{1p}-k_{1s})^2\sigma_p^2\Pi_s^2 + (k_{1p}-k_{1h})^2\sigma_p^2\Pi_h^2\right]}}$$

$$\rho = \frac{-\Pi_s\Pi_h\left[1 + 0.193L^2\sigma_p^2(k_{1p}-k_{1s})(k_{1p}-k_{1h})\right]}{\sqrt{\left[\sigma_p^2 + \Pi_s^2\left(1 + 0.193L^2\sigma_p^2(k_{1p}-k_{1s})^2\right)\right]\left[\sigma_p^2 + \Pi_h^2\left(1 + 0.193L^2\sigma_p^2(k_{1p}-k_{1h})^2\right)\right]}}. \quad (3.39)$$

From these expressions, we can see that the marginal bandwidths are heavily influenced by the filters applied, as expected. We can also see that frequency correlations tend to be negative for short crystal lengths. However, if $(k_{1p}-k_{1s})(k_{1p}-k_{1h})$ is a negative number, positive frequency correlations or uncorrelated spectra are possible with the proper crystal lengths. This condition is often called *extended phasematching*, as it extends the possible

time-frequency states that can be created from pump shaping and filtering alone [190, 191].

Note that the above analysis completely neglects the presence of multiphoton terms, which generally rise as n^{th} power of the single-photon probability (neglecting possible time-ordering corrections [170]). To minimize these terms, it is usually necessary to operate in a regime where producing a photon pair is rare.

3.2.2 Correlations, bandwidths, and coherence times in SPDC

SPDC without spectral phases

To understand behaviour of the two-photon time-frequency distribution of Eq. (3.37), we next break it down into a handful of characteristic times and bandwidths, as seen in Fig. 3.2. We are often interested in the frequency bandwidth of the photons coming out of our SPDC source, as this factors into practical considerations such as which frequencies our optics must remain effective for and the acceptance bandwidths necessary for nonlinear processes. We can define this as the standard deviation of $F_{SPDC}(\omega_s, \omega_h)$ with respect to ω_s, which is found to simply be

$$\sqrt{\langle \omega_s^2 \rangle - \langle \omega_s \rangle^2} = \sqrt{\int \mathrm{d}\omega_s \mathrm{d}\omega_h \, (\omega_s - \omega_{0s})^2 |F_{SPDC}(\omega_s, \omega_h)|^2} = \sigma_s, \qquad (3.40)$$

as shown graphically in Fig. 3.2. Similarly, the marginal bandwidth of the herald photon is simply σ_h, and both can be found in full form in Eq. (3.39). Note that, in the parameterization of Eq. (3.37), neither depends whatsoever on the correlation ρ.

The degree of correlation can be surmised directly from the statistical correlation ρ, and other unitless measures are found to depend strictly on ρ. As we have described the state as pure, we can quantify its entanglement through the purity of the partial trace, as defined for discrete Hilbert spaces in Sec. 1.3.1. For a generic normalized bipartite wavefunction defined as $|\psi\rangle = \iint \mathrm{d}x\mathrm{d}y \, f(x, y)|x\rangle_A|y\rangle_B$, the purity of the partial trace is the same for
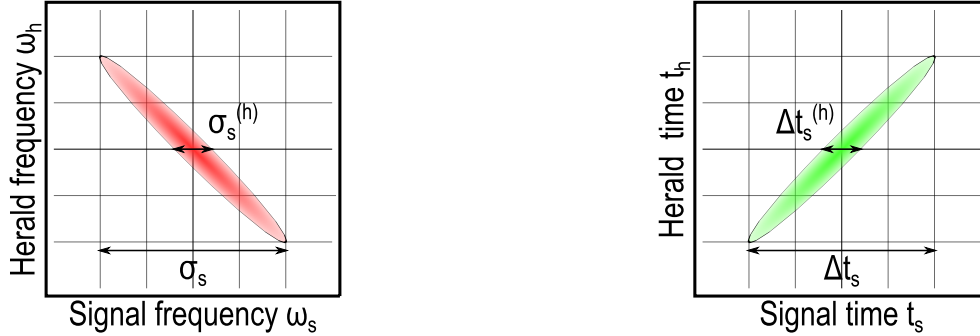
Figure 3.2: **Marginal and joint bandwidths and coherence times for SPDC photons.** The joint spectral intensity (left) and joint temporal intensity (right) are shown for an idealized SPDC state with the spectral anti-correlations typical of loose phasematching. The marginal spectral bandwidth and marginal temporal pulse length, σ_s and Δt, can be much longer than the heralded bandwidth and pulse length, $\sigma_s^{(h)}$ and $\Delta t_s^{(h)}$, if the state is energy-time entangled.

both subsystems and given by

$$v = \text{Tr}_A \left\{ \text{Tr}_B \left[|\psi\rangle\langle\psi| \right]^2 \right\} = \int \mathrm{d}x\mathrm{d}y\mathrm{d}x'\mathrm{d}y' f(x,y) f^*(x',y) f(x',y') f^*(x,y'). \qquad (3.41)$$

For the distribution of Eq. (3.37), the purity of the partial trace is found to be $\sqrt{1-\rho^2}$. Recall that a lower purity of the partial trace indicates more entanglement, so long as the global state is pure [33]. The purity of the partial trace is also linked to the Rényi 2-entropy for pure bipartite states as $\Upsilon(|\psi\rangle\langle\psi|) = -\ln v$ [103].

We can also generalize the Schmidt decomposition of Eq. (1.66) to continuous distributions like $F_{SPDC}(\omega_s, \omega_h)$. Instead of defining the Schmidt decomposition in terms of kets in a discrete Hilbert space, we define it as a sum over continuous orthogonal basis functions $S_i(\omega_s)$ and $H_i(\omega_h)$ as

$$F_{SPDC}(\omega_s, \omega_h) = \sum_i c_i S_i(\omega_s) H_i(\omega_h). \qquad (3.42)$$

The sum is often over a very high number of basis modes for these distributions, but many of the elements are close to zero. To quantify the number of modes, the Schmidt rank or

effective mode number is introduced [192, 193], defined as

$$K = \left(\sum_i c_i^4 \right)^{-1}. \tag{3.43}$$

It is left as an exercise to the reader to show that the Schmidt rank and the purity of the partial trace can be linked[2] as $K = 1/\nu$.

While unitless parameters are useful for apples-to-apples comparisons of vastly different sources and to determine the usefulness of a given source for quantum information processing, in other cases quantities with units provide valuable information regarding the performance of a source. For example, we may be interested in the *joint energy uncertainty* $\Delta(\omega_s + \omega_h)$, defined as the variance in the quantity $\omega_s - \omega_h$, or its counterpart $\Delta(\omega_s - \omega_h)$. For the joint spectral function of Eq. (3.37), these quantities are found to be

$$\Delta(\omega_s \pm \omega_h) = \sqrt{\sigma_s^2 \pm 2\rho\sigma_s\sigma_h + \sigma_h^2} \overset{\sigma_s = \sigma_h}{=} \sqrt{2(1 \pm \rho)}\sigma, \tag{3.44}$$

where the case of equal marginal bandwidths is particularly useful for intuition. When ρ approaches negative one, the photons become perfectly anticorrelated, and there is no uncertainty in the difference of their energies. This is natural for energy conservation, and indeed the joint energy uncertainty is simply the pump bandwidth σ_p if the filter bandwidths Π_i are broader than the pump and phasematching is broad ($L \to 0$).

We can also consider the *heralded* bandwidth of the signal photons $\sigma_s^{(h)}$ as in Fig. 3.2, where we select exactly on the herald central frequency $\omega_h = \omega_{0h}$ and measure the variance of the signal frequency as

$$\sigma_s^{(h)} = \sqrt{\int d\omega_s \, (\omega_s - \omega_{s,0})^2 |F_{SPDC}(\omega_s, \omega_{0h})|^2} = \sqrt{1 - \rho^2}\sigma_s, \tag{3.45}$$

and similarly $\sigma_h^{(h)} = \sqrt{1 - \rho^2}\sigma_h$. Both of these approach zero when the state is maximally entangled, as specifying the frequency of one photon uniquely specifies the frequency of the other.

---

[2] I've always wanted to do that.

Of course, the spectral and temporal domains are inseparably related, and we can define similar quantities for the temporal distribution. The two-dimensional Fourier transform of Eq. (3.37) can be calculated by extending the inverse Fourier transform of Eq. (2.3) naturally to

$$f_{SPDC}(t_s, t_h) = \frac{1}{2\pi} \iint \mathrm{d}\omega_s \mathrm{d}\omega_h \, F_{SPDC}(\omega_s, \omega_h) e^{i\omega_s t_s} e^{i\omega_h t_h}$$
$$= \frac{\sqrt{2\sigma_s \sigma_h}(1-\rho^2)^{\frac{1}{4}}}{\sqrt{\pi}} \exp\left[-\sigma_s^2 t_s^2 + 2t_s t_h \rho \sigma_s \sigma_h + \sigma_h^2 t_h^2\right], \tag{3.46}$$

which is once again a two-dimensional Gaussian function, this time with statistical correlation $-\rho$. If we ignore one of the two photons and consider the *marginal temporal pulse length* Δt of the other, i.e. the variance of $f_{SPDC}(t_s, t_h)$ with respect to t_s, we find that

$$\Delta t_s = \frac{1}{2\sigma_s \sqrt{1-\rho^2}} = \frac{1}{2\sigma_s^{(h)}}. \tag{3.47}$$

If the two photons have maximal correlations in frequency ($|\rho| = 1$), they will individually have infinite extent in time, consistent with idealized CW pumping. If they are unentangled ($\rho = 0$), their marginal temporal bandwidth is simply $1/(2\sigma_i)$, exactly satisfying the time-energy uncertainty relation for transform limited pulses [36],

$$\sigma_\omega \sigma_t \geq \frac{1}{2}. \tag{3.48}$$

For the SPDC state with the parameters of Eq. (3.39) in the limit of broad phasematching, this time is

$$\lim_{L \to 0} \Delta t_i^{(SPDC)} = \frac{1}{2}\sqrt{\frac{1}{\sigma_p^2} + \frac{1}{\Pi_i^2}}, \tag{3.49}$$

which is roughly the temporal length of the pump, $1/(2\sigma_p)$, if the filter Π_i is significantly broader than the pump bandwidth.

Similarly to Eq. (3.44), we can define the *joint temporal uncertainties* as

$$\Delta(t_s \pm t_h) = \frac{\sqrt{\sigma_s^2 \mp 2\rho\sigma_s\sigma_h + \sigma_h^2}}{2\sigma_s\sigma_h\sqrt{1-\rho^2}} \stackrel{\sigma_s=\sigma_h}{=} \frac{1}{\sigma\sqrt{2(1\pm\rho)}}. \tag{3.50}$$

If we once again compare with the SPDC parameters of Eq. (3.39) in the limit of broad phasematching, we find that

$$\begin{aligned} \Delta(t_s - t_h) &= \frac{1}{2}\sqrt{\frac{1}{\Pi_s^2} + \frac{1}{\Pi_h^2}} \\ \Delta(t_s + t_h) &= \frac{1}{2}\sqrt{\frac{1}{\Pi_s^2} + \frac{1}{\Pi_h^2} + \frac{4}{\sigma_p^2}}. \end{aligned} \tag{3.51}$$

The variance in the difference of the arrival times is simply the quadrature sum of the variances expected of each individually classically given their bandwidth, but the variance in the sum also depends on the pump bandwidth σ_p, blowing up when the pump is long in time (small σ_p).

Note that the time-energy uncertainty relationship for joint time and frequency measurements, when the marginal bandwidths are equal, are

$$\Delta(\omega_s \pm \omega_h)\Delta(t_s \pm t_h) = 1, \qquad \Delta(\omega_s \pm \omega_h)\Delta(t_s \mp t_h) = \sqrt{\frac{1\pm\rho}{1\mp\rho}}. \tag{3.52}$$

If one looks at correlations or anti-correlations in both time and frequency, the joint relations respect a time-frequency uncertainty relation much like Eq. (3.48), simply scaled by 2 as the uncertainties of each are added in quadrature. However, if one looks at correlations in time and anti-correlations in frequency (or vice-versa), the quantity may either blow up or approach zero as $|\rho| \to 1$. For an entangled state, it is possible to know to a high degree of certainty the simultaneous sum of the frequencies and the difference of the times-of-arrival in the case of $\rho = -1$. This case is the most intuitive, as the sum of the frequencies is restricted by the frequencies of the pump pulse, and the photons must be created together at the exact same time.

We can also look at the heralded temporal pulse length of the signal, $\Delta t_s^{(h)}$ in Fig. 3.2,

99

by selecting on a narrow temporal slice of the herald photon and measuring the variance of $f_{SPDC}(t_s, t_h)$ with respect to t_s, finding that

$$\Delta t_s^{(h)} = \frac{1}{2\sigma_s}. \tag{3.53}$$

This is exactly the temporal width we would expect for a transform-limited signal photon given the bandwidth σ_s. Indeed, the marginal and heralded time and frequency widths satisfy the uncertainty relations

$$\sigma_s \Delta t_s^{(h)} = \frac{1}{2}, \qquad \sigma_s^{(h)} \Delta t_s = \frac{1}{2}. \tag{3.54}$$

In many ways, this heralded temporal pulse length can be thought of as the coherence time of the biphoton, as adding a delay larger than $\Delta t_s^{(h)}$ will result in a completely distinguishable temporal distribution relative to the original field. This timescale will be particularly relevant when matching two SPDC processes to create polarization entanglement, as described in Sec. 3.2.3.

When designing photonic experiments, it is important to be aware of which timescales are relevant. In many experiments, the marginal temporal pulse width Δt_s and the heralded pulse width $\Delta t_s^{(h)}$ differ by orders of magnitude. For example, photons which can produce a femtosecond-scale HOM feature may originate from bulk SPDC with continuous-wave pumping [194], as the HOM dip width between two entangled photons depends of $\Delta(t_s - t_h)$. However, a nonlinear cross-correlation scan on one of the two photons with a classical pump would be insensitive to these features, as it is dependent on the marginal pulse width, Δt_s.

SPDC with spectral phases

The above analysis is only valid for transform-limited pure pulses with a joint spectral field well-represented by Eq. (3.37). Impurities arising from laser jitter or coupling with other degrees of freedom will skew the temporal distribution from the ideal, even if the joint spectral intensity is still close to $|F_{SPDC}(\omega_s, \omega_h)|^2$. Even if the state remains pure, spectral phases such as chirps will drastically change the temporal representation. While spectral phases do not change the joint spectral intensity, the marginal temporal pulse lengths with

chirps A_s and A_h on each photon are transformed to

$$\Delta t_i = \sqrt{\frac{1}{4(1 - \rho^2)\sigma_i^2} + 4A_i^2\sigma_i^2}, \tag{3.55}$$

which initially depends on the heralded bandwidth but grows with chirp according to the marginal bandwidth. In the large-chirp limit, the temporal features will be significantly blurred. With enough chirp, the frequency components will be stretched so far that measurement in time effectively measures frequency. In this limit, the temporal profile will be a faithful map of the frequency profile, which is often used to measure the joint spectral intensity based on detection times, avoiding the need for step-by-step scanning or detector arrays [162, 163].

If the two marginal bandwidths are equal, $\sigma_s = \sigma_h = \sigma$, the joint time-energy uncertainty relation of Eq. (3.52) changes to

$$\Delta(\omega_s \pm \omega_h)\Delta(t_s \mp t_h) = \sqrt{\frac{1 \pm \rho}{1 \mp \rho} + 8(1 \pm \rho)\left(A_s^2 \mp 2A_sA_h\rho + A_h^2\right)\sigma^4}. \tag{3.56}$$

In the case of an anti-correlated joint spectrum ($\rho < 0$), the variance of the sum of the frequencies and difference of the times is minimized when there is no chirp, but remains robust against equal-and-opposite chirps, $A_h = -A_s$. A correlated joint spectrum ($\rho > 0$) instead minimizes the variance $\Delta(\omega_s - \omega_h)\Delta(t_s + t_h)$, and is also more resilient against broadening for $A_h = -A_s$. Indeed, this can be clearly seen by examining the statistical correlation of the joint temporal intensity,

$$\rho_{t_s,t_h} = -\rho\frac{(1 - 16A_sA_h(1 - \rho^2)\sigma_s^2\sigma_h^2)}{\sqrt{(1 + 16A_s^2(1 - \rho^2)\sigma_s^4)(1 + 16A_h^2(1 - \rho^2)\sigma_h^4)}}, \tag{3.57}$$

which is invariant under chirp if $A_s\sigma_s^2 = -A_h\sigma_h^2$ regardless of the sign of ρ. While chirps will stretch the temporal distribution, properly balanced chirps will not change its statistical correlation. As seen in Eq. (3.55), the marginal temporal pulse width is not significantly changed until the chirp is strong enough to stretch the heralded pulse width to the length of the pump pulse. Therefore, for chirps below this level, the detrimental effects of chirp on

101

timing accuracy can be cancelled. This effect can be exploited in quantum imaging [195, 196] and in a nonlocal manner [197, 198, 199], although oftentimes frequency correlated classical states can be employed in analogous fashions [200, 201, 124, 202, 160].

So far, we have only considered separable spectral phases, which can be compensated easily in principle with pulse shaping techniques. It is also possible that the spectral phase function is inseparable between the signal and herald frequencies. For example, if the pump is chirped, it's contribution to the SPDC state in Eq. (3.30) will change to

$$\xi(\omega_s + \omega_h) \mapsto \xi(\omega_s + \omega_h)e^{iA_p(\omega_s+\omega_h)^2} = \xi(\omega_s + \omega_h)e^{i\left(A_p\omega_s^2 + 2A_p\omega_s\omega_h + A_p\omega_s^2\right)}. \tag{3.58}$$

The terms quadratic in ω_i can be compensated locally, but the cross-term defines a correlation between the frequency of one photon and the time-of-arrival of the other.

While extra correlations in the joint spectral phase increase correlations in time-vs-frequency joint intensities, they may reduce the correlations in the joint temporal intensity. For this reason, it is difficult to make concrete statements about entanglement purely from the joint spectral intensity, as different spectral phases dramatically affect the joint distributions in the Fourier domain. We next show that, for a pure state, any inseparable spectral phase can only increase the amount of entanglement. To do so, we define our joint spectral amplitude in polar form as $F(\omega_s, \omega_h)e^{i\phi(\omega_s, \omega_h)}$, where $F(\omega_s, \omega_h)$ is by definition positive for all frequencies. The purity of the partial trace can be found from Eq. (3.41) as

$$\upsilon = \int d\omega_s d\omega_h d\omega_s' d\omega_h' F(\omega_s, \omega_h)F(\omega_s', \omega_h)F(\omega_s', \omega_h')F(\omega_s, \omega_h')e^{i\left[\phi(\omega_s,\omega_h)-\phi(\omega_s',\omega_h)+\phi(\omega_s',\omega_h')-\phi(\omega_s,\omega_h')\right]}. \tag{3.59}$$

To show that entanglement can only increase by introducing a spectral phase, it suffices to show that the purity of the partial trace can only decrease, which follows from the relation

$$\int d\vec{x} \, |f(\vec{x})| \geq \left| \int d\vec{x} \, f(\vec{x}) \right|, \tag{3.60}$$

as proven for a complex function $f(\vec{x})$ in Theorem 2.1 of Ref. [203]. Therefore, if purity is assumed, judging the amount of entanglement from the absolute value of the joint spectral intensity alone provides a lower bound on the amount of entanglement in the system,

$\Upsilon_{ABS} \leq \Upsilon$. This means that the joint spectral intensity can show evidence of entanglement in systems where purity can be taken for granted, but additional assumptions are required when using it to verify the time-frequency separability of a two-photon state. Techniques centring on HOM interference can be used to verify time-frequency separability when the spectral phase is inaccessible [204].

3.2.3 Spatial and temporal walkoff

We next briefly discuss some linear optical effects that play a large role in designing nonlinear optical setups, particularly the sandwich source. As the beams of light involved in wave-mixing processes generally have different polarizations and different wavelengths, simple effects such as refraction and material delay have different effects for each beam. In waveguides, these problems are often pronounced, and great effort must be made to ensure each beam is in the same mode, but even in bulk experiments these effects need to be understood and managed. In this section, we quickly discuss temporal walkoff, where two beams split from each other by travelling at different group velocities in a medium, and spatial walkoff, where the angle of propagation in a material changes for different polarizations of light, and how this can be managed in SPDC source design.

Temporal walkoff

Temporal walkoff is a simple consequence of light travelling at different group velocities depending on its central wavelength and polarization. In SHG, SFG, and SPDC, the red and blue beams will spread due to the this effect, leading to temporally broad second harmonics and temporal entanglement in downconversion. These effects are all contained within the first order expansion of the phasematching function, as in Sec. 2.1.3. When two crystals are used in sequence, as in the sandwich source [105] discussed in Sec. 1.3.4, it is also necessary to consider the temporal spread between the two processes, as distinguishability in time will degrade the desired polarization entanglement.

We consider the case of degenerate type-I SPDC, sketched in Fig. 3.3a. For concreteness, we consider SPDC in BBO crystals, where an extraordinary blue beam downconverts

103

into two ordinarily polarized photons (sometimes abbreviated $e \to o + o$). BBO is a negative uniaxial crystal, so the extraordinary index is lower than the ordinary index, and is normally dispersive, meaning that blue light experiences a larger index of refraction than red light. This is, of course, not generally the case. For example, BiBO, another crystal used commonly in this thesis, differs in many regards: it is biaxial, its type-I downconversion is $o \to e + e$, and $n_e > n_o$ (see Fig. 2.2). However, the intuitive picture of BBO adapts fairly straightforwardly to other crystal arrangements.

In one possible orientation of sandwich source (as in Fig. 3.3a), the pump pulse enters the two crystals diagonally polarized, and the BBO crystals are aligned such that a horizontal (vertical) pump stimulates the downconversion of two vertical (horizontal) photons in the first (second) crystal. On average, the extraordinary pump will downconvert in the middle of the crystal, and the total group delay in the downconverting crystal will be

$$\tau_{xtal} = \frac{L}{2} \left(\frac{1}{v_{g,e,b}} + \frac{1}{v_{g,o,r}} \right) = \frac{L}{2} \left(k_{1,e,b} + k_{1,o,r} \right), \tag{3.61}$$

where v_g is the group velocity, $k_1 = \frac{\partial}{\partial k} \omega |_{\omega_0} = \frac{1}{v_g}$, e and o correspond to polarization relative to the crystal, and r and b correspond to red and blue. This group delay is common to both processes, but the photons created in the first crystal traverse the second crystal as extraordinarily polarized red photons, with group delay $Lk_{1,e,r}$, whereas the photons created in the second crystal have the group delay of the ordinarily polarized blue beam, $Lk_{1,o,b}$.

The state generated at the output of the sandwiched crystals (ignoring spatial dependence) can be described as

$$|\psi\rangle = \frac{1}{\sqrt{2}} \iint d\omega_a d\omega_b \, F(\omega_a, \omega_b) \left[e^{i\tau_{HH}(\omega_a + \omega_b)} \hat{a}^\dagger_{\omega_a, H} \hat{b}^\dagger_{\omega_b, H} + e^{i\tau_{VV}(\omega_a + \omega_b)} \hat{a}^\dagger_{\omega_a, V} \hat{b}^\dagger_{\omega_b, V} \right] |00\rangle, \tag{3.62}$$

where $\iint d\omega_a d\omega_b \, |F(\omega_a, \omega_b)|^2 = 1$ and we have assumed that both photons a and b experience the same group delay (arising from the degeneracy assumption). If we trace out the

104

frequency degree of freedom, we can express the state in two-qubit density matrix form as

$$\iint \mathrm{d}\omega_a \mathrm{d}\omega_b \, \hat{a}_{\omega_a} \hat{b}_{\omega_b} |\psi\rangle \langle\psi| \hat{a}^\dagger_{\omega_a} \hat{b}^\dagger_{\omega_b} = \frac{1}{2} \begin{pmatrix} 1 & 0 & 0 & \mu \\ 0 & 0 & 0 & 0 \\ 0 & 0 & 0 & 0 \\ \mu^* & 0 & 0 & 1 \end{pmatrix}, \tag{3.63}$$

where the coherence term μ is

$$\mu = \iint \mathrm{d}\omega_a \mathrm{d}\omega_b \, |F(\omega_a, \omega_b)|^2 e^{i(\tau_{HH} - \tau_{VV})(\omega_a + \omega_b)}, \tag{3.64}$$

where $\tau_{HH} - \tau_{VV} = (k_{1,e,r} - k_{1,o,b})L$. This coherence term should have an absolute value of 1 for maximal entanglement, which is only true if the difference in group delays is much less than the coherence time of the biphoton $(\Delta t_s^{(h)})$, as the relative delay will otherwise be present as distinguishing information between the two processes. In the limit of a large relative delay, only the classical correlations remain.

Thankfully, the problem of temporal walkoff can be corrected relatively easily by introducing an additional polarization dependent delay to the biphoton, for example delaying the horizontal photons by $\tau_{HH} - \tau_{VV}$ relative to the vertical photons. This can be done using thin birefringent materials, often called *compensation crystals* [95]. Compensation of this sort is usually not required in Sagnac-style loop arrangements, as the photons have the same polarization when traveling through the birefringent elements regardless of the direction of travel.

Spatial walkoff

When a beam of light is incident upon a boundary between two media, it undergoes refraction and may change direction depending on the angle of incidence. The change in the direction of the k-vector is summed up by Snell's law, $n_1 \sin\theta_1 = n_2 \sin\theta_2$, which tells a complete story for lossless isotropic media. However, if the medium has an anisotropic index of refraction, the situation becomes more complicated. For a uniaxial crystal with the extraordinary axis in the plane of incidence, the medium's index of refraction for light
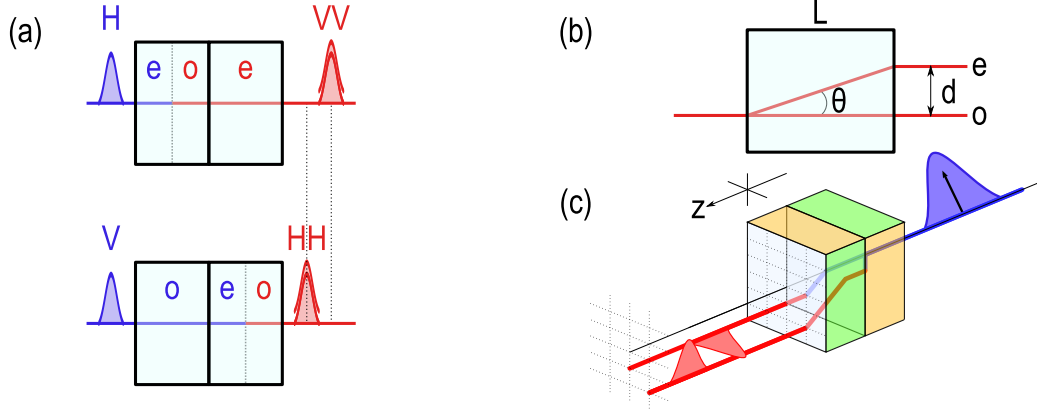
Figure 3.3: **Spatial and temporal walkoff in SPDC polarization entanglement sources.** (a) Temporal walkoff in a sandwich source occurs between the processes that create vertical and horizontal photons since they experience different group delays in the crystal where they experience no nonlinearity. The situation shown corresponds to two type-I BBO crystals. (b) The extraordinary component of light incident on a birefringent crystal will experience spatial walkoff if the optic axis is not aligned to the boundary, with walkoff angle θ resulting in a spatial separation d over a crystal of length L. (c) Spatial walkoff results in spatial distinguishability between two downconversion processes in sandwich sources.

polarized in the plane of incidence is given, per Eq. 2.37, as

$$\frac{1}{n_e(\theta)^2} = \frac{\sin^2 \theta}{\bar{n}_e^2} + \frac{\cos^2 \theta}{n_o^2}. \tag{3.65}$$

Meanwhile, light polarized out of plane has the angle-independent index n_o, which differs from $n_e(\theta)$ in all cases except for $\theta = 0$. Therefore, the k-vectors of the ordinarily and extraordinarily polarized beams will differ as they propagate through the medium, a process known as *double refraction*.

However, the k-vectors do not tell the whole story. The direction of energy flux, which can be thought of as the "ray" in ray optics, is associated with the Poyntyng vector. While the Poyntyng and k vector are parallel in isotropic media, this is not the case for media with angle-dependent refractive indices (arising from the electric displacement field not

being necessarily parallel to the electric field) [205, 206]. Indeed, according to Snell's law, the k-vector does not change direction when an extraordinarily polarized beam is normally incident into a medium with an optic axis 45° to the surface normal, which is inconsistent with the effect of a block of calcite glass on top of graph paper; indeed, this separation is the working principle of a polarizing beam displacer, as seen in Fig. 3.3b. Finding the direction of propagation is generally not trivial, and leads to some odd phenomena in systems with even slight complexity, such as conical refraction in biaxial crystals when light propagates along a principle optical axis [206, 207].

Resorting to derivations from heuristic arguments proves sufficient for one of the simplest and most relevant cases, where light is normally incident on a uniaxial crystal with the extraordinary axis in the plane of incidence. This situation is sketched in Fig 3.3b, and to find the displacement d between the beams at the output of the crystal, we must find the angle θ at which the extraordinary (e) ray travels in the medium. This can be accomplished relatively simply by resorting to Fermat's principle, or the principle of least time, which states that light will travel the path that minimizes its transit time. The problem then reduces to finding the minimal effective extraordinary path, $L_{eff} = L\frac{n_e(\theta)}{\cos\theta}$, with respect to theta. Taking the derivative and solving for zero gives the spatial displacement d as

$$d = L\tan\theta = -\frac{1}{n_e(\theta)}\frac{\partial n_e}{\partial\theta} = L\frac{(\bar{n}_e^2 - n_o^2)\cos\theta\sin\theta}{\bar{n}_e^2\cos^2\theta + n_o^2\sin^2\theta}, \tag{3.66}$$

where the final equality assumes an extraordinary index as in Eq. (3.65). More rigourous treatments also arrive at the same relation [127, 205], but the least-time principle is the simplest for this case.

Spatial walkoff is of great concern in downconversion schemes. Beam spreading during the downconversion process between the three fields will result in highly non-Gaussian beam profiles, which will couple poorly into single-mode fibres. Using thin crystals mediates this effect, but walkoff between two crystals aligned differently as in the sandwich source will prevent coupling photons from both the $H \to VV$ and $V \to HH$ processes simultaneously, as sketched in Fig. 3.3c. As the photon beams have different polarizations, they can be translated separately using small beam displacers which walks both back to a common point. Note that spatial walkoff is non-existent in nonlinear experiments that use

107

temperature tuning and periodic poling rather than angle tuning, as the optic axis lines up with the material surface.

3.3 Quantum ultrafast sum-frequency generation

When describing SPDC in the previous section, we assumed the highest-energy mode was a strong coherent state. For SFG, we instead take one of the lower energy modes to be a strong coherent state and label it as the escort pulse in mode e, which is defined similarly to Eq. (3.24) with

$$\alpha_e(\omega_e, x, y) = \sqrt{N_e} G_e(\omega_e) u_e(x, y). \tag{3.67}$$

We label the input and output modes with the creation and annihilation operators $\hat{a}$ and $\hat{c}$, respectively, to retrieve the evolution unitary transformation

$$
\begin{aligned}
\hat{U}_{SFG} = \exp\Big\{ & -\frac{i\chi^{(2)}L}{12}\sqrt{\frac{\hbar N_e}{\pi c^3 \epsilon_0}\frac{\omega_{01}\omega_{0e}\omega_{03}}{n_{01}n_{0e}n_{03}}} \int \mathrm{d}\omega_1 \mathrm{d}\omega_3 \mathrm{d}x \mathrm{d}y \\
& \times \left[\hat{a}_{x,y,\omega_1}\hat{c}^\dagger_{x,y,\omega_h} G(\omega_3 - \omega_1) u_e(x,y) \Phi(\omega_1, \omega_3 - \omega_1, \omega_3) + \mathrm{H.c.}\right]\Big\},
\end{aligned}
\tag{3.68}
$$

The intuitive picture is the same as for the simplified case, where the escort mediates a beamsplitter transition between the input and output modes. The escort is only able to mediate such a transition in regions where it has amplitude, and only transitions which possibly obey the energy conservation relation $\omega_3 = \omega_1 + \omega_e$. Once again, the lack of a coupling between space and energy arises from the assumption that the index of refraction is not highly angle-dependent. We will see a case in Sec. 5.2.1 where this separability is clearly unfounded, but we ignore these effects for simplicity.

We are usually concerned with the case of a single photon in the input mode which has some bandwidth and spatial distribution defined by

$$|\psi_0\rangle = u_1(x,y)F(\omega_1)\hat{a}^\dagger_{x,y,\omega_1}|0\rangle \overset{FT}{=} u_1(x,y)f(t)\hat{a}^\dagger_{x,y,t}|0\rangle \tag{3.69}$$

The input state may also be part of a larger entangled state, but we will ignore this for now. We will investigate the sum-frequency interaction between this state and the

escort using a first-order treatment, and then using a full treatment without phasematching considerations. This assumption on the input state does not take full advantage of the beamsplitter-like nature of sum-frequency generation (SFG) , which can coherently control transitions between photons of distinct frequencies [63, 208, 209]

3.3.1 First-order treatment

In the low-efficiency regime, a first-order treatment is usually sufficient to describe the spectral wavefunctions resulting from sum-frequency generation even with phasematching considerations. Taking the first-order expansion of Eq. (3.68), collecting all constant terms as C, and applying it to the state of Eq. (3.69) gives

$$
\hat{U}_{SFG}|\psi_0\rangle = |\psi_0\rangle - O(C^2)
$$
$$
- iC \int \mathrm{d}\omega_1 \mathrm{d}\omega_3 \mathrm{d}x \mathrm{d}y \, u_e(x,y) u_1(x,y) G(\omega_3 - \omega_1) F(\omega_1) \Phi(\omega_1, \omega_3 - \omega_1, \omega_3) \hat{c}^\dagger_{x,y,\omega_3}|0\rangle.
$$
$$
(3.70)
$$

In the limit of flat phasematching, the first order term is the convolution of the input and escort spectra, which is simply their temporal representations multiplied via the convolution theorem. Additionally, the spatial profile is simply the multiplication of the two spatial profiles.

We can trace out this spatial degree of freedom easily as, to first order, it does not couple to the spectral degrees of freedom. We represent it simply as the effective area function

$$
\frac{1}{\mathcal{A}_{eff}} = \iint \mathrm{d}x \mathrm{d}y \, |u_e(x,y)|^2 |u_1(x,y)|^2.
\tag{3.71}
$$

Intuitively, tighter focusing increases the efficiency to first order as interactions are more likely to occur when confined together; subtleties to this will be discussed in the high order treatment. Even without the high-order corrections, focusing too tightly will render the paraxial approximation and the approximation of angle-independent phasematching

invalid. We group this into the coupling constant C,

$$C = \frac{\chi^{(2)} L}{12} \sqrt{\frac{\hbar N_e}{\pi \mathcal{A}_{eff} c^3 \epsilon_0} \frac{\omega_{01} \omega_{0e} \omega_{03}}{n_{01} n_{0e} n_{03}}}. \tag{3.72}$$

The remaining first-order spectral function is

$$|\psi^{(1)}\rangle \overset{renorm.}{=} \iint \mathrm{d}\omega_3 \mathrm{d}\omega_1 \, G(\omega_3 - \omega_1) F(\omega_1) \Phi(\omega_1, \omega_3 - \omega_1, \omega_3) \hat{c}^\dagger_{\omega_3} |0\rangle. \tag{3.73}$$

In the following sections, we will see that this simple relation is the foundation of many useful techniques. However, by virtue of being a first-order treatment, it is not a good prediction of behaviour near high-efficiency. To model that, we next make further simplifications to gain intuition on how the key mechanics behave when extended to high order.

3.3.2   High-order treatment

For many sum-frequency processes, specifically shaped phasematching is absolutely essential for ideal operation. For others, such as temporal imaging, it is entirely detrimental. When attempting to minimize the effects of phasematching, one can also neglect time-ordering effects and use the temporal version of the three-wave mixing Hamiltonian, Eq. (3.22). Using the Taylor expansion from the temporal version of the Hamiltonian (Eq. (3.22)), we can express the final state as $|\psi\rangle = \sum_n |\psi^{(n)}\rangle$ where

$$\begin{aligned}
|\psi^{(n)}\rangle &= \left\{ \frac{\chi^{(2)} L}{3i(n!)} \sqrt{\frac{\hbar N_e}{2c^3 \epsilon_0} \frac{\omega_{01} \omega_{02} \omega_{03}}{n_{01} n_{02} n_{03}}} \int \mathrm{d}t' \mathrm{d}x' \mathrm{d}y' \left[g(t') u_e(x', y') \hat{a}_{x',y',t'} \hat{c}^\dagger_{x',y',t'} + \mathrm{H.c.} \right] \right\}^n |\psi_0\rangle \\
&= \frac{(-i)^n C^n}{n!} \left[g(t) u_e(x, y) \hat{a}_{x,y,t} \hat{c}^\dagger_{x,y,t} + \mathrm{H.c.} \right]^n u_1(x, y) f(t) \hat{a}^\dagger_{x,y,t} |0\rangle
\end{aligned} \tag{3.74}$$

From inspection, every even-numbered term will correspond to a photon in the input mode a, and every odd-numbered term to a photon in the upconverted mode c. The temporal creation and annihilation operators force every action to happen at the same time (a

110

consequence of the neglect of time ordering), allowing us to write the interaction in terms of a single time.

We next break the state into its even and odd components, which exist in distinguishable modes a and c. We find that

$$\begin{aligned}
|\psi\rangle_a &= \left[\sum_n \frac{(-1)^n}{(2n)!} C^{2n} |g(t)|^{2n} |u_e(x,y)|^{2n}\right] u_1(x,y) f(t) \hat{a}^\dagger_{x,y,t} |0\rangle \\
&= \cos\left[C|g(t) u_e(x,y)|\right] u_1(x,y) f(t) \hat{a}^\dagger_{x,y,t} |0\rangle
\end{aligned}$$
(3.75)

and

$$\begin{aligned}
|\psi\rangle_c &= -i\left[\sum_n \frac{(-1)^n}{(2n+1)!} C^{2n+1} |g(t)|^{2n+1} |u_e(x,y)|^{2n+1}\right] u_1(x,y) f(t) \hat{c}^\dagger_{x,y,t} |0\rangle \\
&= -i \frac{g(t)}{|g(t)|} \sin\left[C|g(t) u_e(x,y)|\right] u_1(x,y) f(t) \hat{c}^\dagger_{x,y,t} |0\rangle
\end{aligned}$$
(3.76)

Note that this form conserves the total photon number and oscillates between populating mode a and c depending on the strength of the escort. However, it does not necessarily ever convert the entire photonic wavepacket to mode c from mode a. Additionally, in this form the state is no longer separable in its spatial and spectral degrees of freedom. For simplicity, we introduce the assumption that the spatial envelope of the escort overlaps the input spatial envelope completely, and $u_e(x,y)$ may be taken to be a constant. We could have easily done this for the temporal envelope instead, and analogous effects to those we discuss in the next chapter could be viewed from the perspective of spatial overlap. We replace the spatial wavefunctions with the effective area of Eq. (3.71) and absorb it into the constant. The high-order toy state we will use from this point forward is

$$|\psi\rangle_a = \cos\left[\gamma|g(t)|\right] f(t) \hat{a}^\dagger_t |0\rangle$$
(3.77)

$$|\psi\rangle_c = \frac{g(t)}{|g(t)|} \sin\left[\gamma|g(t)|\right] f(t) \hat{c}^\dagger_t |0\rangle,$$
(3.78)
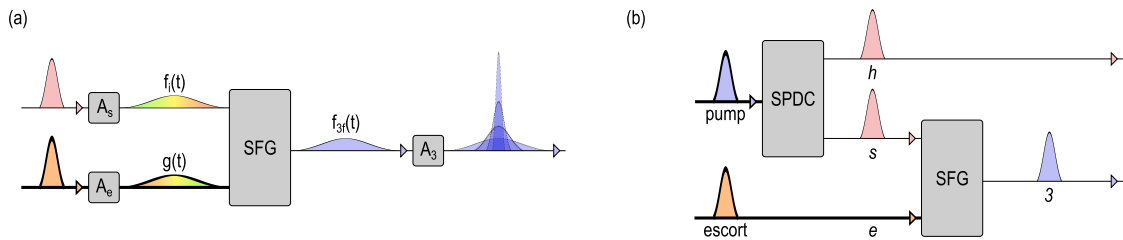
Figure 3.4: **Sum-frequency generation for optical waveform manipulation.** (a) An optical waveform may be shaped through a combination of pulse shaping and sum frequency generation. Depending on the value of the chirps A and the shape of the escort pulse, the shape of the output optical waveform may be modulated in both wavelength and spectral shape. (b) A schematic of the setup as imagined is shown. A pair of photons may be created through, for example, spontaneous parametric downconversion, with a signal photon in mode 1 and its herald in mode h. The signal photon is then mixed with a strong escort pulse in mode 2 to produce an upconverted signal photon in mode 3. Bold lines represent strong pulses and thin lines represent single photons.

where

$$\gamma = \frac{\chi^{(2)} L}{3} \sqrt{\frac{\hbar N_e}{2\mathcal{A}_{eff} c^3 \epsilon_0} \frac{\omega_{01} \omega_{02} \omega_{03}}{n_{01} n_{02} n_{03}}}. \tag{3.79}$$

The form of this solution is the same as the classical group-velocity matched solution in Eq. (2.32).

3.4 Efficiency limits of quantum sum-frequency generation

3.4.1 Optical waveform conversion with pulse shaping and upconversion

Single photons are the natural choice for many quantum technologies as they are an ideal carrier of quantum information for communication protocols and coupling quantum

nodes [1, 210]. To form an effective interface between two quantum systems, it is important that the photon properties, such as the spectrum or spatial mode, match those of the receiver. Ensuring compatibility will, in general, necessitate adapting properties of the source photon to match those of the receiver using waveform manipulation methods. Constraints imposed by the no-cloning theorem [211] forbid direct amplification or detect-and-resend approaches, creating a need for highly efficient low-noise quantum waveform conversion methods.

The temporal waveforms of single photons are of particular importance in quantum optics and quantum information science. Photon pairs produced through spontaneous parametric downconversion (SPDC) have controllable energy-time entanglement dependent on the pump and crystal properties [179, 180, 212, 204, 104], as seen in Eq. (3.27). Quantum information may be encoded as a superposition of discretized time [213] or frequency [56] bins or modes [58, 63] and multiplexed in either case to increase the rate of information transmission [214, 215, 216, 217]. Control over this degree of freedom is necessary for coupling to quantum memories [218, 219], quantum frequency conversion [220, 221, 133, 222], temporal mode selection [58, 60, 223], and quantum measurement [68]. In order for general control over temporal waveforms, it is necessary that the waveform conversion methods remain effective on the ultrafast timescale [224, 161, 225]. In the experiments performed in this thesis, a first-order perturbative treatment was sufficient to explain the results as the efficiency was low. However, it is important that these techniques remain effective in the high-efficiency regime. Investigating this regime is necessary to enable practical bandwidth compression and time lensing for the quantum domain, as aberrations occurring at high efficiency could greatly degrade the quality of the signal.

Here, we focus on waveform manipulation using sum-frequency generation with shaped pulses, as seen in Fig. 3.4a. By upconverting an input signal with a shaped escort pulse, the shape of the escort leaves a fingerprint on the signal, which can be further customized to change the spectral shape of the photon [58, 224, 134, 223]. Using upconversion to translate the central wavelength of single photons has been explored by many labs, particularly in the context of upconversion detectors. Fibre has a peak transmission around 1,550 nm, but cheap, efficient detectors work best around 800 nm [16], although that is changing with the advent of superconducting nanowire detectors [14]. By upconverting the light to

113

visible wavelengths, higher detection efficiencies with lower dark counts are possible than with InGaAs telecom APDs [221, 226, 227, 228, 229]. However, controlling the fine details spectral shape of single photons is a much more recent development, and has the potential to fully exploit the time-frequency photonic degree of freedom.

While the work done in this thesis focuses on three-wave mixing, this is far from the only avenue for quantum optical waveform conversion. The same techniques can be adapted relatively straightforwardly to four-wave mixing, which offers much greater flexibility in terms of target central wavelengths, multi-pulse control, and fibre-based media at the expense of additional noise sources [221, 229, 133, 230, 135]. The spectral shape of photons coming out of some broadband quantum memories can be altered by changing the properties of the optical read-out pulse [231, 27]. Electro-optic modulation can be used to accomplish many similar tasks [148, 149], similar to the EOM time lens mentioned in Sec. 2.2.4. Finally, while unable to losslessly manipulate the bandwidth and central frequency, passive pulse shaping elements may be used to phase-modulate the spectral shape of photonic waveforms and shape their temporal profiles [158, 232].

3.4.2 Waveform conversion of a single photon from a model energy-time entangled pair

In order to characterize the effectiveness and efficiency of these processes, we model our input state as part of a photon pair produced through SPDC as in Eq. (3.37) which is dispersed by a chirp A_s as in Eq. (2.55), as shown in Fig. 3.4b. The initial joint temporal distribution of this two-photon state is then given by

$$
\begin{aligned}
f_i(t, t_h) = & \frac{\sqrt{2\sigma_s\sigma_h}(1-\rho^2)^{\frac{1}{4}}}{\sqrt{\pi}\sqrt{1-4iA_s\sigma_s^2}} \exp\left[-\frac{\sigma_s^2 t^2 + 2tt_h\rho\sigma_s\sigma_h + \sigma_h^2 t_h^2\left(1 + 16A_s^2(1-\rho^2)\sigma_s^4\right)}{1+16A_s^2\sigma_s^4}\right] \\
& \times \exp\left[-i\frac{4A_s\sigma_s^2(t\sigma_s + t_h\rho\sigma_h)^2}{1+16A_s^2\sigma_s^4}\right].
\end{aligned}
\tag{3.80}
$$

The marginal temporal pulse length of the chirped signal photon in this model is

$$\Delta t_s^2 = \frac{1}{4(1-\rho^2)\sigma_s^2} + 4A_s^2\sigma_s^2. \tag{3.81}$$

We model the escort beam as described by a normalized Gaussian spectrum with group velocity dispersion,

$$G(\omega_e) = \frac{1}{(2\pi\sigma_e^2)^{\frac{1}{4}}} e^{-\frac{(\tilde{\omega}_e)^2}{4\sigma_e^2}} e^{i\omega_e\tau} e^{iA_e(\tilde{\omega}_e)^2}, \tag{3.82}$$

where σ_e is the bandwidth of the escort about central frequency ω_{0e}, A_e applied dispersion, and τ a time delay relative to the signal photon. The escorts temporal field is thus

$$g(t) = \frac{\left(\frac{2}{\pi}\right)^{\frac{1}{4}}\sqrt{\sigma_e}}{\sqrt{1-4iA_e\sigma_e^2}} \exp\left[-\frac{\sigma_e^2(t+\tau)^2}{1+16A_e^2\sigma_e^4}\right] \exp\left[-i\frac{4A_e\sigma_e^4(t+\tau)^2}{1+16A_e^2\sigma_e^4}\right], \tag{3.83}$$

which has a temporal length of

$$\Delta t_e^2 = \frac{1+16A_e^2\sigma_e^4}{4\sigma_e^2}. \tag{3.84}$$

We can then use Eqs. (3.83) and (3.80) with Eq. (3.78) to find the total sum-frequency waveform produced in the third mode. We calculate the probability of successfully converting the single photon from mode 1 to mode 3, by finding the expectation value of the number of photons in mode 3, $\langle \hat{n}_3 \rangle$ as

$$\langle \hat{n}_3 \rangle = \int \mathrm{d}t \mathrm{d}t_h |f_{3f}(t, t_h)|^2$$

$$= \frac{1}{2} \sum_{k=1}^{\infty} \frac{(-1)^{k-1}}{(2k)!} \frac{e^{\frac{-kT^2}{1+qk}}}{\sqrt{1+qk}} p^{2k} \tag{3.85}$$

where we have made the following substitutions:

$$p = \frac{2\sqrt{\sigma_e}\gamma}{\left[\left(\frac{\pi}{2}\right)\left(1 + 16A_e^2\sigma_e^4\right)\right]^{\frac{1}{4}}} = \frac{\sqrt{2}\gamma}{\left(\frac{\pi}{2}\right)^{\frac{1}{4}}\sqrt{\Delta t_e}} \, , \tag{3.86}$$

$$T = \frac{\sqrt{2}\sigma_e\tau}{\sqrt{1 + 16A_e^2\sigma_e^4}} = \frac{\tau}{\sqrt{2}\Delta t_e} \, , \tag{3.87}$$

$$q = \frac{\sigma_e^2}{1 + 16A_e^2\sigma_e^4} \times \frac{\frac{1}{(1-\rho^2)} + 16A_s^2\sigma_s^4}{\sigma_s^2} = \frac{\Delta t_s^2}{\Delta t_e^2} \, . \tag{3.88}$$

The *scaled coupling constant* p is defined such that p^2 is proportional to the peak power of the escort pulse, noting that γ^2 is proportional to the number of photons in the pulse. The *dimensionless time delay* T corresponds to a relative time delay between the escort pulse and the photon normalized to the temporal width of the escort pulse. Finally, the *pulse length ratio* q is the ratio of temporal widths for the escort pulse and the input photon, with a low value implying that the single photon is much shorter in duration than the escort pulse. While it is difficult to check its physicality for any values of the three parameters, this series is provably convergent for any value of p, q, or T through the Cauchy-Hadamard lemma [233], as

$$\lim_{k\to\infty}\left|\frac{1}{(2k)!}\frac{e^{\frac{-kT^2}{1+qk}}}{2\sqrt{1+qk}}p^{2k}\right|^{\frac{1}{k}} = 0 \quad \forall\, p, q, T. \tag{3.89}$$

The three parameters of Eqs. (3.86-3.88) characterize the important figures of merit for the conversion process. In particular, the pulse length ratio q describes the potential efficiency of a given sum-frequency process. In the low-q limit, where $1 + qk \approx 1$ for all k with appreciable contributions to Eq. (3.85), it is seen that

$$\lim_{q\to 0}\langle \hat{n}_3 \rangle = \sin^2\left(\frac{1}{2}e^{-\frac{T^2}{2}}p\right), \tag{3.90}$$

as one would find by treating the escort pulse as monochromatic [28]. In this limit, perfect upconversion efficiency ($\langle \hat{n}_3 \rangle = 1$) is achievable with sufficient escort power. In the high-q limit, Eq. (3.85) does not readily present a closed-form solution and must be studied

numerically. Fig. 3.5(a) shows numerical calculations of $\langle \hat{n}_3 \rangle$ as a function of the scaled coupling constant p for a wide range of q values with zero time delay ($T = 0$). It is apparent that high SFG efficiency may only be achieved for low values of the pulse length ratio, $q \lesssim 1$. Fig. 3.5(b) shows $\langle \hat{n}_3 \rangle$ as a function of p as the dimensionless time delay T is varied, for equal escort and photon pulse lengths ($q = 1$). These calculations show that adding a time delay will also reduce the peak efficiency, as expected due to the decrease in overlap between the escort pulse and single photon.

To find the optimal conversion efficiency, we aim to find the maximal $\langle \hat{n}_3 \rangle$ for any given q and T. We estimate the optimum p value as the first zero of the derivative of Eq. (3.85) with respect to p, corresponding to the first efficiency peak in Fig. 3.5(a-b). As this derivative is not in closed form, we truncate the sum of Eq. (3.85) after four terms to obtain an approximate maximum; this works well for oscillatory solutions, but may underestimate the optimal p for large values of $|T|$ as no well-defined peak efficiencies are present. In Fig. 3.5(c), we show the optimal efficiency using this method as a function of q and T. This optimal efficiency is nearly unity for small pulse length ratios $q \lesssim 1$ and very robust against time delays for $q \ll 1$. However, note that higher escort power is required to reach the optimal efficiency as the time delay moves away from zero. A more parsable approximate solution can be found using Eureqa Formulize data analysis software [234] as

$$p_{opt}(q, T) \approx \left(4.06 - \frac{1.135}{1.236 + q} \right) e^{\frac{T^2}{2 + 3.856q}}. \tag{3.91}$$

However, the solution from the slopes is considerably more accurate in the $q \sim 1$ regime.

A first-order perturbative approach, as used in previous works, always predicts a Gaussian sum-frequency photon given a Gaussian input photon and escort pulse. This is an ideal target photon for many applications, and it is important to determine how well this relatively simple prediction describes the result expected at high efficiency. By defining $|\psi^{(1)}\rangle$ to be the photonic waveform found through first-order perturbation theory, with a temporal waveform $f_{3f}^{(1)}(t, t_h)$ found by expanding Eq. (3.78) to first order in γ, we can calculate how well our total photonic waveform overlaps with the first-order description through the quantum state fidelity and determine the validity of first-order approximations.

117
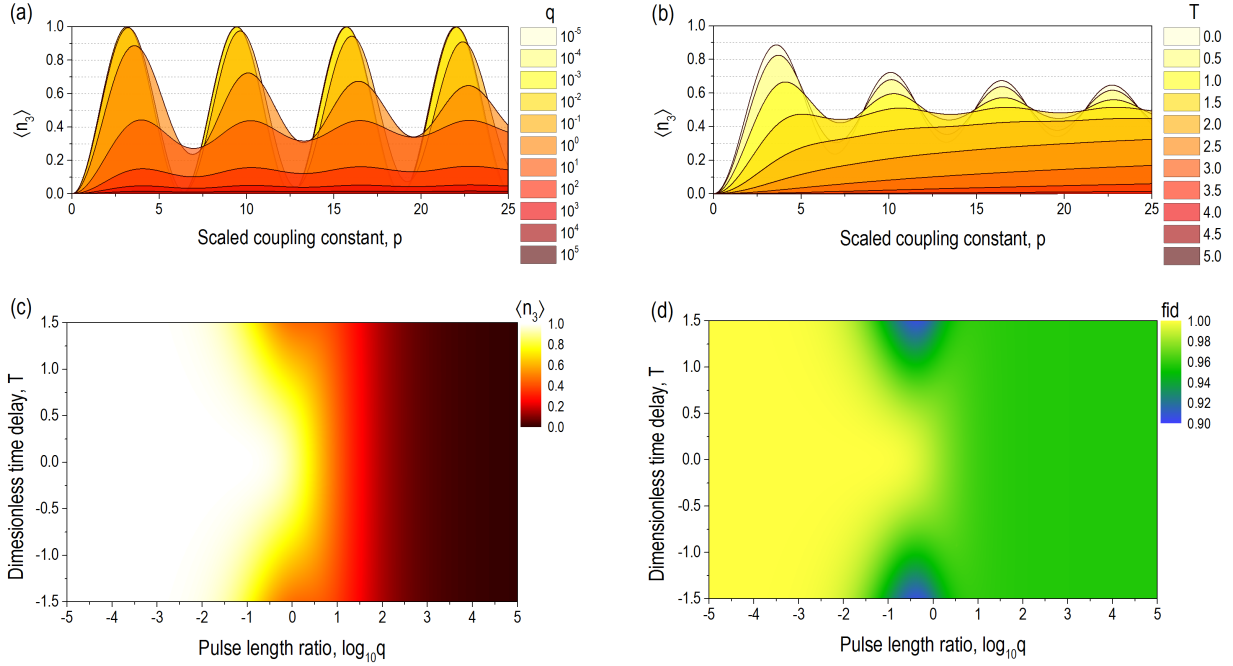
Figure 3.5: **Single-photon upconversion efficiency and fidelity.** (a) The probability of successful upconversion $\langle \hat{n}_3 \rangle$ is shown as a function of the scaled coupling constant p for various pulse width ratios q, with the dimensionless time delay T held constant. As p increases in the regime where the escort is much broader in time than the input photon (low q), the efficiency of upconversion follows a sine pattern, reaching unit efficiency at $p = \pi$. In the regime where the escort is much narrower in time than the photon, high upconversion efficiency is not achievable. (b) Here we show the probability as a function of p for various dimensionless time delays T, with the pulse width ratio q held at one. As the time delay is increased, the pulses cease to overlap well and the maximum efficiency is seen to drop. Notably, the peak efficiency is no longer well defined past $|T| \approx 1.5$, as the first local maximum in efficiency is no longer the global maximum. (c) The maximum possible efficiency is numerically calculated as a function of q and T, with the optimal p estimated as the first peak of a fourth-order expansion of Eq. (3.85). In the low-q regime, the efficiency is also robust against time delays T. (d) By numerically calculating the fidelity of the temporal waveform at the estimated optimal efficiency with that expected from first-order perturbation theory via Eq. (3.92), we see that the first-order approximation is an excellent description in the low-q regime. Time delays disturb the symmetry of the system and further reduce the fidelity.

118

The fidelity is defined for pure states as

$$\left|\langle\psi^{(1)}|\psi\rangle\right|^2 = \frac{\left|\iint \mathrm{d}t\mathrm{d}t_h f_{3f}^*(t,t_h)f_{3f}^{(1)}(t,t_h)\right|^2}{\langle\hat{n}_3^{(1)}\rangle\langle\hat{n}_3\rangle}, \tag{3.92}$$

where we normalize by dividing by both $\langle\hat{n}_3\rangle$ and $\langle\hat{n}_3^{(1)}\rangle = \iint \mathrm{d}t\mathrm{d}t_h \left|f_{3f}^{(1)}(t,t_h)\right|^2$ as we are primarily concerned with the shape of the temporal waveforms. We numerically calculate this fidelity at the optimal efficiency as a function of q and T, with the results shown in Fig. 3.5(d). It is seen that the first-order approximation describes the high-efficiency waveform well in the low-q regime, but is less accurate when q is large; however, the fidelity is numerically always above 0.95 as long as there is no relative time delay between the photon and the escort ($T = 0$). When a time delay is introduced, the fidelity dips as a function of T for moderate values of q, as considerable pulse reshaping occurs.

Efficiency limitations of the upconversion time lens

The upconversion time lens, as described in Sec. 2.2.4, falls under the umbrella of quantum optical waveform conversion as defined above. However, it is also subject to other limitations to work effectively. In order to avoid amplitude modulation, the temporal width of the escort must be much broader than the temporal width of the input signal, as in Eq. (2.69). This limit, where $\sin(\gamma|g(t)|) \approx \sin(\gamma|g(0)|)$, is the same as the low-q limit of Eq. (3.90), and thus is potentially highly efficient. In fact, for a time lens to perform the required phase-only modulation, it *must* also have at least the potential to be efficient. This is also conveniently the limit where the first-order description is highly accurate.

3.4.3 Effect of waveform conversion on entanglement

Entanglement is essential for many quantum technologies, and to retain these advantages, it is essential that the waveform manipulation process maintains entanglement. We quantify the entanglement in the system through the Rényi 2-entropy $\Upsilon(\varrho)$ [103] as in Eq. (1.79),

defined for a pure bipartite state $|\psi\rangle_{AB}$ as

$$\Upsilon(|\psi\rangle) = -\ln \mathrm{Tr}_A \left\{ \mathrm{Tr}_B \left[|\psi\rangle\langle\psi| \right]^2 \right\}. \tag{3.93}$$

This measure is a function of the purity of the partial trace, as defined for continuous pure systems in Eq. (3.41); a high value indicates a high degree of entanglement and a correspondingly low purity for the individual subsystems. For simplicity, we denote the purity of the partial trace as $\upsilon = e^{-\Upsilon}$. For a pure state with some normalized joint temporal field function $f(t, t_h)$, the purity of the partial trace can be found as

$$\upsilon = \int \mathrm{d}t \mathrm{d}t_h \mathrm{d}t' \mathrm{d}t'_h f(t, t_h) f^*(t', t_h) f(t', t'_h) f^*(t, t'_h). \tag{3.94}$$

For the input joint temporal field of Eq. (3.80), the purity is found to be

$$\upsilon_i = \sqrt{1 - \rho^2}, \tag{3.95}$$

which tends toward zero as the statistical correlation $|\rho|$ approaches one (maximal entanglement) and one as ρ approaches zero (separable).

For the upconverted photon, the purity can be found as a double series in terms of υ_i and the parameters of Eq. (3.85) by expanding the sin terms as

$$\upsilon_3 = \frac{1}{2\sqrt{2}\langle \hat{n}_3 \rangle^2} \sum_{j,k=1} \frac{(-1)^{j+k}}{(2j)!(2k)!} \frac{\upsilon_i e^{-\frac{2T^2\left(j+k+2jkq\upsilon_i^2\right)}{2+q\left[j+k+(j+k+2jkq)\upsilon_i^2\right]}}}{\sqrt{2 + q\left[j + k + (j + k + 2jkq)\upsilon_i^2\right]}} p^{2(j+k)} \tag{3.96}$$

Note that if $\upsilon_i = 0$, $\upsilon_3 = 0$ as well regardless of the other parameters, implying that maximal entanglement is unaltered. Similarly, if $\upsilon_i = 1$, $\upsilon_3 = 1$ as entanglement cannot be created between two distant photons with a local process.

For moderate amounts of entanglement, entanglement is maintained only in the low-q limit, as seen in Fig. 3.6, which compares the Rényi entropy of the input photon pair to the joint state of the upconverted with the herald. Entanglement decreases in the high-q case as the escort is shorter in time than the input signal, and acts as a temporal filter. In
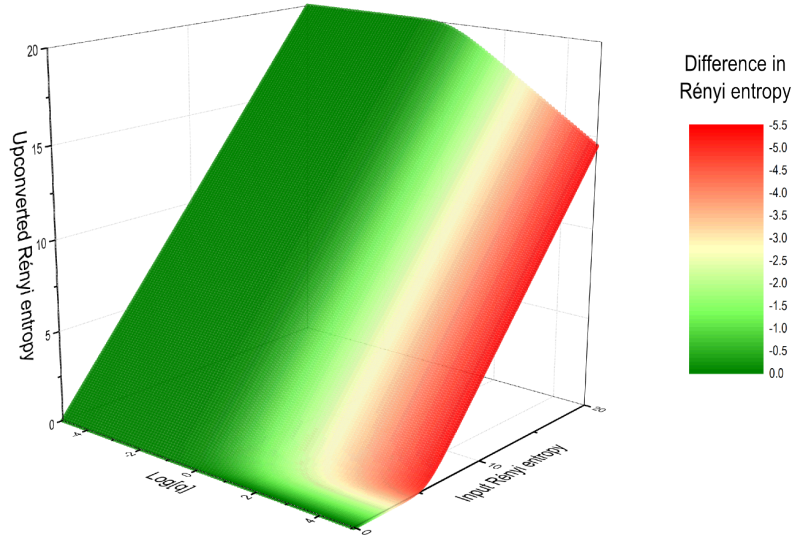
Figure 3.6: **Rényi 2-Entropy after upconversion at peak efficiency.** The Rényi 2-entropy, a measure of entanglement, is shown for the upconverted subsystem as a function of the initial Rényi 2-entropy and the pulse length ratio q, with T set to zero and p at approximately its optimal value. Numerical calculations using Eqs. (3.85) and (3.96) were taken to 10 terms. The bipartite energy-time entanglement is unaltered after post-selecting on successful upconversion if the pulse length ratio q is small. However, if the input photon is of temporal length comparable to or longer than the strong escort pulse (high-q), the post-selection results in an effective loss of entanglement in addition to imperfect efficiency.

much the same way that entanglement can be minimized in SPDC sources by spectrally filtering the state, it can also be destroyed by temporally filtering it. Importantly, the regime in which entanglement is maintained is also the regime in which high efficiency is possible, as expected.

For the calculations presented here, the entanglement of the final state is always lower than the initial. However, for other spectral shapes, it could be that the upconverted subsystem actually has a higher degree of entanglement than the initial state if the upconversion process increases the number of significant Schmidt modes, akin to the Procrustean method of entanglement concentration [235].

121

3.5 Spectral compression of single photons

Photons created through downconversion in nonlinear media generally have very wide bandwidths, often on the THz scale [236]. Since the pump bandwidth only controls how tightly correlated the photons are per Eq. (3.30), it is possible to generate photons with incredibly wide bandwidths even when pumped by a narrowband laser [194]. A broadband structure is highly advantageous for constructing frequency and time bins for information encoding or multiplexing [237, 56, 216], as well as for applications where temporal resolution is essential [195, 238, 196].

On the other hand, it can be very difficult to generate photons with spectral linewidths that match those of long-lifetime quantum memories. Atomic and solid-state memories can be highly efficient at visible wavelengths with microsecond-scale storage times, but with acceptance bandwidths on the MHz scale [239, 240, 218, 241]. Efforts have been made from both ends, though. Downconversion sources in resonant cavities can be engineered to have very narrow linewidths [242, 243, 244], and atomic ensemble or quantum dot sources are naturally very narrowband with long coherence times [245, 246, 247]. Some memories, such as those exploiting off-resonant solid state phonon modes [248, 219], are able to store photons with THz bandwidths efficiently, but at the expense of storage time.

One option is to narrow the bandwidth of the photon after it has already been created using optical waveform conversion. Passive filters can accomplish the same task, but in a necessarily lossy manner. As we will show, upconversion-based bandwidth compression has the potential to be highly efficient (as does electro-optic bandwidth compression [148]), albeit with idealized escort powers and nonlinear materials. We also show experimentally that the technique is effective for single photons, and even though the experimental demonstration is low efficiency, the signal is clearly visible above all background sources.

3.5.1 Chirped-pulse upconversion

Bandwidth compression can be viewed from the perspective of the time lens of Sec. 2.2.4 as the temporal analogy to collimation of a tightly focused beam into a broad beam, seen in Fig. 3.7a. In the spatial case, a tightly focused beam is allowed to expand over a distance z

before striking a lens of focal length $f = z$. The output beam can be much larger spatially than the input beam, and contain fewer momentum components, extending its Rayleigh range. The waist of the output beam w'_0 is proportional to the focal length over the initial waist, f/w_0, so long as the distance between the focus and the lens is significantly greater than the Rayleigh range. Additionally, if the beam is off-centre relative to the lens, that spatial shift will translate to a momentum kick, altering the output beam's angle of propagation. Indeed, as can be understood through this space-to-momentum transfer, this type of optical setup is key to the lens Fourier transform [35, 36, 138][3].

The equivalent time-frequency effect can be modelled in terms of upconversion as in Sec. 2.1.2 and Sec. 3.3. For consistency, we will stick to the quantum formalism of Sec. 3.3, in particular the first-order expression of Eq. (3.73). We assume that our input state is a pure single photon; if it were heralded, we assume that the joint spectrum is separable. The photon's wavefunction is then described as $\int d\omega_s F(\omega_s)\hat{a}_s^\dagger|0\rangle$, where

$$F(\omega_s) = \frac{1}{(2\pi\sigma_s^2)^{\frac{1}{4}}} e^{-\frac{(\tilde{\omega}_s)^2}{4\sigma_s^2}} e^{iA_s(\tilde{\omega}_s)^2}. \tag{3.97}$$

When mixed with an escort with a spectral profile defined by Eq. (3.82) in a crystal with broad phasematching ($\Phi \approx 1$), the first-order upconverted spectral intensity can be found from Eq. (3.73) as

$$|F_3(\omega_3)|^2 \propto e^{-\frac{(\omega_3 - \omega_{03})^2}{2\sigma_3^2}}, \tag{3.98}$$

where ω_{03} is the upconverted central frequency and the upconverted width σ_3 is

$$\sigma_3^2 = \frac{(\sigma_s^2 + \sigma_e^2)^2 + 16(A_e + A_s)^2\sigma_s^4\sigma_e^4}{\sigma_s^2 + \sigma_e^2 + 16(A_s^2\sigma_s^2 + A_e^2\sigma_e^2)\sigma_s^2\sigma_e^2}. \tag{3.99}$$

The escort chirp A_e which minimizes the bandwidth σ_3 of the upconverted beam can

---

[3]Note that the lens Fourier transform then requires further propagation of an additional distance $f = z$. This is necessary to ensure that the process is a momentum-to-space converter as well as a space-to-momentum converter, but immediately after the lens the momentum profile is set. For our purposes in the time-frequency analogy, we only measure the spectral profile, rendering this extra step experimentally irrelevant.
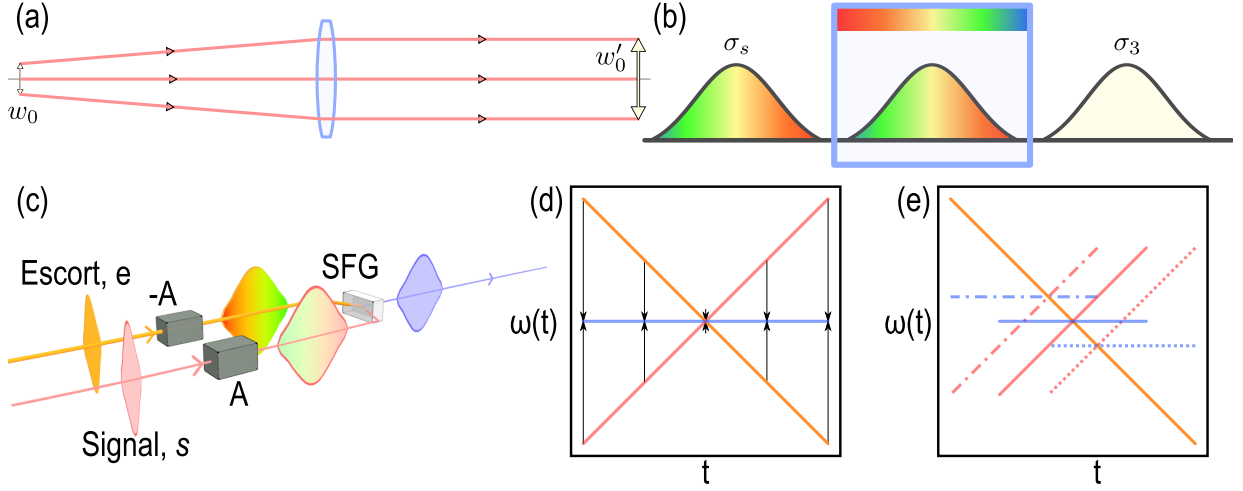
Figure 3.7: **Bandwidth compression via chirped-pulse upconversion.** (a) A beam is collimated by placing a lens one focal length from the beam focus, broadening its spatial profile. (b) The equivalent operation with a time lens is to let a beam disperse before encountering a matched time lens, which narrows the beam to a small bandwidth σ_3 and a correspondingly longer temporal length. (c) Using an upconversion time lens, bandwidth compression can be implementing by upconverting a target signal with chirp A with an oppositely chirped escort pulse, such that the upconverted light (blue) is narrowband and long in time. (d) The process can be understood intuitively in the large-chirp limit by noting that, at any time in the crystal, a signal photon with instantaneous frequency $\omega(t) = \omega_0 + \delta(t)$ meets a slice of the escort pulse with detuning $-\delta(t)$. Each frequency shift cancels the other out, resulting in a narrowband signal, visualized in blue. (e) By delaying the signal relative to the escort, the central frequency of the upconverted light can be fine-tuned without a loss in compression over the bandwidth of the escort, as seen by the signals arising from the three delayed inputs. Note that each input signal in red has the same frequency bandwidth.

be found to be

$$A_e = -\frac{\sigma_e^2 + \sigma_s^2 + 16A_s^2\sigma_e^2\sigma_s^4}{16A_s\sigma_e^2\sigma_s^2} \stackrel{LCL}{=} -A_s. \tag{3.100}$$

For simplicity, we restrict our attention to the large-chirp limit and set $A_s = A$ and $A_e = -A$, as in Fig. 3.7c. We consider our spectral description in terms of a Gaussian spectral intensity $|F_3(\omega_3)|^2$, a spectral phase $\phi(\omega_3)$, and a delay-dependant decay $\Delta(\tau)$,

124

such that the unnormalized spectral field is given by $F(\omega_3) = |F(\omega_3)|e^{i\phi_3(\omega_3)}e^{-\Delta(\tau)}$. In this limit, the upconverted spectral waveform has a bandwidth, central frequency, and spectral phase of

$$\sigma_3 = \sqrt{\frac{\sigma_s^2 + \sigma_e^2}{1 + 16A^2\sigma_s^2\sigma_e^2}} \overset{LCL}{=} \frac{1}{4A}\sqrt{\frac{1}{\sigma_s^2} + \frac{1}{\sigma_e^2}} \tag{3.101}$$

$$\omega_{03} = \omega_{0s} + \omega_{0e} + \frac{8A\sigma_s^2\sigma_e^2}{1 + 16A^2\sigma_s^2\sigma_e^2}\tau \overset{LCL}{=} \omega_{0s} + \omega_{0e} + \frac{\tau}{2A} \tag{3.102}$$

$$\phi_3(\omega_3) = i\frac{\sigma_e^2\tau\omega_3}{\sigma_s^2 + \sigma_e^2} + iA\frac{\sigma_s^2 - \sigma_e^2}{\sigma_s^2 + \sigma_e^2}(\omega_3 - \omega_{0s} - \omega_{0e})^2. \tag{3.103}$$

In the large-chirp limit, the bandwidth is compressed with a strength proportional to the chirp. This arises as the instantaneous frequency of a beam is well-defined when chirped strongly, and the signal and escort always meet with anti-correlated shifts, as seen in Fig. 3.7d. The compression is most effective from broadband pulses, as they will have a longer temporal duration in the large-limit. From Eq. (3.101), it is seen that broader bandwidth input leads to narrower band output, and vice versa; therefore, a pulse initially narrow in time converts to a pulse with a narrow spectrum. Additionally, from Eq. (3.102), if a relative time delay τ is introduced, the relationship between the instantaneous frequencies changes, and the time delay is mapped to a frequency shift, as pictured in Fig. 3.7e. In this manner, upconversion of equally and oppositely chirped pulses acts as time-to-frequency converter [249, 250]. Similar effects can be seen using equally chirped pulses and difference-frequency generation [251]. The range of tunability is defined by the length of the input chirped pulses, and the first-order relative efficiency of the process at different delay values is given by the decay term

$$e^{-\Delta(\tau)} = e^{-\frac{2\sigma_s^2\sigma_e^2}{(\sigma_s^2+\sigma_e^2)(1+16A^2\sigma_s^2\sigma_e^2)}\tau^2} = e^{-\frac{\tau^2}{2(\Delta t_s^2 + \Delta t_e^2)}}. \tag{3.104}$$

We next focus on two regimes of interest for chirped-pulse upconversion: the time-lens limit and the equal-bandwidth case. In the time-lens limit, the chirped escort is much longer in time than the chirped signal, such that it doesn't shape the temporal amplitude of signal. Taken together with the large-chirp limit, the time-lens limit implies that $\sigma_e \gg \sigma_s$.

In this limit, the bandwidth of the upconverted light is $\sigma_3 = 1/(4A\sigma_s)$, which is the inverse of the chirped temporal length. Therefore, in this limit, the Fourier-limited temporal length of the photon is identical to its chirped length before upconversion. To compress the photon in time back to Fourier-limited, an additional chirp of $+A$ is required, as seen from Eq. (3.103) in the $\sigma_e \gg \sigma_s$ limit. This is analogous to the propagation of $z_2 = f$ needed in a lens Fourier transform.

In the lab, the weak signal and escort often arise from the same laser source. Even if the photon bandwidth is in principle independent of the escort pulse, the condition $\sigma_e \approx \sigma_s$ is often closer to truth than $\sigma_e \gg \sigma_s$. The results also simplify nicely if we assume that $\sigma_e = \sigma_s = \sigma_1$, but have a slightly different interpretation. The upconverted pulse is still greatly compressed, but to a width of $\sigma_3 = \sqrt{2}/(4A\sigma_1)$ instead. As the escort does not extend well beyond the duration of the signal, it reshapes the amplitude as well, and thus the upconverted signal is not quite as temporally wide as the chirped input. However, in this limit, the output signal is exactly Fourier limited without the need for an output chirp. The reason for this cancellation can be seen clearly from the temporal representation. In simplified upconversion of a classical signal and escort pulse, the upconverted temporal profile is given by $f_3(t) = f_s(t)f_e(t)$, as per Eq. (2.29). If $f_s(t)$ and $f_e(t)$ have the same bandwidth and no relative delay, $f_s(t) = f_e^*(t)$, and the quadratic phase terms cancel each other. The minor benefit of automatic chirp compensation comes with the detriments of non-ideal pulse overlap ratios and slightly larger bandwidths, but nonetheless is more representative of the regime in which the experiments in this thesis were conducted.

3.5.2 Efficiency limitations of bandwidth compression

The time-lens limit corresponds to a high overlap of the two pulses, or the low-q regime of Fig. 3.5c, as can be seen from as

$$q_{BC} = \frac{\sigma_e^2}{1 + 16A^2\sigma_e^4} \times \frac{1 + 16A^2\sigma_s^4}{\sigma_s^2} \overset{LCL}{=} \frac{\sigma_s^2}{\sigma_e^2}. \qquad (3.105)$$

In the time lens limit, $\sigma_e \gg \sigma_s$, and perfect upconversion efficiency is possible over a wide range of relative time delays. However, in the equal-bandwidth case with unentangled

input, the pulse overlap ratio of Eq. (3.88) is

$$q_{BC} = \frac{\sigma_e^2}{1 + 16A^2\sigma_e^4} \times \frac{1 + 16A^2\sigma_s^4}{\sigma_s^2} \overset{\sigma_e = \sigma_s}{=} 1, \qquad (3.106)$$

and perfect upconversion efficiency isn't guaranteed, even with an idealized medium. However, bandwidth compression can still vastly outperform a filter with the same bandwidth in either case, with a maximum potential efficiency of approximately 88.7% for $q = 1$.

In the equal-bandwidth case in particular, the pulse length ratio q is unaffected as the compression ratio is increased, as q is independent of A. However, as the degree of compression is increased, the scaled coupling constant p of Eq. (3.86) decreases. Indeed, the compression ratio σ_3/σ_s and the efficiency to first-order are both proportional to $\frac{1}{A}$. Therefore, to achieve a high degree of compression, higher and higher laser powers are needed (recall that p^2 is proportional to the peak power of the escort pulse). As seen in Fig. 3.8a, as the chirp is increased, a greater integrated power (proportional to γ^2) is required to reach the optimal efficiency. Classically, efficiencies of up to 30% have been demonstrated [252].

In addition to the efficiency of upconversion, it is also important to consider if the process is still effective at high efficiency. Effectively, we next ask ourselves if the first-order approximation remains valid at the peak efficiencies of Fig. 3.8a, and specifically whether the bandwidth of the high-efficiency signal will be broader or narrower than expected. By Taylor-expanding the output temporal waveform $f_{3f}(t, t_h)$ about γ and Fourier-transforming the result, we may express the spectrum as a summation. We numerically evaluate the effective width $\sigma_3 = \sqrt{\langle \omega_3^2 \rangle - \langle \omega_3 \rangle^2}$ of the upconverted signal with no time delay ($\tau = 0$) for various chirps A and input bandwidths σ_1 and σ_2. In Fig. 3.8b, we show the ratio of this effective width to the first-order prediction as a function of the q parameter and of the initial pulse length ratio $q_0 = (\sigma_e^2/\sigma_s^2)$, representing the q value before applying chirps. In the low-q limit, the high-order spectral width is identical to the expected value from a first-order calculation. In the case where the two temporal widths are exactly equal ($\sigma_s = \sigma_e$), the full-order spectrum after bandwidth compression is actually *narrower* than first-order calculations predict. This is because in this case the temporal waveform is flattened and thus has a larger full-width at half-maximum. This effect is seen to persist near

the diagonals of Fig. 3.8b. One can also see that the bandwidth is increased relative to the first-order calculation in the high-q regime far from the diagonals; however, the relative increase in bandwidth is fairly small.
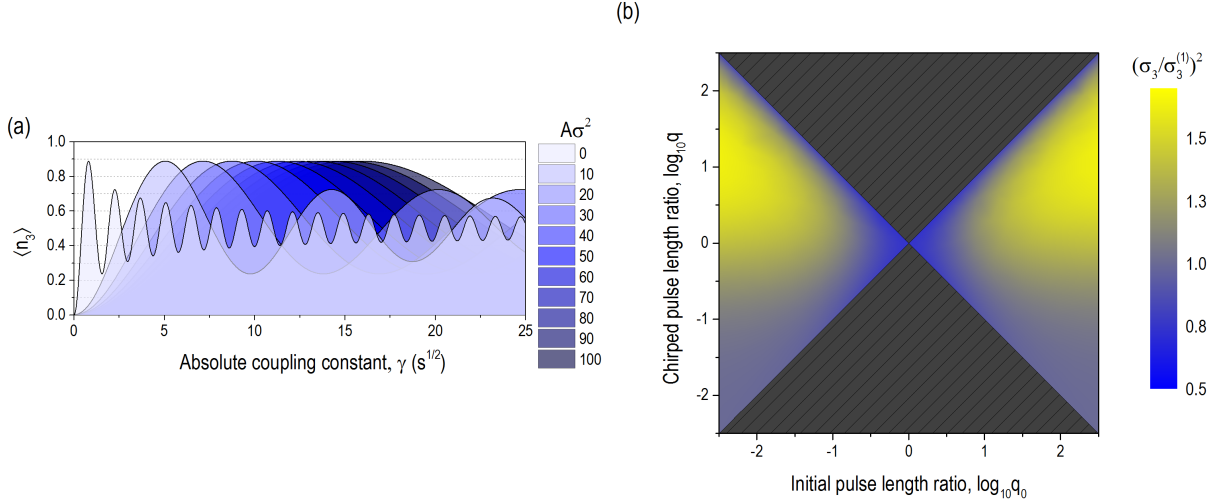

Figure 3.8: **Efficiency and effectiveness of bandwidth compression.** (a) The success probability $\langle \hat{n}_3 \rangle$ of bandwidth compression is shown as a function of the absolute coupling constant γ, with $\tau = 0$, $\sigma_s = \sigma_e = \sigma$, and $A_s = -A_e = A$. As the chirp applied is increased, the compression achieved is stronger at the expense of peak power in the escort pulse; however, while more escort power is required to achieve optimal efficiency, the potential peak efficiency is constant. (b) In the regime where the pulse length ratio q is low, the spectral width of the upconverted signal σ_3 is seen to be identical to the width $\sigma_3^{(1)}$ expected from a first-order approximation regardless of the input bandwidths (the gray region at the bottom of the plot). However, as q grows, the ratio of the two widths is seen to depend on the pulse length ratio before chirp, q_0. The gray lined region is algebraically inaccessible for real-valued chirp parameters $A_1 = -A_2$, with the $q = q_0$ line corresponding to zero applied chirp and the $q = \frac{1}{q_0}$ line corresponding to the large-chirp limit (they cross at $q_0 = 1$, where the q values are chirp-independent). Note that in the large-chirp limit and the no chirp limit, the high-efficiency signal is actually spectrally narrower than expected, as seen in the blue portions of the graph.

128

3.5.3 Effect of entanglement on bandwidth compression

When creating photon pairs, entanglement in energy-time is often difficult to eliminate, as discussed in Sec. 3.2. As we propose to use bandwidth compression on photons from these pair sources, it is important to qualify the effect of entanglement on the effectiveness of the procedure [161]. While we have discussed the effect of waveform conversion on entanglement in Sec. 3.4.3, here we focus more plainly on the effect of entanglement on the bandwidth of the upconverted photon. For simplicity, we will only consider a first-order treatment.

We consider the generic two-dimensional Gaussian $F(\omega_s, \omega_h)$ of Eq. (3.37) as representative of our joint photon spectrum, with signal frequencies ω_s and herald frequencies ω_h. Convolving the two spectral representations as per Eq. (3.73) in the bandwidth compression scenario $A_s = -A_e = A$ and integrating out the herald spectrum, we find the marginal bandwidth of the upconverted signal to be

$$\sigma_3 = \left[\frac{1}{\sigma_s^2 + \sigma_e^2} + 16A^2 \sigma_e^2 \left(1 - \frac{\sigma_e^2}{\sigma_e^2 + \sigma_s^2(1 - \rho^2)} \right) \right]^{-\frac{1}{2}}. \tag{3.107}$$

We can see from this expression that, if the state is maximally entangled ($|\rho| = 1$), the chirp has no effect on the bandwidth of the upconverted photon. Indeed, in that limit,

$$\lim_{|\rho| \to 1} \sigma_3 = \sqrt{\sigma_e^2 + \sigma_s^2}, \tag{3.108}$$

which simply adds the energy uncertainty of the escort to the signal. The ineffectiveness of bandwidth compression in the entangled limit is due to an inability to effectively chirp half of an entangled photon source. In a perfectly entangled source (we'll assume anti-correlated spectra for simplicity), the sum of the frequencies and difference in the times-of-arrival is well known, but each individually is entirely random. It is therefore impossible to stretch the input signal photon such that the strict energy relationships of Fig. 3.7d are met. From another point of view, the signal photon individually before the chirp is much longer than its marginal spectrum would indicate, and thus it takes a much greater chirp to enter the large-chirp limit.

For further intuition, we examine Eq. (3.107) in the time-lens and equal-bandwidth limits. If the bandwidth compressor acts as a time lens, the compressed photon bandwidth will be

$$\lim_{\sigma_e \to \infty} \sigma_3 = \frac{1}{4A\sigma_s\sqrt{1-\rho^2}}, \tag{3.109}$$

which gives the expected result if $\rho = 0$ and decreases in effectiveness as more entanglement is added. Meanwhile, in the equal-bandwidth case, the upconverted bandwidth will be

$$\sigma_3|_{\sigma_e = \sigma_s = \sigma} = \frac{1}{\sqrt{\frac{1}{2\sigma^2} + 16A^2\sigma^2\left(\frac{1-\rho^2}{2-\rho^2}\right)}}. \tag{3.110}$$

3.5.4 Experiment

The first experimental demonstration of single-photon bandwidth compression via chirped-pulse upconversion was reported in 2013 [161], and appears in the PhD thesis of Jonathan Lavoie [253]. As many of the same experimental techniques will be detailed in Chapters 4 and 5, the setup and results will only be briefly summarized here.

The basic experimental setup for chirped-pulse upconversion is shown in Fig. 3.9. Photon pairs are created with an SPDC source and separated into signal and herald paths (usually through noncollinear downconversion geometry, occasionally through nondegenerate wavelengths). The signal is then sent through a spool of single-mode fibre to pick up a positive chirp, related to the index of the fibre and the length L of the spool by $A_s = \frac{1}{2}k_2L = \frac{\lambda^2 D_\lambda}{4\pi c}L$, as in Sec. 2.2.2. The remainder of the strong laser pulse is split into an escort and a weak beam. The weak beam can be switched into the single-photon path and used as an alignment pulse; note that this requires it is delay-matched to the photons. The escort goes through a grating-based compressor, as described in Sec. 2.3.2, where it gains a negative chirp. The two pulses are then combined in a nonlinear material for sum-frequency generation, and the output signal is measured in coincidence with the herald photon. In other classical demonstrations, the chirping has been accomplished in an integrated fashion using chirped volume Bragg gratings [254].

In Ref. [161], we used the setup of Fig. 3.9 to experimentally demonstrate photonic

bandwidth compression. Photons are 811 nm with a bandwidth of 3.8 nm (1.74 THz) were compressed to photons at 399.7 nm with a bandwidth of 0.04 nm (74 GHz, 43 GHz when corrected for limited spectrometer resolution) using an escort pulse at 786.6 nm with a bandwidth of 11.5 nm (5.6 THz). The central wavelength was found to be tunable over a range of 3 nm, more than seventy times the output bandwidth. The photon and es-
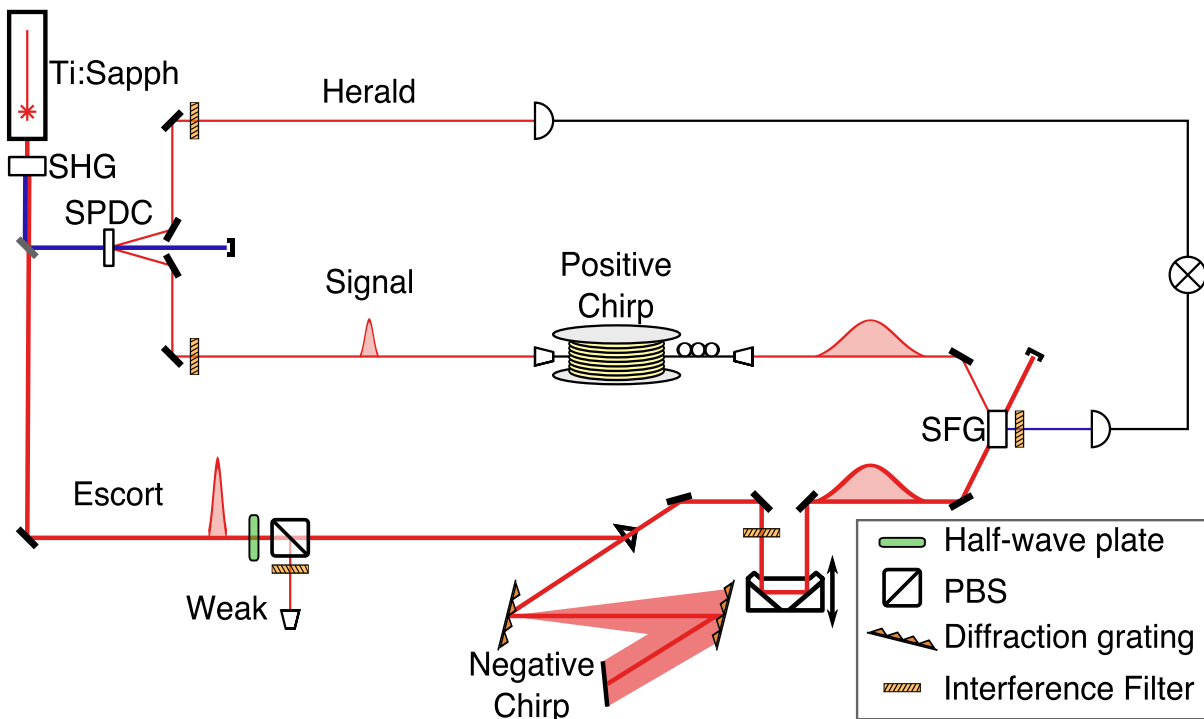
Figure 3.9: **Chirped-pulse upconversion experimental setup.** The chirped-pulse upconversion of single photons is accomplished as shown above. Photons are created through spontaneous parametric downconversion (SPDC) of a pump created through second-harmonic generation (SHG) of a Ti:Sapph pulse. The signal photons are coupled into a fibre spool, where they disperse and gain a positive chirp. The remainder of the Ti:Sapph is repurposed as the escort pulse. A piece of it may be separated and used as a weak pulse for alignment. The rest is sent to a grating-based compressor, where it gains a negative chirp. A retroreflector is used to match the delays, and the signal and escort are combined in a nonlinear material for sum-frequency generation (SFG). The upconverted signal and herald are then detected and measured in coincidence.

cort chirps were set to be equal by minimizing the output bandwidth, and the chirp value extracted from the tunability curve was $|A| = 661 \times 10^3 \, \text{fs}^2$. The efficiency of the upconversion process in this experiment was estimated to be 0.06%, with 300 mW of average power from the escort and a 1 mm BiBO crystal acting as the upconversion medium. In the next three sections, we will discuss how similar systems can be used to coherently measure time bin superposition states, read out densely packed information in time, and extended to temporally image correlated photon spectra.

Common to all of these experiments is background noise arising from the second harmonic of the escort pulse. We generally use two techniques to minimize the amount of SHG that reaches our detectors. Firstly, we usually upconvert the escort and photonic signal in a non-collinear geometry. In this setup, the majority of the escort SHG is directed into a different path than the upconverted signal, and can be blocked with a simple iris. However, due to scatter in the medium and the sheer intensity of the SHG relative to the photon signal, a significant portion of the SHG still reaches the detector. To remove the escort once and for all, the escort and signal are designed to have non-degenerate wavelengths. In the setups described in this thesis, the escort is centred near 785 nm, and the photon signal near 810 nm. The upconverted SFG signal will then be around 398.5 nm, while the escort SHG will be near 392.5 nm, and the two can be separated spectrally. While the upconverted signal is often narrow in frequency, the escort SHG is not necessarily, and it is important to ensure that it contains no amplitude near 795 nm, where the SHG will mask the upconverted signal. This can be done with bandpass or edge filters, but it more easily accomplished by inserted a razor blade into the pulse compressor when the beam is at its largest, controllably cutting off the high-wavelength components.

Also common to all of these experiments is a relatively low upconversion efficiency. Using the parameters of the first chirped-pulse upconversion experiment [161] and the theoretical model of Sec. 3.4.2, the upconversion efficiency in the experiment was expected to be 0.043%, fairly close to the 0.06% extrapolated from the data. This calculation assumes a second-order nonlinear susceptibility of BiBO of 7.52 pm/V, a length of 1 mm, and perfectly overlapped Gaussian photon and escort beams with an 18.5 μm waist radius. In order to reach 50% efficiency by simply turning up the power, an escort pulse with an average power of over 400 W would be required. On the other hand, a much

greater nonlinear coefficient can be obtained by using a material such as periodically poled lithium niobate (PPLN) instead. Exchanging one millimeter of BiBO for one millimeter of PPLN increases the expected efficiency by a factor of ten; with 3 mm of PPLN and a five watt escort pulse, our model predicts 50% upconverison efficiency is achievable with no other changes required. Longer nonlinear crystals increase the efficiency quadratically, but phasematching restrictions becomes more and more of a problem. Efficiency gains are linear in crystal length once phasematching becomes restrictive, in analogy to the SPDC case examined in Eq. (3.36). By using the phasematching function directly for photon bandwidth compression rather than pulse shaping, higher efficiencies can be achieved, as recently demonstrated experimentally [255]. However, the time-to-frequency conversion property essential to the experiments in Ch. 4 and 5 is lost, as the nonlinear medium only supports upconversion to a narrow range of frequencies (refer to the curves for type-I materials in Fig. 2.2 as illustrative examples).

Chapter 4

Coherent ultrafast measurement of time-bin encoded photons

Notes and acknowledgements

Author Contributions

Kevin Resch and **Jonathan Lavoie** conceived of the study.

Jonathan Lavoie built the initial photon source and pulse compressor.

John Donohue wrote data acquisition software and built time-bin portions of the apparatus.

John Donohue and **Megan Agnew** carried out the experiment, analyzed the data, and wrote the first draft of the manuscript.

All authors contributed to the final version.

Chapter Overview

Qubits encoded in the time-bin degree of freedom are particularly well suited for long-distance quantum communication and fundamental experiments [50, 64, 66, 237, 51, 67]. Time-bin states can be prepared using an unbalanced interferometer [256, 257], where photons may take a short path and arrive early ($|e\rangle$) or a long one and arrive late ($|\ell\rangle$) with a time difference $\tau_{e\ell}$ greater than the photon coherence time. Measurements of time-bin states are typically performed with an identical interferometer (see Fig. 4.1a). However, high-fidelity measurements require that $\tau_{e\ell}$ be greater than the detector time resolution, which is typically much longer than the coherence time. Experimentally, delays on the order of nanoseconds have been used [66, 67]; recent advances in photon counting technology could conceivably reduce this delay to 30 ps [16]. Even faster detectors would improve time-bin encodings, allowing a higher information density while reducing the demands on interferometric stabilization.

Ultrafast laser pulses and nonlinear optics provide a framework for single-photon measurement on timescales much faster than electronics [258, 259]. A promising coherent nonlinear effect for single-photon ultrafast measurements is sum-frequency generation (SFG), a process in which two pulses interact in a nonlinear material to produce a third with frequency equal to the sum of the inputs [260, 226, 52, 261]. SFG in conjunction with pulse-shaping techniques is a powerful tool for manipulating single-photon temporal waveforms [224, 58, 161].

In this chapter, adapted from Ref. [68], we show how sum-frequency generation and pulse shaping enable coherent measurements of time-bin states with a temporal separation on the picosecond timescale. To explicitly demonstrate the coherent aspects of our technique, we perform a tomographically complete set of measurements on an entangled time-bin state for state reconstruction [262, 263, 264]. Furthermore, we show that our measurement proceeds with sufficiently high fidelity to convincingly violate the CHSH-Bell inequality [81, 82].
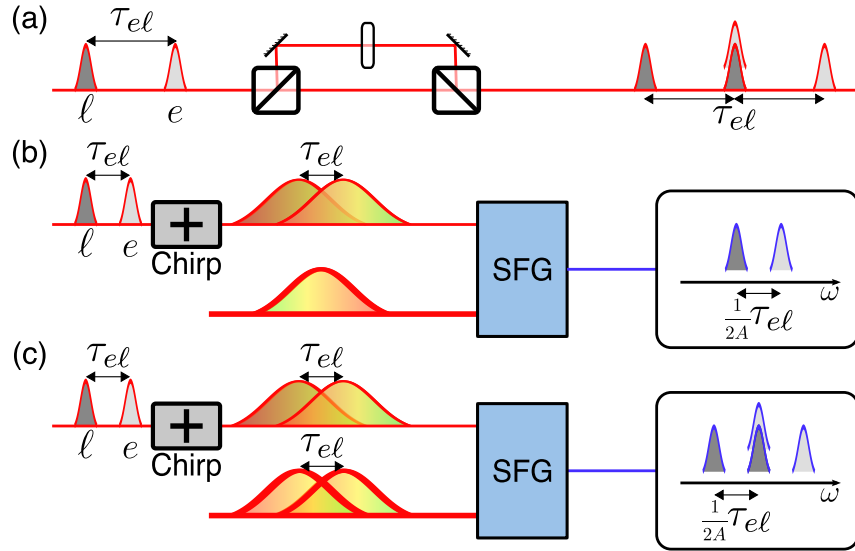
Figure 4.1: **Measuring time-bin qubits.** (a) In typical time-bin measurement schemes, an input time-bin state is sent through an unbalanced interferometer matched to the bin separation. High-fidelity measurement requires isolating the middle output pulse, necessitating a large delay $\tau_{e\ell}$. (b) A photon prepared in a time-bin superposition is chirped and undergoes SFG with an equal and oppositely chirped strong laser pulse. The SFG contains two peaks separated in frequency by an amount proportional to the time delay, $\tau_{e\ell}$. (c) If the chirped strong laser pulse is itself in a superposition of two time bins, the output spectrum contains three peaks. In this case, high-fidelity measurement requires isolating the middle frequency. The process is directly analogous to conventional time-bin measurement, with the signal converted from time to frequency.

4.1 Time-bin measurement by time-to-frequency conversion

4.1.1 Derivation of time-bin interference

Chirped-pulse upconversion of a time-bin superposition

The principle of our measurement scheme is based on SFG with oppositely-chirped pulses, as in Sec. 3.5. A chirped pulse is stretched such that its instantaneous frequency varies linearly in time. By combining two oppositely chirped pulses through SFG, the bandwidth of the resulting pulse is drastically narrowed. Additionally, by delaying one of the pulses, the central frequency of the generated light changes by an amount proportional to the delay, as seen in Sec. 3.5. This has been shown for laser pulses [249, 250] and a single photon with a strong laser pulse [161]. If a pulse (or photon) is in a superposition of two time bins, it will exit the process in a superposition of two frequencies (see Fig. 4.1b). The process is thus a coherent interface between time and frequency. If *both* inputs are in superpositions of time bins with the same separation, the spectrum of the SFG output is analogous to the temporal profile of interferometric time-bin measurement, with three distinct frequencies. The middle peak results from the interference of two contributions, with an intensity proportional to the probability expected for a controllable projective measurement (see Fig. 4.1c).

To show this, we first define a time-bin qubit in terms of an early and late time bin, delayed relative to each other by a time $\tau_{e\ell}$. We can write these states in terms of the signal frequency ω_s as

$$
\begin{aligned}
|e\rangle &= \frac{1}{(2\pi\sigma_s^2)^{\frac{1}{4}}} \int \mathrm{d}\omega_s \, e^{-\frac{\tilde{\omega}_s^2}{4\sigma_s^2}} \hat{a}_{\omega_s}^\dagger |0\rangle, \\
|\ell\rangle &= \frac{1}{(2\pi\sigma_s^2)^{\frac{1}{4}}} \int \mathrm{d}\omega_s \, e^{-\frac{\tilde{\omega}_s^2}{4\sigma_s^2}} e^{i\omega_s \tau_{e\ell}} \hat{a}_{\omega_s}^\dagger |0\rangle.
\end{aligned}
\tag{4.1}
$$

137

Note that the overlap of these two states is

$$|\langle e|\ell\rangle|^2 = e^{-\sigma_s^2 \tau_{e\ell}^2}, \tag{4.2}$$

and therefore the two are only orthogonal in the limit where $\tau_{e\ell} \gg \frac{1}{\sigma}$. However, while chirping these two states strongly may cause them to overlap in time, they remain orthogonal ($|\langle e|\ell\rangle|^2$ is preserved) as the instantaneous frequency at any time will uniquely identify each, and they are in-principle recompressible. We write a pure state as a superposition of two time bins, with weight defined by θ and phase ϕ and some chirp A_s, as

$$\begin{aligned}
|\psi\rangle &= \cos\frac{\theta}{2}|e\rangle + e^{i\phi}\sin\frac{\theta}{2}|\ell\rangle \\
&= \frac{1}{(2\pi\sigma_s^2)^{\frac{1}{4}}} \int d\omega_s\, e^{-\frac{\tilde{\omega}_s^2}{4\sigma_s^2}} e^{iA_s\tilde{\omega}_s^2} \left(\cos\frac{\theta}{2} + e^{i\omega_s\tau_{e\ell}} e^{i\omega_s\frac{\phi}{\omega_{0s}}}\sin\frac{\theta}{2}\right).
\end{aligned} \tag{4.3}$$

Note that the phase ϕ is represented here as a time delay scaled by the period of the optical oscillations.

We also construct an escort pulse in a superposition of time bin modes with a spectral representation

$$G(\omega_e, \alpha, \beta) = e^{-\frac{\tilde{\omega}_e^2}{4\sigma_e^2}} e^{iA_e\tilde{\omega}_e^2} \left(\cos\frac{\alpha}{2} + e^{i\omega_e\tau_{e\ell}} e^{i\omega_e\frac{\beta}{\omega_{0e}}}\sin\frac{\alpha}{2}\right). \tag{4.4}$$

If we set $A_s = -A_e = A$ and mix the photon state of Eq. (4.3) with the escort of Eq. (4.4) in a nonlinear material, as shown in Fig. 4.1c, we obtain an output photon with a large-chirp limit spectral amplitude proportional to

$$\begin{aligned}
F_3(\omega_3) &\overset{LCL}{\propto} e^{i\frac{A(\sigma_s^2-\sigma_e^2)}{\sigma_s^2+\sigma_e^2}(\omega_3-\omega_{0s}-\omega_{0e})^2} \left[\cos\frac{\theta}{2}\sin\frac{\alpha}{2} \left(e^{-\frac{4A^2\sigma_s^2\sigma_e^2}{\sigma_s^2+\sigma_e^2}(\omega_3-\omega_{0s}-\omega_{0e}-\frac{\tau_{e\ell}}{2A})^2} e^{i\beta\frac{\sigma_s^2\omega_{0e}+\sigma_e^2(\omega_3-\omega_{0s})}{(\sigma_s^2+\sigma_e^2)\omega_{0e}}} e^{i\frac{\sigma_e^2\tau_{e\ell}\omega_3}{\sigma_s^2+\sigma_e^2}} \right) \right. \\
&\quad + \left(\cos\frac{\theta}{2}\cos\frac{\alpha}{2} + e^{i\beta\frac{\sigma_s^2\omega_{0e}+\sigma_e^2(\omega_3-\omega_{0s})}{(\sigma_s^2+\sigma_e^2)\omega_{0e}}} e^{i\phi\frac{\sigma_e^2\omega_{0s}+\sigma_s^2(\omega_3-\omega_{0e})}{(\sigma_s^2+\sigma_e^2)\omega_{0s}}} e^{i\omega_3\tau_{e\ell}}\sin\frac{\theta}{2}\sin\frac{\alpha}{2}\right) e^{-\frac{4A^2\sigma_s^2\sigma_e^2}{\sigma_s^2+\sigma_e^2}(\omega_3-\omega_{0s}-\omega_{0e})^2} \\
&\quad + \left. \sin\frac{\theta}{2}\cos\frac{\alpha}{2} e^{-\frac{4A^2\sigma_s^2\sigma_e^2}{\sigma_s^2+\sigma_e^2}(\omega_3-\omega_{0s}-\omega_{0e}+\frac{\tau_{e\ell}}{2A})^2} e^{i\phi\frac{\sigma_e^2\omega_{0s}+\sigma_s^2(\omega_3-\omega_{0e})}{(\sigma_s^2+\sigma_e^2)\omega_{0s}}} e^{i\frac{\sigma_s^2\tau_{e\ell}\omega_3}{\sigma_s^2+\sigma_e^2}} \right].
\end{aligned} \tag{4.5}$$

The terms associated with phases β and ϕ carry frequency-dependent terms, which we approximate away by assuming our pulses are not very broadband, such that $\frac{\omega_3 - \omega_{0e}}{\omega_{0s}} \approx 1$ for all contributing frequencies; this approximation is effectively the same as assuming that we could have treated the phases as overall phases rather than delays from the start, and is particularly valid for the equal-and-opposite chirp case since the range of frequencies available to ω_3 is significantly smaller than the input due to bandwidth compression. With this approximation, we can write the output spectral waveform as

$$
\begin{aligned}
F_3(\omega_3) \overset{LCL}{\propto}\ & e^{i\frac{A(\sigma_s^2-\sigma_e^2)}{\sigma_s^2+\sigma_e^2}(\omega_3-\omega_{0s}-\omega_{0e})^2} \left[\cos\frac{\theta}{2}\sin\frac{\alpha}{2}\left(e^{-\frac{4A^2\sigma_s^2\sigma_e^2}{\sigma_s^2+\sigma_e^2}(\omega_3-\omega_{0s}-\omega_{0e}-\frac{\tau_{e\ell}}{2A})^2} e^{i\beta} e^{i\frac{\sigma_e^2\tau_{e\ell}\omega_3}{\sigma_s^2+\sigma_e^2}} \right) \right. \\
& + \left(\cos\frac{\theta}{2}\cos\frac{\alpha}{2} + e^{i(\phi+\beta+\omega_3\tau_{e\ell})}\sin\frac{\theta}{2}\sin\frac{\alpha}{2} \right) e^{-\frac{4A^2\sigma_s^2\sigma_e^2}{\sigma_s^2+\sigma_e^2}(\omega_3-\omega_{0s}-\omega_{0e})^2} \\
& \left. + \sin\frac{\theta}{2}\cos\frac{\alpha}{2} e^{-\frac{4A^2\sigma_s^2\sigma_e^2}{\sigma_s^2+\sigma_e^2}(\omega_3-\omega_{0s}-\omega_{0e}+\frac{\tau_{e\ell}}{2A})^2} e^{i\phi} e^{i\frac{\sigma_s^2\tau_{e\ell}\omega_3}{\sigma_s^2+\sigma_e^2}} \right]. \\
\propto\ & e^{i\beta}\cos\frac{\theta}{2}\sin\frac{\alpha}{2}F_B(\omega_3) + e^{i\phi}\sin\frac{\theta}{2}\cos\frac{\alpha}{2}F_R(\omega_3) \\
& + \left(\cos\frac{\theta}{2}\cos\frac{\alpha}{2} + e^{i\phi+\beta+\omega_3\tau_{e\ell}}\sin\frac{\theta}{2}\sin\frac{\alpha}{2} \right) F_M(\omega_3),
\end{aligned}
\tag{4.6}
$$

where $F_R(\omega_3)$ and $F_B(\omega_3)$ represent spectral components which are red-shifted and blue-shifted relative to the middle component, $F_M(\omega_3)$. If the three spectral peaks are clearly separable, we can see interference between the two contributions to the middle peak, which arise from the early component of the photon upconverting with the early component of the escort, and late photonic component upconverting with the late escort component.

Isolation of the interference term

Consistent with Sec. 3.5, the three spectral peaks each have the same spectral width,

$$
\sigma_3 = \sqrt{\frac{\sigma_s^2 + \sigma_e^2}{1 + 16A^2\sigma_s^2\sigma_e^2}} \overset{LCL}{=} \frac{1}{4A}\sqrt{\frac{1}{\sigma_s^2} + \frac{1}{\sigma_e^2}} \leq \frac{1}{2\sqrt{2}A\sigma_{\text{in}}},
\tag{4.7}
$$

where $\sigma_{\text{in}} = \min\{\sigma_s, \sigma_e\}$ is defined by the input with the minimum bandwidth, and thus the longest coherence time. The peaks have central frequencies

$$\omega_{03} = \omega_{0s} + \omega_{0e} + c_i \frac{8A\sigma_s^2\sigma_e^2\tau_{e\ell}}{1 + 16A^2\sigma_s^2\sigma_e^2} \overset{LCL}{=} \omega_{0s} + \omega_{0e} + c_i \frac{\tau_{e\ell}}{2A}, \tag{4.8}$$

where c_R, c_M, and c_B are -1, 0, and +1, respectively. To clearly isolate the central peak, it is necessary that $\delta\omega_{03} > \sigma_3$, ergo

$$\frac{\tau_{e\ell}}{2A} > \frac{1}{2\sqrt{2}A\sigma_{\text{in}}} \quad \text{i.e.} \quad \tau_{e\ell} > \frac{1}{\sqrt{2}\sigma_{\text{in}}}. \tag{4.9}$$

Therefore, to ensure clear separability of the spectral peaks, it is only necessary that the initial time bins were clearly distinct in time (if σ_{in} refers to the signal rather than the escort). This is a direct consequence of the time-to-frequency conversion, as the distinguishability in time before the process presents itself clearly as spectral distinguishability after upconversion.

Assuming that we can isolate the central peak, we find that the spectral intensity of the middle peak is

$$S_M(\omega_3) \propto \left| \left(\cos\frac{\theta}{2}\cos\frac{\alpha}{2} + e^{i\phi+\beta+\omega_3\tau_{e\ell}}\sin\frac{\theta}{2}\sin\frac{\alpha}{2} \right) F_M(\omega_3) \right|^2. \tag{4.10}$$

Integrating over ω_3, the overall central peak intensity is found to be

$$I_M = 1 + \cos\alpha\cos\theta + e^{-\frac{\sigma_s^2+\sigma_e^2}{32A^2\sigma_s^2\sigma_e^2}\tau_{e\ell}^2}\cos\left(\phi + \beta + \omega_{03}\tau_{e\ell}\right)\sin\alpha\sin\theta, \tag{4.11}$$

which (absorbing the constant phase $\omega_{03}\tau_{e\ell}$ into β) is equal to the success probability of a projective measurement onto a state $|\Lambda\rangle = \cos\frac{\alpha}{2}|e\rangle + e^{-i\beta}\sin\frac{\alpha}{2}|\ell\rangle$ as per Eq. (1.49) (i.e. $|\langle\Lambda|\psi\rangle|^2$) so long as $\tau_{e\ell} \ll 1/\sigma_3$, i.e. the time difference between bins is less than the coherence length of the bandwidth-compressed signal. This condition is necessary to ensure that the upconverted signal arising from early-early upconversion is indistinguishable in time from the late-late upconversion. While the blue- and red-shifted peaks were discarded in our experiment, they can be measured simultaneously for additional data, and corre-

spond to projective measurements on $|e\rangle$ and $|\ell\rangle$; however, they cannot be used to measure coherent superpositions.

In summary, to create and measure time-bin qubit states using chirped-pulse upconversion, the time difference between bins must be set such that

$$\sqrt{\frac{1}{\sigma_s^2} + \frac{1}{\sigma_e^2}} \ll \tau_{e\ell} \ll \frac{1}{\sigma_3} \overset{LCL}{=} \frac{4A\sigma_s\sigma_e}{\sqrt{\sigma_s^2 + \sigma_e^2}}, \tag{4.12}$$

which can be interpreted as meaning that the time difference must be long enough that the time bins are clearly distinguishable for both the signal and escort, but short enough that the upconverted signals overlap in time.

4.1.2 Extension to time-bin qudits

Time-bin encodings naturally extend to higher dimensions by simply adding more bins. To extend our measurement technique to higher dimensions, we similarly require more pulses in the classical beam. In doing so, photons in a certain time bin will upconvert to the central frequency ω_M only if they are upconverted by the strong laser pulse component with the same time delay. Before discussing the experiment performed on qubits, we briefly discuss how this technique easily extends to time-bin systems of higher dimensionality.

For a time-bin qudit of dimension N, we define basis states with a time delay of τ between them as

$$|t_j\rangle \propto \int \mathrm{d}\omega F(\omega_s) e^{ij\omega_s\tau} \hat{a}_{\omega_s}^\dagger |0\rangle. \tag{4.13}$$

We represent an arbitrary superposition state $|\psi\rangle$ with complex constants c_j as

$$|\psi\rangle = \sum_{j=0}^{N-1} c_j |t_j\rangle \tag{4.14}$$

and set $F(\omega_s)$ (after chirping) to be a Gaussian envelope,

$$F(\omega_s) = e^{-\frac{(\omega_s - \omega_{0s})^2}{4\sigma_s^2}} e^{iA(\omega_s - \omega_{0s})^2}. \tag{4.15}$$

We similarly define a strong laser pulse as before to be a superposition of N classical fields with complex constants d_j as

$$G(\omega_e) = e^{-\frac{(\omega_e - \omega_{0e})^2}{4\sigma_e^2}} e^{-iA(\omega_e - \omega_{0e})^2} \left(\sum_{j=0}^{N-1} d_j e^{ij\omega_e\tau} \right). \tag{4.16}$$

By following the same procedure as for the two-dimensional case, we find that the upconverted pulse once again consists of numerous frequency peaks. We concentrate on the middle peak, with a field $F_M(\omega_3)$ centered on $\omega_{03} = \omega_{0s} + \omega_{0e}$, which arises when the $|t_j\rangle$ term of the qudit field is upconverted by the jth strong laser pulse. This middle field can be found as

$$F_M(\omega_3) = \int d\omega_s e^{-\frac{(\omega_s - \omega_{0s})^2}{4\sigma_s^2}} e^{iA(\omega_s - \omega_{0s})^2} e^{-\frac{(\omega_3 - \omega_s - \omega_{0e})^2}{4\sigma_s^2}} e^{-iA(\omega_3 - \omega_s - \omega_{0e})^2} \left(\sum_{j=0}^{N-1} c_j d_j e^{ij\omega_3\tau} \right). \tag{4.17}$$

The integrated spectral intensity of the middle peak can then be calculated as

$$I_M(\omega_3) = \int d\omega_3 F_M^*(\omega_3) F_M(\omega_3) \propto \sum_{j=0}^{N-1} \sum_{k=0}^{N-1} e^{-(j-k)^2 \frac{\sigma_3^2 \tau^2}{2}} e^{i(j-k)\omega_{03}\tau} c_k^* d_k^* c_j d_j. \tag{4.18}$$

The success probability of a general projective measurement of $|\psi\rangle$ onto $|\chi\rangle = \sum_{j=0}^{N-1} x_j |t_j\rangle$ can be expressed as

$$|\langle \chi | \psi \rangle|^2 = \sum_{j=0}^{N-1} \sum_{k=0}^{N-1} c_k^* x_k c_j x_j^*. \tag{4.19}$$

Thus, in an analogous fashion to the qubit case, if the peaks are clearly separable and $\tau \ll \frac{1}{\sigma_3}$, the intensity of the middle peak is proportional to the success probability of a projective measurement onto

$$|\Lambda\rangle = \sum_{j=0}^{N-1} d_j^* e^{-ij\omega_{03}\tau} |t_i\rangle. \tag{4.20}$$

Thus, the scheme generalizes to higher-dimensional time-bin states in a straightforward

manner.

4.2   Experiment and results

4.2.1   Experimental setup and spectra

Our setup is shown in Fig. 4.2. A pulsed Ti:Sapphire laser (Spectra-Physics Tsunami 3960, repetition rate 80 MHz, average power 2.4 W) centered at 790.2 nm with bandwidth 11.8 nm (FWHM) produces laser pulses of 0.8 W average power centered at 393.8 nm with a bandwidth of 1.2 nm through frequency doubling in bismuth borate (BiBO). The narrower bandwidth of the UV pump is due to restrictive phasematching in the BiBO crystal. The UV beam is rotated to diagonal polarization before passing through two orthogonally-oriented β-barium borate (BBO) crystals to produce photon pairs via type-I down-conversion (SPDC) in the polarization state $|\Phi^+\rangle = \frac{1}{\sqrt{2}}(|HH\rangle + |VV\rangle)$ [105], where $|H\rangle$ and $|V\rangle$ are horizontal and vertical polarizations respectively. To compensate for walkoff, we inserted 1 mm of α-BBO into the UV beam path and 1 mm of BiBO with a cut angle of 152.6° into the signal arm [95]. The signal is filtered to 810.4 nm with bandwidth 4.53±0.09 nm FWHM, and the herald to 767.1 nm with bandwidth 2.37±0.02 nm. We directly detect the signal and herald photons using avalanche photodiodes (APD, Perkin-Elmer SPCM-AQ4C). Summing the coincidence rates over all H/V combinations yields a total of 135 kHz.

We convert the signal photon from polarization to time-bin encoding by inserting 5 mm of α-BBO cut at 90° into the signal arm such that $|H\rangle$ is aligned with the extraordinary (fast) axis and project onto diagonal polarization with a polarizing beamsplitter to erase polarization information, leaving the state $|\tilde{\Phi}^+\rangle = \frac{1}{\sqrt{2}}(|He\rangle + |V\ell\rangle)$. The α-BBO introduces a relative group delay of $\tau_{e\ell} = 2.16\pm0.03$ ps between the polarization components, measured through chirped-pulse interferometry [160]. This delay is significantly greater than the photon coherence time, $1/\sigma = 0.362$ ps, fulfilling the requirements for distinct time bins.

A strong laser pulse with a field $G(\omega_e, \alpha, \beta)$ is prepared by sending the remaining
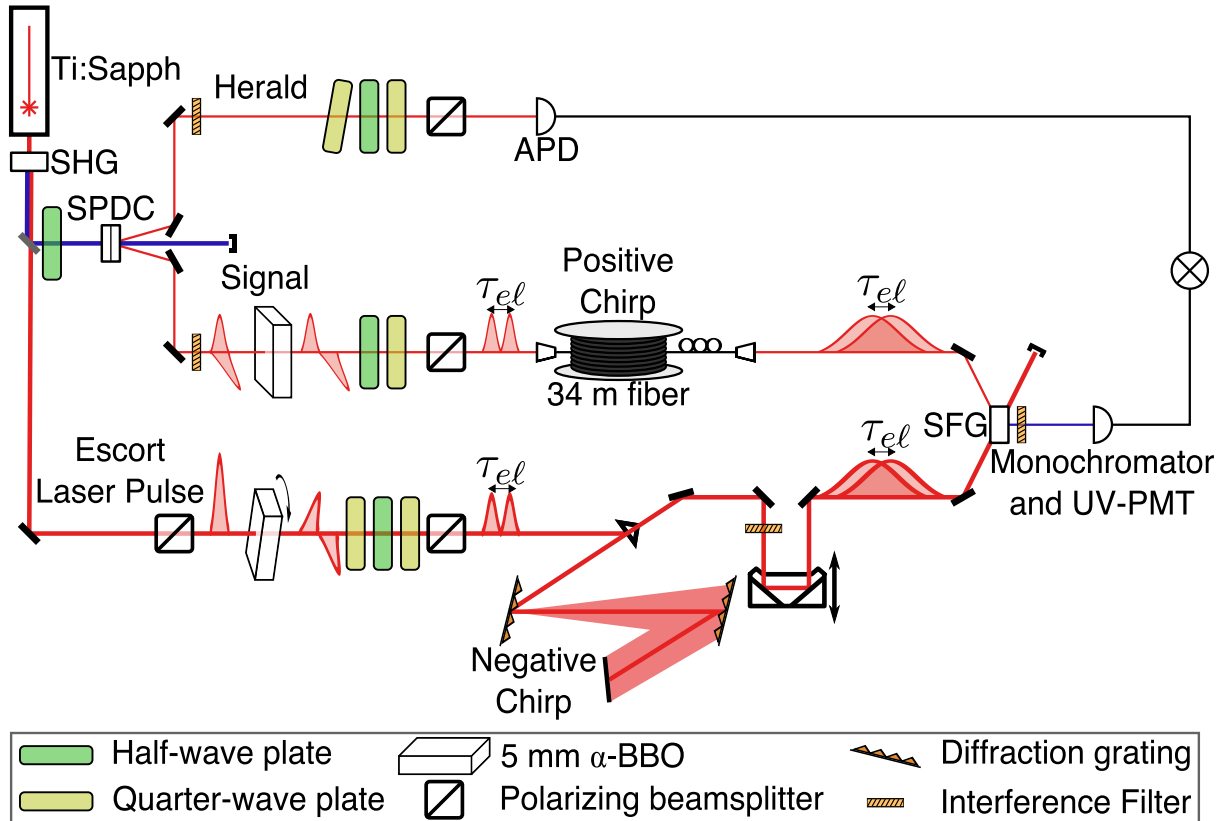
Figure 4.2: **Experimental setup.** Polarization-entangled photon pairs (signal and herald) are generated via down-conversion (SPDC) in orthogonally oriented nonlinear crystals (extra crystals used for compensation not shown). The signal photon is converted to a time-bin qubit using a birefringent crystal (5-mm α-BBO) and polarizer. The signal acquires a positive chirp in 34 m of optical fiber. The strong laser pulse is prepared using an identical birefringent crystal and a series of waveplates to set the phase, then negatively chirped using gratings. The photon and laser pulse are combined in a nonlinear crystal to produce SFG. The middle frequency is detected using a photon counter after a monochromator.

fundamental through another 5-mm α-BBO crystal, where rotation about the beam axis controls α, the relative weighting of early and late components. We can control the phase β between the components through the rotation of a half-wave plate between two quarter-wave plates set to 0°. Polarization information is then removed using another polarizing beam-splitter. The phase β is four times the half-wave plate angle, with an offset due to the birefringence in the system. This sequence simplifies projections onto the standard states: $|e\rangle$, $|\ell\rangle$, and $\frac{1}{\sqrt{2}}(|e\rangle + e^{i\phi}|\ell\rangle)$ with $\phi = \{-\pi/2, 0, \pi/2, \pi\}$. To extend to arbitrary projections, the rotatable α-BBO may be replaced by a rotatable half-wave plate and an α-BBO set at 45 degrees.

The positive chirp of $A = (670 \pm 1) \times 10^3$ fs^2 is applied to the single photons by passing through 34 m of single-mode fiber. The opposite chirp on the strong laser pulse is applied using gratings [155]. The strong laser beam is then filtered to 785.7 nm with a bandwidth of 11.9±0.3 nm and passed through a delay line, with average power 146 mW output. The two pulses are focused on a 1-mm BiBO crystal phase-matched for type-I SFG, producing a UV signal detected by photon counter (UV-PMT, Hamamatsu H10682-210).

The resulting signal is sent to a fiber-coupled spectrometer (Princeton Instruments Acton Advanced SP2750A), which we use as either a monochromator for photon counting or a full spectrometer. With β set to 0, the upconverted signal spectrum, averaged over five 90 minute runs, is seen in Fig. 4.3 and exhibits three distinct peaks. The middle peak, centered at 399.82 nm, has a bandwidth of 0.043±0.002 nm. This in reasonable agreement with the prediction of 0.035±0.002 nm from the expected bandwidth corrected for our 0.03-nm spectrometer resolution [161]. The side peaks are centered at 399.68 nm and 399.96 nm. The average separation from the main peak $\Delta\lambda_{exp}$=0.138±0.003 nm agrees with the prediction $\Delta\lambda_{th}$=0.137±0.002 nm calculated from the measured chirp and α-BBO birefringence. The separation is sufficiently large compared to the linewidth, enabling effective filtering of the side peaks with a monochromator window of 0.11 nm.
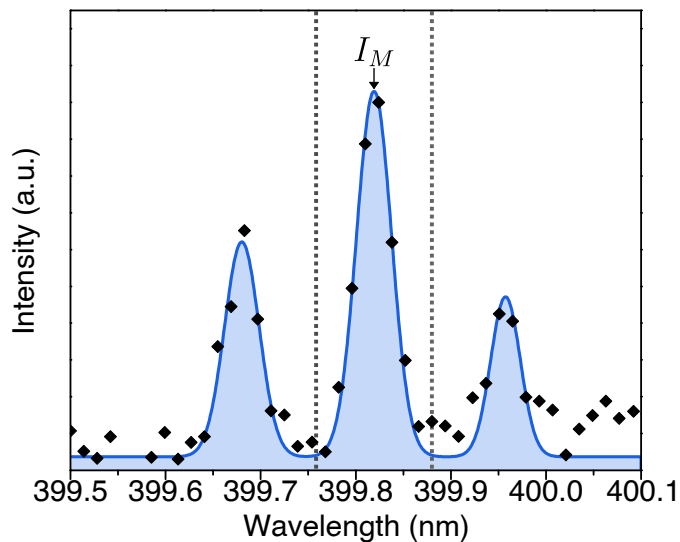
Figure 4.3: **Sum-frequency spectrum.** The upconverted signal spectrum (background subtracted) taken using our spectrometer, with β set to 0. A fit to the data is shown in blue. The monochromator selected those wavelengths that fall between the dotted lines.

4.2.2 Hybrid polarization/time-bin state characterization

Nonlocal interference fringes and Bell inequality violation

For an entangled state of the form $|\tilde{\Phi}^+\rangle = \frac{1}{\sqrt{2}}(|He\rangle + |V\ell\rangle)$, we take separable measurements on bases unbiased from the H/V and e/ℓ bases, written in the form

$$|M_1(\gamma)\rangle \otimes |M_2(\beta)\rangle = \frac{1}{\sqrt{2}}(|H\rangle + e^{i\gamma}|V\rangle) \otimes \frac{1}{\sqrt{2}}(|e\rangle + e^{i\beta}|\ell\rangle). \tag{4.21}$$

In doing so, we expect to see a coincidence rate proportional to

$$|(\langle M_1(\gamma)| \otimes \langle M_2(\beta)|)|\tilde{\Phi}^+\rangle|^2 = \frac{1}{2}\cos^2\frac{\gamma+\beta}{2}, \tag{4.22}$$

which can vary between 0 and $\frac{1}{2}$ as the phases β and γ are altered. If we instead look at only half of the two-qubit system, we find the single-event rate for each side to be

146
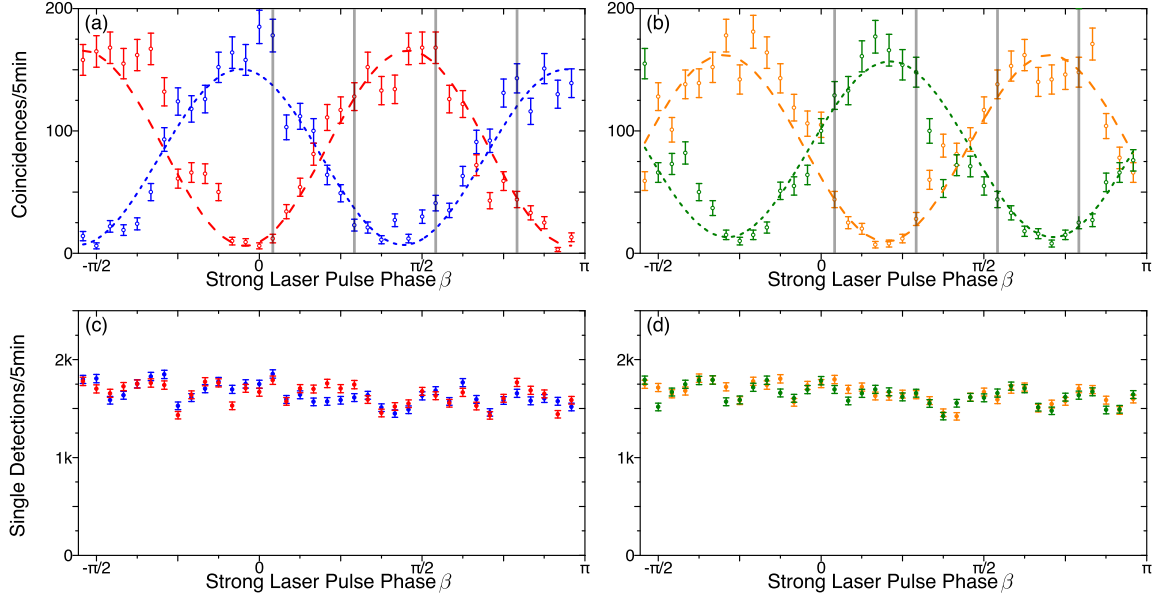
Figure 4.4: **Coincidence counts versus β.** The herald is projected into the diagonal basis in (a) ($|D\rangle$ in blue and $|A\rangle$ in red) and the circular basis in (b) ($|L\rangle$ in orange and $|R\rangle$ in green). The CHSH-Bell inequality was violated using the data points indicated by the grey lines with a value S=2.54±0.08. The corresponding single-detection events in the upconverted arm are shown in (c) and (d), and exhibit no obvious phase dependence.

proportional to

$$\langle M_1(\gamma)|\mathrm{Tr}_2[|\tilde{\Phi}^+\rangle\langle\tilde{\Phi}^+|]|M_1(\gamma)\rangle = \langle M_2(\beta)|\mathrm{Tr}_1[|\tilde{\Phi}^+\rangle\langle\tilde{\Phi}^+|]|M_2(\beta)\rangle = \frac{1}{2}. \qquad (4.23)$$

Thus, when the phases are varied, we expect oscillations in the coincidence rate but a stable rate of single-event detections [256].

Fig. 4.4 shows the coincidence rate (Fig. 4.4(a-b)) and single-event rate (Fig. 4.4(c-d)) of the time-bin state detections as the phase β is varied for four different herald projections γ, with an integration time of 5 min per data point. In Fig. 4.4a and Fig. 4.4c, γ is set to 0 (diagonal polarization $|D\rangle$) for the blue curve and π (anti-diagonal polarization $|A\rangle$) for the red curve. In Fig. 4.4b and Fig. 4.4d, γ is set to $\frac{\pi}{2}$ (left-circular polarization $|L\rangle$) for the orange curve and $\frac{3\pi}{2}$ (right-circular polarization $|R\rangle$) for the green curve. The four

147

coincidence curves have visibilities (without background subtraction) of $91 \pm 3\%$, $93 \pm 3\%$, $89 \pm 4\%$, and $84 \pm 4\%$ for $|D\rangle$, $|A\rangle$, $|L\rangle$, and $|R\rangle$ respectively, for an average visibility of $89.3 \pm 1.7\%$. The single-detection events are nearly constant. This shows a non-local form of interference only visible when the entire system is measured, demonstrating the fidelity of phase measurement. No active phase stabilization was implemented over the experimental run time (12 hours).

The coincidences oscillate sinusoidally with an average visibility among the four curves of $89.3\pm1.7\%$. A subset of this data, for phases indicated by vertical lines in Fig. 4.4(a-b), are sufficient to test the CHSH-Bell inequality [81, 82], written as

$$S = E(a,b) + E(a,b') + E(a',b) - E(a',b') \leq 2 \qquad (4.24)$$

where $E(a,b)$ is the correlation and $\{a, a', b, b'\}$ are measurement settings. This inequality holds for local hidden-variable models but can be violated by entangled quantum states (see Sec. 1.3.3). We measure polarization states of the form $\frac{1}{\sqrt{2}}(|H\rangle \pm e^{i\xi}|V\rangle)$ and time-bin states of the form $\frac{1}{\sqrt{2}}(|e\rangle \pm e^{i\zeta}|\ell\rangle)$, where the "+" and "−" outcomes are assigned values +1 and -1, respectively. Choosing $\xi_a=0$, $\xi_{a'}=\frac{\pi}{4}$, $\zeta_b=0.066\pi$, and $\zeta_{b'}=0.316\pi$, the CHSH-Bell parameter was found to be $S=2.54\pm0.08$, corresponding to a violation of the inequality by 6.8 standard deviations.

Quantum state reconstruction

We next apply our technique to measure the time-bin state of our signal photon. First, using the entanglement between the time-bin state of the signal photon and the polarization state of the idler, we look at the different spectral peaks while projecting the herald onto a specific preparation, effectively preparing the time-bin state remotely [265]. We fixed the phase of the escort laser pulse to $\beta = 0$ with equal weight in each escort bin ($\alpha = \pi/4$) and used the monochromator to select frequencies corresponding to the peaks in Fig. 4.3. We measured the coincidence counts between the herald for polarization measurements $\{H, V, D, A, R, L\}$ and the UV-PMT when the monochromator was centered on each peak.

The coincidence counts for each setting and bin are shown in Fig. 4.5. As the polarization-
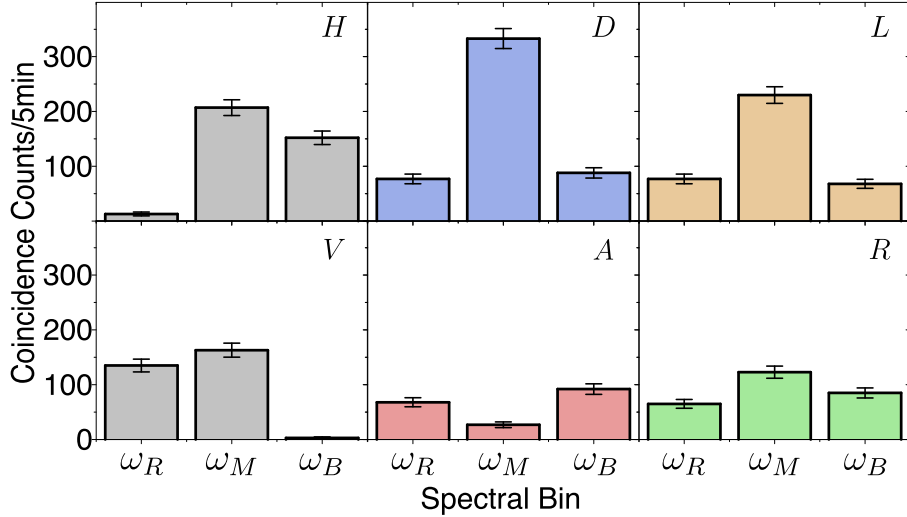
Figure 4.5: **Binned spectral dependence on polarization.** Coincidence counts between the herald and the SFG photon in each peak from Fig. 3, for $\beta=0$ and the indicated polarization measurement of the herald.

to-time-bin translation mapped horizontal polarization to the early time bin, projecting the herald photon onto horizontal polarization projects the signal photon to the early time bin. The middle and blue-shifted bins are both populated in this case, consistent with the early photon meeting the early and late escort pulse, respectively. The opposite is true for projecting the herald to vertical polarization, which projects the photon to the late time bin. The slight difference between the population of the middle bin and the side bins can be attributed to phasematching, which is optimized for upconversion to the middle bin. When projecting the herald onto a polarization on the XY plane of the Bloch sphere, all three bins are populated, and the intensity in the middle spectral bin depends on the phase between H and V in the herald projection. The contrast in the middle bin intensity between projecting the herald onto diagonal or anti-diagonal is more than 12:1.

Continuing this approach for different settings of α and β, we performed two-qubit tomography on our time-bin/polarization state using an overcomplete set of 36 measurements [262] and iterative maximum-likelihood reconstruction [44]; see Sec. 1.2.1 for details. The initial polarization state was measured with an integration time of 5 s per setting

and tomography on the initial polarization state, shown in Fig. 4.6a, yielded a fidelity of $94.01 \pm 0.02\%$ with the Bell state $|\Phi^+\rangle$. The purity of this density matrix, defined as $\mathrm{Tr}\rho^2$, was found to be 0.9129 ± 0.0004. We determined errors on our fidelities and purities using Monte Carlo techniques with 400 iterations and assuming Poissonian error.

Fig. 4.6b shows the reconstructed density matrix of the polarization state after the α-BBO was inserted. This density matrix has a fidelity of $96.83 \pm 0.02\%$ with the classically-correlated state $(|HH\rangle\langle HH| + |VV\rangle\langle VV|)/2$ and a purity of 0.4811 ± 0.0002. The entanglement in the system is no longer noticeable through polarization measurements as the time delay has separated horizontal and vertical components to outside of their coherence length.

The polarization/time-bin state was detected at a rate of 1 Hz after upconversion and spectral filtering, necessitating an integration time of fifteen minutes per setting. To wash out any time-dependent drifts, the measurements were performed in three loops, each with an integration time of 300 s per measurement setting. The fidelity of the reconstructed output state, seen in Fig. 4.6c, with the state $|\tilde{\Phi}^+\rangle$ was found to be $89.4 \pm 0.7\%$, and the fidelity with the reconstructed density matrix of the initial polarization state was found to be $95.0 \pm 0.8\%$. It's purity was 0.818 ± 0.013. Thus, our chirped-pulse upconversion technique was able to retrieve the correlations through quantum state tomography with high fidelity.

Conclusion

We have demonstrated ultrafast time-bin measurements using chirped-pulse upconversion as a coherent time-to-frequency interface. We showed the control necessary to perform quantum state tomography on time-bin entangled states and sufficiently high fidelity to convincingly violate the CHSH Bell inequality. This technique operates at the fundamental limit for time-bin states where the coherence time of the light, not the time resolution of the detector, constrains the bin separation. Future work will focus on improving the efficiency of our scheme. With the use of periodically-poled materials, nearly perfect single-photon upconversion efficiency has been achieved [226, 228]; combining such materials with cavities
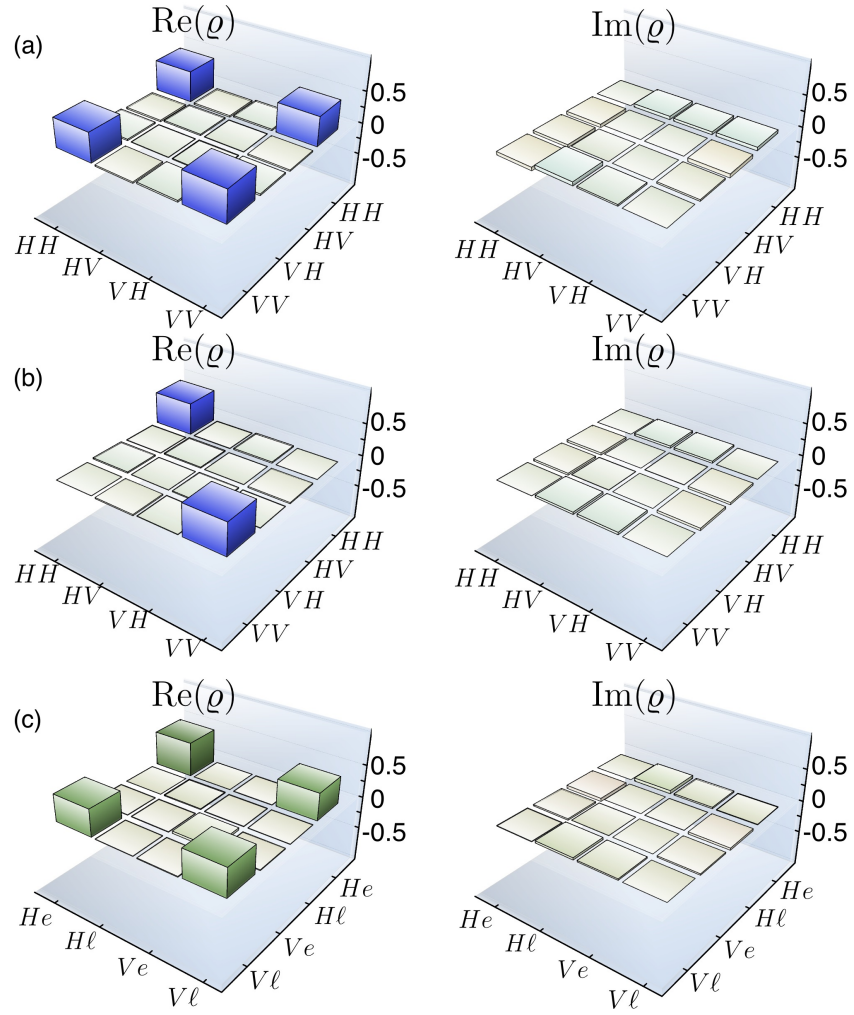
Figure 4.6: **Hybrid polarization/time-bin state reconstruction.** (a) Tomography of the initial two-qubit polarization state. b) Tomography of the polarization state after the α-BBO crystal has been inserted. (c) Tomography on the polarization/time-bin state using chirped-pulse upconversion to implement measurements, retrieving the correlations of the initial state.

has been shown to significantly improve efficiencies for weak fields or biphotons [266]. High-transmission filters [267] or restrictive phase-matching conditions may be used to increase the filtering efficiency. At higher efficiencies, this scheme may be extended to time-bin qudits, increasing the information density of time-bin encodings.

Chapter 5

Ultrafast time-division demultiplexing of polarization entangled states

Notes and acknowledgements

The content of this chapter was published on 2014 October 16 as [217]:

J. M. Donohue, J. Lavoie, and K. J. Resch. Ultrafast time-division demultiplexing of polarization-entangled photons. *Physical Review Letters* **113**, 163602 (2014)

Author Contributions

Kevin Resch and **Jonathan Lavoie** conceived of the study.

Jonathan Lavoie built the initial photon source and pulse compressor.

John Donohue built the upconversion setup, carried out the experiment, analyzed the data, and wrote the first draft of the manuscript.

All authors contributed to the final version.

Chapter Overview

Quantum communication promises unconditionally secure information transmission by exploiting fundamental features of quantum mechanics [4]. For many protocols, transmission channels capable of distributing entanglement between distant parties are required [268, 269, 270]. Furthermore, to be practical, these protocols must allow communication at high rates. One strategy which has successfully increased transmission rates in classical telecommunication is multiplexing, where ancillary degrees of freedom are utilized to carry independent modes co-propagating through a single physical link, such as an optical fibre [271, 272]. Some of these techniques have been adapted to quantum scenarios [273, 274, 275, 276, 277, 278, 216, 279] and lay the groundwork for future quantum communication networks.

Time-division multiplexing [272] uses the arrival time of light pulses relative to an external clock to distinguish multiple communication modes. It is compatible with fibre-optic systems and is robust against birefringent effects. The delay between subsequent pulses must be greater than the timing jitter of the detection system to avoid cross-talk between signals; for high rates, the delay must also be greater than detector dead time to detect photons from subsequent pulses. State-of-the-art single photon counting detectors have demonstrated 30 ps timing jitter and nanosecond-scale dead times [16]. However, it is possible in principle to distinguish between two pulses as long as they are separated by their coherence time, which can be orders of magnitude smaller in ultrafast applications. Single-photon measurement techniques for these timescales are therefore critical to optimize the quantum information capacity.

Techniques incorporating short laser pulses and nonlinear optical effects are key to manipulating light on ultrafast timescales [132, 122, 140, 280]. In the quantum regime, such methods have enabled single- and entangled-photon frequency conversion [281, 282, 283, 52, 284], all-optical routing of quantum information [285, 146], and ultrafast coincidence measurement for biphotons [232, 286, 287]. Additionally, ultrafast pulse shaping provides a diverse set of tools to tailor nonlinear optical interactions for customizing quantum optical waveforms [224, 58, 288, 161, 289], having found application in realizing coherent time-bin measurements on the picosecond timescale [68].
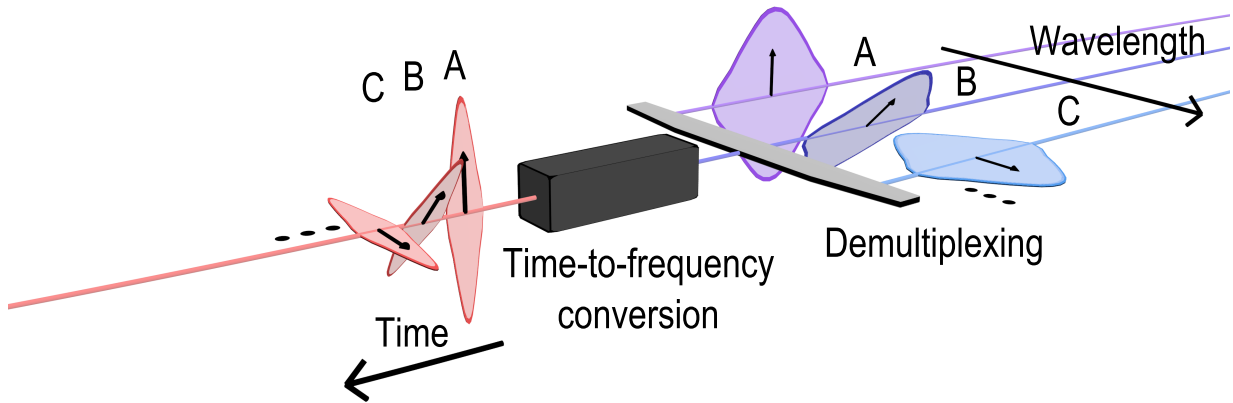
Figure 5.1: **Time-to-frequency conversion concept.** A train of temporally narrow polarized photonic signals A-C are converted into a comb of spectrally narrow and correspondingly polarized photons with a central frequency dependent on their time of arrival. The different frequency modes may then be demultiplexed using diffraction techniques.

Drawing from these techniques, here we show a method for demultiplexing a rapidly pulsed sequence of polarization-encoded quantum states (Fig. 5.1). Any attempt to directly measure the polarization state of an individual pulse with a photon counter will be subject to crosstalk from the other pulses due to the limited detector time resolution, appearing as an incoherent mixture of the different states. We employ polarization-maintaining sum-frequency generation (SFG) with chirped pulses as a time-to-frequency converter to map ultrafast-scale time delays to measurable frequency shifts, thus allowing the individual quantum states to be read out using conventional diffraction techniques and photon detectors. Furthermore, our method manipulates the time-frequency characteristics of polarization-entangled photons, compressing their spectral bandwidth while preserving entanglement.

5.1   Concept and theory

Our approach is once again based on sum-frequency generation between chirped single photons and an oppositely chirped escort laser pulse. As shown in Sec. 3.5, this process

will drastically narrow the bandwidth of the photons, and the central frequency will depend on the relative time delay between the photons and the escort. If there are multiple input photon modes separated in time[1], those shifts in time will translate to shifts in frequency in the upconverted beam. These narrow frequency peaks can be separated using standard spectroscopic methods, rather than the ultrafast gating required for separating temporal peaks. In this section, we show mathematically how this process applies to polarization-entangled photons from an SPDC source.

To begin, we treat the pump for the initial SPDC process as having an electric field frequency representation of

$$E_p(\omega_p) \propto \sum_j \sqrt{b_j} \xi(\omega_p) e^{i\omega_p \tau_j} \left(\cos \frac{\theta_j}{2} + e^{i\phi_j} \sin \frac{\theta_j}{2} \right), \tag{5.1}$$

which defines a train of pulses each with an identical spectral intensity $|\xi(\omega_p)|^2$ with individual time delays τ_j, intensity weights b_j, and pure polarization states defined by θ_j and ϕ_j as per Eq. 1.44. Plugging this spectral representation into the SPDC evolution unitary of Eq. 3.26 (ignoring spatial dependencies) and assuming type-I phasematching, we find the first-order renormalized SPDC state to be

$$|\psi_i\rangle = \sum_j \sqrt{b_j} \iint \mathrm{d}\omega_s \omega_h \, e^{i(\omega_s + \omega_h)\tau_j} \xi(\omega_s + \omega_h) \Phi(\omega_s, \omega_h, \omega_s + \omega_h)$$
$$\times \left(\cos \frac{\theta_j}{2} |H, \omega_s\rangle_s |H, \omega_h\rangle_h + e^{i\phi_j} \sin \frac{\theta_j}{2} |V, \omega_s\rangle_s |V, \omega_h\rangle_h \right), \tag{5.2}$$

where the kets define polarization, spatial mode, and frequency, e.g. $|H, \omega\rangle_i = \hat{a}_{i,H,\omega}|0\rangle$. We then apply filters to the SPDC photons which we assume to be narrow relative to the pump field, such that we can write the SPDC state as spectrally separable with spectral amplitude functions $F_s(\omega_s)$ and $F_h(\omega_h)$.

We next subject the signal mode to polarization-maintaining sum-frequency generation, which can be thought of as two distinct sum-frequency processes (one for each polarization) which are otherwise indistinguishable [284]. We assume that phasematching in the SFG

---

[1]Note that the "modes" we refer to in this chapter are time bin modes, as opposed to the temporally overlapping modes of, for example, Ref. [63].
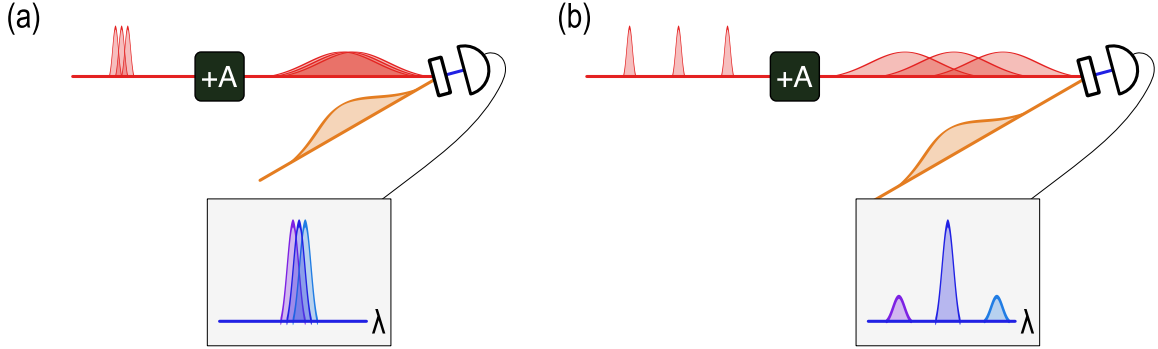
Figure 5.2: **Bounds on the time separations for TDM-to-WDM conversion.** (a) A train of temporally multiplexed modes must be separated by greater than their coherence length to be distinguishable, and if they are not, they will remain equally indistinguishable when converted to frequency bins, as seen on the spectrometer cartoon. (b) If the temporally multiplexed modes are separated by a time longer than the chirped duration of the pulses, the different bins will not upconvert with comparable efficiencies.

crystal is uniform ($\Phi \approx 1$), an approximation that holds well for equally-and-oppositely chirped in a type-I medium, and denote the spectral amplitude of the escort as $G(\omega_e)$. Per Sec. 3.3, to first order this process transforms the spectral amplitude of *each individual mode* to

$$F_{3,j}(\omega_3) = \int d\omega_s \, F_s(\omega_s) e^{i\omega_s \tau_j} G(\omega_3 - \omega_s), \tag{5.3}$$

and the final state will be

$$|\psi_f\rangle = \sum_j \sqrt{b_j} \iint d\omega_h d\omega_3 \, F_h(\omega_h) e^{i\omega_h \tau_h} F_{3,j}(\omega_3) \left(\cos\frac{\theta_j}{2} |H, \omega_3\rangle_3 |H, \omega_h\rangle_h + e^{i\phi_j} \sin\frac{\theta_j}{2} |V, \omega_3\rangle_3 |V, \omega_h\rangle_h \right). \tag{5.4}$$

If the signal photon and the strong escort pulse both have Gaussian spectra and are

oppositely chirped, their spectral amplitudes may be described (ignoring phase) as

$$F_s(\omega_s) = \frac{1}{(2\pi\sigma_s^2)^{\frac{1}{4}}} e^{-\frac{(\omega_s-\omega_{0s})^2}{4\sigma_s^2}} e^{iA(\omega_s-\omega_{0s})^2} \tag{5.5}$$

$$G(\omega_e) = \frac{1}{(2\pi\sigma_e^2)^{\frac{1}{4}}} e^{-\frac{(\omega_e-\omega_{0e})^2}{4\sigma_e^2}} e^{-iA(\omega_e-\omega_{0e})^2}, \tag{5.6}$$

and the spectrum of the upconverted photon may be written as

$$|F_{3,j}(\omega_3)|^2 \propto e^{-\frac{1+16A^2\sigma_e^2\sigma_s^2}{2(\sigma_e^2+\sigma_s^2)}\left(\omega_3-\omega_{03}+\frac{8A\sigma_s^2\sigma_e^2}{1+16A^2\sigma_e^2\sigma_s^2}\tau_j\right)^2} e^{-\frac{2\sigma_e^2\sigma_s^2}{(\sigma_e^2+\sigma_s^2)(1+16A^2\sigma_e^2\sigma_s^2)}\tau_j^2}$$

$$\overset{LCL}{\approx} e^{-\frac{8A^2\sigma_e^2\sigma_s^2}{\sigma_e^2+\sigma_s^2}\left(\omega_3-\omega_{03}+\frac{\tau_j}{2A}\right)^2} e^{-\frac{2\tau_j^2}{(\sigma_e^2+\sigma_s^2)(16A^2)}}, \tag{5.7}$$

where $\omega_{03} = \omega_{0e} + \omega_{0s}$ and the approximation takes the large chirp limit, $A\sigma_i^2 \gg 1$. Note that, in this large-chirp approximation, the RMS intensity bandwidth of each spectral component is

$$\sigma_g \approx \frac{1}{4A}\sqrt{\frac{1}{\sigma_e^2} + \frac{1}{\sigma_s^2}}. \tag{5.8}$$

Each component is also shifted in central frequency by $\Delta\omega \approx \tau_j/2A$ and has an exponential decay factor proportional to τ_j^2.

If we exactly measure a frequency $\omega_{03} - \tau_m/2A$, the signal due to an input delayed by τ_j will be proportional to

$$\left|F_{3,j}\left(\omega_{03} - \frac{\tau_m}{2A}\right)\right|^2 \propto \exp\left[-\frac{2\sigma_e^2\sigma_s^2}{\sigma_e^2+\sigma_s^2}(\tau_j-\tau_m)^2 - \frac{\tau_j^2}{8A^2(\sigma_e^2+\sigma_s^2)}\right]. \tag{5.9}$$

To ensure that the crosstalk from neighbouring modes is negligible (i.e. $\left|F_{3,j}\left(\omega_{03} - \frac{\tau_m}{2A}\right)\right|^2 \approx 0$ for $j \neq m$), we define $\Delta\tau_{min}$ as the separation between any directly adjacent temporal modes and require that

$$\Delta\tau_{min} > 2\frac{1}{\sqrt{2}}\frac{\sqrt{\sigma_e^2+\sigma_s^2}}{\sigma_e\sigma_s} \tag{5.10}$$

is satisfied, which is equivalent to requiring that the separation is greater than Fourier-

limited temporal width of the input pulses. We also define $\Delta\tau_{max}$ as the maximum temporal separation of any individual temporal mode and the escort pulse. To ensure comparable efficiencies for each temporal mode, we require that the chirped fields overlap well, i.e. the time between the first and last time bin is less than the chirped length of the pulse,

$$\Delta\tau_{max} < 2\sqrt{2}|A|\sqrt{\sigma_e^2 + \sigma_s^2}. \tag{5.11}$$

These upper and lower bounds on the delay between modes are illustrated in Fig. 5.2.

5.2 Experimental setup

In this section, we present an overview of the experiment setup, show in Fig. 5.3. We provide details on the polarization-maintaining sum-frequency generation in Sec. 5.2.1.

Our experiment uses a titanium-sapphire laser with a repetition rate of 80 MHz, centre wavelength 790.1 ± 0.2 nm, bandwidth (FWHM) of 12.27 ± 0.08 nm, and average power of 2.3 W. It was frequency-doubled in 2 mm of BiBO cut at $152.4°$ to a second-harmonic centred at 394.7 nm with a bandwidth of 1.45 ± 0.02 nm and an average power of 0.6 W. Down-conversion is produced in a pair of orthogonally oriented 1-mm BBO crystals cut at $30°$ for type-I down-conversion [105, 109], where the signal and herald are separated by a noncollinear geometry with an opening angle of approximately $6°$. In order to compensate for the effects of temporal and spatial walkoff, additional birefringent crystals were required: 1 mm of α-BBO and 1 mm of crystal quartz were inserted in the path of the UV pump to correct for temporal walkoff [109] and 1 mm of BiBO cut at an angle of $152.6°$ was inserted in the signal arm to correct for spatial walkoff[2]. To remove energy-time entanglement, the signal was filtered to 809.06 nm with a bandwidth of 3.9 nm (approximately 1.8 THz) and the herald to 770.58 nm with a bandwidth of 2.27 nm. A quarter-wave plate at zero degrees was tilted to apply a controllable phase to the herald, aligned such that the state $|\Phi^+\rangle = \frac{1}{\sqrt{2}}(|HH\rangle + |VV\rangle)$ was detected between D_h and the detector before upconversion, D_{in}.

---

[2]The angle the BiBO was cut at was chosen such that it adjusts spatial walkoff while not imparting any additional temporal walkoff.
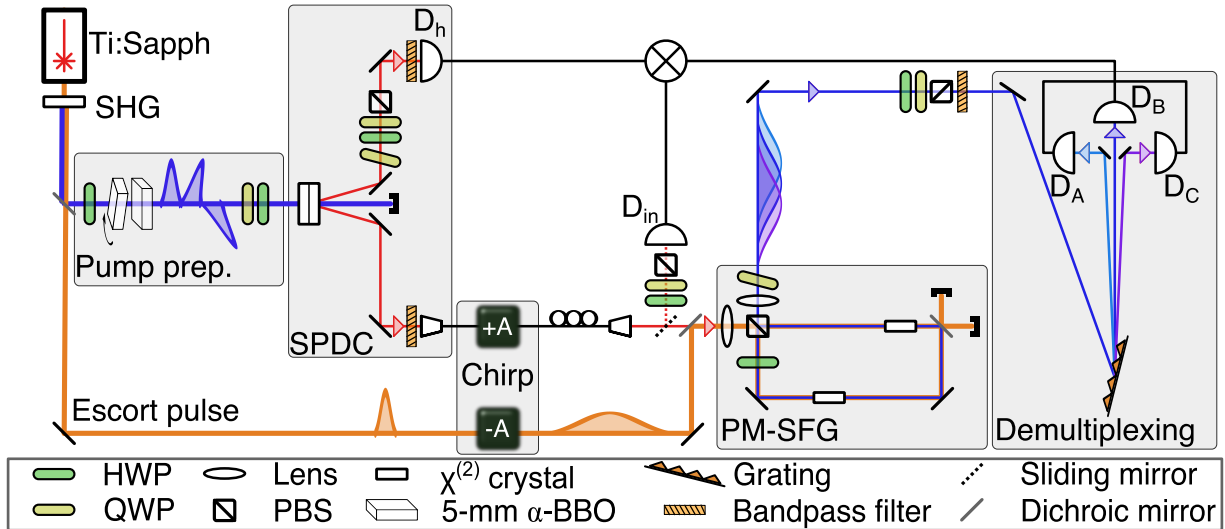
Figure 5.3: **Time-to-frequency demultiplexing experimental setup.** Two α-BBO crystals and a series of wave plates prepared a train of pump pulses 2.69 ps apart, which were then used to create a pulse sequence of polarization-entangled states through SPDC. The single photons were chirped in single-mode fibre and combined with an anti-chirped strong escort pulse using a dichroic mirror. This beam was then focused in two 10-mm BiBO crystals arranged in a Sagnac configuration for polarization-maintaining sum-frequency generation (PM-SFG). The polarizations of the output photons were measured, and the three signals were then separated with a diffraction grating and coupled to detectors D_{A-C}. A removable mirror to D_{in} enabled measurement of the input state.

To create a dense train of pulsed photon pairs, we pass the pump through a series of rotatable birefringent crystals. As the pump exits each crystal, the component polarized along the fast axis will lead the one polarized along the slow axis. If the temporal walkoff between these components is greater than the coherence time of the pump, the pump will exit as two pulses which are distinguishable in arrival time relative to a reference from the ultrafast laser source. Using n crystals of identical birefringence, a train of $n+1$ pulses may be created; if the crystal lengths differ, it is possible to create up to 2^n pulses [290].

The SPDC crystal is aligned such that one crystal downconverts a horizontal pump to a vertical photon pair, and the other does the opposite, such that a pump prepared in the

160

state $\alpha|H\rangle + \beta|V\rangle$ downconverts to the state $\beta|HH\rangle + \alpha|VV\rangle$. As seen in Fig. 5.4, the initially horizontal pump passes through two 5-mm α-BBO crystals to create up to three temporally distinct down-conversion signals, which each introduce a birefringent delay of (2.69 ± 0.17) ps between pulse components polarized along the fast and slow axes. This prepared pump creates a train of pulsed down-conversion, where the polarization state of each pair is determined by the polarization of the corresponding pump pulse. As the first and last pulse of the train are necessarily polarized on opposite axes in the last crystal, they are necessarily orthogonally polarized. Therefore, if the first pump pulse consists of photons described by the polarization state $|\psi\rangle$, the last pulse must be described by the orthogonal state, $|\psi^\perp\rangle$. In a three-pulse preparation, there are also restrictions on the middle state. To create three pulses with two identical birefringent crystals, two orthogonal pulses must be created in the first crystal. The second crystal will once again split each pulse in two, and the component of the leading pulse on the slow axis of the crystal will overlap in time with the component of the lagging pulse on the fast crystal axis. As these two components were on different axes, they are necessarily orthogonal. In the case where the leading and lagging pulses are of equal amplitude, the middle pulse will be in some polarization state describable as $\frac{1}{\sqrt{2}}\left(|\psi\rangle + e^{i\phi}|\psi^\perp\rangle\right)$ and have twice the photon number of the other modes. The parameter ϕ may be manipulated by controlling the pump polarization with waveplates QWP-1 and HWP-2.

The signal photons are then coupled into 34 m of single-mode fibre, applying positive dispersion corresponding to a chirp parameter of $A = (696 \pm 3) \times 10^3$ fs^2. Using a grating-based compressor [155], matched negative dispersion is applied to a 225 mW escort pulse at 786.2 nm with a 6.3 nm bandwidth (FWHM). The escort was filtered to a narrower bandwidth than the fundamental of the Ti:Sapph to reduce UV background due to its second harmonic in the SFG process. The signal photons and escort pulse are then combined into a single beam with a dichroic mirror for polarization-maintaining sum-frequency generation (PM-SFG), detailed in Sec. 5.2.1.

After polarization measurement, the remaining near-infrared and escort second harmonic were removed with a bandpass filter. The signals were then separated with a 3600-lines/mm diffraction grating in near-Littrow configuration and allowed to propagate for 4.3 m in free space before being coupled via multimode fibre into three separate detectors,
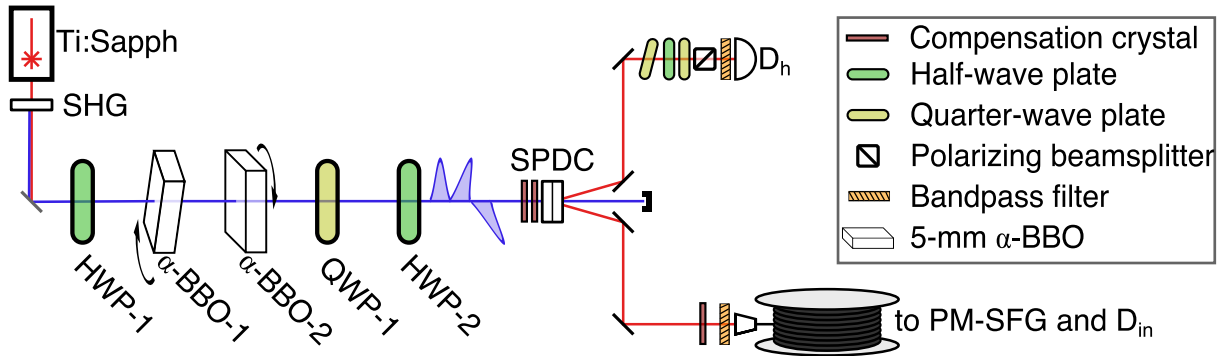
Figure 5.4: **Pump preparation and down-conversion.** Schematic of down-conversion setup and pump temporal preparation. α-BBO crystals are used to temporally separate polarization states of the pump, which are then controlled using a series of wave plates. Compensation crystals are used to correct for spatial and temporal walkoff.

D_{A-C}. The combined diffraction and coupling efficiency was measured to be approximately 13%. The measured single-photon spectra were found to have an average bandwidth of (0.047 ± 0.007) nm, or equivalently (88 ± 13) GHz, shown in Fig. 5.5. The spectra measured in modes A-C had respective central wavelengths of 398.936 nm, 399.099 nm, and 399.262 nm. This clearly shows that the three down-conversion pulses, 2.69 ps apart, were mapped to three distinct wavelengths separated by (0.163 ± 0.007) nm, or equivalently 307 GHz. This spacing is on the same order of magnitude as telecommunication standards for dense wavelength-division multiplexing [54].

Near-infrared detectors D_h and D_{in} were Perkin-Elmer SPCM-AQ4C photon counting modules, with a quantum efficiency of approximately 50% near 800 nm and a single-photon timing jitter of approximately 600 ps. Near-UV detectors D_{A-C} were Hamamatsu H10682-210 photon counting heads, with a quantum efficiency of approximately 30% around 400 nm and a single-photon timing jitter of approximately 200 ps.

As the downconversion process is random and unlikely to occur for any given pump pulse, we assume that whenever a demultiplexed photon is detected, the herald photon is part of the same pair. As the photons are generated at a rate of slightly less than 50,000 pairs per second with an 80 MHz pump repetition rate and a Klyshko efficiency of

162
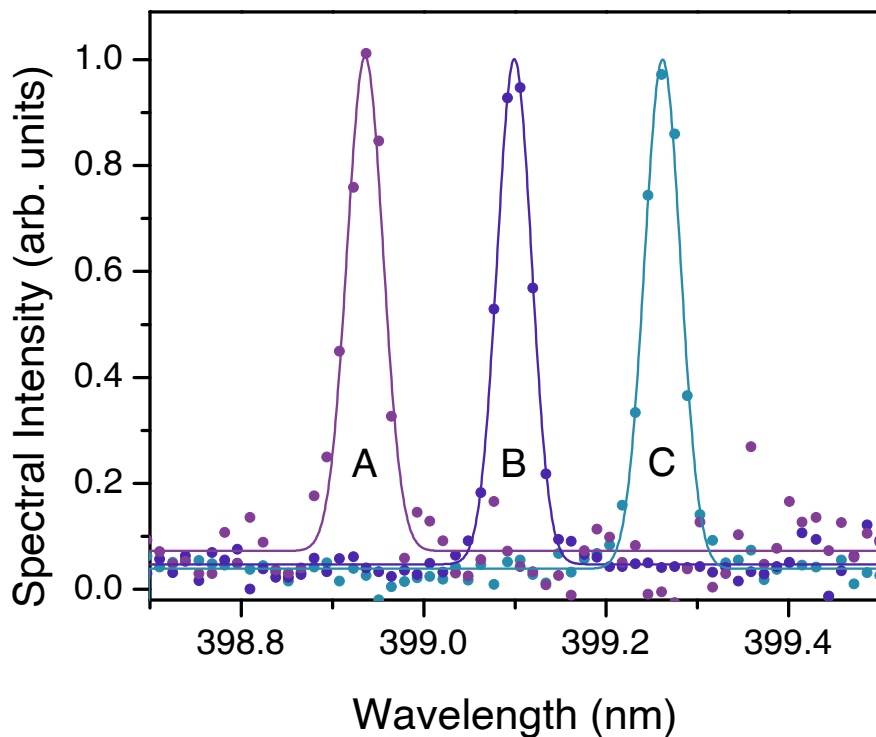
Figure 5.5: **Upconverted single-photon spectra for each temporal mode.** We prepared the pump to maximize the count rate in each of the three temporal modes and measured each background-subtracted spectra shown for four hours using the Acton SP-2750 spectrograph with a PIXIS 2048B CCD camera. The time delay between the modes maps each to a distinct central wavelength and the spectral bandwidth is compressed by a factor of 20 relative to the input.

approximately 12% in each arm, the probability of a pump pulse generating a pair in any channel is approximately 4%. If two temporal channels are pumped, in 2% of the cases where a photon pair is generated in one, a photon is also generated in the second, which will manifest as crosstalk in our measurements. For bright or deterministic sources, the herald photon would also need to be demultiplexed.
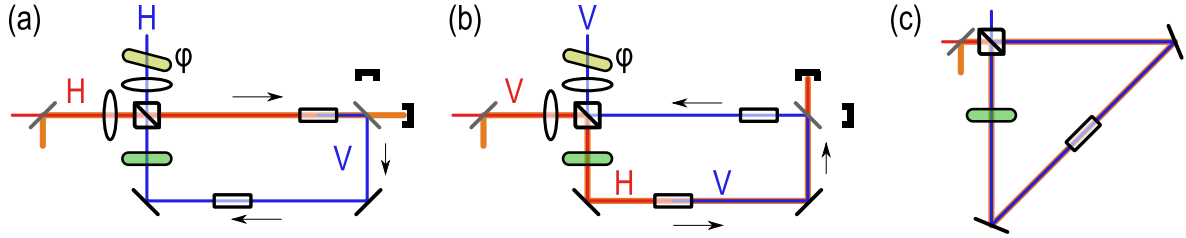
Figure 5.6: **Polarization-maintaining sum-frequency generation.** A folded Mach-Zehnder-esque design can be used to upconvert a signal pulse (red) with an escort pulse (orange) by dividing the upconversion processes for horizontal and vertical polarization into clockwise and counterclockwise paths, sketched in (a) and (b), respectively. The beam is focused to the first crystal in each path, and both crystals are aligned for type-I $H + H \rightarrow V$ SFG. The dichroic mirror in the top-right corner reflects blue light and transmits NIR, separating the majority of the escort beam inside the interferometer, while the half-wave plate (green) is set to rotate horizontal polarization to vertical. A quarter-wave plate (yellow) is used at the end to set the relative phase. Alternatively, in principle, polarization-maintaining SFG can be accomplished using sandwiched orthogonal crystals [105, 284] or a triangular Sagnac scheme, the latter of which is shown in (c), but the rectangular setup has the added advantage of being resilient against spatial walkoff.

5.2.1 Polarization-maintaining sum-frequency generation

In order to implement polarization-maintaining SFG, we use a rectangular folded Mach-Zehnder interferometer, as seen in Fig. 5.6a-b. In this configuration, the horizontally and vertically polarized components of the signal photon are split on a polarizing beamsplitter (PBS) and the vertical component is rotated to horizontal polarization using an achromatic half-wave plate. Each beam is then upconverted independently in 10 mm of BiBO cut at 150.9° for type-I SFG. The SFG signal continues inside the Sagnac loop while the remaining escort is removed using a dichroic mirror. The horizontal component is flipped on the same achromatic half-wave plate and the two components are coherently recombined on the input PBS. A tilted quarter-wave plate sets the phase of the upconverted signal, ensuring that coherent superpositions of $|H\rangle$ and $|V\rangle$ are also maintained. The internal SFG efficiency was estimated to be 0.3%. The Sagnac geometry enables passive phase stability, preserving
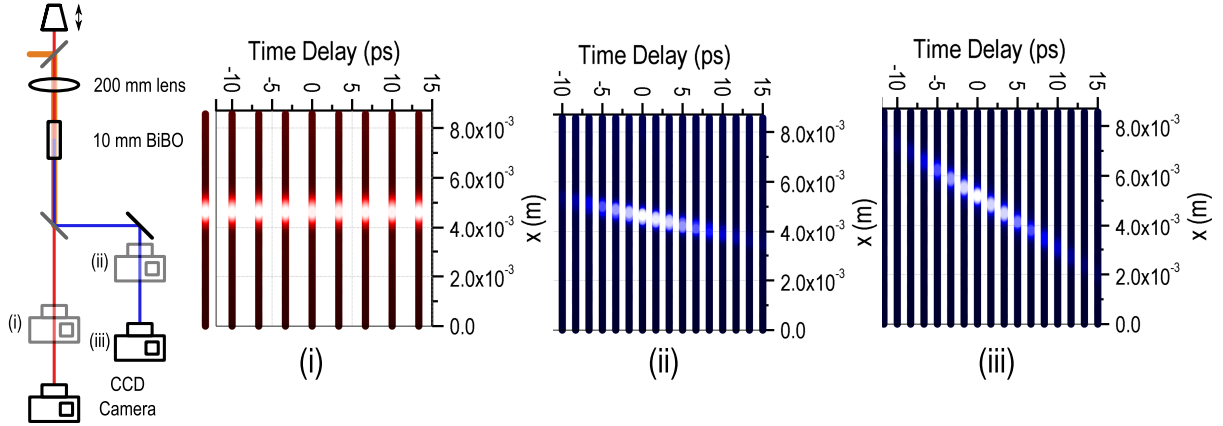
Figure 5.7: **Delay-dependent beam tilt measurement.** Chirped signal and escort pulses, set up identically to Fig. 5.3 before PM-SFG, are focused and combined in a 10-mm BiBO crystal. The remaining unconverted and the upconverted signal are separated with a dichroic mirror, and the beam profile is measured with a CMOS camera at various positions. NIR measurement point (i) is approximately 40 cm from the BiBO crystal, whereas UV measurement points (ii) and (iii) are approximately 25 and 65 cm away, respectively. The input signal can be delayed in time with a motorized translation stage, changing the upconverted central wavelength. The measured NIR beam profiles in (i) are, to the precision of the beam camera, independent of the delay, indicating that spatial shifts are not due to misalignment of the motorized translation. However, the beam profiles of the upconverted light in (ii) and (iii) depend strongly on the time delay, with shifts of approximately 0.07 $\frac{\text{mm}}{\text{ps}}$ and 0.21 $\frac{\text{mm}}{\text{ps}}$, respectively. The difference between the two measurement points indicates that the frequency-space coupling produces a tilt rather than a purely translational shift, as would be expected for walkoff.

the input polarization state through the sum-frequency process over the 32-hour runtime of the experiment.

In principle, PM-SFG can also be accomplished using any geometry which allows for a coherent superposition of two frequency conversion processes. This can be done, for example, in a traditional triangular Sagnac-type interferometer (Fig. 5.6c) or with two sandwiched orthogonal crystals. These alternatives, while involving fewer optical components, are complicated by the coupling between the spectral and spatial degrees of freedom

165
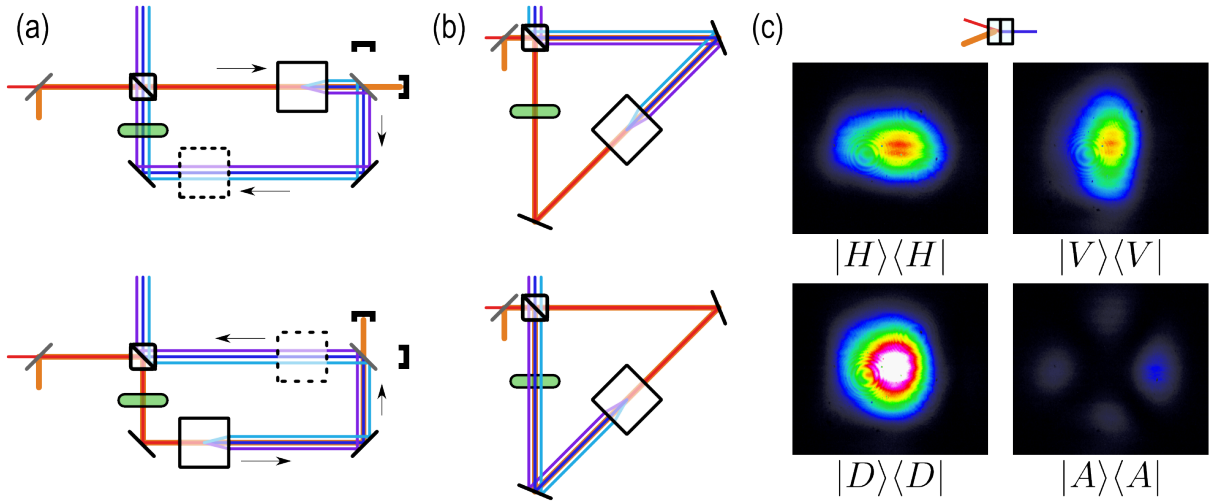
Figure 5.8: **Rectangular vs. triangular Sagnac for PM-SFG.** A rectangular Sagnac (a) is contrasted with a triangular setup (b) when spatial walkoff occurs between the three upconverted channels (cyan, blue, and purple). In the rectangular setup, the walkoff does not change the final result, with the channels ordered purple-blue-cyan at the output of both the clockwise and counter-clockwise processes. This is because both undergo the same number of reflections (three) after upconversion. However, in the triangular setup, the counter-clockwise path is reflected twice while the clockwise path is reflected only once, and the ordering of the channels is mirrored and the two paths cannot be made indistinguishable for all channels simultaneously. While, based on Fig. 5.7, we conclude that the discrepancy between channels is angular rather than spatial walkoff, the same intuition holds. (c) A pair of sandwiched crystals can also be used as a polarization-maintaining upconversion, but the upconverted beam from each profile will have different shapes due to phasematching. This is seen in the beam profiles taken by upconverting a diagonally polarized laser beam in two 1-mm BiBO crystals, where the horizontal spatial mode is an ellipse rotated 90 degrees relative to the vertical spatial mode. When projected to anti-diagonal polarization, a clover pattern is seen corresponding the area where the modes do not overlap. However, coupling into single-mode fibre can effectively extinguish these non-interfering portions at the expense of efficiency.

in SFG. To demonstrate this coupling, we set up the small experiment of Fig. 5.7 within the larger experimental setup of Fig. 5.3, which measured the spatial shift of the upconverted beam as a function of the relative delay between the chirped signal and escort (and thus

166

effectively as a function of the upconverted wavelength). We found that the angle at which the beam exits the crystal was a highly dependent on the wavelength of the upconversion, which we surmise is due to the tight phasematching of the material causing a coupling between frequency and transverse momenta, i.e. the $\Phi(\omega_1, \omega_2, \omega_3, \mathbf{k}_{T1}, \mathbf{k}_{T2}, \mathbf{k}_{T3})$ of Eq. 3.6. This frequency-dependent shift is larger than expected from purely walkoff as described in Sec. 3.2.3, which would also manifest as a spatial translation rather than an angular dependence. This effect also leads to a highly elliptical beam shape far from the focus, as only a narrow range of momenta are represented in the upconverted beam, and thus a cylindrical lenses are required to properly recollimate the beam after PM-SFG.

This frequency-dependent shift places strict geometry requirements on PM-SFG, particularly for the multiplexing application. As seen by contrasting Fig. 5.8a-b, in the rectangular scheme the three channels exit in the same spatial order whether travelling the clockwise or counter-clockwise path, whereas in the triangular scheme they are reversed because of an odd number of reflections in the interferometer. This makes it impossible to overlap all three modes simultaneously in the triangular scheme without an intricate realignment step post-upconversion. While the rectangular design overcomes these issues, it is still subject to a frequency-dependent phase due to slightly longer and shorter path lengths depending on process. In the sandwich upconverter, the two processes will result in ellipses with perpendicular major axes, which will have a limited area of overlap, as seen in Fig. 5.8c. While single-mode fibre can be used to couple solely the overlapping region, the two beams cannot be simultaneously coupled with high efficiency without a complicated polarization-dependent shaping step [291]. However, in both the rectangular and triangular setups, the upconversion crystal is aligned along the same axis for the same process (e.g. $H + H \rightarrow V$ in Fig. 5.6), and therefore the ellipses have the same shape.

5.3 Experimental results

To demonstrate the ability of our design, we prepare the pump in various ways to create eight different multiplexed states, as given by Table 5.1. Full measurement results for each of these preparations are displayed in Table 5.2, with the tangle and fidelity explicitly

	State			Angle			
	A	B	C	α-BBO-1	α-BBO-2	QWP-1	HWP-2
(i)	-	-	$|\Phi^{+1}\rangle$	0	0	$\pi/2$	$\pi/8$
(ii)	-	$|\Phi^{+1}\rangle$	-	$\pi/2$	0	$\pi/2$	$\pi/8$
(iii)	$|\Phi^{+1}\rangle$	-	-	$\pi/2$	$\pi/2$	$\pi/2$	$\pi/8$
(iv)	$|HH\rangle$	$|VV\rangle$	-	$\pi/2$	$\pi/4$	$3\pi/4$	$\pi/8$
(v)	$|\Phi^{-i}\rangle$	$|\Phi^{+i}\rangle$	-	$\pi/2$	$\pi/4$	$\pi/2$	$\pi/8$
(vi)	$|\Phi^{-i}\rangle$	$|VV\rangle$	$|\Phi^{+i}\rangle$	$\pi/4$	0	$3\pi/4$	$3\pi/8^{*}$
(vii)	$|\Phi^{-i}\rangle$	$|\Phi^{+1}\rangle$	$|\Phi^{+i}\rangle$	$\pi/4$	0	$3\pi/4$	$\pi/4^{*}$
(viii)	$|VV\rangle$	$|\Phi^{-1}\rangle$	$|HH\rangle$	$\pi/4$	0	$\pi/2$	0

Table 5.1: **Experimental settings for pump laser preparation.** We show the target states and settings for 8 different pump preparations labelled (i)–(viii). The corresponding target states in modes A–C are given; entangled states are expressed in the form $|\Phi^{\nu}\rangle = \frac{1}{\sqrt{2}}\left(|HH\rangle + \nu|VV\rangle\right)$. The angles of the two α-BBO crystals and the waveplates that follow are shown where a crystal angle of zero defines that a horizontally polarized beam is polarized along the slow axis. HWP-1 is always set to zero. Note that, in practice, settings (vi) and (vii) are subject to an additional phase due to wavelength-scale differences in the lengths of the two crystals; the states were set by rotating HWP-2 from the angle in the table until the two-photon measurements at D_{idler} and D_{in} matched the expected statistics. We indicated this experimental deviation from theory using the symbol * in the table. This same additional phase also necessitates that the phase set by the tilted quarter-wave plate in the idler arm must be adjusted for setting (viii).

plotted in Fig. 5.9. Each set of tomographic data required 36 projective measurements. Coincidences were recorded for five seconds for the input state. For the single-mode measurements, six loops of thirty-second coincidence measurements were recorded, for a total of three minutes per setting. For all other settings, twelve loops of thirty-second measurements were recorded, for a total of six minutes per setting. The background results presented are the average of two such runs, where the signal was blocked but the idler and escort were unchanged.

To characterize the preservation of entanglement through our setup, we first prepared the pump to produce the maximally entangled state $|\Phi^+\rangle = \frac{1}{\sqrt{2}}\left(|HH\rangle + |VV\rangle\right)$ in a *single* temporal mode at a time, labelled preparations (i)-(iii). We performed two-photon polar-
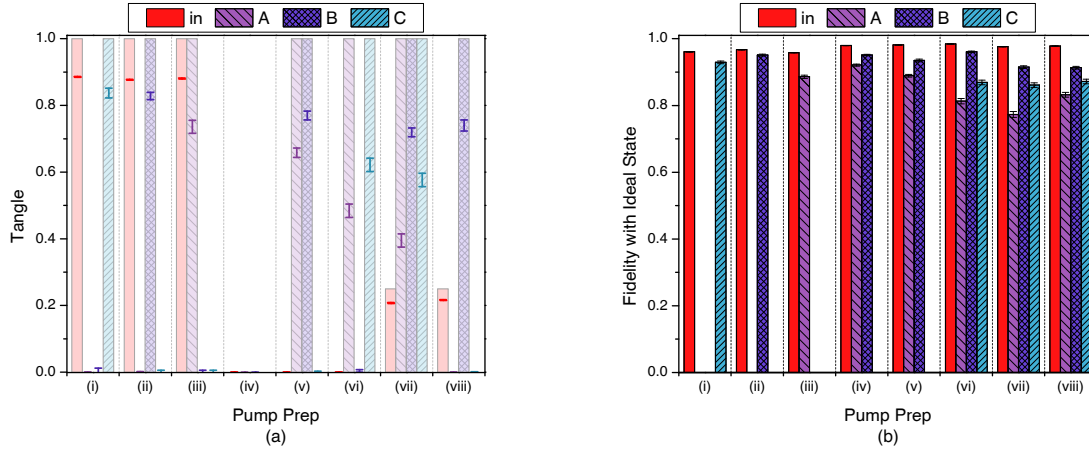
Figure 5.9: **Tangle and fidelity measurements.** (a) Measurements of the tangle [101] for each preparation and mode are shown, with their theoretical ideals transparent in the background. Note that the situation where entanglement is expected are consistently many standard deviations (at least twenty) above zero tangle, and that there are cases where no entanglement is measured in the input state yet presents itself in the demultiplexed subsystems. (b) The fidelity [37] of the reconstructed density matrix with the theoretical ideal is seen to be high for all cases (at minimum 77.3%). Background modes, i.e. those with no pump pulse, omitted for clarity.

ization state tomography [43] both before and after upconversion using an overcomplete set of 36 projective measurements. Because of the polarization-dependent diffraction efficiency of our grating, we performed projective polarization measurements before diffraction. A removable mirror was used to couple the single-photon signal into D_{in} to characterize the input state, which was found to have an average fidelity [37] of 96.2% with $|\Phi^+\rangle$ over the three potential modes and an average tangle [101] of 0.88. The upconverted states were reconstructed without background subtraction and found to have fidelities $(88.6 \pm 0.3)\%$, $(95.1 \pm 0.3)\%$, and $(92.9 \pm 0.4)\%$ with $|\Phi^+\rangle$ and tangles of 0.737 ± 0.020, 0.828 ± 0.011, and 0.836 ± 0.015, for modes A-C respectively, where the error bars are determined by Monte Carlo simulation assuming Poissonian counting statistics. These two figures of merit explicitly demonstrate that quantum correlations are maintained through the bandwidth compression process.

169

In preparations (iv) and (v), we prepared the pump to produce down-converted states in modes A and B. We contrast the case (iv) where the pump was set to produce the separable states $|VV\rangle$ and $|HH\rangle$ (Fig. 5.10i) with the case (v) where the pump was set to produce the maximally entangled states $|\Phi^{+i}\rangle = \frac{1}{\sqrt{2}} \left(|HH\rangle + i|VV\rangle \right)$ and $|\Phi^{-i}\rangle = \frac{1}{\sqrt{2}} \left(|HH\rangle - i|VV\rangle \right)$ (Fig. 5.10ii), in modes A and B respectively. The reconstruction from the coincidence measurements between D_{in} and D_{idler} produced the density matrix on the left-hand side of Fig. 5.10, with large populations in $|HH\rangle$ and $|VV\rangle$ but negligible coherence; both reconstructions have fidelities of 98% with an equal mixture of $|HH\rangle$ and $|VV\rangle$. This arises because the detector is not fast enough to resolve the pulses, instead measuring a mixture of the two signals and obfuscating the underlying quantum coherences of the individual states. By measuring the photons after the upconversion setup, the density matrices shown on the right side of Fig. 5.10 were reconstructed. The density matrices in case (v) exhibit large quantum coherences, which are required for entanglement, while those for case (iv) do not, as expected for separable states. Indeed, the density matrices reconstructed in case (iv) have an average fidelity of $(93.6\pm0.3)\%$ with the target separable states, and those in case (v) have an average fidelity of $(91.2 \pm 0.5)\%$ with the expected maximally entangled states and an average tangle of 0.714 ± 0.014.

We finally prepared the pump to produce maximally entangled states into all three modes, using the pump polarization sequence $|-i\rangle$, $|+\rangle$, and $|+i\rangle$ for modes A-C, as described as preparation (vii). We measured the states initially and after the upconversion process, shown in (Fig. 5.11). The initial state has fidelity 97.6% with the non-maximally entangled mixed state resulting from an incoherent mixture of the three expected maximally entangled states in modes A-C with weighting 0.25, 0.5, and 0.25, determined by the ratios of the intensities of the three pump pulses. The output states each exhibit different quantum correlations yet are all highly entangled, with fidelities of $(77.3 \pm 0.9)\%$, $(91.5 \pm 0.4)\%$, and $(86.1 \pm 0.7)\%$ with the expected maximally entangled states and tangles of (0.40 ± 0.2), (0.720 ± 0.013), and (0.58 ± 0.02) for modes A-C, respectively. The coincidence rates for modes A and C were half that of mode B due to the distribution of pump power, and their reconstructed states were thus more affected by background noise; however, crosstalk between signals was not a significant issue in our experiment.

Conclusion

We have demonstrated the conversion of a train of up to three temporally spaced single-photon pulses to a comb of distinct frequencies while maintaining quantum correlations in polarization. We have shown that this method can distinguish picosecond-separated single photons using detectors with nanosecond-scale time resolution. Improvements to the efficiency may be possible through the use of periodically poled nonlinear materials [282, 283] and cavity enhancements [292]. With higher conversion efficiencies, this ultrafast readout of time-division-multiplexed entangled quantum signals could be used to increase the density of quantum information carried through a single physical medium or to distribute quantum states throughout a multi-user network by applying time-to-frequency conversion to both signal and idler photons. Our results also demonstrate entanglement-preserving tunable bandwidth compression [161] of polarization-encoded [284] photons. More generally, our work demonstrates how shaped laser pulses may be used to manipulate the spatiotemporal waveforms of single photons while preserving quantum information.

Prep.	Det.	Counts (cps)	Tangle meas.	Tangle theo.	Purity meas.	Purity theo	Fidelity
(i)	in	$(45.36 \pm 0.10) \times 10^3$	$0.8857^{+0.0011}_{-0.0011}$	1	0.9435 ± 0.0006	1	0.9605 ± 0.0003
	A	0.67 ± 0.06	$0.0000^{+0.0009}_{-0.0000}$	0	0.349 ± 0.018	$^1/_4$	
	B	0.42 ± 0.05	$0.000^{+0.012}_{-0.000}$	0	0.35 ± 0.03	$^1/_4$	
	C	14.5 ± 0.3	$0.836^{+0.015}_{-0.014}$	1	0.919 ± 0.008	1	0.929 ± 0.004
(ii)	in	$(44.56 \pm 0.09) \times 10^3$	$0.877^{+0.0010}_{-0.0009}$	1	0.9394 ± 0.0005	1	0.9669 ± 0.0003
	A	0.64 ± 0.06	$0.0000^{+0.0019}_{-0.0000}$	0	0.35 ± 0.02	$^1/_4$	
	B	13.9 ± 0.3	$0.828^{+0.011}_{-0.011}$	1	0.913 ± 0.006	1	0.951 ± 0.003
	C	0.28 ± 0.04	$0.000^{+0.006}_{-0.000}$	0	0.30 ± 0.03	$^1/_4$	
(iii)	in	$(44.35 \pm 0.09) \times 10^3$	$0.8807^{+0.0012}_{-0.0012}$	1	0.9409 ± 0.0006	1	0.9581 ± 0.0003
	A	12.5 ± 0.3	$0.737^{+0.019}_{-0.020}$	1	0.866 ± 0.011	1	0.886 ± 0.005
	B	0.49 ± 0.06	$0.000^{+0.006}_{-0.000}$	0	0.34 ± 0.03	$^1/_4$	
	C	0.39 ± 0.05	$0.000^{+0.005}_{-0.000}$	0	0.38 ± 0.03	$^1/_4$	
(iv)	in	$(42.22 \pm 0.09) \times 10^3$	$0.00005^{+0.00002}_{-0.00002}$	0	0.4857 ± 0.0003	$^1/_2$	0.9794 ± 0.0003
	A	7.26 ± 0.14	$0.00000^{+0.00004}_{-0.00000}$	0	0.854 ± 0.006	1	0.921 ± 0.003
	B	7.60 ± 0.15	$0.00000^{+0.00008}_{-0.00000}$	0	0.912 ± 0.005	1	0.951 ± 0.002
	C	0.32 ± 0.03	0^{+0}_{-0}	0	0.282 ± 0.017	$^1/_4$	
(v)	in	$(43.63 \pm 0.09) \times 10^3$	$0.0001^{+0.0004}_{-0.0003}$	0	0.4843 ± 0.0003	$^1/_2$	0.9812 ± 0.0003
	A	7.77 ± 0.15	$0.658^{+0.014}_{-0.014}$	0	0.824 ± 0.008	1	0.889 ± 0.004
	B	6.42 ± 0.13	$0.769^{+0.014}_{-0.012}$	0	0.883 ± 0.007	1	0.935 ± 0.004
	C	0.26 ± 0.03	$0.000^{+0.003}_{-0.000}$	0	0.300 ± 0.021	$^1/_4$	
(vi)	in	$(43.61 \pm 0.09) \times 10^3$	$0.00019^{+0.00005}_{-0.00004}$	0	0.6074 ± 0.0005	$^5/_8$	0.9843 ± 0.0002
	A	3.97 ± 0.11	$0.48^{+0.02}_{-0.02}$	1	0.728 ± 0.012	1	0.813 ± 0.008
	B	7.01 ± 0.14	$0.001^{+0.007}_{-0.001}$	0	0.933 ± 0.004	1	0.961 ± 0.002
	C	3.78 ± 0.10	$0.62^{+0.02}_{-0.02}$	1	0.798 ± 0.011	1	0.869 ± 0.007
(vii)	in	$(43.41 \pm 0.09) \times 10^3$	$0.2075^{+0.0012}_{-0.0013}$	$^1/_4$	0.5953 ± 0.0007	$^5/_8$	0.9760 ± 0.0003
	A	3.36 ± 0.10	$0.40^{+0.02}_{-0.02}$	1	0.676 ± 0.013	1	0.773 ± 0.009
	B	6.79 ± 0.14	$0.720^{+0.012}_{-0.014}$	1	0.857 ± 0.007	1	0.915 ± 0.004
	C	3.51 ± 0.10	$0.58^{+0.02}_{-0.02}$	1	0.779 ± 0.012	1	0.861 ± 0.007
(viii)	in	$(42.97 \pm 0.09) \times 10^3$	$0.2165^{+0.0013}_{-0.0013}$	$^1/_4$	0.6010 ± 0.0007	$^5/_8$	0.9780 ± 0.0003
	A	3.24 ± 0.09	$0.0000^{+0.0006}_{-0.0000}$	0	0.716 ± 0.011	1	0.832 ± 0.007
	B	6.00 ± 0.13	$0.739^{+0.017}_{-0.016}$	1	0.867 ± 0.009	1	0.913 ± 0.004
	C	3.23 ± 0.09	$0.0002^{+0.0013}_{-0.0002}$	0	0.782 ± 0.010	1	0.872 ± 0.005
(bkgd)	A	0.55 ± 0.04	0^{+0}_{-0}	0	0.332 ± 0.013	$^1/_4$	
	B	0.34 ± 0.03	$0.0000^{+0.0007}_{-0.0000}$	0	0.320 ± 0.017	$^1/_4$	
	C	0.40 ± 0.03	$0.0000^{+0.0005}_{-0.0000}$	0	0.317 ± 0.015	$^1/_4$	

Table 5.2: **Full experimental results.** The preparations correspond to the eight preparations in Table S-5.1, and each measurement was taken in coincidence with D_{idler}. Grayed-out rows correspond to background counts. Uncertainties in tangle, purity, and fidelity were calculated with the assumption of Poissonian errors and a Monte Carlo calculation.

172
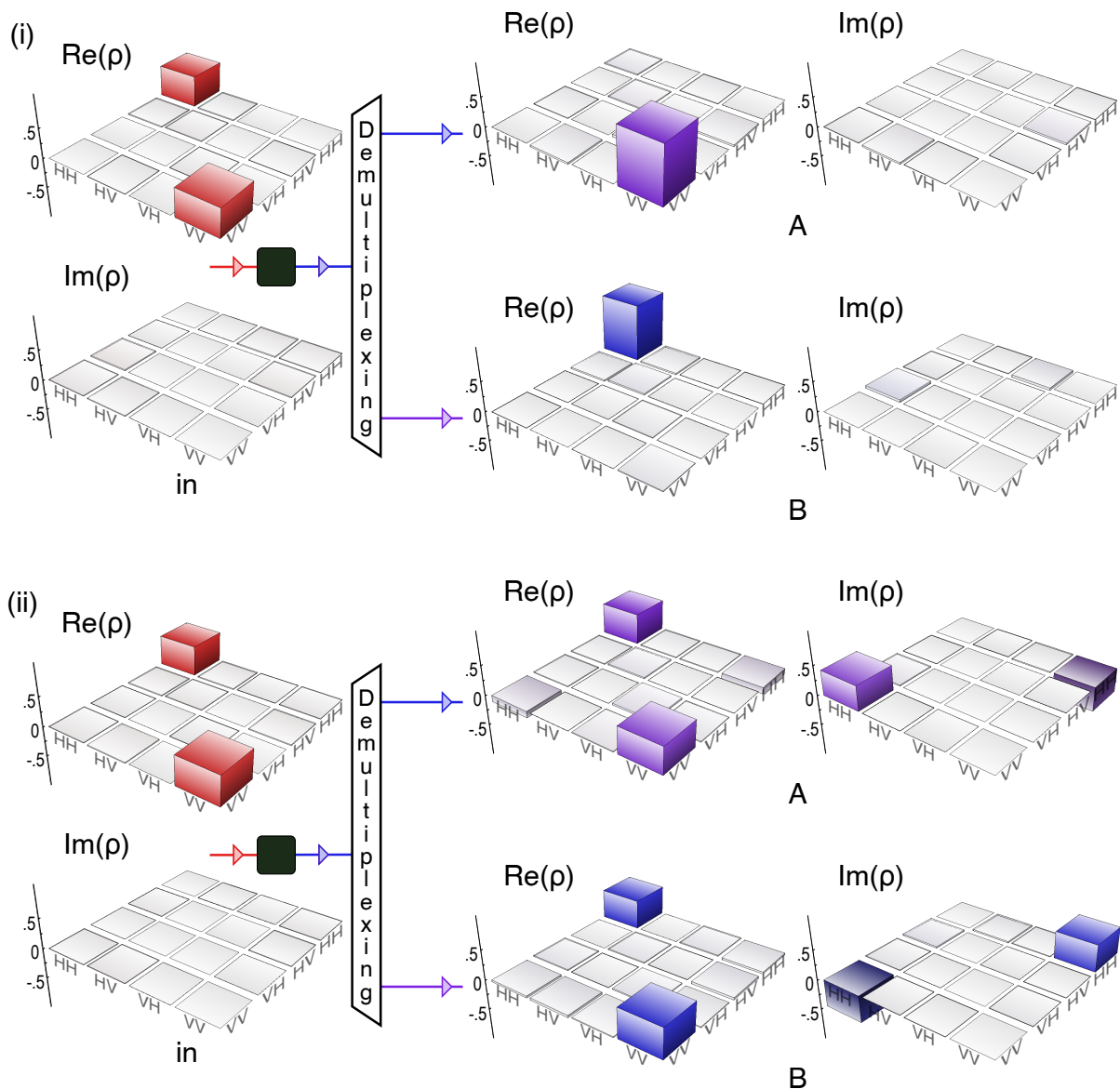
Figure 5.10: **Demultiplexing two orthogonal states.** With the pump prepared in modes A and B to either produce (i) orthogonal separable states or (ii) orthogonal maximally entangled states, as per settings (iv) and (v) of Tab. 5.1, the density matrices measured before time-to-frequency conversion (left) appear the same, with negligible coherences. After demultiplexing, the experimentally reconstructed output density matrices (right) are revealed to describe vastly different quantum states, which are separable in case (i) but show a high degree of entanglement in case (ii).
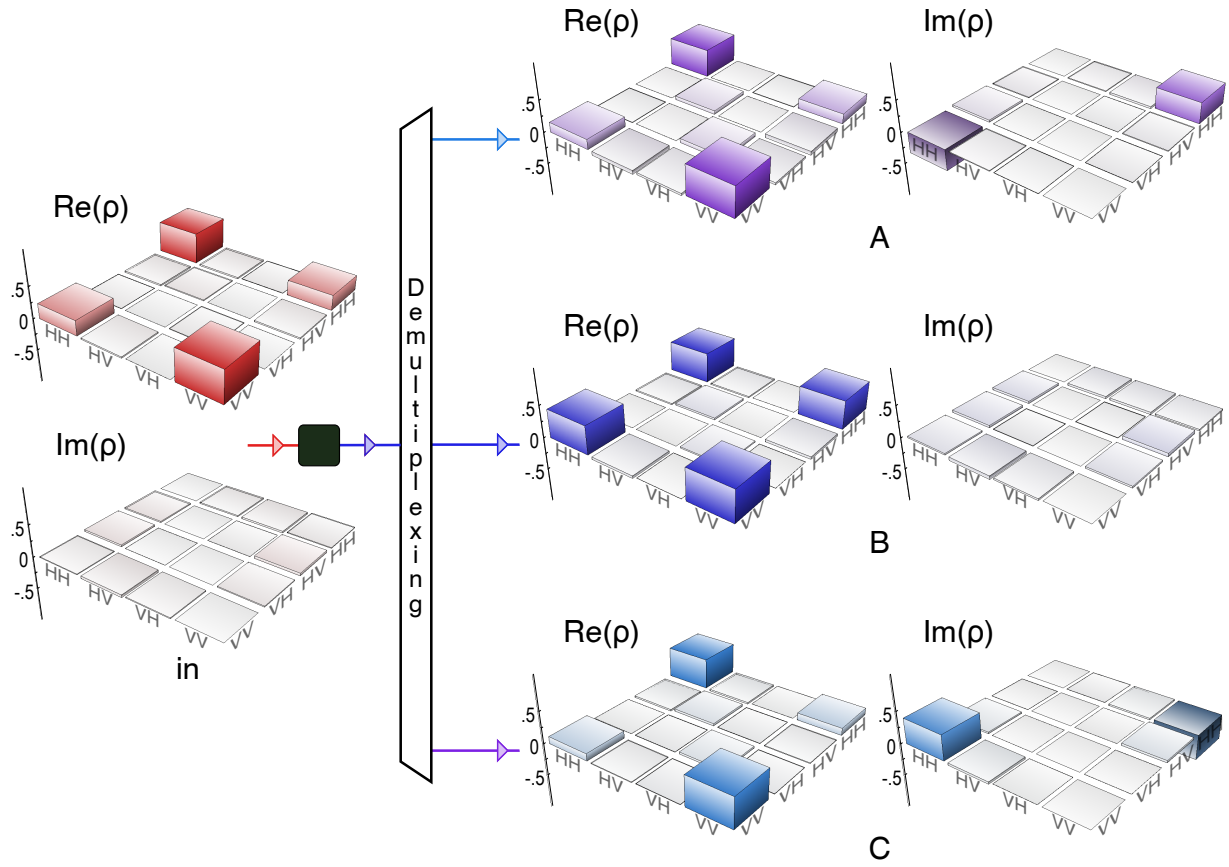
Figure 5.11: **Demultiplexing three entangled states.** The pump was prepared to produce a train of three maximally entangled states, as per setting (vii) of Tab. 5.1. Weak coherences are seen in the density matrix measured before time-to-frequency conversion (left), with a calculated tangle of 0.21. After being demultiplexed, all three experimentally reconstructed density matrices show much stronger coherence and larger entanglement, with tangles of 0.40, 0.72, and 0.58 in modes A-C respectively.

Chapter 6

Spectrally engineering photonic entanglement with an upconversion time lens

Notes and acknowledgements

Author Contributions

John Donohue and **Kevin Resch** conceived of the study.

John Donohue designed the experimental apparatus.

John Donohue and **Morgan Mastrovich** built the experimental apparatus.

John Donohue carried out the experiment, analyzed the data, and wrote the first draft of the manuscript.

All authors contributed to the final version.

Chapter Overview

Sources of single photons with precisely controlled properties are necessary for effective and efficient photonic quantum communication, computation, and metrology. The spectral, or energy-time, degree of freedom is of particular interest, as it can be used to encode information in a high-dimensional Hilbert space [293] and is naturally robust when transmitting through both long-distance fiber links [52] and photonic waveguides [63]. Entanglement in this degree of freedom is essential for applications such as high-dimensional quantum key distribution [293] and quantum-enhanced clock synchronization [7]. The nonlinear process of spontaneous parametric downconversion (SPDC), for example, provides a reliable source of energy-time entangled photons. Due to energy conservation, most SPDC sources tend to produce photons with frequency anti-correlations. However, photon pairs with positively correlated spectra may be useful for dispersion cancellation in long-distance channels [183] and quantum-enhanced clock synchronization [7]. Using SPDC sources with extended phasematching conditions, joint spectra with positive spectral correlations have been produced before [294, 182, 184, 183], but control over the correlations after state generation has not yet been demonstrated.

Control over the spatial or polarization degrees of freedom of a single photon can be accomplished with passive linear optics, but universal control over spectral waveforms requires more complex techniques such as fast electro-optic devices or nonlinear optical processes. Overcoming these challenges is essential for many quantum applications, such as interfacing with quantum memories [26], ultrafast photon switching [146], manipulating time-bin qubits [29, 68, 57], and temporal mode selection [58, 63]. These tasks cannot be accomplished in general with passive optics, filtering, or spectral phase-only manipulations [232] even if one is willing to accept loss, as they may change the energy of the photons. Spectral control over a photon after it has been created is therefore highly desirable for ultrafast manipulation and state engineering, especially at wavelengths where materials with suitable phasematching do not exist. Since entanglement cannot be increased or decreased in an lossless local process, shaping cannot be used to create frequency uncorrelated states [180], but can be used to change the specific energy relations between the two photons, or convert the correlation between the photon frequencies to a correlation between the frequency of

one and the time-of-arrival of the other.

In this work, we demonstrate ultrafast control of quantum-optical waveforms with sub-picosecond features. We construct a temporal imaging system based on ultrafast nonlinear effects to manipulate the spectral profile of single photons. We apply this technique to half of an energy-time entangled pair produced with SPDC, and observe that the frequency anti-correlations are converted to positive correlations after the time lens through joint spectral intensity measurements, in addition to an adjustable central frequency shift. It is straightforward to adjust the spectral magnification by changing the chirp parameters, and our scheme is free of intense broadband noise such as Raman scattering. A similar, as-yet-unrealized application of time lenses was proposed using electro-optic modulators [295].

6.1 Concept and theory

6.1.1 Spectral reversal with an upconversion time lens

Temporal imaging can be understood in direct analogy with its spatial counterpart [121, 122], as outlined in Sec. 2.2. As a quick review, it is instructive to compare the corresponding elements in each, as shown in Fig. 6.1. In spatial imaging, free-space propagation causes the momentum components to diverge in space, resulting in a spatial spread of the beam. The action of the lens is to shift the transverse momenta in a spatially dependent way, such that after further propagation the beam may refocus. Analogously, in temporal imaging, propagation through a dispersive material (such as optical fiber) causes the constituent frequencies of a pulse to diverge in time, resulting in a temporal spread of the pulse. Constructing the equivalent of a lens for temporal imaging requires a time-dependent frequency shift in the same way that a spatial lens requires a spatially dependent transverse momentum shift. Self-phase modulation can approximate the required effect [122], but is ineffective for single-photon signals. Four-wave mixing has been shown to be effective for classical signals [137, 136, 138, 139, 140, 296], but suppression of broadband noise sources presents a challenge for quantum signals. Recent work has shown great promise using cross-phase modulation in photonic crystal fiber [145], Raman memories [27], and electro-optic modulators [297, 148] to shape broadband single-photon waveforms.

177
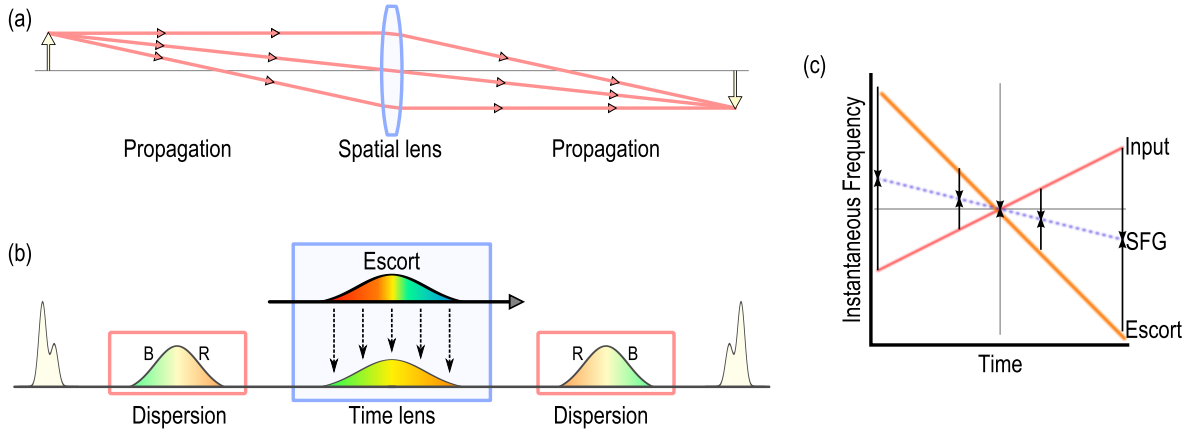
Figure 6.1: **Temporal shaping with an upconversion time lens.** (a) In a spatial imaging system, free-space propagation spreads the spatial extent of the beam such that each portion of the beam has a distinct transverse momentum, visualized with arrows. The lens shifts the momenta in a spatially dependent fashion, which effectively reverses the momenta for off-centre components, and the beam refocuses with further spatial propagation. (b) The temporal imaging system operates through an analogous principle, where chromatic dispersion spreads the temporal profile of the beam such that each temporal slice of the beam has a distinct central frequency, ranging from a red-shifted leading edge, R, to a blue-shifted tail, B. The time lens introduces a time-dependent frequency shift, which can reverse the frequency shifts and allow the wavepacket to refocus itself after more chromatic dispersion is applied. The temporal structure of the pulse will be reversed, akin to an imaging system with negative magnification. In our realization, we use sum-frequency generation with a dispersed escort pulse to implement an upconversion time lens. At each time in the interaction, the signal interacts with a different frequency of the escort, effectively enforcing a time-dependent relative frequency shift as well as a change in carrier frequency. (c) In the case where $A_e = -A_s/2$, the reversal of the frequency spectrum can be seen by comparing the instantaneous frequency shift of the escort and input signal at any given time in the crystal. If, at some point in the process, the input is frequency shifted by δ from its centre, the escort is shifted by -2δ, and the sum-frequency is thus shifted overall by $-\delta$ from its centre. In this way, red shifts are converted to blue shifts.

The upconversion time lens [131], seen in Fig. 6.1b, is based on sum-frequency generation (SFG), a type of three-wave mixing in which two pulses may combine to produce a pulse at the sum of their frequencies. In the case of interest, one pulse is considered to

contain a single photon and the other to be a strong classical pulse. This strong classical pulse, referred to as the *escort*, upconverts the photon to a new frequency, leaving its own imprint on the spectral shape of the photon. SFG has been shown to be a powerful and potentially efficient tool for ultrafast waveform manipulation which remains effective at the single-photon level [260, 226, 52, 225, 168, 208]. The combination of SFG and pulse shaping enables manipulation of ultrafast single-photon waveforms for techniques such as bandwidth compression [161], quantum pulse gates [58], and time-to-frequency conversion [138, 68].

We represent the spectral field of a dispersed optical pulse as $F(\omega)e^{i\phi(\omega)}$, where the spectral phase has a quadratic frequency dependence, $\phi(\omega) = A(\omega - \omega_0)^2$, with chirp parameter, A. We characterize the dispersion applied to the input signal, escort pulse, and output waveform by the chirp parameters A_i, A_e, and A_o, respectively, which in the case of normal dispersion are proportional to the length of material passed through. We assume that the pulses are all chirped to many times their initial widths, known as the large-chirp limit. In this limit, the imaging equation for the time lens system shown in Fig. 6.1b can be found in Refs. [131, 168] and simplifies to relation [122, 168],

$$\frac{1}{A_i} + \frac{1}{A_o} = -\frac{1}{A_e}. \tag{6.1}$$

This equation has the same form as the thin lens equation, with dispersion playing the role of propagation distance and the escort chirp the role of the focal length.

In analogy to spatial imaging, the output temporal waveform will have the same features as the input but scaled by a magnification factor [131, 122, 168]

$$M_{\text{temporal}} = \frac{1}{M_{\text{spectral}}} = -\frac{A_o}{A_i} = \left(1 + \frac{A_i}{A_e}\right)^{-1}. \tag{6.2}$$

The inverse relationship of the spectral and temporal magnification is a consequence of the scaling property of the Fourier transform. Spectral measurements, which can be performed with linear optics, can be used to observe the time-lens effect because of this relationship. If $A_i = -2A_e$, the effective temporal and spectral magnification is -1, and both the temporal and spectral shapes will be reversed. If the input signal is a single photon which

is spectrally entangled with a partner, reversing the spectrum of the photon will result in an overall reversal of the two-photon joint spectrum. Intuitively (in the large-chirp limit), the reversal of the spectral profile occurs because every portion of the signal spectrum detuned from the central frequency by $\delta\omega$ meets a segment of the escort pulse detuned by $-2\delta\omega$ from its central frequency, as visualized in Fig. 6.1c. In the large-chirp limit, only an output chirp A_o is required to recompress the joint spectral state temporally, which has no effect on the spectral profile of the output but is vital to obtaining the desired joint temporal distribution.
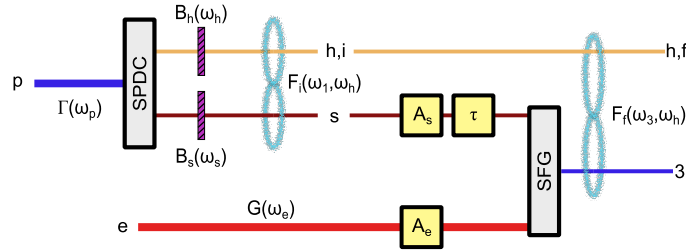

Figure 6.2: **Abstract representation of setup.** The process under study begins with spontaneous parametric downconversion (SPDC) of a pump p with spectrum $\Gamma(\omega_p)$. The photon pair is filtered with bandpass filters $B_j(\omega_j)$. The photon pair, with a signal in mode s and a herald in mode h, share a joint spectral amplitude of $F_i(\omega_s, \omega_h)$. The signal is chirped, represented by the parameter A_s. An escort pulse in mode e with spectrum $G(\omega_e)$ is also chirped, represented by the parameter A_e, as well as delayed in time relative to the input signal by an amount τ. The signal photon and escort are mixed for sum-frequency generation (SFG), and the output joint spectral amplitude between the output signal in mode 3 and the herald is $F_f(\omega_3, \omega_h)$.

6.1.2 Spectral reversal of a two-photon joint spectrum

Following the flow of Fig. 6.2, we show here how the upconversion time lens acts on an inseparable two-photon spectra to first order by describing the joint spectral state generated by SPDC in the low-gain regime post-selected for coincidences (i.e. a single photon pair)

180

as

$$|\psi_i(t)\rangle = \frac{1}{2\pi} \iint \mathrm{d}\omega_s \mathrm{d}\omega_h F_i(\omega_s, \omega_h)|\omega_s\rangle_s|\omega_h\rangle_h, \tag{6.3}$$

where $|\omega_j\rangle = \hat{a}_{\omega_j}^\dagger e^{i\omega_j t}|0\rangle$ represents a single photon of frequency ω_j which is in a single spatial/polarization mode. The initial joint spectral representation $F_i(\omega_s, \omega_h)$ is a function of the pump spectrum $\Gamma(\omega_p)$, the phasematching function $\Phi_{SPDC}(\omega_s, \omega_h, \omega_p)$, and any bandpass filters applied $B_j(\omega_j)$ [180]. If we assume that each of these functions is individually well-approximated by a Gaussian, we can approximate the joint spectral wavefunction as approximated by a two-variable Gaussian,

$$F_i(\omega_s, \omega_h) = \Gamma(\omega_s + \omega_h)\Phi_{SPDC}(\omega_s, \omega_h)B_s(\omega_s)B_h(\omega_h) \tag{6.4}$$

$$= \frac{e^{\left[\frac{1}{1-\rho_i^2}\left(-\frac{(\omega_s-\omega_{0s})^2}{4\sigma_s^2} - \frac{(\omega_h-\omega_{0h,i})^2}{4\sigma_{h,i}^2} - \frac{\rho_i(\omega_s-\omega_{0s})(\omega_h-\omega_{0h,i})}{2\sigma_s\sigma_{h,i}}\right)\right]}}{\sqrt{2\pi}\sigma_s\sigma_{h,i}(1-\rho_i^2)^{1/4}}, \tag{6.5}$$

where the simplified representation has been renormalized. Note that the single-photon marginal spectra in this model are symmetric about their central frequencies, with $1/\sqrt{e}$ widths of σ.

The signal photon is then chirped and delayed, which can be represented respectively as a quadratic and linear phase in frequency as

$$F_i(\omega_s, \omega_h) \mapsto F_i(\omega_s, \omega_h)e^{-i\omega_s\tau + iA_s(\omega_s-\omega_{0s})^2}, \tag{6.6}$$

where τ represents a relative time delay. The $1/\sqrt{e}$ temporal width of the chirped signal is

$$\Delta t = \frac{\sqrt{1 + 16A_s(1-\rho_i^2)\sigma_s^4}}{2\sqrt{1-\rho_i^2}\sigma_s} \tag{6.7}$$

The escort pulse can be represented as a strong coherent state with a field as in Eq. (3.82). The spectrum of the joint state after upconversion can be found as the convolution of the

escort and the input signal spectra [168]

$$|F_f(\omega_3, \omega_h)| = \left| \int_{-\infty}^{\infty} d\omega_s \, G(\omega_3 - \omega_s) \Phi_{SFG}(\omega_s, \omega_3 - \omega_s, \omega_3) F_i(\omega_s, \omega_h) \right| \qquad (6.8)$$

$$= \frac{e^{\left[\frac{1}{1-\rho_f^2} \left(-\frac{(\omega_3 - \omega_{03})^2}{4\sigma_3^2} - \frac{(\omega_h - \omega_{0h,f})^2}{4\sigma_{h,f}^2} - \frac{\rho_f(\omega_3 - \omega_{03})(\omega_h - \omega_{0h,f})}{2\sigma_3\sigma_{h,f}} \right) \right]}}{\sqrt{2\pi}\sigma_3\sigma_{h,f}(1-\rho_f^2)^{1/4}}, \qquad (6.9)$$

where we are able to re-express the state as a Gaussian since the convolution of two Gaussians is once again a Gaussian.

Even with Gaussian approximations to all the input functions, the theoretical final joint spectral intensity is difficult to express concisely. For the sake of intuition, we will look at its behaviour under various simplifications. First, we assume that phasematching is infinitely broad ($\Phi_{SFG}(\omega_s, \omega_3 - \omega_s, \omega_3) \approx 1$). As we will see in Sec. 6.3.2, this assumption is not valid, but the phasematching is not so strong that it destroys the intuition gained from the simpler case. With this simplification, the spectral bandwidth σ_3 of the output is

$$\sigma_3 = \sqrt{\frac{(2 - \rho_i^2)\sigma_s^2\sigma_e^2 + \sigma_e^4 + (1 - \rho_i^2)\sigma_s^4(1 + 16(A_s + A_e)^2\sigma_e^4)}{\sigma_e^2 + (1 - \rho_i^2)\sigma_s^2(1 + 16A_s^2\sigma_s^2\sigma_e^2 + 16A_e^2\sigma_e^4)}} \qquad (6.10)$$

and the statistical correlation is

$$\rho_f = \frac{\{1 + 16(A_s + A_e)(1 - \rho_i^2)\sigma_s^2 [(A_s + 3A_e)(1 - \rho_i^2)\sigma_s^2 + A_e\sigma_e^2 (1 + 16(A_s + A_e)^2(1 - \rho_i^2)\sigma_s^4)]\}}{\sqrt{2}\sqrt{\sigma_e^2 + 2(1 - \rho_i^2)\sigma_s^2 [1 + 8(A_s + A_e)^2(1 - \rho_i^2)\sigma_s^2\sigma_e^2]}}$$
$$\times \frac{-\rho_i\sigma_e^2\sqrt{A_s^2(1 - \rho_i^2)\sigma_s^2 + A_e^2\sigma_e^2}}{\sigma_e^2 + (1 - \rho_i^2)\sigma_s^2 [1 + 16A_s^2(1 - \rho_i^2)\sigma_s^2\sigma_e^2 + 16A_e^2\sigma_e^4]}$$
$$\times \frac{1}{(2 - \rho_i^2)\sigma_s^2\sigma_e^2 + \sigma_e^4 + (1 - \rho_i^2)\sigma_s^4 [1 + 16(A_s + A_e)^2\sigma_e^4]}$$
$$\qquad (6.11)$$

These expressions are difficult to parse without additional assumptions. Firstly, we look at the limit where the escort has infinite spectral support, $\sigma_e \gg \sigma_s$. As any chirp on a pulse with infinite spectral support stretches it infinitely, this is equivalent to the assumption that the chirped escort is much broader in time than the chirped signal if $|A_e| \neq 0$. In this

limit, we find that the width of the upconverted signal is

$$\lim_{\sigma_e \to \infty} \sigma_3 = \frac{\sqrt{\frac{1}{1-\rho_i^2} + 16(A_s + A_e)^2 \sigma_s^4}}{4 A_e \sigma_s} \stackrel{LCL}{=} \frac{|A_s + A_e|\sigma_s}{A_e} = M_{spectral}\sigma_s, \tag{6.12}$$

where $M_{\mathrm{spectral}} = 1/M_{\mathrm{temporal}}$ is as defined in Eq. (2) of the main text, and the statistical correlation is

$$\lim_{\sigma_e \to \infty} \rho_f = -\rho_i \frac{4(A_s + A_e)\sigma_s^2\sqrt{1 + 16(A_s + A_e)^2(1-\rho_i^2)^2\sigma_s^4}}{1 + 16(A_s + A_e)^2(1-\rho_i^2)\sigma_s^4} \stackrel{LCL}{=} -\rho_i \frac{A_s + A_e}{|A_s + A_e|} \tag{6.13}$$

The simplification on the right-hand-side is once again the large-chirp limit (LCL), where we assume that $16(A_s + A_e)^2(1-\rho_i^2)^2\sigma_s^4 \gg 1$. We have also assumed that $A_s \neq -A_e$ in this simplification; if $A_s = -A_e$, the process acts as a time-to-frequency converter, as described in Refs. [161, 168]. This simplification also relies on the initial state not being perfectly entangled, $|\rho_i| < 1$, as the marginal temporal length approaches infinity as the entanglement strengthens (consistent with being generated from truly-continuous-wave pumping). In this large chirp limit, the output waveform is recompressible through spectral phases without need for an additional time lens, and the joint spectrum maintains its degree of correlation. Were it not for the large chirp limit, some information about the spectrum of the herald would be present in the temporal profile of the upconverted signal, and the statistical correlation of the joint spectra would be reduced. This effect could be corrected with a second time lens forming a complete temporal telescope [140].

In our experiment, the escort pulse has a bandwidth on the same order as that of the signal, $\sigma_e \sim \sigma_s$. We next focus on the case studied in our experiment, where $A_e = -A_s/2$. In the large-chirp limit of this scenario, the output width is

$$\sigma_3^{(M=-1)} \stackrel{LCL}{=} \frac{\sigma_s}{\sqrt{\frac{4\sigma_s^2}{\sigma_e^2} + 1}}, \tag{6.14}$$

and the statistical correlation is

$$\rho_f^{(M=-1)} \overset{LCL}{=} \frac{-\rho_i}{\sqrt{\frac{4(1-\rho_i^2)\sigma_s^2}{\sigma_e^2} + 1}}. \tag{6.15}$$

For both the bandwidth and correlation, the final value has the same absolute value as the input if the spectral support of the escort is sufficient, $\sigma_e \gg 4\sigma_s(1 - \rho_i^2)$. Additionally, the sign of the statistical correlation is reversed, $\rho_f = -\rho_i$, consistent with a magnification of -1. The deviations from this are due to lack of spectral support from the escort, and are exaggerated since the input signal is more strongly chirped than the escort; if the escort is not wider in frequency, it will be shorter in time when chirped and not encompass the full waveform [168]. In this case, the escort will act partially as a filter which will degrade the strength of entanglement.

6.2   Experimental setup

Our experimental setup is shown in Fig. 6.3, and is detailed in Fig. 6.4. The experiment uses a titanium sapphire (Ti:Sapph) laser (Coherent Chameleon Ultra II, 80 MHz repetition rate). The fundamental of the Ti:Sapph was frequency-doubled in 2 mm of type-I phasematched BiBO to a second harmonic at 387 nm with a bandwidth of 0.75 nm full-width at half-maximum (FWHM). and a power of 935 mW. The photon pairs were then produced by focusing the second harmonic into 3 mm of type-I BiBO and split with a dichroic mirror, with central wavelengths of 811.0 nm and 740.2 nm for the signal and herald, respectively.

The remaining Ti:Sapph fundamental is re-collimated and used as the escort pulse, which has a central wavelength of 774.6 nm with a bandwidth of 5.5 nm FWHM and a power of 945 mW. Part of the beam was split using a half-wave plate and PBS and delay-matched with the signal photon for alignment. The rest of the pulse passed through a double-pass grating-based pulse compressor which provides an anti chirp of $A_e = -344 \times 10^3$ fs^2 [161], with a razor blade inserted where the beam was at its widest to effectively act as an adjustable shortpass filter. The signal photon was chirped in 34 m of single-mode fiber,
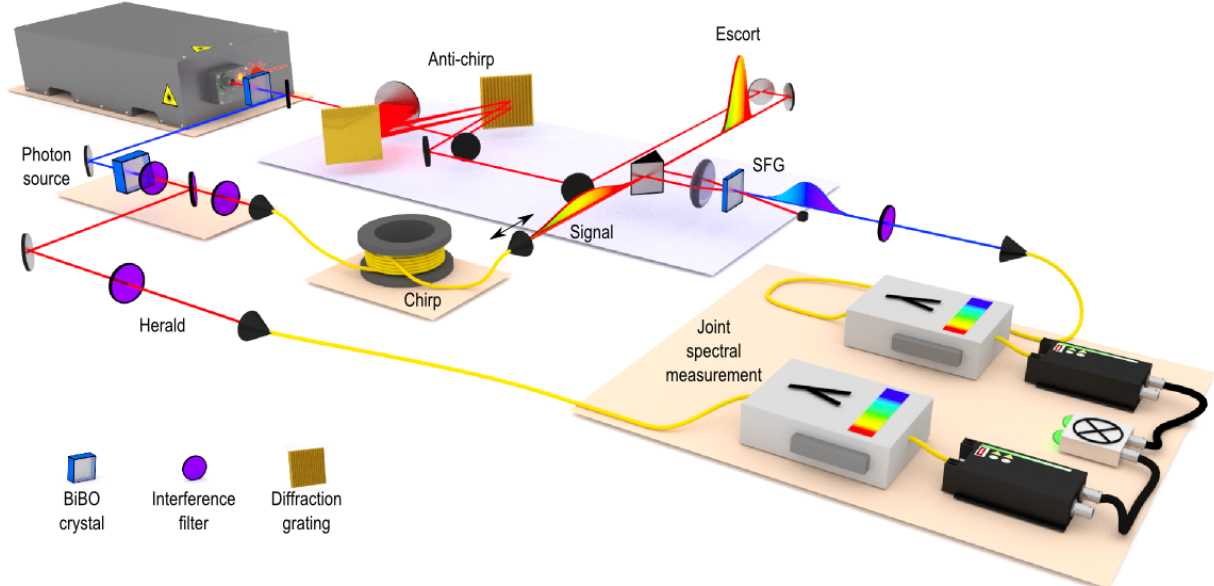
Figure 6.3: **Experimental setup.** Energy-time entangled photons are created through the spontaneous parametric downconversion of ultrafast pulses from a frequency-doubled Ti:Sapph laser. The signal photons are chirped through 34 m of single-mode fiber, while the remaining Ti:Sapph light comprises the escort pulse and anti-chirped in a grating-based pulse compressor. The pulses are recombined with relative delay τ for non-collinear sum-frequency generation (SFG). The upconverted signal is then isolated with bandpass filters and spectrally resolved in coincidence with the herald.

which provides a chirp of $A_i = 696 \times 10^3$ fs^2 through material dispersion. Owing to this fiber delay, the photon originates 13 pulses ahead of the escort. The chirped signal photon and anti-chirped escort pulse co-propagated with a spatial separation of approximately 9 mm and were then focused into 1 mm of type-I BiBO for sum-frequency generation. The upconverted beam, with a central wavelength of 396.1 nm, was then re-collimated and the second harmonic of the escort was removed with a pair of bandpass filters. The upconverted photons were then collected in multimode fiber after passing through a set of polarization optics identical to the herald photon. The combined efficiency of the chirp, upconversion, and fiber coupling is approximately 0.2%. The herald photons are detected with Perkin-Elmer SPCM-AQ4C photon counting modules, with detection efficiencies of

185
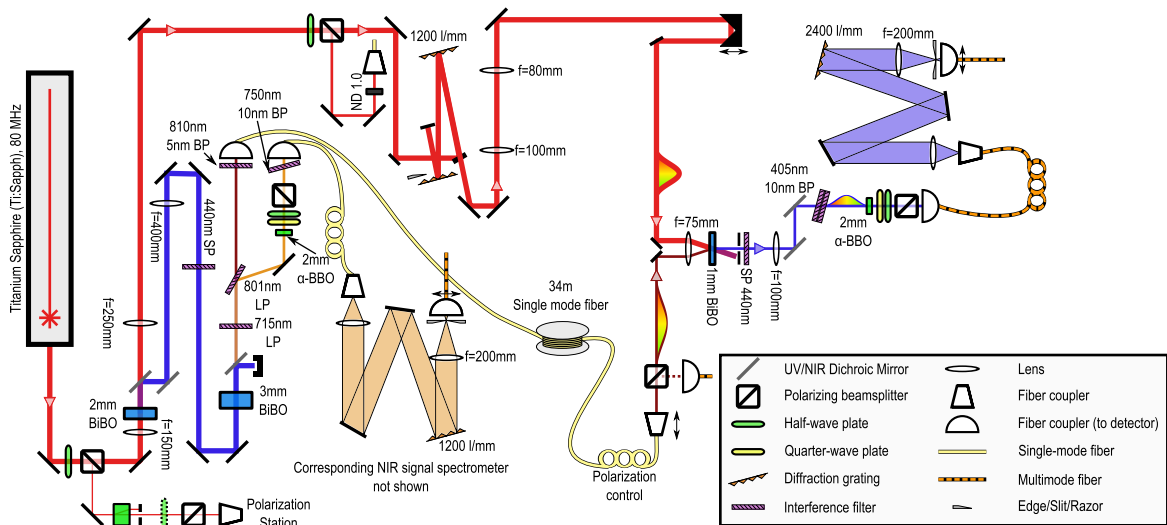
Figure 6.4: **Full-detail experimental setup.** The experimental setup, as sketched in Fig. 6.3, is more accurately represented as seen above. Filters can be longpass (LP), shortpass (SP), or bandpass (BP). Fiber loops with paddles are used to control polarization.

approximately 50% near 800 nm. The upconverted photons were detected with Hamamatsu H10682-210 photon counters, with a quantum efficiency of approximately 30% near 400 nm. Coincidence counts were obtained with a window of 3 ns, which is larger than the timing jitter of the electronics and much smaller than the 12.5 ns pulse separation.

The joint spectra were measured using three scanning spectrometers, one for each of the near-infrared (NIR) SPDC photons and one for the upconverted photon. The beams were expanded to approximately 3.5 mm waist radius and directed to a grating for spectral separation (1200 lines/mm for NIR, 2400 lines/mm for ultraviolet). The beams were then focused onto a slit and multimode fiber coupler, which move together to measure the full spectrum. The resolution of spectrometers, measured using emission spectra of a calibration lamp, were found to be (0.136 ± 0.013) nm, (0.148 ± 0.012) nm, and (0.0741 ± 0.0011) nm, for the NIR signal, NIR herald, and upconverted spectrometers, respectively.

The photons were produced through SPDC at a rate of approximately 415,000 coincidence counts per second, with 2.5×10^6 (3.2×10^6) single-detection events per second for

186
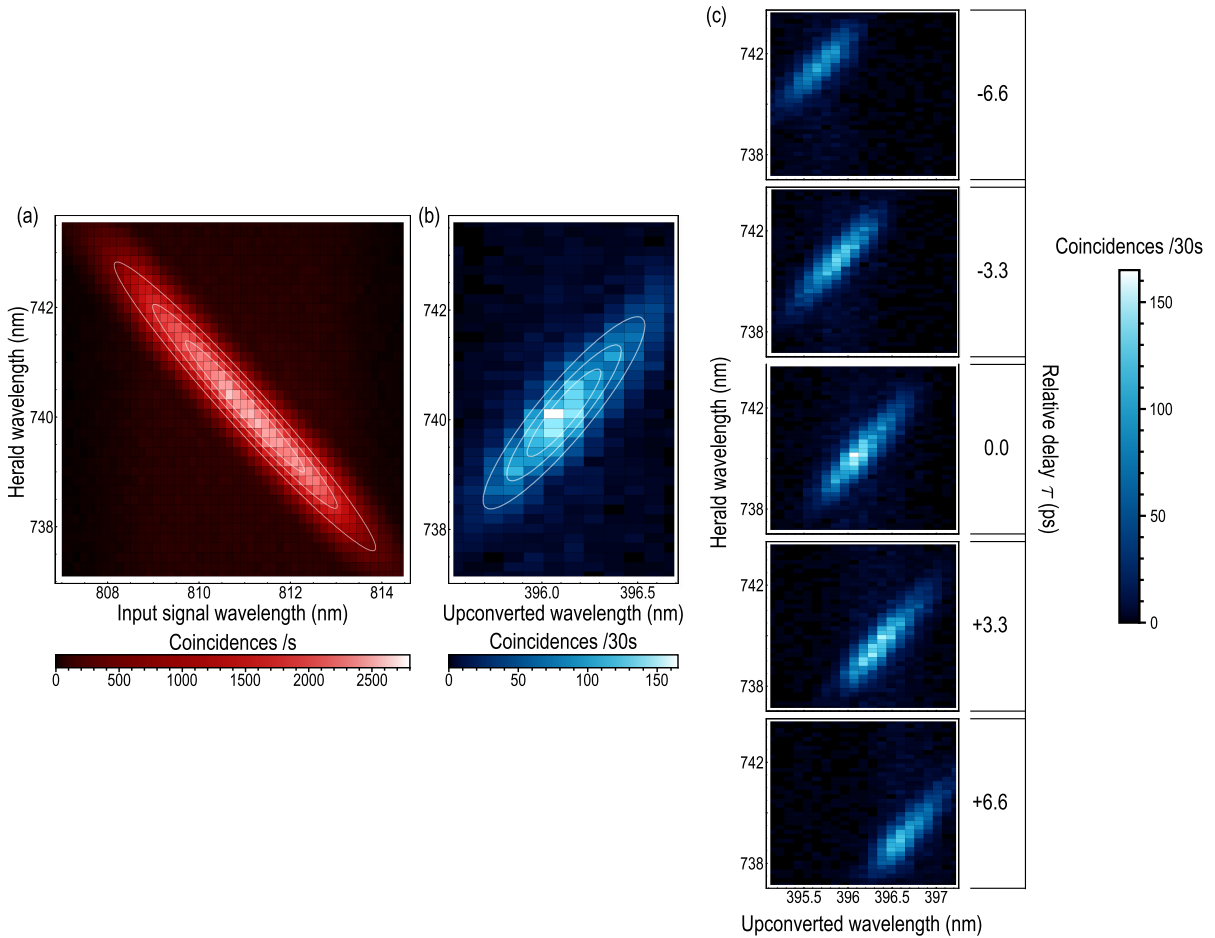
Figure 6.5: **Joint spectra.** (a) The joint spectrum measured between the signal photon and the herald immediately after downconversion has strong frequency anti-correlations. (b) After sum-frequency generation, the joint spectrum between the upconverted signal photon and the herald exhibits strong positive frequency correlations. The white lines on each plot correspond to 25% contours of the resolution-corrected Gaussian fits. Background subtraction has not been employed in either image. (c) The center frequency of the joint spectrum is tunable by introducing a relative delay between the input signal and the escort pulse, as seen in the five measured joint spectra. The herald central frequency is also seen to shift due to the escort acting partially as a temporal filter on the signal.
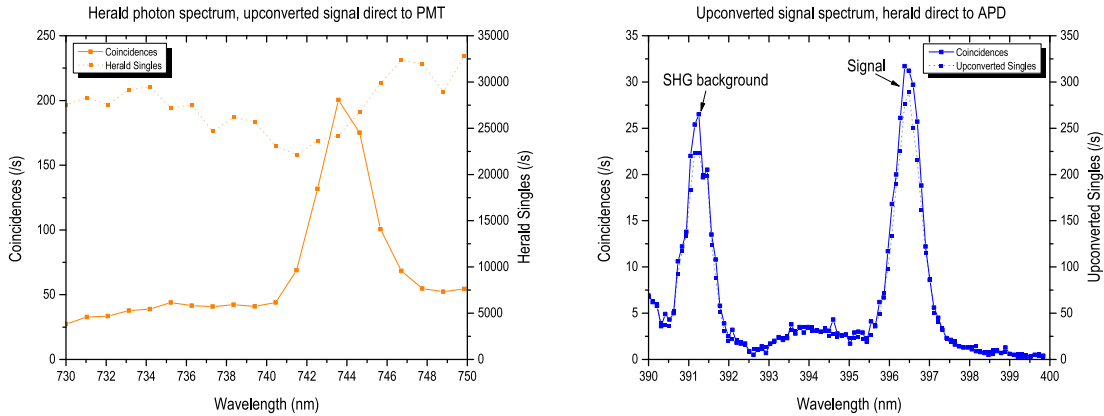
Figure 6.6: **Marginal spectra with spectral filters removed.** The herald (left) and upconverted signal (right) photonic spectra are shown with no spectral filters applied, coincident with their partner which is detected directly (i.e. not spectrally resolved). It is seen that the upconverted signal coincidence spectrum (solid line) is very close to its single-detection event spectrum (dashed line), whereas the herald coincidence spectrum is greatly narrowed relative to its broad singles spectrum, indicating a limited spectral support. Incidentally, the background due to SHG can be seen on the upconverted marginal spectra, and is seen to be clearly spectrally distinguishable.

the signal (herald). After upconversion (but before the spectrometer), approximately 980 coincidence counts (7820 upconverted singles) per second were measured, with approximately 110 (2820) of those being background, of which the most significant source was the second harmonic of the escort pulse. This second harmonic background is spectrally resolvable from the upconverted photons, and thus does not have a significant effect on the joint spectral measurements.

6.3 Joint spectral measurement results

6.3.1 Analysis of the joint spectral intensity

As is natural for SPDC sources, the joint spectrum of the signal and herald before the time lens has negative frequency correlations consistent with energy conservation, as seen

Property	Input		Output	
	Raw	Deconvolved	Raw	Deconvolved
Signal central wavelength	(811.006 ± 0.003) nm		(396.113 ± 0.004) nm	
Signal bandwidth	(4.047 ± 0.005) nm	(4.034 ± 0.006) nm	(0.621 ± 0.010) nm	(0.60 ± 0.01) nm
σ_s	(4.925 ± 0.006) THz	(4.909 ± 0.007) THz	(3.17 ± 0.05) THz	(3.04 ± 0.05) THz
Herald central wavelength	(740.194 ± 0.003) nm		(740.126 ± 0.018) nm	
Herald bandwidth	(3.733 ± 0.005) nm	(3.716 ± 0.006) nm	(2.50 ± 0.04) nm	(2.47 ± 0.04) nm
σ_h	(5.453 ± 0.008) THz	(5.429 ± 0.009) THz	(3.65 ± 0.06) THz	(3.61 ± 0.06) THz
Correlation ρ	-0.97024 ± 0.00015	-0.9776 ± 0.0009	0.863 ± 0.003	0.909 ± 0.005
Schmidt rank K	4.13 ± 0.01	4.75 ± 0.1	1.98 ± 0.03	2.39 ± 0.06
Joint energy uncertainty	(0.334 ± 0.001) THz	(0.333 ± 0.001) THz	(0.468 ± 0.008) THz	(0.455 ± 0.008) THz
$g_{s,h}^{(2)}$	4.190 ± 0.002		3.34 ± 0.03	

Table 6.1: **Joint spectral fit parameters.** Selected properties of the Gaussian fits to the joint spectra seen in Fig. 3 of the main text are given above. The deconvolved values are corrected for the finite resolution of the spectrometers used. All widths are reported full-width at half-maximum. We also calculate the Schmidt rank of the state under the assumption that the state is both pure and that any frequency-dependent phases do not affect the Schmidt decomposition, which is related to the statistical correlation as $K = (1 - \rho^2)^{-1/2}$ from the purity of the partial trace. The joint energy uncertainty is defined as the width of the semi-minor axis of an elliptical Gaussian fit. The error bars are determined from Monte Carlo simulation of the data with the assumption of Poissonian count statistics.

in Fig. 6.5a. On the other hand, the output joint spectrum seen in Fig. 6.5b exhibits clear positive frequency correlations, in contrast with the clear anti-correlations seen in the input joint spectrum. The measured joint spectra were then fit to a two-dimensional Gaussian.

The spectrometers used had a spectral resolution of approximately 0.1 nm. While this resolution allowed us to resolve the essential spectral features, this finite resolution is on the same order of magnitude as our spectra, which artificially broadened their measured features. To account for the limited resolution, we deconvolved the fit spectra with a Gaussian spectrometer response function. The fit parameters of the joint spectra produced from our SPDC source and after SFG are shown in Table 6.1. The statistical correlation ρ, defined as the covariance of two parameters divided by the standard deviation of each, of the signal and herald wavelength is statistically significant both before and after the time lens, and the negative-to-positive change indicates the reversal of the correlations.

The photon timescale in our experiment is on the order of hundreds of femtoseconds, which is well below the timing resolution of our detectors. As we could not measure the spectral phase, the time-domain distribution is not uniquely specified. Indeed, we expect that the upconverted photon is strongly chirped following the time lens. However, if we assume that the two-photon state is pure and coherent, it would be possible to reshape the joint temporal distribution to one with tight temporal anti-correlations using only spectral phase manipulations on the signal photon. Previous experiments have established that photons created through SPDC are genuinely entangled rather than merely correlated [298] and that SFG maintains coherence [52, 68, 208]. It would be possible to confirm genuine energy-time entanglement through a nonlocal interference experiment with spectral phase modulation [232] and additional temporal selection [256]. The timescale of our experiment could be accessible with additional nonlinear processes [294].

We also calculate the second-order cross-correlation function between the signal and herald photon, $g_{s,h}^{(2)} = \frac{P_{s\&h}}{P_s P_h}$ (as explained in Sec. 1.1.3) by comparing the coincidences with the single-detection events before the spectrometers [26, 27], where a value above two indicates nonclassicality if we assume that the individual second-order statistics of the signal and herald are at most thermal (as expected for a pure single-photon state) [27]. The values of the second-order cross-correlation function of the herald with the initial and upconverted signal photon are given in Table 6.1, and are significantly above two in both cases. The lower $g_{s,h}^{(2)}$ value of the upconverted light can be attributed to the spectrally distinguishable uncorrelated second-harmonic background which reaches the detectors.

While the upconversion efficiency of the time lens in our experiment is low, the limi-

190

tations are practical rather than fundamental [168]. As the escort used in our experiment is approximately the same spectral width as the photons and has a chirp half as strong, its chirped temporal duration does not fully envelop the signal photon. As such, it acts partially like a temporal filter, evidenced by the reduction in the herald bandwidth and statistical correlation of the final joint spectrum, as seen clearly in Fig. 6.6. An escort pulse with a significantly broader spectrum than the photon would increase the efficiency of the process. Further efficiency concerns could be addressed with higher power escort pulses and materials with stronger nonlinearities, although phasematching restrictions must be carefully considered.

As the resolution of our detectors is much larger than hundreds of femtoseconds, the time-domain distribution was not directly measured. The temporal distribution is not uniquely specified based strictly on the joint spectral intensity, as the spectral phase is unknown. However, if the two-photon state is pure and coherent, it would be possible to reshape the upconverted joint temporal distribution to one which is transform-limited with tight temporal anti-correlations using only spectral phase manipulations on the signal photon. Additionally, joint spectral phases can only increase the amount of entanglement, as seen in Sec. 3.2.2. The timescale of our experiment could be measurable with additional nonlinear processes [294], and genuine energy-time entanglement could be confirmed through a nonlocal interference experiment with additional temporal selection [256]. Previous experiments have established that photons created through SPDC are energy-time entangled rather than classically correlated [298] and that SFG maintains coherence [52, 68, 208].

6.3.2   Tunability of the joint spectrum

When a spatial lens is off-center relative to the incoming beam, the focus of the beam is translated, as in Fig. 6.7a-b. Analogously, when a relative delay exists between the escort pulse and the input signal in an upconversion time lens, the central frequency of the upconverted signal will shift; a similar behaviour occurs in chirped-pulse bandwidth compression [161]. This occurs as the relationship between the instantaneous frequencies of the chirped signal and anti-chirped escort are shifted, resulting in an overall central
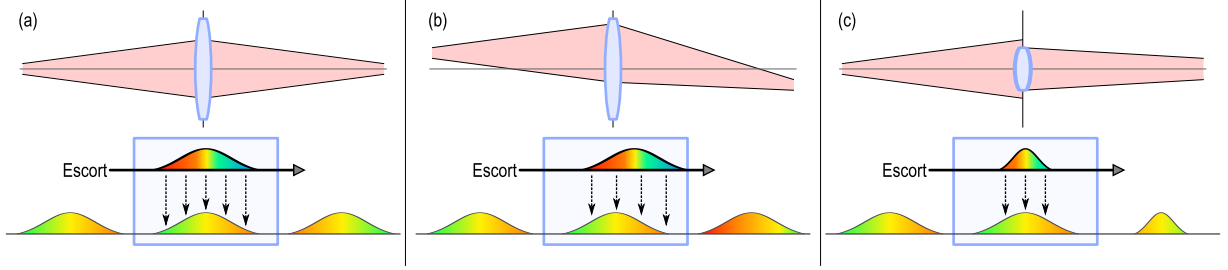
Figure 6.7: **Analogy between spatial and spectral tunability with a time lens.** (a) The effect of the escort pulse on the signal in an upconversion time lens can be understood in analogy with the action of a lens in a spatial imaging system. (b) In an analogous fashion to how shifting the spatial center of a lens causes the deflection of a beam in space, a relative time delay on the escort pulse of an upconversion time lens causes a shift in the center frequency of the upconverted light. (c) If the spectral support of the escort pulse is limited, the upconverted light will have a narrower spectrum and longer temporal duration than the ideal scenario, analogous to a lens with limited clear aperture.

frequency shift. We show this in our experimental joint spectra in Fig 6.5c. By tuning the relative delay over a range of ∼13 ps, the central frequency can be tuned over a range of ∼2 THz. However, it is seen that the central wavelength of the herald also changes as the delay is changed, as the upconversion time lens does not uniformly support the entire bandwidth of the input photon.

When we neglect the effects of limited escort bandwidth and restrictive phasematching (i.e. $\sigma_e \to \infty$ and $\Phi_{SFG}(\omega_1, \omega_3 - \omega_1, \omega_3) \approx 1$) and take the large-chirp limit, the central frequency of the upconverted signal from an $M = -1$ time lens can be found to be simply

$$\omega_{03}^{(ideal)} = \omega_{01} + \omega_{0e} + \frac{\tau}{A_1}, \tag{6.16}$$

where τ is a relative delay applied to the signal, ω_{01} and ω_{0e} are the central frequencies of the input signal and escort pulse respectively, and A_1 is the chirp on the input signal (the escort chirp A_e is assumed to be exactly $-\frac{1}{2}A_1$, as needed for $M = -1$). The shift in herald center frequency, $\delta\omega_{0h,f}$, is zero in this limit.

However, once limited escort bandwidth and phasematching are taken into considera-

192
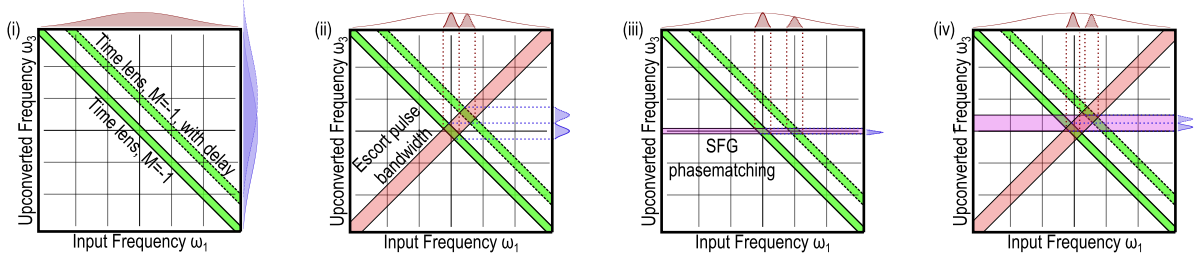
Figure 6.8: **Effect of chirps, escort bandwidth, and phasematching on spectral shifts in an upconversion time lens.** The reason both the output signal and herald central wavelengths may change can be understood by taking into account the effect of the chirp, finite escort bandwidth, and finite phasematching. The four plots shown give the mapping of an input frequency to an output frequency in the time-lens scenario; in the case where the input signal is frequency anti-correlated with a herald, the expected value of herald in the joint state will shift depending on what portions of the input were successfully upconverted. (i) The chirps in the pulse, assuming a magnification of $M = -1$, flip an input frequency blue-shifted relative to its centre to one red-shifted of its new centre. Introducing a time delay effectively changes the centre, as can be visualized with two offset negatively sloped diagonal lines. In the absence of other effects, the input spectra is accepted in full, and thus the herald spectra will be unchanged when measured in coincidence. (ii) The sum-frequency process must conserve energy, and limiting the bandwidth of the escort pulse will enforce stricter conservation. If we consider the limit where the pulses are stretched well beyond their Fourier-limited widths by the chirp, this will result in the escort pulse acting as a filter, causing corresponding shifts in the signal and herald central frequencies when measured in coincidence. (iii) In the limit when the escort and input signal are degenerate in the sum-frequency process, the phasematching is roughly a restriction on the upconverted frequencies accessible. As changing the time delay changes which input frequency converts to a specific upconverted frequency, the herald spectrum may shift while the upconverted spectrum remains stable in this limit. (iv) As we see both central frequencies change as a function of delay but with difference slopes in terms of energy, we conclude that we observe a mixture of these competing effects.

tion, this approximation breaks down. The effect of each of these imperfections is described graphically in Fig. 6.8. In the large-chirp limit, we can look at the limit where $\sigma_e \ll \sigma_1$, i.e. the escort is much narrower spectrally than the input signal. In this case, the chirped escort is much narrower in time than the chirped photon, and the upconversion acts as a
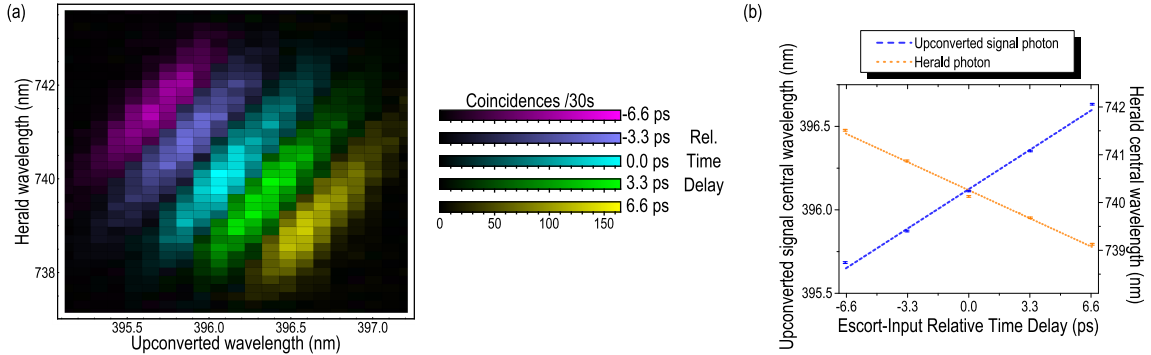
Figure 6.9: **Joint spectrum tunability.** (a) Five measured joint spectra are shown with varied relative time delays between the escort pulse and input signal, rearranged from Fig. 6.5. The shift in both the herald and output signal central wavelength is clearly apparent, but positive correlations are maintained throughout. (b) The fit upconverted (herald) central wavelength is seen to increase (decrease) as the relative delay is increased, with a best-fit slope of 0.071 nm/ps (-0.179 nm/ps).

filter, as shown in Fig. 6.7c. The central frequency shifts are then

$$\lim_{\sigma_e \ll \sigma_1} \delta\omega_{03} \overset{LCL}{=} \frac{\tau}{2A_1} \tag{6.17}$$

$$\lim_{\sigma_e \ll \sigma_1} \delta\omega_{0h,f} \overset{LCL}{=} \frac{\rho\sigma_{h,i}\tau}{2A_1\sigma_1}. \tag{6.18}$$

If $\sigma_{h,i} \approx \sigma_1$ and the initial photon pair has strong frequency anti-correlations $\rho_i \approx -1$, the shift in each is simply opposite, which is due to selecting different parts of the input rather than upconverting the entire pulse.

We next look at the limit where the phasematching is restrictive. As we experimentally consider a sum-frequency process which is nearly degenerate between the escort and input signal, we make the approximation that the group velocities in the sum-frequency media of the two inputs are roughly equal. In this case, the phasematching function $\Phi_{SFG}(\omega_1, \omega_e, \omega_3) \approx \Phi_{SFG}(\omega_3)$, which we approximate to a Gaussian which grows tighter as the effective crystal length L is increased. In the large-chirp long-crystal limit, the upconverted signal is effectively untunable as phasematching restricts it to a specific output

194

waveform, but the herald central frequency is found to be

$$\lim_{LCL} \lim_{L\to\infty} \delta\omega_{0h,f} = \frac{\rho\sigma_{h,i}\tau}{A_1\sigma_1}. \tag{6.19}$$

The herald changes since the phasematching only allows one frequency to be upconverted to, and the chirps applied force every interaction to be nearly monochromatic. Delaying the input signal changes which combination of frequencies from the escort and signal will combine to the accepted upconversion frequency, and will change which part of the input signal is upconverted.

We took five joint spectra as the delay between the escort and input signal was altered, as seen in Fig 6.5c and Fig. 6.9a, and saw a shift in both the herald and signal central frequencies, as seen in Fig. 6.9b. Given our chirp parameter of $A_1 = 696 \times 10^3 \text{fs}^2$, we

		Upconverted signal tunability		Herald tunability	
Effective crystal length L	Effective escort band-width σ_e	$\delta\omega_{03}/2\pi$	$\delta\lambda_{03}$	$\delta\omega_{0h}/2\pi$	$\delta\lambda_{0h}$
Measured		0.14 THz/ps	0.071 nm/ps	-0.097 THz/ps	-0.18 nm/ps
$L_{meas.}$	$\sigma_{e,meas.}$	0.12 THz/ps	0.061 nm/ps	-0.12 THz/ps	-0.22 nm/ps
$0.65 \times L_{meas.}$	$\sigma_{e,meas.}$	0.14 THz/ps	0.071 nm/ps	-0.099 THz/ps	-0.18 nm/ps
0	∞	0.23 THz/ps	0.121 nm/ps	0 THz/ps	0 nm/ps
0	$\sigma_{e,meas.}$	0.16 THz/ps	0.081 nm/ps	-0.080 THz/ps	-0.14 nm/ps
$L_{meas.}$	∞	0.12 THz/ps	0.063 nm/ps	-0.11 THz/ps	-0.21 nm/ps

Table 6.2: **Expected tunabilities with various assumptions.** The expected tunabilities of the central frequency for the upconverted signal and herald are given for a variety of assumptions, and can be compared with the tunabilities measured in the experiment, shown in Fig. S-6.9. The experimental results are in agreement with the theory when the length is scaled to 65% of its physical value, likely due to the non-collinear geometry of the interaction. The ideal-world theory corresponds to where the phasematching is nonrestrictive ($L = 0$) and the escort has infinite spectral support ($\sigma_e \to \infty$). The experimental values are $L_{meas.} = 1$ mm and $\sigma_{e,meas.} = 7.38 \times 10^{12} \text{s}^{-1} = 5.53$ nm FWHM.
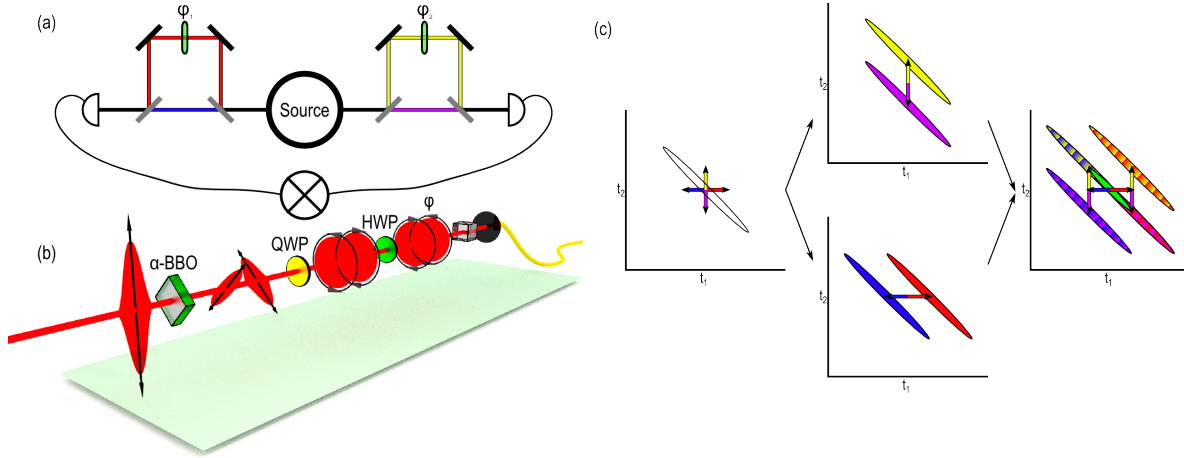
Figure 6.10: **Two-photon spectral interference concept.** (a) Nonlocal interference fringes can be seen by sending each photon of a two-photon energy-time entangled pair through an unbalanced interferometer and altering the phase in one arm. In the ideal case, fringes should be visible in the coincidence measurements but not the single-detection events. (b) In our experiment, the unbalanced interferometer and phases are implemented through birefringent materials and wave-plates. A birefringent crystal splits a horizontally polarized photon into a diagonal portion and a delayed anti-diagonal portion. A quarter-wave plate converts diagonal and anti-diagonal to left- and right-circularly polarized light. A half-wave plate then introduces a phase between the circularly polarized photons. The polarization information is then erased with a polarizing beamsplitter. (c) When the state is anti-correlated in time (positive spectral correlations), the interference is between the semi-indistinguishable late-early and early-late paths (blue-yellow and red-magenta). The visibility should be proportional to their overlap, visualized in green.

would expect a tunability of $0.23\frac{THz}{ps} = 0.12\frac{nm}{ps}$ in an idealized case, but instead measure $0.14\frac{THz}{ps} = 0.071\frac{nm}{ps}$. The herald central frequency is also shifted, which would not occur ideally, with a slope of $-0.097\frac{THz}{ps} = -0.18\frac{nm}{ps}$. Our results are inconsistent with the idealized theory, as mentioned above, but are relatively consistent with a process modelled by the bandwidths we measured and a shortened effective crystal length, as seen in Table 6.2. The shortened effective crystal length is expected as the signal photon and escort are combined non-collinearly in the upconversion medium and therefore do not interact for the entire length of the crystal.

196
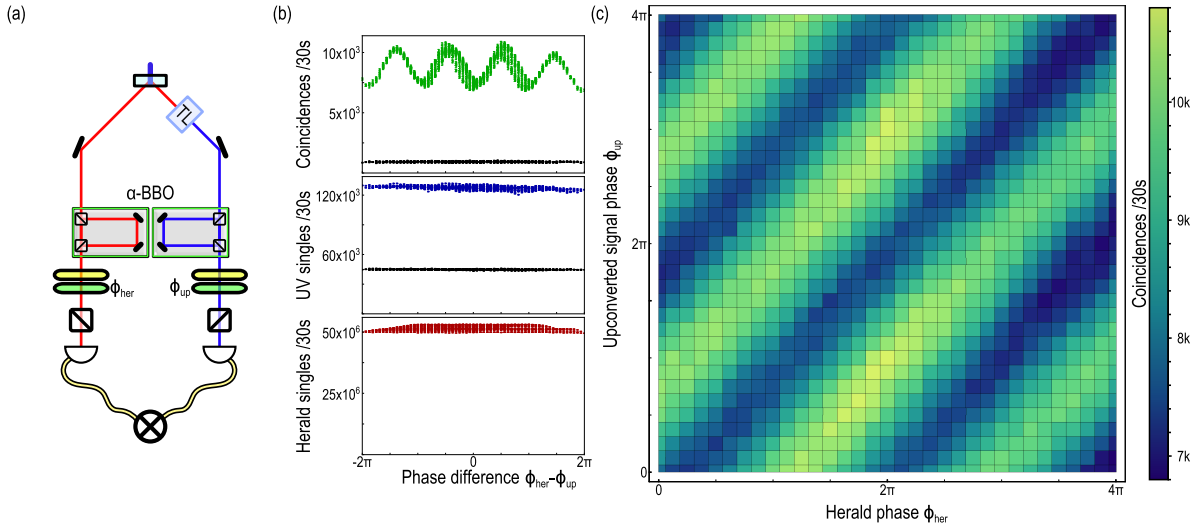
Figure 6.11: **Two-photon interference fringes.** (a) The two-photon interferometer [256] produces interference fringes when two photons from a correlated source are split into early and late time bins and recombined with a phase applied to one bin. In our experiment, this interferometer was implemented on a picosecond timescale using short birefringent crystals (α-BBO), waveplates, and polarizers, occurring after the time lens (TL) in the case of the signal. (b) The fringe visibility of the coincidences between the upconverted signal and herald viewed as a function of the phase difference display oscillations of $(15.6 \pm 1.0)\%$ visibility, while the single-detection events of the upconverted photons and herald display are nearly flat with no discernable periodicity. Background counts obtained by blocking the input signal photon are shown in black. (c) A correlated interference pattern can be seen in the coincidences by the dependence of fringe oscillation on the difference of the two phases applied.

6.4 Two-photon spectral interference

As an independent measure of the spectral correlation of the upconverted signal, we measure two-photon interference using an ultrafast Franson-style interferometer [256, 298, 199], as sketched in Fig. 6.10a. Two optical paths from a common source are split into a short and long path, with controllable phases ϕ between them. The difference between the short and long paths should be larger than the individual coherence time of each photon such

that no interference is seen in each individual path as the phase is varied. However, if the two photons have a joint coherence time as well, it is possible to see interference in the coincidence rate between the two potentially distant arms. If the photon source is frequency correlated, it will exhibit temporal anti-correlations, such that if one photon is ahead of the central time, the other will be delayed. As seen in Fig. 6.10c, if the two photons take different paths (i.e. short-long or long-short), there will be interference in the coincidence terms. However, the short-short and long-long paths are distinguishable and will not interfere, placing an intuitive 50% visibility limit without further temporal selection.

If the two-photon spectrum can be described in the Gaussian form with time delays τ_i and phases in the long arm of ϕ_i as

$$
\begin{aligned}
F(\omega_1, \omega_2) = & \frac{\exp\left[\frac{1}{1-\rho^2}\left(-\frac{(\omega_1-\omega_{01})^2}{4\sigma_1^2} - \frac{(\omega_2-\omega_{02})^2}{4\sigma_{h,i}^2} - \frac{\rho_i(\omega_1-\omega_{01})(\omega_2-\omega_{02})}{2\sigma_1\sigma_2}\right)\right]}{\sqrt{2\pi}\sigma_1\sigma_2(1-\rho^2)^{1/4}} \\
& \times \frac{1}{2}(1 + e^{-i\omega_1\tau_1+i\phi_1})(1 + e^{-i\omega_2\tau_2+i\phi_2}),
\end{aligned}
\tag{6.20}
$$

then the overall coincidence rate without spectral or temporal resolution can be found as

$$
\begin{aligned}
C(\phi_1, \phi_2) = & \iint_{-\infty}^{\infty} \mathrm{d}\omega_1 \mathrm{d}\omega_2 \left|F(\omega_1, \omega_2)\right|^2 \\
\propto & \, 1 + e^{-\frac{1}{2}\sigma_1^2\tau_1^2}\cos\phi_1 + \frac{1}{2}e^{-\frac{1}{2}\left(\sigma_1^2\tau_1^2 - 2\rho\sigma_1\sigma_2\tau_1\tau_2 + \sigma_2^2\tau_2^2\right)}\cos(\phi_1 - \phi_2) \\
& + \frac{1}{2}e^{-\frac{1}{2}\left(\sigma_1^2\tau_1^2 + 2\rho\sigma_1\sigma_2\tau_1\tau_2 + \sigma_2^2\tau_2^2\right)}\cos(\phi_1 + \phi_2) + e^{-\frac{1}{2}\sigma_2^2\tau_2^2}\cos\phi_2
\end{aligned}
$$

The single-detection events, on the other hand, have interference fringes described by

$$
S_j(\phi_j) \propto 1 + e^{-\frac{1}{2}\sigma_j^2\tau_j^2}\cos\phi_j.
\tag{6.21}
$$

Since Eq. (6.21) depends on the intensity rather than the field, the interference is independent of chirps and other applied dispersion.

For frequency anti-correlations ($\rho < 0$), we expect to see nonlocal interference depending on $\phi_1 + \phi_2$; for positive frequency correlations, we expect to see the interference depen-

dent on $\phi_1 - \phi_2$ instead. As a special case, we consider a Gaussian frequency anti-correlated source from SPDC whose terms depend on phasematching, filters, and pump bandwidth as in Eq. (3.39). If the two time delays τ are equal, the frequency anti-correlated interference will decay as $\exp\left[-\frac{1}{2}\left(\sigma_1 + 2\rho\sigma_1\sigma_2 + \sigma_2^2\right)\tau^2\right]$. In the limit where phasematching is loose $(L \to 0)$ and the filter bandwidths are much broader than the pump bandwidth, this decay is exactly equal to the temporal duration of the pump pulse, which defines the overall temporal duration of the biphoton waveform. To see high visibility coincident interference and no single-detection event visibility, it is necessary to set the time delays τ_i to be much larger than the individual coherence time of each photon (defined mainly by filtering) but smaller than the joint coherence time of the biphoton (often defined primarily by the pump length).

We use 2-mm birefringent α-barium borate (α-BBO) crystals at 45 degrees to split the upconverted signal and herald into two time bins with orthogonal polarizations separated by approximately 1.02 ps and 0.82 ps, respectively, where the difference is due to their central wavelengths. We control the phase between the two bins with two waveplates and measure in superposition by projecting into linear polarization with a polarizing beam-splitter, as seen in Fig. 6.11a and Fig. 6.10b. The average visibility of the coincidence detection events seen in Fig. 6.11b is $(15.6 \pm 1.0)\%$, or $(17.5 \pm 1.2)\%$ when background subtracted. In contrast, the visibility in the single-detection events in the upconverted and herald arms are, respectively, $(0.4 \pm 0.4)\%$ and $(0.06 \pm 0.04)\%$. In Fig. 6.11c, it can be seen that the fringe phase depends on the difference of the two phases, which is indicative of spectral correlation, and Fig. 6.11b shows that this periodicity is only notable for the coincidence detections.

While we cannot use the interference observed to verify entanglement, we can use it to verify correlation independently of the joint spectral analysis. Generally, an interference fringe can be represented as $a(1 + V\cos\theta)$, where θ is a hidden variable which may depend on some hidden distribution. The visibility, defined as $V = \frac{max - min}{max + min}$, of two-site uncorrelated interference is limited to $V_{uncorr} = \frac{V_1 + V_2}{1 + V_1 V_2}$. In the limit of no entanglement ($\rho = 0$), Eq. (6.21) simplifies to this. To show correlation, we simply need to show a visibility greater than V_{uncorr}. Using the data displayed in Fig. 6.11b-c, we fit each slice (i.e. holding either ϕ_{up} or ϕ_{her} constant) to a sinusoid and find an average visibility in the coincidence counts

199

of $(15.6\pm1.0)\%$, which increases to $(17.5\pm1.2)\%$ when the background is subtracted. The upconverted singles have a visibility of only $(0.4\pm0.4)\%$, or $(0.9\pm0.5)\%$ when background subtracted, and the herald singles have a visibility of just $(0.06\pm0.04)\%$. Using these visibilities, we find that $V_C-V_{uncorr} = (15.2\pm1.1)\%$ or $(16.6\pm1.3)\%$ background subtracted, more than 13 standard deviations above uncorrelated in either case. Additionally, the fringes of Fig. 6.11b display the expected $\cos(\phi_1 - \phi_2)$ dependence of positive frequency correlations. Given the joint spectrum of Fig. 6.5, a coincidence visibility of 21.3% is expected, and single-detection event visibilities of 0.8% and 1.3% were expected for the upconverted and herald arms respectively. In addition to second-harmonic background, double-pair emission and a small but non-negligible walkoff in the α-BBO reduce the observed visibilities.

Note from Eq. (6.21) that, without temporal selection, the coincidence rate is entirely dependent on the joint spectral *intensity*, not the field, and therefore gives no information on the temporal domain. With temporal filtering to eliminate unwanted coincidences, or with spectral resolution and frequency shifts replacing the time delays, it is possible to use this interference as a genuine measure of entanglement [256, 298]; as the timescales in our experiment were much smaller than detector resolution, this was unfortunately not an option. These timescales are accessible, however, with additional nonlinear processes [294].

Conclusion

We have demonstrated control of a twin-photon joint spectral intensity through the use of an upconversion time lens on the ultrafast timescale. The technique presented maintains two-photon correlations and introduces minimal background noise at the target wavelengths. The time lens demonstrated here is an essential component of a general quantum temporal imaging system, capable of essential tasks such as bandwidth compression, time-to-frequency conversion, and all-optical transformations on time-bin encoded qubits. Control of the correlation of joint spectra as demonstrated here can be used to create spectrally correlated two-photon states at wavelengths where efficient nonlinear materials with extended phasematching conditions do not exist [180, 294, 182, 183]. Such a technique may

be directly useful for shaping the spectra of entangled pairs for long-distance communications, quantum-enhanced metrology [7], and more generally to mold the time-frequency distributions of single photons for experiments both fundamental and practical.

Chapter 7

Conclusion and Outlook

We have examined and experimentally demonstrated the use of sum-frequency generation and pulse shaping for quantum optical waveform conversion. In Chapter 3, we showed that these tools can be used to efficiently manipulate single photons, and gave the conditions required to obtain such efficiency. In Chapter 4, we implemented a superposition of time-to-frequency converters to coherently measure a superposition of time bins into an upconverted mode. In Chapter 5, we used these tools as a time-to-frequency converter to read an ultrafast train of single-photon pulses into discernable frequency bins. In Chapter 6, we used these tools to implement an upconversion time lens, which we then used to shape the joint spectrum of a photon pair.

The most obvious route forward from our current experimental work is to improve the efficiency. While this can be difficult to do while maintaining assumptions such as unrestrictive phasematching, we have shown in Chapter 3 that it is possible in principle. Moving our experiments to the telecommunications wavelengths opens the door to a wide range of nonlinear materials that we were unable to explore. Contemporary experiments on temporal modes may offer a way forward through dispersion engineered waveguides, which greatly increase the interaction length and are capable of isolating input temporal modes into upconverted modes with high efficiencies [58, 62, 299]. By re-converting the upconverted mode with a different shaped escort pulse, a great deal of control over the spectra form of single photons could be exercised. Certain quantum memory schemes

also have great potential for read-out/read-in waveform manipulation [27]. For on-the-fly reshaping, for which mode selectivity is unnecessary and often undesirable, broadband engineered waveguides may find application, such as those with chirped poling periods to allow for broadband operation [300, 194]. Additionally, electro-optic modulators can be used to effectively and efficiently impart linear and quadratic spectral phases on ultrafast single-photon waveforms [148, 149].

A complete waveform manipulation toolkit would be incredibly useful for reasons outlined throughout this thesis and others. In particular, interfacing different types of photon sources could be used to combine the advantages of each. Single-photon quantum emitters such as quantum dots generally have very narrowband frequency profiles with exponentially decaying temporal profiles, but by shaping them to short Gaussian profiles, they could be integrated much more easily into telecommunications networks based on fast pulse sequences [224, 225, 301]. We have only scratched the surface of source engineering applications as well. Combining shaping of the pump pulse with manipulation of the downconverted photons could potentially be used to create a wide range of time-frequency photon states. Combining time-frequency state engineering with information in other degrees of freedom, such as polarization or spatial mode, could be used to create and manipulation highly multimode carriers of quantum information, with numerous options for information-containing modes and control modes to allow for precise manipulation [29].

Photonics has played a key role since the birth of quantum information science [1], and is expected to continue to do so as we make the transition from theory to laboratory to real-world implementation. Control over the temporal waveforms of photons is paramount to exploiting their full potential, and it is our hope that the toolbox outlined in this thesis will play an important role in realizing this.

References

[1] Knill, E., Laflamme, R. & Milburn, G. J. A scheme for efficient quantum computation with linear optics. *Nature (London)* **409**, 46–52 (2001). 1, 113, 203

[2] Kok, P. *et al.* Linear optical quantum computing with photonic qubits. *Reviews of Modern Physics* **79**, 135 (2007). 1

[3] Ladd, T. D. *et al.* Quantum computers. *Nature* **464**, 45–53 (2010). 1

[4] Bennett, C. H. & Brassard, G. Quantum cryptography: Public key distribution and coin tossing. In *Proceedings of IEEE International Conference on Computers, Systems and Signal Processing*, vol. 175 (IEEE (New York, NY), 1984). 1, 154

[5] Gisin, N. & Thew, R. Quantum communication. *Nat Photon* **1**, 165–171 (2007). 1

[6] Boto, A. N. *et al.* Quantum interferometric optical lithography: exploiting entanglement to beat the diffraction limit. *Phys. Rev. Lett.* **85**, 2733 (2000). 1

[7] Giovannetti, V., Lloyd, S. & Maccone, L. Quantum-enhanced positioning and clock synchronization. *Nature* **412**, 417–419 (2001). 1, 176, 201

[8] Gerry, C. C. & Knight, P. L. *Introductory Quantum Optics* (Cambridge University Press, Cambridge, 2005). 2, 5, 8, 9, 11, 15

[9] Fox, M. *Quantum Optics: An Introduction* (Oxford Univ. Press, Oxford, 2006). 2, 7, 8, 9

[10] Resch, K. J. *Quantum Optics Course Notes* (2012). University of Waterloo. 2, 3, 8, 11

[11] Blow, K. J., Loudon, R., Phoenix, S. J. D. & Shepherd, T. J. Continuum fields in quantum optics. *Phys. Rev. A* **42**, 4102–4114 (1990). 3, 4

[12] Hong, C. K., Ou, Z. Y. & Mandel, L. Measurement of subpicosecond time intervals between two photons by interference. *Phys. Rev. Lett.* **59**, 2044–2046 (1987). 6, 245

[13] Lita, A. E., Miller, A. J. & Nam, S. W. Counting near-infrared single-photons with 95% efficiency. *Opt. Express* **16**, 3032–3040 (2008). 6, 16

[14] Marsili, F. *et al.* Detecting single infrared photons with 93% system efficiency. *Nature Photon.* **7**, 210–214 (2013). 6, 16, 113

[15] Harder, G. *et al.* A source for mesoscopic quantum optics. *arXiv:1510.05801* (2015). 6, 16

[16] Hadfield, R. H. Single-photon detectors for optical quantum information applications. *Nat. Photon.* **3**, 696–705 (2009). 6, 75, 113, 135, 154

[17] Achilles, D., Silberhorn, C., Śliwa, C., Banaszek, K. & Walmsley, I. A. Fiber-assisted detection with photon number resolution. *Opt. Lett.* **28**, 2387–2389 (2003). 6

[18] Miatto, F., Safari, A., Boyd, R. W. *et al.* Theory of multiplexed photon number discrimination. *arXiv:1601.05831* (2016). 6

[19] Bartlett, S. D., Rudolph, T. & Spekkens, R. W. Dialogue concerning two views on quantum coherence: factist and fictionist. *International Journal of Quantum Information* **4**, 17–43 (2006). 7

[20] Agarwal, G. & Tara, K. Nonclassical properties of states generated by the excitations on a coherent state. *Physical Review A* **43**, 492 (1991). 7

[21] Hanbury-Brown, R. & Twiss, R. Q. Correlation between photons in two coherent beams of light. *Nature* **177**, 27–29 (1956). 9, 245

[22] Kimble, H. J., Dagenais, M. & Mandel, L. Photon antibunching in resonance fluorescence. *Physical Review Letters* **39**, 691 (1977). 11

[23] Christ, A., Laiho, K., Eckstein, A., Cassemiro, K. N. & Silberhorn, C. Probing multimode squeezing with correlation functions. *New Journal of Physics* **13**, 033027 (2011). 11, 12

[24] Clauser, J. F. Experimental distinction between the quantum and classical field-theoretic predictions for the photoelectric effect. *Phys. Rev. D* **9**, 853 (1974). 11

[25] Weisstein, E. W. Schwarz's inequality. URL http://mathworld.wolfram.com/SchwarzsInequality.html. 12

[26] Albrecht, B., Farrera, P., Fernandez-Gonzalvo, X., Cristiani, M. & de Riedmatten, H. A waveguide frequency converter connecting rubidium-based quantum memories to the telecom C-band. *Nat. Commun.* **5**, 3376 (2014). 12, 176, 190

[27] Fisher, K. A. G. *et al.* Frequency and bandwidth conversion of single photons in a room-temperature diamond quantum memory. *Nat. Commun.* **7**, 11200 (2016). 12, 114, 177, 190, 203

[28] Boyd, R. W. *Nonlinear Optics* (Academic, New York, 2008), 3rd edn. 13, 36, 40, 41, 43, 47, 51, 62, 63, 66, 116

[29] Humphreys, P. C. *et al.* Linear optical quantum computing in a single spatial mode. *Phys. Rev. Lett.* **111**, 150501 (2013). 16, 26, 176, 203

[30] Mair, A. *et al.* Entanglement of the orbital angular momentum states of photons. *Nature* **412**, 313–316 (2001). 16

[31] Leach, J., Padgett, M. J., Barnett, S. M., Franke-Arnold, S. & Courtial, J. Measuring the orbital angular momentum of a single photon. *Phys. Rev. Lett.* **88**, 257901 (2002). 16

[32] Agnew, M., Salvail, J. Z., Leach, J. & Boyd, R. W. Generation of orbital angular momentum bell states and their verification via accessible nonlinear witnesses. *Phys. Rev. Lett.* **111**, 030402 (2013). 16

[33] Nielsen, M. A. & Chuang, I. L. *Quantum Computation and Quantum Information* (Cambridge University Press, 2000). 17, 18, 20, 29, 34, 96

[34] Shor, P. W. Fault-tolerant quantum computation. In *Foundations of Computer Science, 1996. Proceedings., 37th Annual Symposium on*, 56–65 (IEEE, 1996). 17

[35] Hecht, E. *Optics* (Addison Wesley, San Francisco, 2002), 4th edn. 17, 64, 70, 123

[36] Saleh, B. E. A. & Teich, M. C. *Fundamentals of Photonics* (John Wiley and Sons, Hoboken, New Jersey, 2007), 2nd edn. 17, 52, 53, 66, 67, 69, 70, 98, 123

[37] Jozsa, R. Fidelity for mixed quantum states. *J. Mod. Opt.* **41**, 2315–2323 (1994). 19, 169

[38] Heinosaari, T., Reitzner, D. & Stano, P. Notes on joint measurability of quantum observables. *Foundations of Physics* **38**, 1133–1147 (2008). 20

[39] Donohue, J. M. & Wolfe, E. Identifying nonconvexity in the sets of limited-dimension quantum correlations. *Phys. Rev. A* **92**, 062120 (2015). 20, 30, 32

[40] Hamel, D. R. Realization of novel entangled photon sources using periodically poled materials (2010). 21, 49

[41] Vermeyden, L. Fundamental tests of quantum mechanics using two-photon entanglement (2014). 21, 38

[42] Agnew, M. Quantum tests of causal structures and non-orthogonal states (2014). 21

[43] James, D. F., Kwiat, P. G., Munro, W. J. & White, A. G. Measurement of qubits. *Phys. Rev. A* **64**, 052312 (2001). 21, 22, 169

[44] Ježek, M., Fiurášek, J. & Hradil, Z. Quantum inference of states and processes. *Phys. Rev. A* **68**, 012305 (2003). 21, 22, 149

[45] Langford, N. K. Encoding, manipulating and measuring quantum information in optics (2007). 21, 22

[46] Cholesky, A.-L. Sur la résolution numérique des systèmes déquations linéaires. *Bulletin de la Sabix. Société des amis de la Bibliothèque et de l'Histoire de l'École polytechnique* 81–95 (2005). 22

[47] Bhandari, R. Synthesis of general polarization transformers. a geometric phase approach. *Phys. Lett. A* **138**, 469–473 (1989). 24

[48] Ursin, R. *et al.* Entanglement-based quantum communication over 144 km. *Nat. Phys.* **3**, 481–486 (2007). 24

[49] Yan, Z. *et al.* Novel high-speed polarization source for decoy-state bb84 quantum key distribution over free space and satellite links. *J. Lightwave Tech.* **31**, 1399–1408 (2013). 24

[50] Tittel, W. *et al.* Violation of Bell inequalities by photons more than 10 km apart. *Phys. Rev. Lett.* **81**, 3563–3566 (1998). 24, 135

[51] Marcikic, I. *et al.* Distribution of time-bin entangled qubits over 50 km of optical fiber. *Phys. Rev. Lett.* **93**, 180502 (2004). 24, 25, 135

[52] Tanzilli, S. *et al.* A photonic quantum information interface. *Nature (London)* **437**, 116–120 (2005). 24, 135, 154, 176, 179, 190, 191

[53] ITU Recommendation. G.694.2 Spectral grids for WDM applications: CWDM wavelength grid (2002). 24

[54] ITU Recommendation. G.694.1 Spectral grids for WDM applications: DWDM frequency grid (2012). 24, 162

[55] Thew, R. T., Acin, A., Zbinden, H. & Gisin, N. Bell-type test of energy-time entangled qutrits. *Phys. Rev. Lett.* **93**, 010503 (2004). 24

[56] Olislager, L. *et al.* Frequency-bin entangled photons. *Phys. Rev. A* **82**, 013804 (2010). 24, 113, 122

[57] Nowierski, S., Oza, N. N., Kumar, P. & Kanter, G. S. Experimental reconstruction of time-bin-entangled qutrit states using polarization projective measurements. In *CLEO: QELS_Fundamental Science*, FTu2A–5 (Optical Society of America, 2015). 24, 176

[58] Eckstein, A., Brecht, B. & Silberhorn, C. A quantum pulse gate based on spectrally engineered sum frequency generation. *Opt. Express* **19**, 13770–13778 (2011). 25, 79, 85, 113, 135, 154, 176, 179, 202

[59] Huang, Y.-P. & Kumar, P. Mode-resolved photon counting via cascaded quantum frequency conversion. *Opt. Lett.* **38**, 468–470 (2013). 25

[60] Reddy, D. V., Raymer, M. G., McKinstrie, C. J., Mejling, L. & Rottwitt, K. Temporal mode selectivity by frequency conversion in second-order nonlinear optical waveguides. *Opt. Express* **21**, 13840–13863 (2013). 25, 85, 113

[61] Reddy, D. V., Raymer, M. G. & McKinstrie, C. J. Efficient sorting of quantum-optical wave packets by temporal-mode interferometry. *Opt. Lett.* **39**, 2924–2927 (2014). 25, 85

[62] Brecht, B. *et al.* Demonstration of coherent time-frequency Schmidt mode selection using dispersion-engineered frequency conversion. *Phys. Rev. A* **90**, 030302 (2014). 25, 202

[63] Brecht, B., Reddy, D. V., Silberhorn, C. & Raymer, M. G. Photon temporal modes: A complete framework for quantum information science. *Phys. Rev. X* **5**, 041017 (2015). 25, 85, 109, 113, 156, 176

[64] Brendel, J. *et al.* Pulsed energy-time entangled twin-photon source for quantum communication. *Phys. Rev. Lett.* **82**, 2594–2597 (1999). 25, 26, 135

[65] Thew, R. T., Tanzilli, S., Tittel, W., Zbinden, H. & Gisin, N. Experimental investigation of the robustness of partially entangled qubits over 11 km. *Phys. Rev. A* **66**, 062304 (2002). 25

[66] Tittel, W. *et al.* Quantum cryptography using entangled photons in energy-time Bell states. *Phys. Rev. Lett.* **84**, 4737–4740 (2000). 26, 135

[67] Martin, A. *et al.* Cross time-bin photonic entanglement for quantum key distribution. *Phys. Rev. A* **87**, 020301 (2013). 26, 135

[68] Donohue, J. M., Agnew, M., Lavoie, J. & Resch, K. J. Coherent ultrafast measurement of time-bin encoded photons. *Phys. Rev. Lett.* **111**, 153602 (2013). 26, 113, 134, 135, 154, 176, 179, 190, 191

[69] Scholz, V. B. & Werner, R. F. Tsirelson's problem. *arXiv:0812.4305* (2008). 27

[70] Horodecki, R., Horodecki, P., Horodecki, M. & Horodecki, K. Quantum entanglement. *Rev. Mod. Phys.* **81**, 865 (2009). 28, 35

[71] Gühne, O. & Tóth, G. Entanglement detection. *Physics Reports* **474**, 1–75 (2009). 28, 29, 35

[72] Schmidt, E. Zur theorie der linearen und nichtlinearen integralgleichungen. *Math. Annalen.* **63**, 433–476 (1907). 29

[73] Peres, A. Higher order schmidt decompositions. *Phys. Lett. A* **202**, 16–17 (1995). 29

[74] Barrett, J. *et al.* Nonlocal correlations as an information-theoretic resource. *Phys. Rev. A* **71**, 022101 (2005). 30

[75] Jones, N. S. & Masanes, L. Interconversion of nonlocal correlations. *Phys. Rev. A* **72**, 052312 (2005). 30

[76] Barrett, J. & Pironio, S. Popescu-Rohrlich correlations as a unit of nonlocality. *Phys. Rev. Lett.* **95**, 140401 (2005). 30

[77] Acín, A. *et al.* Device-independent security of quantum cryptography against collective attacks. *Phys. Rev. Lett.* **98**, 230501 (2007). 30

[78] Brunner, N., Cavalcanti, D., Pironio, S., Scarani, V. & Wehner, S. Bell nonlocality. *Rev. of Mod. Phys.* **86**, 419 (2014). 30, 32, 33, 34

[79] Fine, A. Hidden variables, joint probability, and the Bell inequalities. *Phys. Rev. Lett.* **48**, 291 (1982). 32, 33

[80] Popescu, S. & Rohrlich, D. Quantum nonlocality as an axiom. *Foundations of Physics* **24**, 379–385 (1994). 32, 34

[81] Bell, J. On the Einstein-Podolsky-Rosen paradox. *Physics* **1**, 195–200 (1964). 33, 135, 148

[82] Clauser, J. F. *et al.* Proposed experiment to test local hidden-variable theories. *Phys. Rev. Lett.* **23**, 880–884 (1969). 33, 135, 148, 245

[83] Cirel'son, B. S. Quantum generalizations of Bell's inequality. *Letters in Mathematical Physics* **4**, 93–100 (1980). 34

[84] Lundeen, J. S., Sutherland, B., Patel, A., Stewart, C. & Bamber, C. Direct measurement of the quantum wavefunction. *Nature* **474**, 188–191 (2011). 34

[85] Salvail, J. Z. *et al.* Full characterization of polarization states of light via direct measurement. *Nat. Photon.* **7**, 316–321 (2013). 34

[86] Pan, J.-W. *et al.* Multiphoton entanglement and interferometry. *Rev. Mod. Phys.* **84**, 777 (2012). 34

[87] Freedman, S. J. & Clauser, J. F. Experimental test of local hidden-variable theories. *Phys. Rev. Lett.* **28**, 938 (1972). 34

[88] Aspect, A., Grangier, P. & Roger, G. Experimental tests of realistic local theories via Bell's theorem. *Phys. Rev. Lett.* **47**, 460 (1981). 34

[89] Aspect, A., Dalibard, J. & Roger, G. Experimental test of Bell's inequalities using time-varying analyzers. *Phys. Rev. Lett.* **49**, 1804 (1982). 34

[90] Hensen, B. *et al.* Loophole-free Bell inequality violation using electron spins separated by 1.3 kilometres. *Nature* **526**, 682–686 (2015). 34

[91] Shalm, L. K. *et al.* Strong loophole-free test of local realism. *Phys. Rev. Lett.* **115**, 250402 (2015). 34

[92] Giustina, M. *et al.* Significant-loophole-free test of bells theorem with entangled photons. *Phys. Rev. Lett.* **115**, 250401 (2015). 34

[93] Howell, J. C., Lamas-Linares, A. & Bouwmeester, D. Experimental violation of a spin-1 bell inequality using maximally entangled four-photon states. *Phys. Rev. Lett.* **88**, 030401 (2002). 34

[94] Genovese, M. Research on hidden variable theories: A review of recent progresses. *Physics Reports* **413**, 319–396 (2005). 34

[95] Lavoie, J., Kaltenbaek, R. & Resch, K. J. Experimental violation of Svetlichny's inequality. *New J. Phys.* **11**, 073051 (2009). 34, 38, 105, 143

[96] Erven, C. *et al.* Experimental three-photon quantum nonlocality under strict locality conditions. *Nature photonics* **8**, 292–296 (2014). 34

[97] Arrazola, J. M., Gittsovich, O. & Lütkenhaus, N. Accessible nonlinear entanglement witnesses. *Phys. Rev. A* **85**, 062327 (2012). 35

[98] Arrazola, J. M. *et al.* Reliable entanglement verification. *Phys. Rev. A* **87**, 062331 (2013). 35

[99] Vidal, G. & Werner, R. F. Computable measure of entanglement. *Phys. Rev. A* **65**, 032314 (2002). 35

[100] Lavoie, J., Kaltenbaek, R., Piani, M. & Resch, K. J. Experimental bound entanglement in a four-photon state. *Physical review letters* **105**, 130501 (2010). 35

[101] Coffman, V., Kundu, J. & Wootters, W. K. Distributed entanglement. *Physical Review A* **61**, 052306 (2000). 35, 169

212

[102] Vermeyden, L. *et al.* Experimental violation of three families of Bell's inequalities. *Physical Review A* **87**, 032105 (2013). 35, 38

[103] Horodecki, R., Horodecki, P. & Horodecki, M. Quantum α-entropy inequalities: independent condition for local realism? *Phys. Lett. A* **210**, 377–381 (1996). 36, 96, 119

[104] Bennink, R. S. Optimal collinear Gaussian beams for spontaneous parametric down-conversion. *Phys. Rev. A* **81**, 053805 (2010). 36, 88, 90, 91, 113

[105] Kwiat, P. G. *et al.* Ultrabright source of polarization-entangled photons. *Phys. Rev. A* **60**, R773–R776 (1999). 37, 38, 103, 143, 159, 164

[106] Kim, T., Fiorentino, M. & Wong, F. N. Phase-stable source of polarization-entangled photons using a polarization Sagnac interferometer. *Phys. Rev. A* **73**, 012316 (2006). 37, 38

[107] Fedrizzi, A., Herbst, T., Poppe, A., Jennewein, T. & Zeilinger, A. A wavelength-tunable fiber-coupled source of narrowband entangled photons. *Optics Express* **15**, 15377–15386 (2007). 37, 38

[108] Midwinter, J. & Warner, J. The effects of phase matching method and of uniaxial crystal symmetry on the polar distribution of second-order non-linear optical polarization. *British J. of Appl. Phys.* **16**, 1135 (1965). 36

[109] Kim, Y.-H., Kulik, S. P. & Shih, Y. High-intensity pulsed source of space-time and polarization double-entangled photon pairs. *Phys. Rev. A* **62**, 011802 (2000). 38, 159

[110] Fiorentino, M., Messin, G., Kuklewicz, C. E., Wong, F. N. & Shapiro, J. H. Generation of ultrabright tunable polarization entanglement without spatial, spectral, or temporal constraints. *Phys. Rev. A* **69**, 041801 (2004). 38

[111] Griffiths, D. J. *Introduction to Electrodynamics*, vol. 3 (Prentice Hall Upper Saddle River, NJ, 1999). 40, 41

[112] Weisstein, E. W. Convolution theorem. URL http://mathworld.wolfram.com/ConvolutionTheorem.html. 44

[113] Quesada, N. & Sipe, J. Time-ordering effects in the generation of entangled photons using nonlinear optical processes. *Phys. Rev. Lett.* **114**, 093903 (2015). 49, 84

[114] Polyanskiy, M. RefractiveIndex.INFO. URL http://refractiveindex.info/. 49, 50

[115] AS-Photonics. SNLO. URL http://www.as-photonics.com/snlo. 50

[116] Kato, K. & Takaoka, E. Sellmeier and thermo-optic dispersion formulas for KTP. *Appl. Opt.* **41**, 5040–5044 (2002). 50

[117] Umemura, N., Miyata, K. & Kato, K. New data on the optical properties of BiB3O6. *Optical Materials* **30**, 532–534 (2007). 50

[118] Eimerl, D., Davis, L., Velsko, S., Graham, E. & Zalkin, A. Optical, mechanical, and thermal properties of barium borate. *J. Appl. Phys.* **62**, 1968–1983 (1987). 50

[119] Hum, D. S. & Fejer, M. M. Quasi-phasematching. *Comptes Rendus Physique* **8**, 180–198 (2007). 49

[120] Kolner, B. H. & Nazarathy, M. Temporal imaging with a time lens. *Opt. Lett.* **14**, 630–632 (1989). 52, 57, 63

[121] Kolner, B. Space-time duality and the theory of temporal imaging. *IEEE J. Quantum Electron.* **30**, 1951–1963 (1994). 52, 54, 57, 59, 64, 177

[122] Walmsley, I. A. & Dorrer, C. Characterization of ultrashort electromagnetic pulses. *Adv. Opt. Photon.* **1**, 308–437 (2009). 52, 58, 63, 75, 154, 177, 179

[123] Torres-Company, V., Lancisc, J. & Andrés, P. Space-time analogies in optics. *Progress in Optics* **56**, 1 (2011). 52

[124] Lavoie, J. *Chirped-pulse interferometry: classical dispersion cancellation and analogues of two-photon quantum interference.* Master's thesis, University of Waterloo (2009). 56, 70, 102

[125] Paschotta, R. Group velocity dispersion. URL https://www.rp-photonics.com/group_velocity_dispersion.html. 56

[126] Diels, J.-C. & Rudolph, W. *Ultrashort Laser Pulse Phenomena* (Academic press, 2006), 2nd edn. 57

[127] Weiner, A. *Ultrafast optics*, vol. 72 (John Wiley & Sons, 2011). 57, 66, 67, 70, 75, 107

[128] Paye, J. The chronocyclic representation of ultrashort light pulses. *IEEE J. of Quantum Electron.* **28**, 2262–2273 (1992). 58

[129] Brecht, B. & Silberhorn, C. Characterizing entanglement in pulsed parametric down-conversion using chronocyclic wigner functions. *Physical Review A* **87**, 053810 (2013). 58

[130] Donohue, J. M., Mastrovich, M. & Resch, K. J. Spectrally engineering photonic entanglement with a time lens. *arXiv:1604.03588* (2016). 59, 71, 175

[131] Bennett, C. V., Scott, R. P. & Kolner, B. H. Temporal magnification and reversal of 100 Gb/s optical data with an up-conversion time microscope. *Appl. Phys. Lett.* **65**, 2513–2515 (1994). 61, 178, 179

[132] Bennett, C. V. & Kolner, B. H. Upconversion time microscope demonstrating 103× magnification of femtosecond waveforms. *Opt. Lett.* **24**, 783–785 (1999). 61, 154

[133] McGuinness, H. J., Raymer, M. G., McKinstrie, C. J. & Radic, S. Quantum frequency translation of single-photon states in a photonic crystal fiber. *Phys. Rev. Lett.* **105**, 093604 (2010). 62, 113, 114

[134] Raymer, M. G. & Srinivasan, K. Manipulating the color and shape of single photons. *Physics Today* **65** (11), 32–37 (2012). 62, 113

[135] Li, Q., Davanco, M. & Srinivasan, K. Efficient and low-noise single-photon-level frequency conversion interfaces using silicon nanophotonics. *Nat. Photon.* **AOP** (2016). 62, 114

[136] Watanabe, S., Naito, T. & Chikama, T. Compensation of chromatic dispersion in a single-mode fiber by optical phase conjugation. *IEEE Photon. Tech. Lett.* **5**, 92–95 (1993). 62, 177

[137] Jopson, R., Gnauck, A. & Derosier, R. Compensation of fibre chromatic dispersion by spectral inversion. *IEEE Electron. Lett.* **29**, 576–578 (1993). 62, 177

[138] Foster, M. A. *et al.* Silicon-chip-based ultrafast optical oscilloscope. *Nature* **456**, 81–84 (2008). 62, 123, 177, 179

[139] Salem, R. *et al.* Optical time lens based on four-wave mixing on a silicon chip. *Opt. Lett.* **33**, 1047–1049 (2008). 62, 177

[140] Foster, M. A. *et al.* Ultrafast waveform compression using a time-domain telescope. *Nat. Photon.* **3**, 581–585 (2009). 62, 154, 177, 183

[141] Geng, Z., Corcoran, B., Zhu, C. & Lowery, A. J. Time-lenses for time-division multiplexing of optical OFDM channels. *Opt. Express* **23**, 29788–29801 (2015). 62

[142] Franco, M., Lange, H., Ripoche, J.-F., Prade, B. & Mysyrowicz, A. Characterization of ultra-short pulses by cross-phase modulation. *Opt. Commun.* **140**, 331–340 (1997). 63

[143] Mouradian, L. K., Louradour, F., Messager, V., Barthélémy, A. & Froehly, C. Spectro-temporal imaging of femtosecond events. *IEEE J. of Quant. Electron.* **36**, 795–801 (2000). 63

[144] Ng, T. T. *et al.* Compensation of linear distortions by using xpm with parabolic pulses as a time lens. *IEEE Photon. Tech. Lett.* **20**, 1097–1099 (2008). 63

[145] Matsuda, N. Deterministic reshaping of single-photon spectra using cross-phase modulation. *Sci. Adv.* **2**, e1501223 (2016). 63, 177

[146] Hall, M. A., Altepeter, J. B. & Kumar, P. Ultrafast switching of photonic entanglement. *Phys. Rev. Lett.* **106**, 053901 (2011). 63, 154, 176

216

[147] Dorrer, C. & Kang, I. Complete temporal characterization of short optical pulses by simplified chronocyclic tomography. *Optics letters* **28**, 1481–1483 (2003). 63

[148] Karpiński, M., Jachura, M., Wright, L. J. & Smith, B. J. Bandwidth manipulation of quantum light by an electro-optic time lens. *arXiv:1604.02459* (2016). 63, 70, 114, 122, 177, 203

[149] Wright, L. J., Karpiński, M., Söller, C. & Smith, B. J. Spectral shearing of quantum light pulses by electro-optic phase modulation. *arXiv:1605.00640* (2016). 63, 114, 203

[150] Schawlow, A. L. & Townes, C. H. Infrared and optical masers. *Phys. Rev.* **112**, 1940 (1958). 66

[151] Spence, D. E., Kean, P. N. & Sibbett, W. 60-fsec pulse generation from a self-mode-locked ti: sapphire laser. *Optics letters* **16**, 42–44 (1991). 66

[152] Spectra-Physics. *User Manual for Tsunami Mode-Locked Ti:sapphire Laser, Part Number 0000-232A, Rev. D* (2002). 67

[153] Paschotta, R. Peak power. URL https://www.rp-photonics.com/peak_power.html. 68

[154] Gunther, A. K. Ultrafast coincidence characteristics of entangled photons towards entangled two-photon absorption (2014). 69

[155] Treacy, E. Optical pulse compression with diffraction gratings. *IEEE J. Quantum Electron.* **5**, 454–458 (1969). 70, 71, 72, 145, 161

[156] Mazurek, M. Dispersion-cancelled imaging with chirped laser pulses (2013). 70

[157] Krug, P. *et al.* Dispersion compensation over 270 km at 10 Gbit/s using an offset-core chirped fibre bragg grating. *Electronics Letters* **31**, 1091–1093 (1995). 70

[158] Weiner, A. M. Femtosecond pulse shaping using spatial light modulators. *Rev. Sci. Instrum.* **71**, 1929–1960 (2000). 70, 114

[159] Légaré, F., Fraser, J., Villeneuve, D. & Corkum, P. Adaptive compression of intense 250-nm-bandwidth laser pulses. *Applied Physics B* **74**, s279–s282 (2002). 70

[160] Mazurek, M. D., Schreiter, K. M., Prevedel, R., Kaltenbaek, R. & Resch, K. J. Dispersion-cancelled biological imaging with quantum-inspired interferometry. *Sci. Reports* **3**, 1582 (2013). 70, 102, 143

[161] Lavoie, J., Donohue, J. M., Wright, L. G., Fedrizzi, A. & Resch, K. J. Spectral compression of single photons. *Nat. Photon.* **7**, 363–366 (2013). 72, 81, 113, 129, 130, 132, 135, 137, 145, 154, 171, 179, 183, 184, 191

[162] Avenhaus, M., Eckstein, A., Mosley, P. J. & Silberhorn, C. Fiber-assisted single-photon spectrograph. *Optics letters* **34**, 2873–2875 (2009). 73, 101

[163] Davis, A. O., Saulnier, P. M., Karpinski, M. & Smith, B. J. Pulsed single-photon spectrograph by frequency-to-time mapping using chirped fiber bragg gratings. *arXiv:1610.03040* (2016). 73, 101

[164] Ren, C. & Hofmann, H. F. Time-resolved measurement of the quantum states of photons using two-photon interference with short-time reference pulses. *Phys. Rev. A* **84**, 032108 (2011). 77, 78

[165] Rarity, J. & Tapster, P. Quantum interference: experiments and applications. *Phil. Trans. R. Soc. A* **355**, 2267–2277 (1997). 77

[166] Pittman, T. B. & Franson, J. D. Violation of bells inequality with photons from independent sources. *Phys. Rev. Lett.* **90**, 240401 (2003). 77

[167] Polycarpou, C. *et al.* Adaptively measuring the temporal shape of ultrashort single photons for higher-dimensional quantum information processing. *arXiv:1111.7161v1 [quant-ph]* (2011). 79

[168] Donohue, J. M., Mazurek, M. D. & Resch, K. J. Theory of high-efficiency sum-frequency generation for single-photon waveform conversion. *Phys. Rev. A* **91**, 033809 (2015). 80, 179, 182, 183, 184, 191

[169] Miatto, F. M. *High dimensional spatial entanglement with photon pairs.* Ph.D. thesis, University of Strathclyde (2012). 82

[170] Brańcyzk, A. M. *Non-classical States of Light.* Ph.D. thesis, The University of Queensland (2010). 84, 95

[171] Brańczyk, A. M., Stace, T. M. & Ralph, T. C. Time ordering in spontaneous parametric down-conversion. In Ralph, T. C. & Lam, P. K. (eds.) *Proceedings of the Tenth International Conference on Quantum Communication, Measurement and Computation*, vol. 1363 of *AIP Conf. Proc.*, 335 (AIP, New York, 2011). 84

[172] Christ, A., Brecht, B., Mauerer, W. & Silberhorn, C. Theory of quantum frequency conversion and type-II parametric down-conversion in the high-gain regime. *New J. Phys.* **15**, 053038 (2013). 84, 85

[173] Quesada, N. & Sipe, J. E. Effects of time ordering in quantum nonlinear optics. *Phys. Rev. A* **90**, 063840 (2014). 84, 87

[174] Sakurai, J. J. *Modern quantum mechanics* (Addison-Wesley, 2011). 84

[175] Quesada, N. & Sipe, J. Limits in high efficiency quantum frequency conversion. *arXiv:1508.03361* (2015). 84

[176] Guerreiro, T. *et al.* High efficiency coupling of photon pairs in practice. *Opt. Express* **21**, 27641–27651 (2013). 88, 90, 91

[177] Shalm, L. K. SPDCalc. URL http://spdcalc.org/. 90

[178] Klyshko, D. N. Use of two-photon light for absolute calibration of photoelectric detectors. *Soviet Journal of Quantum Electronics* **10**, 1112 (1980). 91

[179] Grice, W. P. & Walmsley, I. A. Spectral information and distinguishability in type-II down-conversion with a broadband pump. *Phys. Rev. A* **56**, 1627–1634 (1997). 91, 113

[180] Grice, W. P., U'Ren, A. B. & Walmsley, I. A. Eliminating frequency and space-time correlations in multiphoton states. *Phys. Rev. A* **64**, 063815 (2001). 91, 94, 113, 176, 181, 200

[181] Brańczyk, A. M., Ralph, T. C., Helwig, W. & Silberhorn, C. Optimized generation of heralded Fock states using parametric down-conversion. *New J. Phys.* **12**, 063001 (2010). 91

[182] Eckstein, A., Christ, A., Mosley, P. J. & Silberhorn, C. Highly efficient single-pass source of pulsed single-mode twin beams of light. *Phys. Rev. Lett.* **106**, 013603 (2011). 91, 176, 200

[183] Lutz, T., Kolenderski, P. & Jennewein, T. Demonstration of spectral correlation control in a source of polarization-entangled photon pairs at telecom wavelength. *Opt. Lett.* **39**, 1481–1484 (2014). 91, 176, 200

[184] Ansari, V., Brecht, B., Harder, G. & Silberhorn, C. Probing spectral-temporal correlations with a versatile integrated source of parametric down-conversion states. *arXiv:1404.7725* (2014). 91, 176

[185] Gajewski, A. & Kolenderski, P. Spectral correlation in down-converted photon pairs at telecom wavelength. *arXiv:1509.01262* (2015). 91

[186] Zukowski, M., Zeilinger, A. & Weinfurter, H. Entangling photons radiated by independent pulsed sources. *Ann. N. Y. Acad. Sci.* **755**, 91–102 (1995). 91

[187] Kaltenbaek, R., Blauensteiner, B., Żukowski, M., Aspelmeyer, M. & Zeilinger, A. Experimental interference of independent photons. *Physical review letters* **96**, 240502 (2006). 91

[188] Huang, Y.-P., Altepeter, J. B. & Kumar, P. Optimized heralding schemes for single photons. *Phys. Rev. A* **84**, 033844 (2011). 91

[189] Weisstein, E. W. Statistical correlation. URL http://mathworld.wolfram.com/StatisticalCorrelation.html. 94

[190] Giovannetti, V., Maccone, L., Shapiro, J. H. & Wong, F. N. Extended phase-matching conditions for improved entanglement generation. *Phys. Rev. A* **66**, 043813 (2002). 95

[191] Kuzucu, O., Fiorentino, M., Albota, M. A., Wong, F. N. C. & Kärtner, F. X. Two-photon coincident-frequency entanglement via extended phase matching. *Phys. Rev. Lett.* **94**, 083601 (2005). 95

[192] Gerrits, T. *et al.* Generation of degenerate, factorizable, pulsed squeezed light at telecom wavelengths. *Opt. Express* **19**, 24434–24447 (2011). 97

[193] Harder, G. *et al.* An optimized photon pair source for quantum circuits. *Opt. Express* **21**, 13975–13985 (2013). 97

[194] Nasr, M. B. *et al.* Ultrabroadband biphotons generated via chirped quasi-phase-matched optical parametric down-conversion. *Phys. Rev. Lett.* **100**, 183601 (2008). 100, 122, 203

[195] Steinberg, A., Kwiat, P. & Chiao, R. Dispersion cancellation in a measurement of the single-photon propagation velocity in glass. *Phys. Rev. Lett.* **68**, 2421 (1992). 102, 122

[196] Abouraddy, A. F., Nasr, M. B., Saleh, B. E., Sergienko, A. V. & Teich, M. C. Quantum-optical coherence tomography with dispersion cancellation. *Phys. Rev. A* **65**, 053817 (2002). 102, 122

[197] Franson, J. Nonlocal cancellation of dispersion. *Phys. Rev. A* **45**, 3126 (1992). 102

[198] Mower, J. *et al.* High-dimensional quantum key distribution using dispersive optics. *Phys. Rev. A* **87**, 062322 (2013). 102

[199] Zhong, T. & Wong, F. N. Nonlocal cancellation of dispersion in franson interferometry. *Phys. Rev. A* **88**, 020103 (2013). 102, 197

[200] Kaltenbaek, R., Lavoie, J., Biggerstaff, D. N. & Resch, K. J. Quantum-inspired interferometry with chirped laser pulses. *Nat. Phys.* **4**, 864–868 (2008). 102

[201] Lavoie, J., Kaltenbaek, R. & Resch, K. J. Quantum-optical coherence tomography with classical light. *Opt. Express* **17**, 3818–3825 (2009). 102

[202] Prevedel, R., Schreiter, K., Lavoie, J. & Resch, K. Classical analog for dispersion cancellation of entangled photons with local detection. *Phys. Rev, A* **84**, 051803 (2011). 102

[203] Berg, C. *Complex Analysis* (Department of Mathematical Sciences, University of Copenhagen, København, 2012), 3rd edn. 102

[204] Mosley, P. J. *et al.* Heralded generation of ultrafast single photons in pure quantum states. *Phys. Rev. Lett.* **100**, 133601 (2008). 103, 113

[205] Butcher, P. N. & Cotter, D. *Cambridge Studies in Modern Optics 9: The Elements of Nonlinear Optics* (Cambridge University Press, Cambridge, 1990), 1st edn. 107

[206] Born, M. & Wolf, E. *Principles of Optics* (Cambridge University Press, Cambridge, 1999), 7th edn. 107

[207] Turpin, A., Loiko, Y. V., Kalkandjiev, T., Tomizawa, H. & Mompart, J. Wave-vector and polarization dependence of conical refraction. *Opt. Express* **21**, 4503–4511 (2013). 107

[208] Clemmen, S., Farsi, A., Ramelow, S. & Gaeta, A. L. Ramsey interference with single photons. *Phys. Rev. Lett.* **117**, 223601 (2016). 109, 179, 190, 191

[209] Kobayashi, T. *et al.* Frequency-domain Hong Ou Mandel interference. *Nature Photon.* . 109

[210] Duan, L.-M., Lukin, M. D., Cirac, J. I. & Zoller, P. Long-distance quantum communication with atomic ensembles and linear optics. *Nature (London)* **414**, 413–418 (2001). 113

[211] Wootters, W. K. & Zurek, W. H. A single quantum cannot be cloned. *Nature (London)* **299**, 802–803 (1982). 113

[212] Kim, Y.-H. & Grice, W. P. Generation of pulsed polarization-entangled two-photon state via temporal and spectral engineering. *J. Mod. Opt.* **49**, 2309–2323 (2002). 113

[213] Brendel, J., Gisin, N., Tittel, W. & Zbinden, H. Pulsed energy-time entangled twin-photon source for quantum communication. *Phys. Rev. Lett.* **82**, 2594 (1999). 113

[214] Jiang, Y.-K. & Tomita, A. Highly efficient polarization-entangled photon source using periodically poled lithium niobate waveguides. *Opt. Commun.* **267**, 278–281 (2006). 113

[215] Christ, A., Lupo, C. & Silberhorn, C. Exponentially enhanced quantum communication rate by multiplexing continuous-variable teleportation. *New J. Phys.* **14**, 083007 (2012). 113

[216] Herbauts, I., Blauensteiner, B., Poppe, A., Jennewein, T. & Huebel, H. Demonstration of active routing of entanglement in a multi-user network. *Opt. Express* **21**, 29013–29024 (2013). 113, 122, 154

[217] Donohue, J. M., Lavoie, J. & Resch, K. J. Ultrafast time-division demultiplexing of polarization-entangled photons. *Phys. Rev. Lett.* **113**, 163602 (2014). 113, 153

[218] Hosseini, M., Sparkes, B. M., Campbell, G., Lam, P. K. & Buchler, B. C. High efficiency coherent optical memory with warm rubidium vapour. *Nat. Commun.* **2**, 174 (2011). 113, 122

[219] England, D. G. *et al.* Storage and retrieval of THz-bandwidth single photons using a room-temperature diamond quantum memory. *Phys. Rev. Lett.* **114**, 053602 (2015). 113, 122

[220] Kumar, P. Quantum frequency conversion. *Opt. Lett.* **15**, 1476–1478 (1990). 113

[221] McKinstrie, C. J., Harvey, J., Radic, S. & Raymer, M. G. Translation of quantum states by four-wave mixing in fibers. *Opt. Express* **13**, 9131–9142 (2005). 113, 114

[222] McGuinness, H. J., Raymer, M. G. & McKinstrie, C. J. Theory of quantum frequency translation of light in optical fiber: application to interference of two photons of different color. *Opt. Express* **19**, 17876–17907 (2011). 113

[223] Kowligy, A. S. *et al.* Quantum optical arbitrary waveform manipulation and measurement in real time. *Opt. Express* **22**, 27942–27957 (2014). 113

[224] Kielpinski, D., Corney, J. F. & Wiseman, H. M. Quantum optical waveform conversion. *Phys. Rev. Lett.* **106**, 130501 (2011). 113, 135, 154, 203

[225] Agha, I., Ates, S., Sapienza, L. & Srinivasan, K. Spectral broadening and shaping of nanosecond pulses: toward shaping of single photons from quantum emitters. *Opt. Lett.* **39**, 5677–5680 (2014). 113, 179, 203

[226] Vandevender, A. P. & Kwiat, P. G. High efficiency single photon detection via frequency up-conversion. *J. Mod. Opt.* **51**, 1433–1445 (2004). 114, 135, 150, 179

[227] VanDevender, A. P. & Kwiat, P. G. Quantum transduction via frequency upconversion. *J. Opt. Soc. Am. B* **24**, 295–299 (2007). 114

[228] Thew, R. T., Zbinden, H. & Gisin, N. Tunable upconversion photon detector. *Appl. Phys. Lett.* **93**, 071104–071104 (2008). 114, 150

[229] Rakher, M. T., Ma, L., Slattery, O., Tang, X. & Srinivasan, K. Quantum transduction of telecommunications-band single photons from a quantum dot by frequency upconversion. *Nat. Photon.* **4**, 786–791 (2010). 114

[230] McKinstrie, C. J., Mejling, L., Raymer, M. G. & Rottwitt, K. Quantum-state-preserving optical frequency conversion and pulse reshaping by four-wave mixing. *Phys. Rev. A* **85**, 053829 (2012). 114

[231] Liu, C., Dutton, Z., Behroozi, C. H. & Hau, L. V. Observation of coherent optical information storage in an atomic medium using halted light pulses. *Nature* **409**, 490–493 (2001). 114

[232] Pe'er, A., Dayan, B., Friesem, A. A. & Silberberg, Y. Temporal shaping of entangled photons. *Phys. Rev. Lett.* **94**, 073601 (2005). 114, 154, 176, 190

[233] Hadamard, J. Sur le rayon de convergence des séries ordonnées suivant les puissances d'une variable. *C. R. Acad. Sci. Paris* **106**, 259–262 (1888). 116

[234] Schmidt, M. & Lipson, H. Distilling free-form natural laws from experimental data. *Science* **324**, 81–85 (2009). URL http://www.nutonian.com/products/eureqa/. 117

[235] Bennett, C. H., Bernstein, H. J., Popescu, S. & Schumacher, B. Concentrating partial entanglement by local operations. *Phys. Rev. A* **53**, 2046 (1996). 121

[236] Eisaman, M. D., Fan, J., Migdall, A. & Polyakov, S. V. Invited review article: Single-photon sources and detectors. *Review of Scientific Instruments* **82**, 071101 (2011). 122

[237] Marcikic, I. *et al.* Time-bin entangled qubits for quantum communication created by femtosecond pulses. *Phys. Rev. A* **66**, 062308 (2002). 122, 135

[238] Dayan, B. *et al.* Two photon absorption and coherent control with broadband down-converted light. *Phys. Rev. Lett.* **93**, 023005 (2004). 122

[239] De Riedmatten, H., Afzelius, M., Staudt, M. U., Simon, C. & Gisin, N. A solid-state light–matter interface at the single-photon level. *Nature* **456**, 773–777 (2008). 122

[240] Choi, K. S., Deng, H., Laurat, J. & Kimble, H. Mapping photonic entanglement into and out of a quantum memory. *Nature* **452**, 67–71 (2008). 122

[241] Lvovsky, A. I., Sanders, B. C. & Tittel, W. Optical quantum memory. *Nature photonics* **3**, 706–714 (2009). 122

[242] Ou, Z. & Lu, Y. Cavity enhanced spontaneous parametric down-conversion for the prolongation of correlation time between conjugate photons. *Physical Review Letters* **83**, 2556 (1999). 122

[243] Bao, X.-H. *et al.* Generation of narrow-band polarization-entangled photon pairs for atomic quantum memories. *Phys. Rev. Lett.* **101**, 190501 (2008). 122

[244] Wolfgramm, F. *et al.* Bright filter-free source of indistinguishable photon pairs. *Optics express* **16**, 18145–18151 (2008). 122

[245] McKeever, J. *et al.* Deterministic generation of single photons from one atom trapped in a cavity. *Science* **303**, 1992–1994 (2004). 122

[246] Reimer, M. E. *et al.* Bright single-photon sources in bottom-up tailored nanowires. *Nature communications* **3**, 737 (2012). 122

[247] Jayakumar, H. *et al.* Deterministic photon pairs and coherent optical control of a single quantum dot. *Physical review letters* **110**, 135505 (2013). 122

[248] England, D., Bustard, P., Nunn, J., Lausten, R. & Sussman, B. From photons to phonons and back: a THz optical memory in diamond. *Physical review letters* **111**, 243601 (2013). 122

[249] Raoult, F. *et al.* Efficient generation of narrow-bandwidth picosecond pulses by frequency doubling of femtosecond chirped pulses. *Opt. Lett.* **23**, 1117–1119 (1998). 125, 137

[250] Osvay, K. & Ross, I. N. Efficient tuneable bandwidth frequency mixing using chirped pulses. *Opt. Comm.* **166**, 113–119 (1999). 125, 137

[251] Veitas, G. & Danielius, R. Generation of narrow-bandwidth tunable picosecond pulses by difference-frequency mixing of stretched pulses. *J. Opt. Soc. Am. B* **16**, 1561 (1999). 125

[252] Nejbauer, M. & Radzewicz, C. Efficient spectral shift and compression of femtosecond pulses by parametric amplification of chirped light. *Opt. Express* **20**, 2136–2142 (2012). 127

[253] Lavoie, J. *Experimental quantum information processing with photons.* Ph.D. thesis, University of Waterloo (2013). 130, 234

[254] Nejbauer, M., Kardaś, T. M., Stepanenko, Y. & Radzewicz, C. Spectral compression of femtosecond pulses using chirped volume bragg gratings. *Opt. Lett.* **41**, 2394–2397 (2016). 130

[255] Allgaier, M. *et al.* Highly efficient frequency conversion with bandwidth compression of quantum light. *arXiv:1610.08326* (2016). 133

[256] Franson, J. D. Bell inequality for position and time. *Phys. Rev. Lett.* **62**, 2205–2208 (1989). 135, 147, 190, 191, 197, 200

[257] Franson, J. D. Two-photon interferometry over large distances. *Phys. Rev. A* **44**, 4552–4555 (1991). 135

[258] Shah, J. Ultrafast luminescence spectroscopy using sum frequency generation. *IEEE J. Quantum Electron.* **24**, 276–288 (1988). 135

[259] Dayan, B., Pe'er, A., Friesem, A. A. & Silberberg, Y. Two photon absorption and coherent control with broadband down-converted light. *Phys. Rev. Lett.* **93**, 023005 (2004). 135

[260] Huang, J. & Kumar, P. Observation of quantum frequency conversion. *Phys. Rev. Lett.* **68**, 2153–2156 (1992). 135, 179

[261] Ramelow, S. *et al.* Polarization-entanglement-conserving frequency conversion of photons. *Phys. Rev. A* **85**, 013845 (2012). 135

[262] de Burgh, M. D. *et al.* Choice of measurement sets in qubit tomography. *Phys. Rev. A* **78**, 052122 (2008). 135, 149

[263] Takesue, H. & Noguchi, Y. Implementation of quantum state tomography for time-bin entangled photon pairs. *Opt. Express* **17**, 10976–10989 (2009). 135

[264] Wang, S. X. *et al.* High-speed tomography of time-bin-entangled photons using a single-measurement setting. *Phys. Rev. A* **86**, 042122 (2012). 135

[265] Bennett, C. H. *et al.* Remote state preparation. *Phys. Rev. Lett.* **87**, 077902 (2001). 148

[266] Sensarn, S., Yin, G. Y. & Harris, S. E. Generation and compression of chirped biphotons. *Phys. Rev. Lett.* **104**, 253602 (2010). 152

[267] Kuo, P. S. *et al.* Spectral response of an upconversion detector and spectrometer. *Opt. Express* **21**, 22523–22531 (2013). 152

[268] Bennett, C. H. *et al.* Teleporting an unknown quantum state via dual classical and Einstein-Podolsky-Rosen channels. *Phys. Rev. Lett.* **70**, 1895 (1993). 154

[269] Ekert, A. K. Quantum cryptography based on Bell's theorem. *Phys. Rev. Lett.* **67**, 661 (1991). 154

[270] Acin, A., Gisin, N. & Masanes, L. From Bell's theorem to secure quantum key distribution. *Phys. Rev. Lett.* **97**, 120405 (2006). 154

[271] Brackett, C. A. Dense wavelength division multiplexing networks: Principles and applications. *IEEE J. Sel. Area. Commun.* **8**, 948–964 (1990). 154

[272] Kawanishi, S. Ultrahigh-speed optical time-division-multiplexed transmission technology based on optical signal processing. *IEEE J. Quant. Electron.* **34**, 2064–2079 (1998). 154

[273] Townsend, P. D. Simultaneous quantum cryptographic key distribution and conventional data transmission over installed fibre using wavelength-division multiplexing. *Electron. Lett.* **33**, 188–190 (1997). 154

[274] Brassard, G., Bussieres, F., Godbout, N. & Lacroix, S. Multiuser quantum key distribution using wavelength division multiplexing. In *Applications of Photonic Technology*, 149–153. International Society for Optics and Photonics (SPIE (Bellingham, WA), 2003). 154

[275] Chen, J. *et al.* Stable quantum key distribution with active polarization control based on time-division multiplexing. *New J. Phys.* **11**, 065004 (2009). 154

[276] Qi, B., Zhu, W., Qian, L. & Lo, H.-K. Feasibility of quantum key distribution through a dense wavelength division multiplexing network. *New J. Phys.* **12**, 103042 (2010). 154

[277] Choi, I., Young, R. J. & Townsend, P. D. Quantum key distribution on a 10Gb/s WDM-PON. *Opt. Express* **18**, 9600–9612 (2010). 154

[278] Sasaki, M. *et al.* Field test of quantum key distribution in the Tokyo QKD network. *Opt. Express* **19**, 10387–10409 (2011). 154

[279] Ghalbouni, J., Agha, I., Frey, R., Diamanti, E. & Zaquine, I. Experimental wavelength-division-multiplexed photon-pair distribution. *Opt. Lett.* **38**, 34–36 (2013). 154

[280] Shayovitz, D. *et al.* High resolution time-to-space conversion of sub-picosecond pulses at 1.55 μm by non-degenerate sfg in ppln crystal. *Opt. Express* **20**, 27388–27395 (2012). 154

[281] Kim, Y.-H., Kulik, S. P. & Shih, Y. Quantum teleportation of a polarization state with a complete bell state measurement. *Phys. Rev. Lett.* **86**, 1370 (2001). 154

[282] Vandevender, A. P. & Kwiat, P. G. High efficiency single photon detection via frequency up-conversion. *J. Mod. Opt.* **51**, 1433–1445 (2004). 154, 171

[283] Langrock, C. *et al.* Highly efficient single-photon detection at communication wavelengths by use of upconversion in reverse-proton-exchanged periodically poled LiNbO3 waveguides. *Opt. Lett.* **30**, 1725–1727 (2005). 154, 171

[284] Ramelow, S., Fedrizzi, A., Poppe, A., Langford, N. K. & Zeilinger, A. Polarization-entanglement-conserving frequency conversion of photons. *Phys. Rev. A* **85**, 013845 (2012). 154, 156, 164, 171

[285] VanDevender, A. P. & Kwiat, P. G. High-speed transparent switch via frequency upconversion. *Optics Exp.* **15**, 4677–4683 (2007). 154

[286] Harris, S. Chirp and compress: toward single-cycle biphotons. *Phys. Rev. Lett.* **98**, 063602 (2007). 154

[287] ODonnell, K. A. & URen, A. B. Time-resolved up-conversion of entangled photon pairs. *Phys. Rev. Lett.* **103**, 123602 (2009). 154

[288] Rakher, M. T. *et al.* Simultaneous wavelength translation and amplitude modulation of single photons from a quantum dot. *Phys. Rev. Lett.* **107**, 083602 (2011). 154

[289] Lukens, J. M. *et al.* Orthogonal spectral coding of entangled photons. *Phys. Rev. Lett.* **112**, 133602 (2014). 154

[290] Dromey, B. *et al.* Generation of a train of ultrashort pulses from a compact birefringent crystal array. *Appl. Opt.* **46**, 5142–5146 (2007). 160

[291] Schmid, D. *et al.* Adjustable and robust methods for polarization-dependent focusing. *Opt. Express* **21**, 15538–15552 (2013). 167

[292] Sensarn, S., Ali-Khan, I., Yin, G. & Harris, S. Resonant sum frequency generation with time-energy entangled photons. *Phys. Rev. Lett.* **102**, 053602 (2009). 171

[293] Nunn, J. *et al.* Large-alphabet time-frequency entangled quantum key distribution by means of time-to-frequency conversion. *Opt. Express* **21**, 15959–15973 (2013). 176

[294] Kuzucu, O., Wong, F. N., Kurimura, S. & Tovstonog, S. Joint temporal density measurements for two-photon state characterization. *Phys. Rev. Lett.* **101**, 153602 (2008). 176, 190, 191, 200

[295] Tsang, M. & Psaltis, D. Propagation of temporal entanglement. *Phys. Rev. A* **73**, 013822 (2006). 177

[296] Gu, C., Ilan, B. & Sharping, J. E. Demonstration of nondegenerate spectrum reversal in optical-frequency regime. *Opt. Lett.* **38**, 591–593 (2013). 177

[297] Lukens, J. M., Odele, O. D., Leaird, D. E. & Weiner, A. M. Electro-optic modulation for high-speed characterization of entangled photon pairs. *Opt. Lett.* **40**, 5331–5334 (2015). 177

[298] Kwiat, P. G., Steinberg, A. M. & Chiao, R. Y. High-visibility interference in a Bell-inequality experiment for energy and time. *Phys. Rev. A* **47**, R2472–R2475 (1993). 190, 191, 197, 200

[299] Ansari, V. *et al.* Temporal-mode tomography of single photons. *arXiv:1607.03001* (2016). 202

[300] Carrasco, S. *et al.* Enhancing the axial resolution of quantum optical coherence tomography by chirped quasi-phase matching. *Opt. Lett.* **29**, 2429–2431 (2004). 203

[301] Pedrotti, L. M. & Agha, I. Theoertical investigation of quantum waveform shaping for single-photon emitters. *Bulletin of the American Physical Society* (2016). 203

APPENDICES

Appendix A

Experimental tips

In this appendix, we outline a few practical tips for aligning optical setups like those described in the thesis. Many of these are hinted at throughout the thesis, but collected here for the convenience of panicked MSc students.

Jonathan Lavoie deserves a special thanks for this section, as most of the following techniques were directly passed down from him.

A.1   Aligning bulk single-photon upconversion

The goal of bulk upconversion is to mix two pulses, one of which is a strong escort, the other of which is a weak pulse or single photon. The most important step when aligning these experiments is timing, and properly preparing for pulse matching can save weeks of effort. The first step is to match the single photon source with a weak alignment pulse, usually picked off of the escort pulse (see Fig. 3.9, for example). To match these, a measuring tape is an obvious first step, and they can be matched more exactly through Hong-Ou-Mandel interference, as in Sec. 2.3.5, where the weak beam is attenuated using neutral density filters to the approximate same intensity as the single-photon beam. Generally, the HOM interferometer will be aligned with two fibre-connected inputs, such that a fibre-to-fibre link leads to the interferometer. Since the length of the fibres leading to the interferometer

may differ, generally we take the HOM measurement with the weak pulse in one port and the single photons in the other, then switch which input goes to which port and consider them matched when switching the port has no effect on the location of the HOM dip. Note that this HOM method is only applicable to cases where the weak beam is at the same wavelength as the photons, which may not be possible if the escort does not have sufficient bandwidth.

Once the weak and photons are matched, the escort and weak must be matched. Mounting the escort on a retroreflector on a rail allows for quick, reliable on-the-fly delay adjustment, but in cases where the escort and photons originate from different pulses of the Ti:Sapph (as is unavoidable in experiments using fibre spools to chirp photons and gratings to chirp escort pulses), there is still a 12.5 ns (3.75 m) "dead zone" to avoid. To more closely align the pulses, the single-photon APD detectors can be used. While their time resolution is on the order of 1 ns (tens of centimeters), taking a histogram of time tags with respect to a common clock pulse (for example, a small pickoff of the escort) and fitting the result can provide a reasonably accurate measure of how matched the two are (at least to bring them within the range of the retroreflector). The weak and the escort can be matched this way by coupling a small amount of light at a common point, such as the point where the beams combine for SFG. However, the timing of the APDs (at least of those used in this thesis) is oddly dependent on the photon count rate that they register, with more intense sources registering as "earlier" than dim ones. For this reason, when using this method, it is important to work well below detector saturation (preferably near 100,000 counts per second), and ensure through attenuation that the count rates of the signals being matched are closely comparable.

Once the coarse-grained timing has been taken care of, there remain a handful of degrees of freedom remaining to optimize sum-frequency generation: polarization, spatial overlap, phasematching, focus, and fine-tuned time delay. As the sum-frequency signal only appears if all of these are reasonably well-aligned, we recommend the method outlined in Fig. A.1 to start alignment of a non-collinear sum-frequency process [253]. For a collinear process, as in Sec. 5, the same tips apply, except that the two beams are generally combined on a dichroic filter. To ensure they occupy the same spatial mode after combination, a camera can be used, or both can be coupled into the same single-mode fibre.
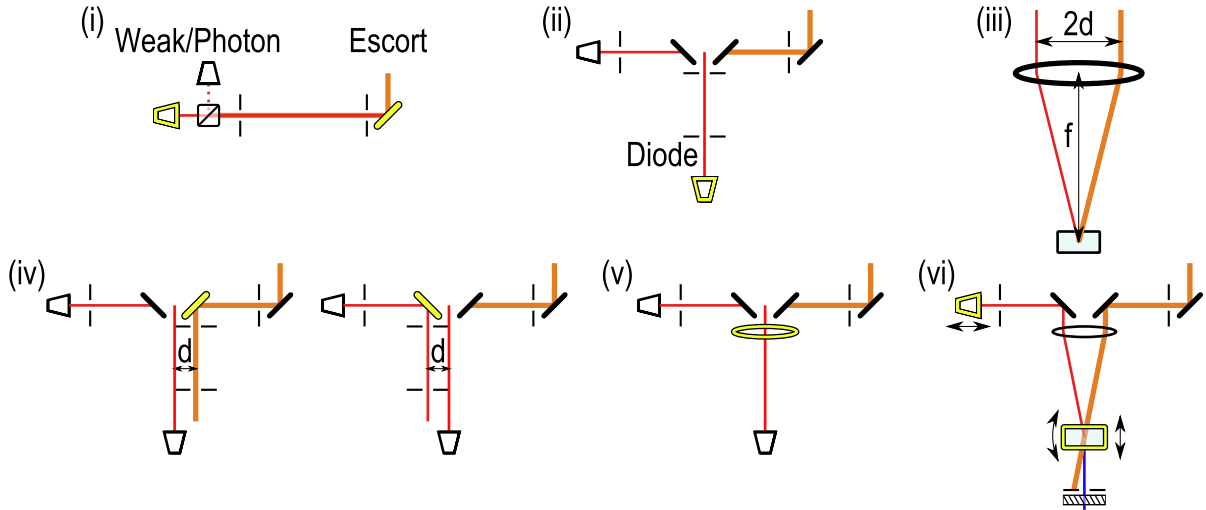
Figure A.1: **Alignment of noncollinear sum-frequency generation.** The optics being adjusted at any point in the alignment procedure are highlighted in yellow. (i) For ease of realignment, the weak pulse (which substitutes for the photon) and escort should follow the same path and in particular at the same height. Beam blocking is important for this step, as the strong escort pulse may damage the fibre if it reaches it. A PBS in conjunction with bat ears or wave plates should be used to set the polarization of the weak pulse. (ii) Using the table holes to define a centre, a diode should be aligned to run exactly in between the eventual weak and escort paths. Once aligned, the irises on the table should be replaced with irises on translation mounts, which are then centred using the diode light. (c) The distance between the escort and weak path is determined by the desired incidence angle in the crystal, $\tan\theta = d/f$. A smaller angle allows for greater overlap throughout the crystal, but makes it more difficult to isolate the second-harmonic background spatially and align the two prism mirrors. An angle of $\theta \approx 5°$ is usually manageable. (iv) The two mirrors are then adjusted to align the escort and weak to be parallel with separation $2d$, set by translating the irises. The mirrors are usually quite close to avoid clipping while maintaining a small angle θ, and may bump each other; it is always prudent to double-check both after alignment. (v) The lens should then be backreflected using the diode. (vi) The nonlinear crystal should be placed a distance f from the lens, and the fine-tuned timing, fine-tuned spatial overlap, phasematching, and focus adjusted until a blue signal is seen. A dark room and a filter that removes the NIR light are very useful for spotting the upconverted signal.

Firstly, it is important to start with two well-collimated beams. The escort generally will not have been fibre coupled, but travels over a longer distance, usually necessitating a reshaping telescope. The weak/photon input will usually be fibre coupled, and while a lot of the alignment that follows can be performed with a bright visible red diode for ease, the beam must be collimated with a beam near the wavelength of intended use to overcome chromatic aberrations. The fibre-coupled beam must also be polarization-controlled using bat-ears or a series of waveplates. If a PBS is inserted after the polarization control and the vertical port is fibre-coupled (potentially with multimode fibre), this extra port can be used to ensure proper polarization control of single-photon signals. A back-propagating diode and irises mounted on translation stages can then be used to align the weak and escort in parallel as in Fig. A.1, with a distance $2d$ between them that will define the angle at which they enter the crystal. Right-angled prism-shaped mirrors are recommended at the point where the escort and weak co-propagate, as they can be mounted much closer together than round mirrors.

Once the rough alignment has been performed as in Fig. A.1(i-v), finding the up-converted signal can still present a problem due to the number of adjustable degrees of freedom. A very dark room, plentiful irises, and NIR-removing filters can be useful to see dim UV signals from weak-beam upconversion. The second-harmonic of the escort should be clearly visible, and in certain cases, the second-harmonic of the weak may also be visible. Adjust the focus to maximize the brightness of the second-harmonic signals; this will provide a good starting point, but the sum-frequency signal will be much more sensitive to the focus than the second harmonic. The phasematching can be roughly aligned by finding the optimal angle for the second-harmonic of each beam and setting the crystal tilt to halfway between these two points. If the spatial overlap is not trusted, this can be double-checked by placing a camera at the focus and ensuring that the weak and escort strike the same point. With enough patience, adjusting the timing with the retroreflector should eventually produce a sum-frequency signal. When adjusting, be aware of the length of your pulses, as for unchirped pulses the timing may be extremely sensitive (millimeter scale). Using a motorized translation stage and stepping through small displacements can be very helpful (especially for finding the photon signal), as moving the retroreflector by hand is less than smooth.

To isolate the signal from the SHG background, it is very helpful to have the photon and escort pulse at different centre wavelengths. The upconverted signal at $\omega_{0s} + \omega_{0e}$ will then be spectrally resolvable from the SHG background at $2\omega_{0e}$, as seen in Fig. 6.6. If the escort bandwidth is insufficient to allow a piece of it to be picked off at the non-degenerate wavelength, it may be necessary to align the SFG setup with a weak pulse at a different central wavelength than the eventual photons. This will have minimal effect on the spatial alignment of the beams, but will result in vastly different optimal phasematching conditions. As the photon signal can be difficult to see over the SHG background when plugged directly into PMTs, it is helpful to take some additional pre-photon steps to estimate the optimal phasematching conditions. Firstly, multi-mode fibre is your friend here, as it will be much less sensitive to the minor spatial shifts which will occur. Also, mount the SFG crystal in a tip-tilt mount with graduated adjustment, such that you can keep track of how much you have adjusted it by. If your Ti:Sapph is tunable, set its central frequency to $(\omega_{0s} + \omega_{0e})/2$ after aligning at the initial settings. The spatial alignment shouldn't change, nor should the timing significantly (except for the different in chirp delay), but the phasematching will. Re-adjust the phasematching until the signal is at its brightest, and note how much you had to change the crystal tilt by (if using temperature tuning, note the temperature difference). If the mount does not rotate about the crystal center, the optimal position of the crystal along the beam focus will also shift; note this difference as well. By tracking this change with the weak beam, this step should only need to be taken once; when switching between weak beam and photons later, simply change the phasematching and focus by the amount found earlier. Once the laser is shifted back to its original wavelength and the photons substituted for the weak beam, these conditions should be close to the ideal conditions for escort-photon upconversion.

237
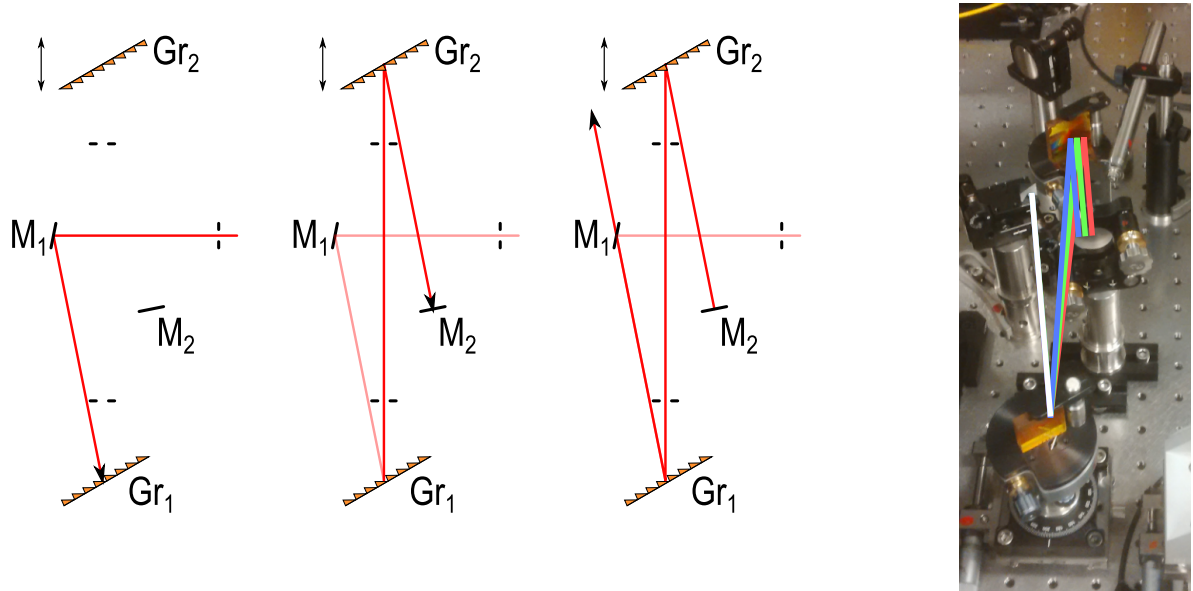
Figure A.2: **Path tracing in a grating-based compressor.**

A.2   Aligning a grating-based pulse compressor

The grating compressor outlined in Sec. 2.3.2 is an essential component of many of the experiments performed in this thesis, and proper alignment of it was essential. In this section, we outline how to align the compressor and ensure its proper operation. A visualization of the beam path taken and a labelling of the elements involved is shown in Fig. A.2. Using pulse compression gratings, the overall efficiency of the pulse compressor should be 65-70%.

When preparing to set up a compressor, it is important to first have an idea of the chirp desired and the input angle. The smaller the angle, the more efficient the compressor will be, as it will be closer and closer to Littrow configuration (depending on the blaze angle of the gratings). For Littrow-designed pulse compression gratings, the efficiency drops off significantly for angles greater than 15 degrees or so, especially since the light is diffracted four times through the compressor. The chirp can be calculated as dependent on the distance between gratings, the input angle, and the grating period, as in Eq. 2.80.

Mounting one of the gratings on a translation stage (preferably Gr_2 to maintain the centre line) will allow for adjustment of the chirp after it has been roughly aligned at the start. Note that the first mirror, M_1, will need to be short such that the beam can travel over it on the return trip. A right-angled prism mirror is ideal for this task, although it may need to be superglued to the stage as a clamp takes up valuable vertical space. A D-shaped mirror may also be effective.

The final compressor must satisfy two primary criteria: the two gratings must be parallel, and the forward and backward path be incident on the gratings at the same angle. Deviations from these criteria will result in a spatially chirped beam (i.e. one with some space-to-frequency coupling in the beam profile). To parallelize the gratings, place Gr_2 in the place of Gr_1 and center it down the irises. If the beam used to align is broadband, this can be difficult as the frequencies will necessarily spread. If possible, kick the pulsed laser into CW mode, which will produce a monochromatic beam near the central wavelength. Use the spread beam to ensure that the vertical tilt is properly aligned with a height-setting mounted Allen key, ensuring that the Allen key bisects the ellipse far from the grating. The height can be carefully set by ensuring both the zeroth and first order diffracted beam propagate parallel to the table, especially for stages with multiple tip adjustment knobs.

To set mirror M_2, it is helpful to mount it on either a translation stage or such that it slides against a platform parallel to the table holes, as seen in the photograph in Fig. A.2. Translate the mirror such that light bounces from M_1 directly onto M_2, and adjust M_2 such that the light backreflects along the same path. Translate M_2 back into place (careful to not clip the beam, which can be difficult for small angles) and tilt it slightly vertically such that the back-propagating light passes overtop of mirror M_1. A bright diode can be used for this instead of difficult-to-see near-infrared light.

Following these alignment steps should produce a beam with a nearly pure chirp. However, slight misalignment will result in spatial chirp. To correct for this, a spectrometer with a real-time fitting program and a thin beam block (such as an Allen key mounted vertically on a post) are useful. Mount the spectrometer to measure the beam after the compressor and note the difference in the fit when blocking the left half of the beam compared to the right half. If the compressor is aligned perfectly, there will be no difference.

Rotate one of the grating stages *slightly* (i.e. less than one degree), noting clockwise or counter-clockwise rotation, realign the beam on the proper path using the horizontal tilt of M_2, and remeasure the spectrum of the left and right sides. Repeat until the two sides are satisfactorily equal. For proper alignment, the input beam and output beam will be directly on top of each other at all points before the output passes over M_1. The alignment and spatial chirp can be fixed to a reasonable degree by adjusting the vertical tilt of M_2 such that the output beam backreflects on M_1, and adjusting the rotation of grating Gr_2 to ensure they are on top of each other at M_1, and the horizontal tilt of M_2 to ensure they are on top of each other at the entrance iris, iterating back and forth until they have converged. If using a tunable laser, the spatial chirp can be made more obvious by checking for a spatial shift of the beam at vastly different wavelengths.

The grating compressor also presents a natural opportunity to implement a high-performance lowpass or highpass filter by simply inserting a beam block to clip the left or right side of the beam at its most stretched point (just before or after Gr_2). A razor blade mounted on a stick can work wonders for this task. In particular, the light from the Chameleon laser has spectral wings that can be easily removed at this point, which otherwise create undesirable background in non-degenerate SFG experiments.

Fine-tuning of the chirp depends greatly on the application. For chirped-pulse upconversion, the bandwidth of the upconverted pulse is minimized for equal and opposite chirps. Adjusting the position of Gr_2 while measuring the upconverted spectrum and setting it at the position with minimal bandwidth is an effective way to set the length of the grating compressor. For situations with no distinct win condition, such as the time lens experiment outlined in Chapter 6, the chirp can be extracted by measuring both the spectrum and an autocorrelation scan of the chirped pulse. For this purpose, it is important to estimate the phasematching conditions of the autocorrelator, as tight phasematching will make a chirped pulse look shorter on an autocorrelation than it actually is.

A.3   Generic tips

- When setting up an optical experiment from scratch, two things should be immediately set as standards for the optical table being worked on: beam height and polarization. Beam height can be set with an small Allen key post-mounted, and tightly secured with a post collar. Irises should be set such that they close on Allen key without bending it, and beam heights can be set by visually ensuring that the Allen key bisects the beam.

- To set the polarization, a zeroing station is recommended as part of the initial setup once the height is set. A beam displacer can be used to generate a very pure polarization state, and if this state is vertically polarized, following it by a PBS will create a space where optics can be inserted and have their axes zeroed in a consistent manner. This setup can be seen in the detailed experimental figure of Fig. 6.4, just after the laser output.

- Be aware of the polarization dependence of gratings. They will usually be effective for horizontal polarization, but only reach high-efficiencies into the first diffracted mode for vertical polarization.

- Keep the coherence time of your pulses in mind, and how to translate that quickly to space. 0.3 ps/mm is a useful set of units to remember the speed of light in for the lab, and a metre of BNC cable or fibre amounts to roughly three nanoseconds.

- The direction of your rotation mounts matters. If data from two rotation mounts are supposed to be compared to one another and one is backwards relative to the other, the data will be inconsistent. This is especially relevant for waveplates, as it can lead to seemingly unphysical density matrices from tomographic reconstruction. I recommend a consistent rule for both the direction the optic and motor/mount faces. For example, the PR50CC motors from Newport have a shiny side and a black side, and the one-inch waveplates from Casix have a slanted side and a notched side. If all your optics are mounted with the notched and shiny side together, and the shiny side facing the detector/power meter, there won't be inconsistencies.

- There is still a potential ambiguity in the alignment of the quarter-wave plate, as if one is zeroed to the fast axis and another to the slow, unphysical density matrices may be measured. If the waveplates are for the same wavelength, put them in series. Two quarter-wave plates at the same angle should act as a half-wave plate; two quarter-wave plates at ϕ and $\pi/2 + \phi$ cancel each other out. If they are at different wavelengths, trial and error works just as well; if you have a Bell state, just see which settings give you a physical density matrix.

- Don't move optical tables in the rain, and if you do cover the holes. If you miss this step, you can tape straws to a wet vacuum (e.g. ShopVac) to suck out the water, one hole at a time. Taping multiple straws to the same vacuum in a toothed formation can expedite this process.

Appendix B

List of IQC publications

J. M. Donohue, M. Mastrovich, and K. J. Resch. Spectrally engineering photonic entanglement with a time lens. arXiv:1604.03588 (2016)

J. M. Donohue and E. Wolfe. Identifying nonconvexity in the sets of limited-dimension quantum correlations. *Physical Review A* **92**, 062120, arXiv:1506.01199 (2015)

J. M. Donohue, M. D. Mazurek, and K. J. Resch. Theory of high-efficiency sum-frequency generation for single-photon waveform conversion. *Physical Review A* **91**, 033809, arXiv:1412.5516 (2015)

J. M. Donohue, J. Lavoie, and K. J. Resch. Ultrafast time-division demultiplexing of polarization-entangled photons. *Physical Review Letters* **113**, 163602, arXiv:1410.4524 (2014)

J. M. Donohue, M. Agnew, J. Lavoie, and K. J. Resch. Coherent ultrafast measurement of time-bin encoded photons. *Physical Review Letters* **111**, 153602, arXiv:1306.1250 (2013)

J. Lavoie, J. M. Donohue, L. G. Wright, A. Fedrizzi, and K. J. Resch. Spectral compression of single photons. *Nature Photonics* **7**, 363, arXiv:1308.0069 (2013)

J. M. Arrazola, O. Gittsovich, J. M. Donohue, J. Lavoie, K. J. Resch, and N. Lütkenhaus. Reliable entanglement verification. *Physical Review A* **87**, 062331, arXiv:1302.1182 (2013)

L. Vermeyden, M. Bonsma, C. Noel, J. M. Donohue, E. Wolfe, and K. J. Resch. Experimental violation of three new families of Bell's inequalities. *Physical Review A* **87**, 032105 (2013)

Appendix C

Reference lists

For ease of reading, this appendix can be used to quickly reference acronyms and symbols used throughout the thesis.

C.1   List of acronyms

3WM: Three wave mixing ($\chi^{(2)}$ process)

APD: Avalanche photodiode

BBO: Barium borate (may be α or β cut), BaB_2O_4

BiBO: Bismuth triborate, BiB_3O_6

CHSH: Clauser-Horne-Shimony-Holt [82], see Sec. 1.3.3

CW: Continuous wave

EOM: Electro-optic modulator

FWHM: Full width at half maximum

H.c.: Hermitian conjugate

HBT: Hanbury-Brown Twiss [21], see Sec. 1.1.3

HOM: Hong-Ou-Mandel [12], see Sec. 1.1.2 and Sec. 2.3.5

HWP: Half-wave plate ($\frac{\lambda}{2}$), see Sec. 1.2.1

LCL: Large-chirp limit

NIR: Near-infrared

PBS: Polarizing beam splitter

PM-SFG: Polarization-maintaining sum-frequency generation, see Sec. 5.2.1

PMT: Photomultiplier tube

PPKTP: Periodically-poled potassium titanyl phosphate, $KTiOPO_4$

PPLN: Periodically-poled lithium niobate, $LiNbO_3$

QOWC: Quantum optical waveform conversion

QWP: Quarter-wave plate ($\frac{\lambda}{4}$), see Sec. 1.2.1

RMS: Root-mean-square

SFG: Sum-frequency generation, see Sec. 2.1.2 and Sec. 3.3

SHG: Second harmonic generation

SPDC: Spontaneous parametric downconversion, see Sec. 3.2

Ti:Sapph: Titanium sapphire, see Sec. 2.3.1

UV: Ultraviolet

C.2   List of commonly used symbols

$\mathcal{F}[\mathbf{f(x)}]$: The Fourier transform of $f(x)$, see Sec. 2.1.1.

$\mathcal{F}[\varrho, \sigma]$: Quantum state fidelity of density matrices ϱ and σ, see Sec. 1.2.1.

$\mathbf{f(x)} \circ \mathbf{g(x)}$: The convolution of $f(x)$ and $g(x)$.

$\mathbf{A}$: Chirp parameter, which defines the quadratic term of the spectral phase. If arising from dispersion from a length L of material, $A = \frac{L}{2}\frac{\mathrm{d}^2 k}{\mathrm{d}\omega^2}|_{\omega=\omega_0} = -\frac{L}{2}\frac{\lambda_0^2}{2\pi c}D_\lambda$. See Sec. 2.2.2.

σ: Angular frequency $\sqrt{1/e}$ or RMS bandwidth, defined for a Gaussian spectral intensity of the form $|f(\omega)|^2 = e^{-\frac{(\omega-\omega_0)^2}{2\sigma^2}}$.

ρ: Statistical correlation, see Sec. 3.2.

ϱ: Density operator of a quantum state.

$|\mathbf{H}\rangle$, $|\mathbf{V}\rangle$, $|\mathbf{D}\rangle$, $|\mathbf{A}\rangle$, $|\mathbf{R}\rangle$, and $|\mathbf{L}\rangle$: Horizontal, vertical, diagonal, anti-diagonal, right-circular, and left-circular polarized photon states. See Sec. 1.2.1.

$|\mathbf{e}\rangle$ and $|\ell\rangle$: Early and late bins, respectively, in qubit time-bin encoding, see Sec. 1.2.2.

$\tau_{\mathbf{e}\ell}$: The time delay between early and late bins in time-bin encoding.

$\tilde{\omega}$: Difference of angular frequency and its centre, $\tilde{\omega} = \omega - \omega_0$

C.3   List of commonly used functions and identities

Single photon polarization states, $\hat{a}_H^\dagger|0\rangle = |H\rangle = \begin{pmatrix} 1 \\ 0 \end{pmatrix}$, $\hat{a}_V^\dagger|0\rangle = |V\rangle = \begin{pmatrix} 0 \\ 1 \end{pmatrix}$

$$|D\rangle = \tfrac{1}{\sqrt{2}}\left(|H\rangle + |V\rangle\right) = \tfrac{1}{\sqrt{2}}\begin{pmatrix} 1 \\ 1 \end{pmatrix}, \quad |A\rangle = \tfrac{1}{\sqrt{2}}\left(|H\rangle - |V\rangle\right) = \tfrac{1}{\sqrt{2}}\begin{pmatrix} 1 \\ -1 \end{pmatrix},$$

$$|R\rangle = \tfrac{1}{\sqrt{2}}\left(|H\rangle - i|V\rangle\right) = \tfrac{1}{\sqrt{2}}\begin{pmatrix} 1 \\ -i \end{pmatrix}, \quad |L\rangle = \tfrac{1}{\sqrt{2}}\left(|H\rangle + i|V\rangle\right) = \tfrac{1}{\sqrt{2}}\begin{pmatrix} 1 \\ i \end{pmatrix}.$$

$$
\begin{aligned}
|\Psi^-\rangle &= \tfrac{1}{\sqrt{2}}\left(|HV\rangle - |VH\rangle\right) = \tfrac{1}{\sqrt{2}}\left(|DA\rangle - |AD\rangle\right) = \tfrac{i}{\sqrt{2}}\left(|LR\rangle - |RL\rangle\right) \\
|\Psi^+\rangle &= \tfrac{1}{\sqrt{2}}\left(|HV\rangle + |VH\rangle\right) = \tfrac{1}{\sqrt{2}}\left(|DD\rangle - |AA\rangle\right) = \tfrac{i}{\sqrt{2}}\left(|LL\rangle - |RR\rangle\right) \\
|\Phi^+\rangle &= \tfrac{1}{\sqrt{2}}\left(|HH\rangle + |VV\rangle\right) = \tfrac{1}{\sqrt{2}}\left(|DD\rangle + |AA\rangle\right) = \tfrac{i}{\sqrt{2}}\left(|LR\rangle + |RL\rangle\right) \\
|\Phi^-\rangle &= \tfrac{1}{\sqrt{2}}\left(|HH\rangle - |VV\rangle\right) = \tfrac{1}{\sqrt{2}}\left(|DA\rangle + |AD\rangle\right) = \tfrac{i}{\sqrt{2}}\left(|LL\rangle + |RR\rangle\right)
\end{aligned}
$$

Pauli matrices, $\sigma_z = \begin{pmatrix} 1 & 0 \\ 0 & -1 \end{pmatrix}$, $\sigma_x = \begin{pmatrix} 0 & 1 \\ 1 & 0 \end{pmatrix}$, $\sigma_y = \begin{pmatrix} 0 & -i \\ i & 0 \end{pmatrix}$.

$$\text{HWP}(\theta) = \begin{pmatrix} \cos 2\theta & \sin 2\theta \\ \sin 2\theta & -\cos 2\theta \end{pmatrix}, \quad \text{QWP}(\theta) = \tfrac{1}{\sqrt{2}}\begin{pmatrix} 1 + i\cos 2\theta & 2i\cos\theta\sin\theta \\ 2i\cos\theta\sin\theta & 1 - i\cos 2\theta \end{pmatrix}$$

$$\text{Purity} = \text{Tr}\left[\rho^2\right], \quad \text{Fidelity} = \mathcal{F}(\sigma, \rho) = \left(\text{Tr}\sqrt{\sqrt{\sigma}\rho\sqrt{\sigma}}\right)^2$$

$$\text{Angle-tuning}, \quad \frac{1}{n_e(\theta)^2} = \frac{\sin^2\theta}{\bar{n}_e^2} + \frac{\cos^2\theta}{n_o^2}$$

$$\text{Normalized Gaussian amplitude}, \quad f(x) = \frac{1}{(2\pi\sigma^2)^{\frac{1}{4}}} e^{-\frac{(x-x_0)^2}{4\sigma^2}}$$

$$f(x,y) = \frac{1}{\sqrt{2\pi\sigma_x\sigma_y}(1-\rho^2)^{\frac{1}{4}}} e^{-\frac{1}{4(1-\rho^2)}\left[\frac{(x-x_0)^2}{\sigma_x^2} + \frac{(y-y_0)^2}{\sigma_y^2} - \frac{2\rho(x-x_0)(y-y_0)}{\sigma_x\sigma_y}\right]}, \text{ where } \rho = \frac{\langle(x-x_0)(y-y_0)\rangle}{\sqrt{\langle(x-x_0)^2\rangle\langle(y-y_0)^2\rangle}}$$

$$\text{Fourier transform}, \quad F(\omega) = \mathcal{F}\left[f(t)\right] = \frac{1}{\sqrt{2\pi}}\int_\infty^\infty dt\, f(t)e^{-i\omega t},$$
$$f(t) = \mathcal{F}^{-1}\left[F(\omega)\right] = \frac{1}{\sqrt{2\pi}}\int_\infty^\infty dt\, F(\omega)e^{i\omega t}$$

$$g^{(2)} = \frac{\langle\hat{n}_c\hat{n}_d\rangle}{\langle\hat{n}_c\rangle\langle\hat{n}_d\rangle} = \frac{\langle\hat{a}^\dagger\hat{a}^\dagger\hat{a}\hat{a}\rangle}{\langle\hat{a}^\dagger\hat{a}\rangle^2} = \frac{\langle\hat{n}_c\hat{n}_d\hat{n}_h\rangle/\langle\hat{n}_h\rangle}{\langle\hat{n}_c\hat{n}_h\rangle\langle\hat{n}_d\hat{n}_h\rangle/\langle\hat{n}_h\rangle^2} = \frac{P(c\&d\&h)P(h)}{P(c\&h)P(c\&d)} = \frac{N_{cdh}N_h}{N_{ch}N_{dh}}$$
$$g^{(1,1)}_{a,b} = \frac{\langle I_a(t)I_b(t)\rangle}{\langle I_a(t)\rangle\langle I_b(t)\rangle} = \frac{\langle\hat{n}_a\hat{n}_b\rangle}{\langle\hat{n}_a\rangle\langle\hat{n}_b\rangle} = \frac{P(a\&b)}{P(a)P(b)}$$